CHEMIA

STUDIA UNIVERSITATIS BABEȘ-BOLYAI
CHEMIA

S T U D I A
UNIVERSITATIS BABEŞ–BOLYAI
CHEMIA

4

CUPRINS – CONTENT – SOMMAIRE – INHALT

Studia Universitatis Babes-Bolyai Chemia has been selected for coverage in Thomson Reuters products and custom information services. Beginning with V. 53 (1) 2008, this publication is indexed and abstracted in the following:

- Science Citation Index Expanded (also known as SciSearch®)
- Chemistry Citation Index®
- Journal Citation Reports/Science Edition

TECHNO-ECONOMIC AND ENVIRONMENTAL ASSESSMENT OF HYDROGEN PRODUCTION BASED ON NATURAL GAS STEAM REFORMING PROCESS

STEFAN GALUSNYAK, LETITIA PETRESCU, CALIN-CRISTIAN CORMOS[a*]

ABSTRACT. Hydrogen is foreseen as a promising energy vector for the future on the road to develop a low carbon economy. In this respect, developing energy-efficient improved hydrogen production systems with low CO_2 emissions is an important aspect. This study is evaluating the most relevant economic and environmental impact elements for hydrogen production based on catalytic natural gas steam reforming. As an illustrative example, an industrial-relevant hydrogen production plant with an output of 50000 Nm^3/h was investigated. In addition, a pre-combustion carbon capture feature, based on reactive gas-liquid absorption using alkanolamines (Methyl-DiEthanol-Amine - MDEA), was considered to reduce the CO_2 emissions. The overall carbon capture rate was 70%. Similar natural gas reforming plant without decarbonization feature is also discussed to quantify the efficiency and economic penalties for CO_2 capture. As assessment methods, computational tools, thermal integration analysis and an in-depth techno-economic and environmental procedure were used. For instance, to quantify the overall environmental impact, Life Cycle Assessment (LCA) was used. Various relevant technical, economic and environmental indicators are calculated and discussed in the present work.

Keywords: Hydrogen production; Natural gas steam reforming; Carbon capture by chemical scrubbing; Techno-economic and environmental assessment.

---

[a] *Babeş-Bolyai University, Faculty of Chemistry and Chemical Engineering, 11 Arany Janos, RO-400028, Cluj-Napoca, Romania*
* Corresponding author: cormos@chem.ubbcluj.ro

INTRODUCTION

Global warming and climate change are significant challenges of the current time. In an attempt to reduce greenhouse gas emission, low carbon technologies have to be developed and deployed in various industrial sectors [1]. A wide diversity of methods and technologies can be considered to reduce CO_2 emissions e.g., large-scale usage of renewable energy sources, carbon capture, utilization and storage (CCUS) options, improving energy conversion, developing new energy carriers with reduced environmental impact [2]. An important element of all new low carbon technologies should be a promising economic impact of the process compared to current state-of-the-art technologies.

Along these important lines, hydrogen is predicted to become an important energy carrier for the future having significant technical, economic and environmental benefits (e.g., high energy conversion efficiency, no greenhouse gas emission when used, lower environmental impact etc.) [3]. Therefore, new developments are expected for the whole hydrogen value chain (production - transport - storage - utilization). Currently, hydrogen is produced from fossil sources (natural gas, oil, coal) with large CO_2 emissions and it is mostly used in chemical and petro-chemical sectors as reactant (e.g., ammonia, various hydrogenation processes etc.) as presented in Figure 1 [4].
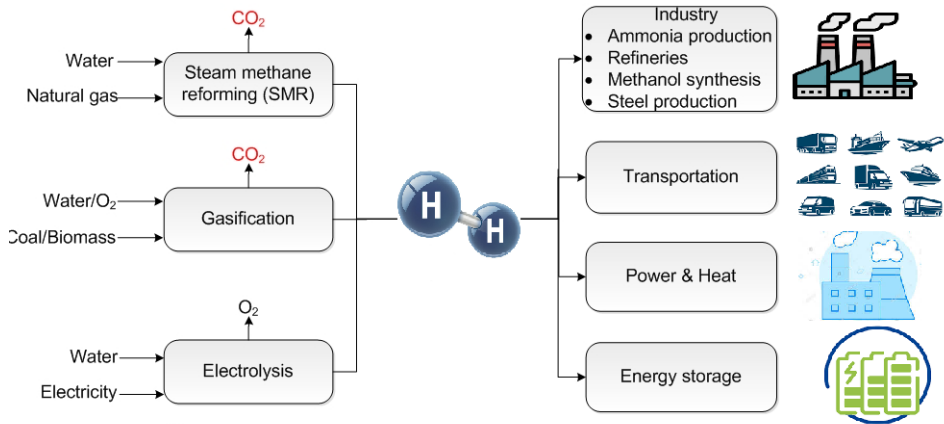
Figure 1. Main hydrogen production routes and applications

This work is aiming to combine the natural gas catalytic steam reforming process (the most used hydrogen production route) with carbon capture feature to significantly reduce the environmental impact of this process. As mentioned before, the new technological concepts must have

techno-economic and environmental advantages over current technologies. In this respect, this analysis will consider similar hydrogen production route without carbon capture as a benchmark case. As key novelty elements of this work, one can mention the usage of an integrated process modeling - thermal integration - techno-economic and environmental assessment methodology to propose improved hydrogen production systems with better performance indicators.

The hydrogen production based on catalytic steam reforming relays of the following reversible chemical reaction:

$$CH_4 + H_2O \leftrightarrow CO + 3H_2 \tag{1}$$
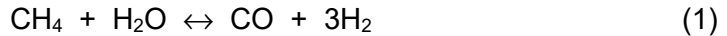
The temperature of the natural gas steam reforming reactor is high (around 800 - 900°C). In addition, the process is highly endothermic, accordingly heat has to be provided. Various configurations can be used, the most important ones are: fired-based reforming reactor (additional natural gas has to be combusted outside of the reactor) and autothermal reforming reactor (heat is generated in-situ using oxygen or air). This work considers the fired-based reforming reactor which has significant benefits than autothermal ones e.g., higher energy efficiency, lower plant complexity, better economics etc. [5-6]. The syngas is then catalytically converted with steam to increase the hydrogen yield and to concentrate the carbon species as CO_2 for subsequent capture. The water gas shift (WGS) reaction is the following:

$$CO + H_2O \leftrightarrow CO_2 + H_2 \tag{2}$$

As decarbonization technology, the chemical scrubbing using MDEA-based gas-liquid absorption process was considered. This carbon capture method is based on the following chemical reaction [7]:

$$CO_2 + MDEA + H_2O \leftrightarrow MDEAH^+ + HCO_3^- \tag{3}$$

The captured CO_2 is then fed to Carbon Processing Unit (CPU) for drying and compression (up to 120 bar) to satisfy the quality requirements of transport (through pipeline) and storage (e.g., saline aquifers, enhanced oil recovery, depleted oil and gas fields etc.) systems. After decarbonization, the hydrogen rich-gas is purified by Pressure Swing Adsorption (PSA) to the required purity (min. 99.95% vol. was considered in this analysis) and then compressed to 60 bar for transport. The tail gas is recycled back to the plant (as fuel to reforming reactor).

PROCESS CONFIGURATION AND MAIN DESIGN ASSUMPTIONS

The following hydrogen production systems based on natural gas catalytic reforming were investigated in term of main techno-economic and environmental performances:

Case 1: Natural gas steam reforming without carbon capture;

Case 2: Natural gas steam reforming with carbon capture.

The conceptual design of decarbonized hydrogen production route based on catalytic natural gas steam reforming process (Case 2) is presented in Figure 2. Several key technological modifications are present in comparison to the correspondent non-decarbonized design (Case 1): carbon capture unit based on chemical scrubbing, carbon processing unit for drying and compression of captured CO_2 stream.
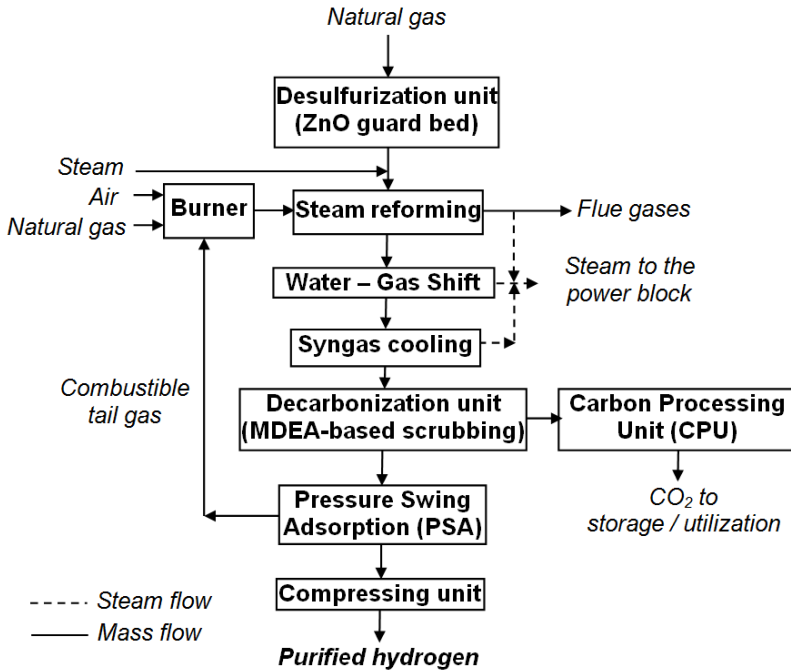
Figure 2. Decarbonized hydrogen production system
based on natural gas steam reforming (Case 2)

The evaluated hydrogen production systems based on natural gas catalytic reforming were simulated using ChemCAD software. Table 1 presents the most important modeling assumptions [8-10].

Table 1. Main design assumptions

Process unit	Design parameters
Plant capacity & purity	50000 Nm^3/h (equivalent to 150 MW_{th}) 99.95% (vol.)
Natural gas characteristics	Composition (% vol.): 89% CH_4, 7% C_2H_6, 1% C_3H_8, 0.1% C_4H_{10}, 0.009% C_5H_{12}, 0.001% C_6H_{14}, 2% CO_2, 0.89% N_2 Lower heating value (LHV): 46.73 MJ/kg Pressure: 30 bar
Desulfurization unit	ZnO guard bed Sulfur removal yield: >99%
Catalytic reformer unit	Outlet temperature: 900°C Gibbs reactor Thermal mode: heat exchanger Pressure drop: 1 bar
Water Gas Shift (WGS) unit	Outlet temperature: 400°C Reactor type: Equilibrium reactor Thermal mode: adiabatic Steam to CO ratio: 2 (molar) Pressure drop: 1 bar
Decarbonization unit Absorption column: Desorption column:	Solvent: Methyl-DiEthanol-Amine (MDEA) Solution concentration: 50 % wt. No. of stages: 20 Column pressure drop: 1 bar No. of stages: 15 Column pressure drop: 1 bar Solvent regeneration with LP steam Heat duty: 0.6 MJ/kg CO_2
CO_2 processing unit (CPU)	Drying agent: Tri-Ethylene-Glycol (TEG) 4 stages with inter-cooling Delivery pressure (at plant gate): 120 bar CO_2 composition (vol. %): >95% CO_2, <2000 ppm CO, <250 ppm H_2O, <100 ppm H_2S, <4% other gases (N_2, Ar, H_2)
Hydrogen compression unit	Delivery pressure: 60 bar Compressor efficiency: 80% Outlet temperature: 30-40°C
Heat recovery unit	Steam conditions: 480°C & 48 bar Steam turbine efficiency: 85% Condensing pressure: 48 mbar Cooling water temperature: 15°C
Heat exchangers	$\Delta T_{min.}$ = 10°C; Pressure drop: 2 - 4% of inlet pressure

PROCESS ASSESSMENT METHODOLOGY

The evaluated cases were simulated using ChemCAD. The thermodynamic package (Soave-Redlich-Kwong - SRK) was selected considering the present chemical species as well as the operational parameters of the processes (e.g., pressure, temperature etc.). For the chemical scrubbing unit, the electrolyte package was used considering the ionic system present in aqueous solution (see reaction 3).

The simulation results were compared with experimental / industrial data for model validation [11-12]. No significant differences were observed. For instance, the methane conversion is about 98% comparable with values from industrial applications. Both hydrogen production designs were optimized in term of energy utilization using pinch method [13]. As an illustrative case, Figure 3 presents the hot and cold composite curves for decarbonized concept (Case 2).
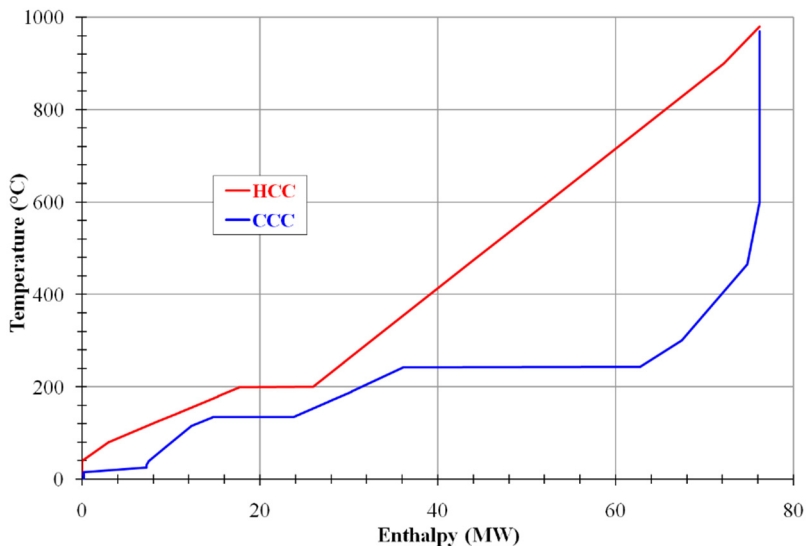
Figure 3. Composite curves for decarbonized hydrogen concept (Case 2)

One can noticed that the available hot streams within the plant (e.g., hot syngas from reforming reactor, shifted gas from WGS reactor, flue gases from reactor burner etc.) are covering the cold stream duties. Even further, an excess heat exists which it is then for steam generation. The generated steam is partly used for catalytic reformer (as reactant) and the rest is expanded in a steam turbine for power generation (to cover the ancillary power consumptions).

Following the thermal integration analysis, the overall mass and energy balances were then used for the quantification of the overall techno-economic and environmental performance indicators. The most important performance indexes are presented below:

- Hydrogen and power generation efficiencies ($\eta_{Hydrogen}$ and η_{power}) show the overall energy yield of the concepts:

$$\eta_{hydrogen} = \frac{Hydrogen\ thermal\ output}{Natural\ gas\ thermal\ input} * 100 \tag{4}$$

$$\eta_{power} = \frac{Net\ power\ output}{Natural\ gas\ thermal\ input} * 100 \tag{5}$$

- Plant decarbonization rate (R_{CO_2}) is quantified as the ratio of captured CO_2 molar flow to the input carbon molar flow of natural gas:

$$R_{CO_2} = \frac{Captured\ CO_2\ molar\ flow}{Input\ carbon\ molar\ flow} * 100 \tag{6}$$

- CO_2 emission factor (E_{CO_2}) is computed considering emitted CO_2 mass flow for each MW power plus hydrogen generated within the process:

$$E_{CO_2} = \frac{Emitted\ CO_2\ mass\ flow}{Hydrogen\ output + Net\ power} * 100 \tag{7}$$

- Capital cost of a specific plant sub-system (C_E) with a given capacity (Q) is calculated by scalling method using the formula which considers the base cost (C_B) corresponding to the base capacity (Q_B):

$$C_E = C_B * (\frac{Q}{Q_B})^M \tag{8}$$

- Specific capital investment (SCI) is calculated as the ratio of total capital cost and the plant energy output (hydrogen and power):

$$SCI = \frac{Total\ capital\ \cos t}{Hydrogen\ output + Net\ power} \tag{9}$$

- Levelized cost of hydrogen (LCOH) is calculated as ratio of annualized capital and operational costs and the plant hydrogen output:

$$LCOH = \frac{Annualized\ capital\ \&\ operational\ \cos ts}{Hydrogen\ output + Net\ power} \quad (10)$$

- CO_2 removal and avoided costs is calculated based on levelized cost of hydrogen and CO_2 emission factors in both non-decarbonized and decarbonized scenarios:

$$CO_2\ removal\ \cos t = \frac{LCOH_{Capture} - LCOH_{No\ capture}}{CO_2\ removed} \quad (11)$$

$$CO_2\ avoided\ \cos t = \frac{LCOH_{Capture} - LCOH_{No\ capture}}{E_{CO_2\ No\ capture} - E_{CO_2\ Capture}} \quad (12)$$

The main economic assumptions used in the evaluation of hydrogen production systems based on natural gas reforming with and without carbon capture are presented in Table 2 [14-16].

Table 2. Main economic assumptions

Natural gas cost, € / GJ	5.0
Boiler feed water (BFW) cost, € / t	0.10
Cooling water (CW) cost, € / t	0.01
CW treatment cost, € / m^3	0.0025
BFW treatment cost, € / month	45000
Personnel number	78
Direct labour cost, € / person / y	50000
Administrative costs, % of direct labour cost	30
Plant maintenance costs, % of CAPEX per year	2.25
Plant capacity factor, %	85.62
Internal rate of return, %	8
CO_2 storage cost, € / t	7
Carbon emission tax, € / t	25
Construction period, years / annual CAPEX share, %	2 / 40, 60
Power plant operation life, years	25

In addition to the global plant environmental indicators (decarbonization rate and CO_2 emission factor), an in-depth Life Cycle Analysis (LCA) was performed for the evaluated cases. The LCA analysis considers not only the

plant but also up-stream (e.g., natural gas, catalysts, solvent chains) and down-stream processes (e.g., CO2 transport and storage, solvent degradation and disposal). As indicators Global Warming Potential (GWP), Freshwater Eutrophication Potential (FEP), Ozone Depletion Potential (ODP), Fossil fuel Depletion Potential (FDP), Freshwater Ecotoxicity Potential (FETP), Human Toxicity Potential (HTP), Metal Depletion Potential (MDP), Photochemical Oxidant Formation Potential (POFP) and Terrestrial Ecotoxicity Potential (TETP) were considered according to the agreed LCA methodology. The LCA results are reported to 1 MW H_2 produced. The full description of the LCA methodology is presented in several different papers of the same authors [17].

RESULTS AND DISCUSSION

Both hydrogen production cases based on natural gas reforming with and without carbon capture were simulated using ChemCAD software. The mass and energy balances of the evaluated concepts were then used for calculation of main performance indicators. Table 3 presents the most important technical indicators.

Table 3. Key technical performance indicators

Performance indicator	UM	Case 1	Case 2
Natural gas flowrate	t/h	15.37	15.37
Natural gas LHV	MJ/kg	46.73	
Natural gas thermal energy	MW$_{th}$	203.63	203.63
Gross power output	MW$_e$	8.51	5.84
Hydrogen thermal output	MW$_{th}$	150.00	150.00
CO$_2$ capture & compression	MW$_e$	0.00	2.12
Hydrogen compression	MW$_e$	2.09	2.09
Power island	MW$_e$	1.05	1.04
Ancillary power consumption	MW$_e$	3.14	5.25
Net power output	MW$_e$	5.37	0.59
Net power efficiency	%	2.63	0.28
Hydrogen thermal efficiency	%	73.66	73.66
Cumulative plant energy efficiency	%	76.29	73.94
Carbon capture rate	%	0.00	70.00
CO$_2$ emissions factor	kg/MWh	267.45	82.50

As can be observed from Table 3, the introduction of pre-combustion carbon capture using a MDEA-based gas-liquid absorption unit involves an energy penalty of about 2.34 net percentage points. On the other hand, the CO_2 specific emission factor was significantly reduced by about 3.24 times (from 267.45 to 82.50 kg/MWh) corresponding to a plant decarbonization rate of 70%. The main reason that the decarbonization rate is not higher than 70% represents the unconverted methane and carbon monoxide in reformer and shift reactors [18]. These chemical compounds are not removed by the chemical scrubbing unit being then combusted in the burner to provide the heat duty required by the reforming reaction. For a higher carbon capture (90%), a post-combustion capture unit has to be used to capture CO_2 from flue gases coming from the reformer burner [19]. This work was not considered an additional post-combustion capture unit due to significant technical elements (increased heat consumption for solvent regeneration) as well as negative influence on economic costs.

Following the technical evaluation of both reforming processes, the next step was to assess the economic performance indicators (e.g., specific investment costs, operational & maintenance costs, levelized cost of hydrogen, CO_2 capture costs). The main economic indicators of hydrogen production concepts based on natural gas reforming with and without decarbonization are presented in Table 4.

Table 4. Key economic performance indicators

Performance indicator	UM	Case 1	Case 2
Total installed cost (ex. contingency)	MM €	69.30	98.91
Total investment cost	MM €	83.16	118.69
Specific investment cost per kW net	€ / kW	535.24	788.15
Total fixed O&M cost (year)	MM €	6.73	7.06
Total fixed O&M cost (MWh)	€/MWh	5.78	6.25
Total variable O&M cost (year)	MM €	28.73	28.50
Total variable O&M cost (MWh)	€/MWh	24.22	25.23
Total fixed and variable costs (year)	MM €	34.96	35.56
Total fixed and variable costs (MWh)	€/MWh	30.00	31.48
Levelized cost of hydrogen (LCOH)	€/MWh	37.57	43.03
CO_2 removal cost	€/t	-	28.95
CO_2 avoided cost	€/t	-	30.71

As can be observed from Table 4, the introduction of pre-combustion carbon capture involves important economic modifications as follows: specific investment cost increases by about 47.25%, the total fixed and variable costs increase by about 5% and the hydrogen production cost increases by about 14.5%. The CO_2 avoided cost is slightly higher than the current CO_2 emission tax (25 - 28 €/t [20]), but the difference is not significant showing the promising perspectives of decarbonization process.

Sensitivity studies (see Figure 4) were performed to see the influence of various key economic elements (e.g., natural gas price, capital and operational costs, internal rate of return, plant availability factor) on hydrogen production cost.
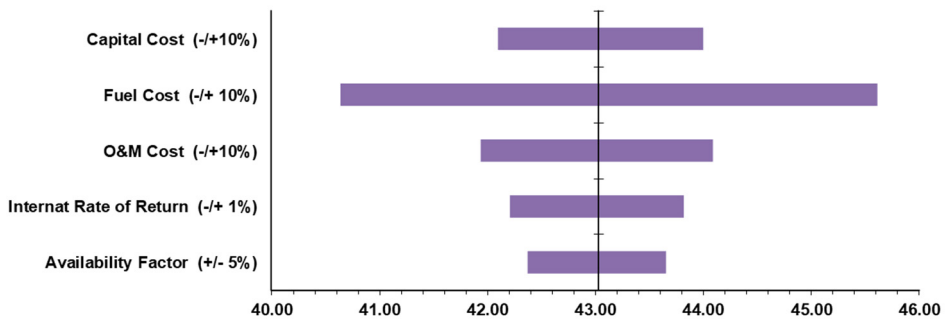
Figure 4. Sensitivity study for decarbonized hydrogen production cost

Finally, an LCA analysis was performed for the investigated cases to determine the most relevant environmental impact indicators. Table 5 presents the key environmental indicators for the evaluated cases.

Table 5. LCA environmental indicators

Performance indicator	UM	Case 1	Case 2
GWP	kg CO_2 eq. / MWh H_2	278.48	101.08
FEP * 10^5	kg P eq. / MWh H_2	39.29	40.28
ODP * 10^9	kg CFC-11 eq. / MWh H_2	5.12	5.27
FDP	kg oil eq. / MWh H_2	107.98	112.56
FETP * 10^2	kg 1,4-DB eq. / MWh H_2	5.30	5.68
HTP	kg 1,4-DB eq. / MWh H_2	3.74	4.25
MDP	kg Fe eq. / MWh H_2	0.53	0.64
POFP * 10^3	kg NMVOC / MWh H_2	11.41	48.28
TETP * 10^3	kg 1,4-DB eq. / MWh H_2	0.44	0.78

It can be noticed that introduction of carbon capture feature involves a reduction of Global Warming Potential (GWP) by about 2.75 times (from 278.48 to 101.08 kg CO_2 eq./MWh H_2). The rest of environmental indicators show low to moderate increases (up to 15%). These can be explained by two main elements: reduction of overall energy efficiency due to carbon capture and usage of additional materials (e.g., chemical solvent) for plant decarbonization. Only Photochemical Oxidant Formation Potential (POFP) shows a significant increase compared to the base case (323%) due to the influence of chemical solvent (MDEA) production process.

CONCLUSIONS

This work is evaluating the main techno-economic and environmental performance indicators of decarbonization process for a hydrogen production plant based on natural gas reforming. As the decarbonization technology, the chemical gas-liquid absorption using MDEA was used. A 70% carbon capture rate was considered for a plant capacity of 50000 Nm^3/h (corresponding to 150 MW hydrogen thermal output). As the results show, the decarbonization process of hydrogen production has a positive influence on key plant performance indicators e.g., low carbon capture energy penalty (about 2.3 net efficiency percentage points), moderate increase of the hydrogen production cost (by about 14.5%), attractive CO_2 avoidance cost in comparison to the current carbon tax (30.7 vs. 25 - 28 €/t) and 2.75 times reduction of global warming potential (assessed by a full LCA analysis). All these promising elements underline the potential of decarbonized hydrogen as a key energy carrier for the future low carbon economy.

ACKNOWLEDGMENTS

REFERENCES

1. S. Akerboom; W. Botzen; B.A. Michels; M. van Rijswicke; *Energy Policy*, **2020**, *138*, 111210
2. C. Ye; Q. Ye; X. Shi; Y. Sun; *Energy Policy*, **2020**, *137*, 111094
3. European Commission; *A policy framework for climate and energy in the period from 2020 to 2030*, **2014**, *COM (2014) 15 final*, Brussels, Belgium

4. K. Liu; C. Song; V. Subramani; *Hydrogen and syngas production and purification technologies,* Wiley AICheE, **2010**, pp. 1 - 12
5. T. L. Le Valley; A.R. Richard; M. Fan; *Int. J. Hydrog. Energy,* **2014**, *39*, 16983-17000
6. F. Dawood; M. Anda; G.M. Shafiullah; *Int. J. Hydrog. Energy,* **2020**, *45*, 3847-3869
7. A.L. Kohl; R. Nielsen; *Gas purification, Gulf Professional Publishing*, **1997**, pp. 40 - 186
8. C.C. Cormos; L. Petrescu; A.M. Cormos; *Comput. Aided Chem. Eng.*, **2014**, *33*, 1081-1086
9. S. Galusnyak; S. Drăgan; *Stud. U. Babes-Bol. Che.*, **2019**, *64*, 7-18
10. M. Voldsund; K. Jordal; R. Anantharaman; *Int. J. Hydrog. Energy,* **2016**, *41*, 4969-4992
11. International Energy Agency - Greenhouse gas R & D Programme; *Decarbonisation of fossil fuels*, **1996**
12. K. Aasberg-Petersen; I. Dybkjær; C.V. Ovesen; N.C. Schjødt; J. Sehested; S.G. Thomsen; *J. Nat. Gas. Sci. Eng.*, **2011**, *3*, 423-459
13. A.M. Cormos; V.C. Sandu; C.C. Cormos; *J. Clean. Prod.*, **2020**, *259*, 120834
14. M. van der Spek; S. Roussanaly; E. S. Rubin; *Int. J. Greenh. Gas Con.*, **2019**, *83*, 91-104
15. International Energy Agency - Greenhouse gas R & D Programme; *Techno - economic evaluation of SMR based standalone (merchant) hydrogen plant with CCS*, **2017**
16. D.A. Chisalita; C.C. Cormos; *Energy*, **2020**, *181*, 331-344
17. D.A. Chisalita; L. Petrescu; C.C. Cormos; *Renew. Sust. Energ. Rev.*, **2020**, *130*, 109964
18. K. Atsonios; K.D. Panopoulos; A. Doukelis; A. Koumanakos; Em. Kakaras; *Energy Convers. Manag.*, **2012**, *60*, 196-203
19. S. Cloete; L. Hirth; *Energy*, **2020**, *192,* 116671
20. Sandbag - Smarter Climate Policy; *Carbon price viewer*, www.sandbag.org.uk/carbon-price-viewer/, **2020**

ASSESSMENT OF FLEXIBLE CARBON CAPTURE AND UTILIZATION OPTIONS APPLIED TO GASIFICATION PLANTS

LETITIA PETRESCU[a], CRISTIAN DINCA[b], CALIN-CRISTIAN CORMOS[a*]

ABSTRACT. The aim of this work is to assess the energy vector poly-generation capabilities of gasification plants equipped with carbon capture and utilization (CCU) features. As evaluated energy carriers, various total or partial decarbonized vectors were investigated (e.g., power, hydrogen, synthetic natural gas, methanol, Fischer-Tropsch fuel). As illustrative examples, the gasification concepts with 100 MW net energy output were considered having an overall plant decarbonization rate of 90%. As decarbonization technologies, the gas – liquid absorption based on chemical and physical scrubbing was assessed. A broad range of process system engineering tools were used (e.g., modeling and simulation, process integration, plant flexibility elements, technical and environmental evaluation). As results show, the application of carbon capture and utilization technologies for gasification-based poly-generation has promising results in term of increasing the overall energy efficiency (up to 68%), reducing CO_2 emissions (down to 7 kg/MWh) and improving cycling capabilities.

Keywords: Carbon capture and utilization (CCU) technologies, Gasification, Energy vectors poly-generation, Technical and environmental assessment.

INTRODUCTION

Greenhouse gas emissions (especially CO_2) represent a significant issue of the modern world. Global warming and climate change are caused by increased anthropogenic greenhouse gas emissions compared to pre-industrial levels [1]. Important technical, economic, social and political efforts

---

[a] *Babeş-Bolyai University, Faculty of Chemistry and Chemical Engineering, 11 Arany Janos, RO-400028, Cluj-Napoca, Romania*
[b] *Politehnica University, Faculty of Power Engineering, 313 Splaiul Independentei, RO-060042, Bucharest, Romania*
* *Corresponding author: cormos@chem.ubbcluj.ro*

are devoted to tackle these significant environmental issues. In this respect, the energy-intensive industrial applications (e.g., heat and power generation, chemical, metallurgical and cement sectors) should be significantly re-design to curb greenhouse gas emissions for future low-carbon economy as well as to improve the overall energy efficiency [2].

Several technical methods are already available for developing the future low-carbon economy e.g., increasing the share of renewable energy sources (e.g., wind, solar, biomass), improving the energy conversion and utilization aspects, developing Carbon Capture, Utilization and Storage (CCUS) applications [3-4]. Since for the heat and power generation, suitable renewable solutions are already in place (e.g., wind mills, thermal and photovoltaic solar systems), for other important energy-intensive and polluting sectors such as chemical, petro-chemical, iron and steel production, cement production, the suitable solutions are still to be developed considering the particular characteristics of these systems. For non-power applications, the renewable energy sources (e.g., wind and solar) have a limited applicability, the conventional fuels (either fossil or renewable) being a more suitable solution [5].

CCUS technologies have a promising development potential since they can be successfully used to make environmental acceptable even the most polluting fossil fuels (e.g., coal, lignite, oil). Carbon capture and utilization methods are aiming to mitigate the carbon dioxide emissions from various industrial applications and then to utilize the captured CO_2 in different ways: production of synthetic fuels, mineralization for construction materials, raw material for organic synthesis [6-7].

Along these important lines, the present paper is aiming to evaluate the potential energy vectors poly-generation based on gasification process. Various total and partial decarbonized energy carriers (e.g., power, hydrogen, substitute natural gas, synthetic liquid fuels) were assessed to be produced based on syngas processing. The following syngas-based reactions are used for energy vectors poly-generation [8-10]:

- Hydrogen production via water gas shift (WGS) conversion:

$$CO \ + \ H_2O \ \rightarrow \ CO_2 \ + \ H_2 \qquad (1)$$
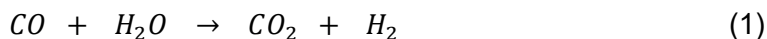
- Synthetic natural gas (SNG) production via methanation:

$$CO \ + \ 3H_2 \ \rightarrow \ CH_4 \ + \ H_2O \qquad (2)$$
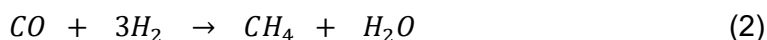
- Methanol production:

$$CO \ + \ 2H_2 \ \rightarrow \ CH_3OH \tag{3}$$

- Fischer-Tropsch synthesis:

$$nCO \ + \ \left(\frac{m}{2} + n\right)H_2 \ \rightarrow \ C_nH_m \ + \ nH_2O \tag{4}$$
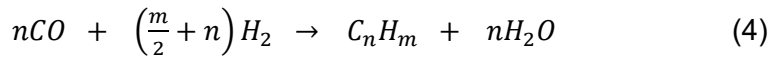
To reduce the carbon dioxide emissions, a carbon capture technology (based on chemical and physical scrubbing) was also fitted in the gasification plant. The overall concepts are characterized by improved overall energy efficiency and low CO_2 emissions. As an illustrative example, chemical gas-liquid abruption using Methyl-Di-Ethanol-Amine (MDEA) was considered according to the following reaction [11]:

$$CO_2 \ + \ MDEA \ + \ H_2O \ \rightarrow \ MDEAH^+ \ + \ HCO_3^- \tag{5}$$

In addition to decarbonization, the syngas-based poly-generation concept has important advantages in improving the plant cycling capabilities. In energy sector, the current fossil-based facilities are under increasing pressure to be re-design to make them more flexible in order to accommodate the time-irregular renewable energy sources. In this respect, a flexible poly-generation concept, which can produce electricity during peak times and other energy carriers (various chemicals) during periods with low electricity demand, is of great importance [12-13].

LAYOUT OF GASIFICATION-BASED POLY-GENERATION CONCEPT AND MAIN DESIGN ASSUMPTIONS

The conceptual design of flexible and decarbonized coal-based gasification plant is presented in Figure 1 [14]. Coal is gasified with oxygen and steam leading to syngas which is furthermore cooled down and the ash is removed. Subsequently, a water gas shift conversion is necessary to increase the hydrogen content simultaneously with reduction of carbon monoxide content to the molar ratio required for various reactions. Carbon

dioxide and hydrogen sulfide are captured separately in an Acid Gas Removal (AGR) unit followed by flexible poly-generation step of total or partial decarbonized energy carriers (electricity, hydrogen, synthetic fuels).
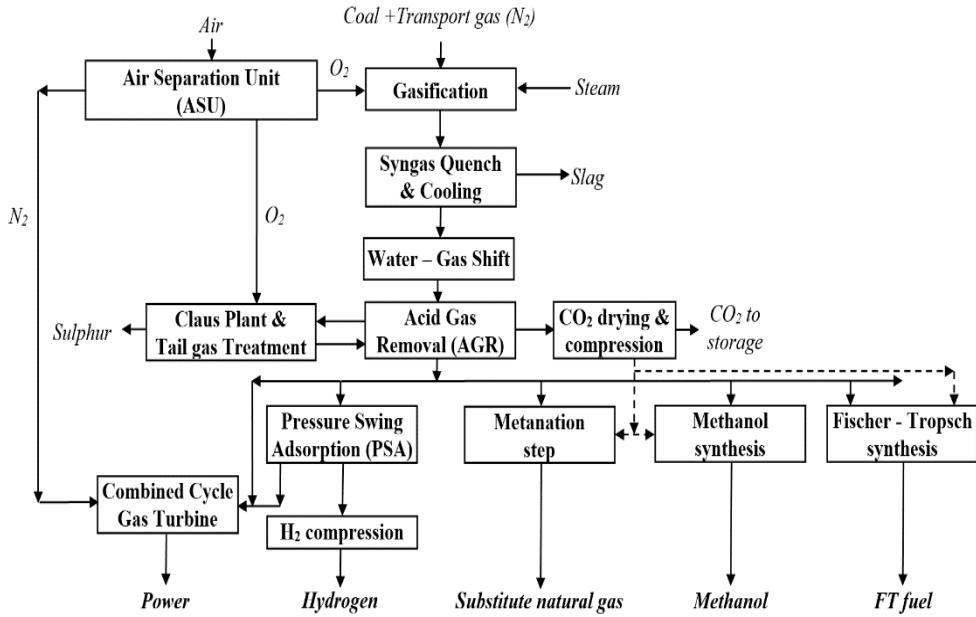
Figure 1. Flexible and decarbonized gasification-based energy vector poly-generation concept

The proposed concept was evaluated in a flexible energy vector poly-generation scenario to generate 100 MW net energy output (for the main energy carrier) with a 90% carbon capture rate for AGR unit. The gasification-based system was modeled and simulated using ChemCAD software. Table 1 presents the main design assumptions used in the evaluation [9,14].

For syngas-processing units into various energy carriers (SNG, methanol, FT fuel), the conventional configurations and process operation conditions based on literature sources [15-18] were considered.

Table 1. Main design assumptions of flexible poly-generation concept

Plant sub-system	Design assumptions
Coal characteristics	Ultimate analysis (% wt. dry): 72.04% carbon, 4.08% hydrogen, 1,67% nitrogen, 7.36% oxygen, 0.65% sulphur, 0.01% chloride, 14.19% ash; Moisture: 8% Lower heating value (LHV): 25.35 MJ/kg
Air separation unit	Purity (% vol.): 95% O_2, 3% N_2, 2% Ar Power consumption: 200 kWh/t oxygen Oxygen delivery pressure: 2 bar
Gasification unit	Shell reactor (dry fed gas quench) Operating pressure: 40 bar Operating temperature: 1400 – 1500°C Pressure drop: 1 bar Gas quench temperature: 800°C
Water Gas Shift (WGS) unit	No. of catalytic beds: 2 Reactor type: equilibrium Thermal mode: adiabatic Steam to CO ratio: 2 (molar) Pressure drop: 1 bar / catalytic bed
Chemical CO_2 capture unit Absorption column: Desorption column:	Solvent: Methyl-DiEthanol-Amine (MDEA) Solution concentration: 50 % wt. No. of stages: 20 Column pressure drop: 1 bar No. of stages: 10 Column pressure drop: 1 bar Solvent regeneration: thermal (LP steam) Heat duty: 0.65 MJ/kg CO_2
Physical CO_2 capture unit Absorption column:	Solvent: Selexol™ (mixture of methyl ethers of poly-ethylene glycol) No. of stages: 20 Column pressure drop: 1 bar Solvent regeneration: pressure reduction (4 stages)
Claus plant	Type: oxygen-fed Inlet gas composition (vol.): > 25% H_2S Sulphur recovery: > 99%
CO_2 processing unit	Drying agent: Tri-Ethylene-Glycol (TEG) 4 compressing stages with inter-cooling Delivery pressure: 120 bar CO_2 composition (vol. %): >95% CO_2, <2000 ppm CO, <250 ppm H_2O, <100 ppm H_2S, <4% other gases (N_2, Ar, H_2)
Power block	Combined cycle gas turbine Net electrical efficiency: 39.5% Pressure ratio: 21 HP / MP / LP steam levels: 120 / 34 / 3 bar Steam turbine efficiency: 85% Condensing pressure: 48 mbar Cooling water temperature: 15°C
Hydrogen processing unit	Delivery pressure: 60 bar Compressor efficiency: 85% Outlet temperature: 30-40°C
Heat exchangers	$\Delta T_{min.}$ = 10°C; Pressure drop: 2 - 3% of inlet pressure

EVALUATION METHODOLOGY

Various energy vectors poly-generation systems were modeled and simulated using ChemCAD software. In selection of the thermodynamic package, the chemical compounds as well as the operating conditions were considered. For instance, in case of gas processing units (e.g., syngas conditioning, physical gas-liquid absorption, chemical reactors for synthesis of various energy carriers), Soave-Redlich-Kwong (SRK) package was used. For chemical gas-liquid absorption, the electrolyte package was used based on the present ionic system. In case of captured CO_2 conditioning system (CO_2 drying), TEG Dehydration package was selected. For steam generation and power block, Thermoflex software was chosen to double-check the simulation results obtained in ChemCAD.

The assessed process configurations were optimized in term of energy utilization by thermal integration analysis. In this aim, the pinch analysis was used to evaluate the overall hot and cold utility consumptions [19]. As an illustrative example, Figure 2 presents the hot and cold composite curves for gasification-based system used for decarbonized power generation (combined cycle power block). The results derived from simulation were compared with available literature and experimental data for model validation [20-21]. No significant differences were observed.
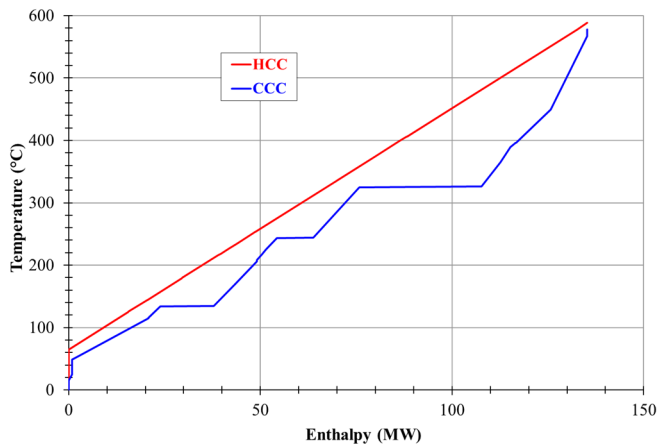
Figure 2. Hot and cold composite curves for decarbonized power generation

As can be noticed from above composite curves, there is no need for external heating utility, the available hot streams within the plant covering the heating duty. Also, one can notice the tight thermal integration which leads to the overall energy optimization within the plant.

The mass and energy balances of optimized systems were then used to quantify the main technical and environmental performances. As benchmark case, the non-carbon capture gasification-based power plant was also considered to evaluate the CO_2 capture energy penalty. The most important performance indexes are presented below:

- Overall energy generation efficiency (η_{Energy}) was calculated considering the global energy output (net power output and energy carrier thermal output) in the overall energy yield of the concepts:

$$\eta_{Energy} = \frac{Net\ power\ output + Energy\ carrier\ termal\ output}{Coal\ thermal\ input} * 100 \quad (6)$$

- Carbon capture rate (CCR) was calculated considering the molar fraction of carbon feedstock that was captured in the Acid Gas Removal unit:

$$CCR = \frac{Captured\ CO_2\ molar\ flow}{Input\ carbon\ molar\ flow} * 100 \quad (7)$$

- Specific CO_2 emissions (SE_{CO_2}) was calculated as emitted CO_2 mass flow for each MW of net energy (net power and energy carrier thermal output) output:

$$SE_{CO_2} = \frac{Emitted\ CO_2\ mass\ flow}{Net\ power\ output + Energy\ carrier\ termal\ output} * 100 \quad (8)$$

RESULTS AND DISCUSSION

The first operation scenario of gasification plant was for power generation only. The following case studies were considered:

Case 1: Coal-based gasification power plant without carbon capture;

Case 2: Coal-based gasification power plant with pre-combustion carbon capture using chemical scrubbing (MDEA);

Case 3: Coal-based gasification power plant with pre-combustion carbon capture using physical scrubbing (Selexol™).

Table 2 shows the most important technical and environmental performance indicators for the above cases.

Table 2. Technical and environmental indicators for gasification power plants

Performance indicator	UM	Case 1	Case 2	Case 3
Coal flowrate	t/h	30.54	38.74	37.89
Coal LHV	MJ/kg		25.35	
Coal thermal energy	MW$_{th}$	215.05	272.85	266.80
Gross power output	MW$_e$	115.45	126.10	125.16
Ancillary power consumption	MW$_e$	15.45	26.10	25.16
Net power output	MW$_e$	100.00	100.00	100.00
Net power efficiency	%	46.50	36.65	37.48
Carbon capture rate	%	0.00	90.00	90.00
Specific CO_2 emission	kg/MWh	745.10	85.81	84.21

As noticed from Table 2, there is an important energy penalty when decarbonization process is integrated in the gasification-based power plant. The decarbonization energy penalty is about 9.85 net efficiency percentage points for chemical scrubbing and about 9.02 net efficiency percentage points for physical scrubbing. The main reason for the higher energy penalty in case of chemical gas-liquid absorption represents the heat duty for solvent regeneration, which is about 0.65 – 0.8 GJ/t in case of pre-combustion capture (as evaluated in this work) and about 3 GJ/t in case of post-combustion capture [22]. The lower power generation efficiency in case of decarbonized concepts has another negative consequence which is the increasing fuel requirements for the same net power output. In addition, the power generation costs for decarbonized gasification plants are also increasing on average by about 30-40% [23].

The positive consequence of decarbonization is the significant reduction of specific CO_2 emissions in comparison to the benchmark case without carbon capture (Case 1). This key element could enable the further utilization of fossil fuels (in decarbonized plants) in the future, even if the environmental constraints are getting stricter.

To illustrate the influence of CO_2 capture solvent on hot and cold energy utility consumptions as well as for the overall power plant efficiency, Table 3 presents such an analysis for one chemical solvent (MDEA) and two physical solvent (Selexol™ and Rectisol®). One can notice the overall benefits of physical absorption over chemical one for pre-combustion cases.

Table 3. Influence of solvent selection on heating and cooling utility consumptions

Performance indicator	UM	MDEA	Selexol™	Rectisol®
Power consumption	kWh/kg	0.09	0.11	0.12
Heating consumption	MJ/kg	0.65	0.22	0.38
Cooling consumption	MJ/kg	3.30	0.56	0.62
Overall net power efficiency	%	36.65	37.48	37.01

Concluding, one can notice that physical solvents require less heating and cooling utility consumptions but higher power consumption for solvent circulation [24]. On the other hand, chemical solvents are more selective when various acid gas components are present in gas stream to be treated.

The next evaluated operational scenario of gasification-based plants was based on flexible energy vector poly-generation as a key element for improving plant cycling. Improved cycling capabilities of fossil-based plants is a fundamental important aspect of modern energy conversion systems which need to integrate more time-irregular renewable sources such as solar and wind [13].

The first evaluated scenario refers to the hydrogen and power co-generation based on decarbonized gasification concept. In this design, a variable share of hydrogen-rich stream (after Acid Gas Removal unit) is not sent to the combined cycle for power generation but it is purified in a Pressure Swing adsorption (PSA) unit to purities suitable for external customers (e.g., chemical applications, hydrogen-driven transport). In this way, the overall plant cycling capability (the ability of the plant to timely change the generated energy vectors in accordance to grid demand) are improved.

To illustrate the influence of flexible hydrogen output on overall plant performances, Table 4 presents the case of coal-based Shell gasification plant equipped with Selexol™-based decarbonization unit (Case 3).

If a fully flexible hydrogen and power co-generation plant is targeted, a separate steam cycle has to be used to cover the ancillary power consumption of the plant [25]. This separate power block will use advantages of existing steam-rising capabilities within the plant (e.g., exothermic chemical reactions such as water gas shift, synthetic fuels reactors). The combined cycle is then used only for export power. To illustrate how the overall energy efficiency is varying in case of modification of operation scenario from only power generation to only hydrogen production, Figure 3 presents the situation in case of coal-based Shell gasification plant equipped with Selexol™-based decarbonization unit (Case 3).

Table 4. Performances of decarbonized hydrogen and power co-production

Performance indicator	UM	Power only	Hydrogen and power	
Coal flowrate	t/h	37.89		
Coal LHV	MJ/kg	25.35		
Coal thermal energy	MW_{th}	266.80		
Gross power output	MW_e	125.16	109.91	94.89
Hydrogen thermal output	MW_{th}	0.00	25.00	50.00
Ancillary power consumption	MW_e	25.16	25.51	25.94
Net power output	MW_e	100.00	84.40	68.95
Net power efficiency	%	37.48	31.63	25.84
Hydrogen thermal efficiency	%	0.00	9.37	18.74
Overall plant efficiency	%	37.48	41.00	44.58
Carbon capture rate	%	90.00	90.00	90.00
Specific CO_2 emission	kg/MWh	84.21	76.97	70.79
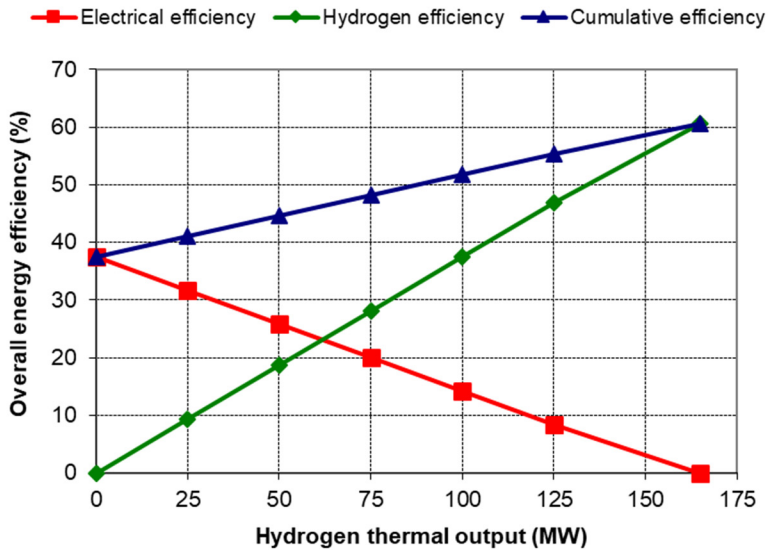
Figure 3. Variation of overall plant energy efficiency vs. hydrogen thermal output

As can be observed from Table 4 and Figure 3, the overall cumulative energy efficiency is favourably influenced by increasing the hydrogen thermal output. Also, the specific CO_2 emission is decreasing with hydrogen thermal output. In addition, fully flexible decarbonized co-generation plants can have a high overall energy efficiency (up to 60%). Accordingly, the flexible hydrogen and power co-generation is a promising operational scenario to improve the gasification plant cycling.

Next evaluated operational scenario for decarbonized gasification plants was energy vector poly-generation based on syngas processing [9]. As evaluated energy vectors (beside electricity), various chemical species were considered as follow: substitute natural gas (SNG), methanol and Fischer-Tropsch fuel. The assessed concepts were designed to be self-sustainable in term of power (available heat sources from various process streams and reactors are used to generate steam which then is converted to electricity in a single cycle power block). All these poly-generation designs consider the once-trough configuration in which the unreacted chemical species from synthetic fuel step are then used for power generation. In this way, the overall flexibility of the plant is improved as well as reducing the design complexity [26].

Table 5 presents the main technical and environmental performances of coal-based Shell gasification plant equipped with Selexol™-based decarbonization unit (Case 3).

Table 5. Performances of decarbonized energy vector poly-generation

Performance indicator	UM	SNG	MeOH	FT fuel
Coal flowrate	t/h	21.93	28.36	25.06
Coal LHV	MJ/kg		25.35	
Coal thermal energy	MW$_{th}$	154.43	199.71	176.50
Gross power output	MW$_e$	20.40	26.07	27.42
SNG thermal output	MW$_{th}$	100.00	-	-
Methanol thermal output	MW$_{th}$	-	100.00	-
FT fuel thermal output	MW$_{th}$	-	-	100.00
Ancillary power consumption	MW$_e$	14.41	15.41	10.69
Net power output	MW$_e$	5.99	10.66	16.73
Net power efficiency	%	3.87	5.34	9.47
Carrier thermal efficiency	%	64.75	50.07	56.65
Overall plant efficiency	%	68.62	55.41	66.12
Carbon capture rate	%	60.12	48.25	47.62
Specific CO_2 emission	kg/MWh	6.98	26.01	39.85

The first important conclusion regarding the partial decarbonized energy vector poly-generation based on syngas processing is that the overall energy efficiency is significantly higher (55 - 68% vs. 37 - 44%) in comparison to power and hydrogen co-production (fully decarbonized energy carriers). This positive result comes however with a lower carbon capture rate (48 – 60% vs. 90%) which, in the end, means higher CO_2 emissions based on whole life cycle assessment (including energy carriers' usage).

In addition, several important elements can be concluded from the results such as: the combination of chemical synthesis with conventional heat and power production induces a higher overall energy efficiency of the system; once-trough poly-generation concepts have more technical and environmental benefits that recycled plants and decarbonized poly-generation plants have lower energy and cost penalties for carbon capture than conventional stand-alone gasification power plants (operated in base load conditions) [27-28].

CONCLUSIONS

The integration of carbon capture and utilization feature into gasification process for flexible energy vectors poly-generation is assessed in the present paper considering various technical and environmental performance indicators. Both total (power and hydrogen) and partial (synthetic natural gas, methanol, FT fuel) decarbonized energy carriers were considered. Two commercial pre-combustion carbon capture options based on chemical and physical gas-liquid absorption were evaluated. For power generation only, the carbon capture energy penalty was about 9 net percentage points for physical absorption and about 9.8 percentage points for chemical absorption. The main explanation for this fact is that physical gas-liquid absorption using SelexolTM has lower ancillary heat duty for solvent regeneration than MDEA-based scrubbing (0.22 vs. 0.65 MJ/kg).

For flexible energy vectors poly-generation, several important conclusions were drawn. For instance, in case of hydrogen and power co-generation, the overall plant energy efficiency is increasing with hydrogen output (about 3.5 percentage points per each 25 MW_{th} hydrogen output). In case of partial decarbonized energy carriers, the overall energy efficiency is higher (55 – 68%) but carbon capture rate is lower (48-60 vs. 90%) than for total decarbonized energy carriers (power and hydrogen). The overall conclusion is that the decarbonized gasification plant has promising potential for flexible energy vectors poly-generation.

ACKNOWLEDGMENTS

REFERENCES

1. Intergovernmental Panel on Climate Change (IPCC); Climate Change 2014. In *Synthesis Report. Contribution of Working Groups I, II and III to the Fifth Assessment Report of the Intergovernmental Panel on Climate Change*. Geneva, Switzerland, **2014**
2. C. Ye; Q. Ye; X. Shi; Y. Sun; *Energy Policy*, **2020**, *137*, 111094
3. European Commission; *A policy framework for climate and energy in the period from 2020 to 2030*, **2014**, *COM (2014) 15 final*, Brussels, Belgium
4. K. Wang; Y. Mao; J. Chen; S. Yu; *J. Clean. Prod.,* **2018**, *1761*, 1065-1077
5. F. Vega; F.M. Baena-Moreno; L.M. Gallego Fernández; E. Portillo; B. Navarrete; Z. Zhang; *Appl. Energy*, **2020**, *260*, 114313
6. G. Leonzio; D. Bogle; P.U. Foscolo; E. Zondervan; *Chem. Eng. Res. Des.*, **2020**, *155*, 211-228
7. Z. Zhang; S.Y.Pan; H. Li; J. Cai; A.G. Olabi; E.J. Anthony; V. Manovic; *Renew. Sust. Energ. Rev.*, **2020**, *125*, 109799
8. A. AlNouss; G. McKay; T. Al-Ansari; *Energy Convers. Manag.*, **2019**, *196*, 664-676
9. A.M. Cormos; C. Dinca; C.C. Cormos; *Appl. Therm. Eng.*, **2015**, 74, 20-27
10. J. Nyári; M. Magdeldin; M. Larmi; M. Järvinen; A. Santasalo-Aarnio; *J. CO_2 Util.*, **2020**, *39*, 101166
11. A.L. Kohl; R.B. Nielsen; *Gas Purification*, Gulf Professional Publishing, Huston, Texas, USA, **1997**, pp. 40-187
12. H. Mikulčić; I.R. Skov; D.F. Dominković; S.R. Wan Alwi; Z.A. Manan; R. Tan; N. Duić; S.N. Mohamad; X. Wang; *Renew. Sust. Energ. Rev.,* **2019**, *114*, 109338
13. S. Szima; S.M. Nazir; S. Cloete; S. Amini; S. Fogarasi; A.M. Cormos; C.C. Cormos; *Renew. Sust. Energ. Rev.,* **2019**, *110*, 207-219
14. A.M. Cormos; C. Dinca; L. Petrescu; D.A. Chisalita; S. Szima; C.C. Cormos; *Fuel*, **2018**, *211*, 883-890
15. S. Zeng; J. Gu; S. Yang; H. Zhou; Y. Qian; *J. Clean. Prod.*, **2019**, *215*, 544-556
16. T.G. Kreutz; E.D. Larson; C. Elsido; E. Martelli; C. Greiga; R.H. Williams; *Appl. Energy*, **2020**, *279*, 115841
17. M. Pérez-Fortes; J.C. Schöneberger; A. Boulamanti; E. Tzimas; *Appl. Energy*, **2016**, *161*, 718-732
18. S. Szima; C.C. Cormos; *J. CO_2 Util.*, **2018**, *24*, 555-563
19. R. Smith; *Chemical Process Design and Integration*, 2nd ed., Wiley, Chichester, West Sussex, UK, **2016**, pp. 457-499

20. International Energy Agency, Greenhouse Gas R&D Programme (IEAGHG); *Potential for improvement in gasification combined cycle power generation with CO_2 capture*, Report PH4/19, Cheltenham, UK, **2003**

21. U.S. Department of Energy, National Energy Technology Laboratory (NETL); *Cost and performance baseline for fossil energy plants. Volume 1a: Bituminous coal (PC) and natural gas to electricity*, Report DOE/NETL-2015/1723, USA, **2015**

22. G. Cau; V. Tola; F. Ferrara; A. Porcu; A. Pettinau; *Fuel*, **2018**, *214,* 423-35

23. S. Budinis; S. Krevor; N. Mac Dowell; N. Brandon; A. Hawkes; *Energy Strateg. Rev.*, **2018**, *22*, 61-81

24. C.C. Cormos; *Energy*, **2012**, *42*, 434-445

25. F. Starr; E. Tzimas; S. Peteves; *Int. J. Hydrog. Energy*, **2007**, *32*, 1477-1485

26. T.G. Walmsley; M.R.W. Walmsley; P.S. Varbanov; J.J. Klemeš; *Renew. Sust. Energ. Rev.,* **2018**, *98*, 328-345

27. A.S. Brouwer; M. van den Broek; A. Seebregts; A. Faaij; *Appl. Energy*, **2015**, *156*, 107-128

28. C.C. Cormos, *Int. J. Hydrog. Energy*, **2013**, *38*, 7855-7866.

ACTIVATED MULTI-WALLED CARBON NANOTUBES FOR ELECTROCHEMICAL DETECTION OF DOPAMINE IN THE PRESENCE OF ASCORBIC AND URIC ACID

**ANDREA KELLENBERGER[a], RODICA GAVRILA[a],
NICOLETA PLESU[b*]**

ABSTRACT. Electrochemical sensors have been prepared using pristine and activated multi-walled carbon nanotubes on glassy carbon electrode. The detection of dopamine in the presence of ascorbic acid was tested by square wave voltammetry and cyclic voltammetry. Best results were obtained for glassy carbon modified with activated carbon nanotubes electrodes. A linear dependence between current intensities and dopamine concentrations is found in both the absence/presence of ascorbic acid, in the range of 4-100 μM / 6-100 μM, with detection and quantification limits of 0.44 / 0.64 and 1.45 / 2.14 μM, respectively and high sensitivity. The developed electrodes also showed very good performance in separating the oxidation potentials of ascorbic acid, dopamine and uric acid, with peak potential differences of 200 and 170 mV. Dopamine detection in synthetic solutions in the presence of both ascorbic and uric acid gave recovery rates of 98%, indicating that the method is reliable.

Keywords: electrochemical sensor, carbon nanotubes, dopamine, ascorbic acid, square wave voltammetry

INTRODUCTION

Dopamine (DA) and ascorbic acid (AA) are organic compounds with biomedical importance. Neurotransmitters are chemicals essential in the transfer of information between the neuron cells. Dopamine is a neurotransmitter present in mammalian brain tissue. Low dopamine levels have been associated with disorders such as schizophrenia and Parkinson's disease or addictions [1].

---

[a] *Politehnica University Timisoara, Faculty of Industrial Chemistry and Environmental Engineering, 6 Vasile Parvan Bd., RO-300223, Timisoara, Romania*
[b] *"Coriolan Dragulescu" Institute of Chemistry, Bd. Mihai Viteazul 24, RO-300223, Timisoara, Romania*
* *Corresponding author: plesu_nicole@yahoo.com*

The concentration of DA in the extracellular fluid of the brain of healthy people is in the submicromolar range, but it is lower for people suffering from the aforementioned disorders. Dopamine usually exists in cationic form at physiological pH and is oxidized to quinone form (DAQ) in a two-proton / two-electron process. Ascorbic acid is an antioxidant with an important role in preventing infectious diseases. AA has been studied in the context of oxidative stress associated with cancer and other diseases. AA is also used in preserving food and beverages. At physiological pH, AA exists as the monodeprotonated ascorbate anion and it is oxidized to dehydro-ascorbic acid in a process involving two electrons and a proton [2].

The concentration of DA in the cerebral extracellular fluid is in the submicromolar domain in the case of healthy people, but it can also reach lower values in the case of diseases such as Parkinson's disease. The AA concentration is in the range of 0.2-0.5 mM.

Two of the most widely used techniques for *in vivo* monitoring of neurotransmitters are microdialysis and fast-scan cyclic voltammetry (FSCV). In microdialysis, a semi-permeable probe is injected into the brain and the analyte that is present in the brain is perfused through the probe and collected for chemical analysis using techniques such as high-performance liquid chromatography (HPLC) with mass spectrometry (MS) or fluorescence as a detector [3]. The main disadvantage of microdialysis is the temporal low resolution. FSCV is a suitable technique for *in vivo* neurotransmitter detection, which presents a high temporal resolution [4].

DA and AA coexist in extracellular fluids and have similar oxidation potentials, especially on conventional electrodes, which results in an overlap of their voltammetric response. In this respect, electrode materials capable of oxidizing DA or AA in distinct potential windows would be most suitable for the selective detection of DA in the presence of AA. The main difficulty in electrochemical detection of DA is the presence of interfering molecules such as ascorbic acid and uric acid (UA). These molecules have an oxidation potential very close to that of DA. This issue can be controlled by modifying the electrode with suitable materials. Carbon-based materials (polymers) and noble metal nanoparticles (rhodium, palladium, iridium, platinum or gold) are suitable materials for electrode modification [5]. Polymer-based dopamine sensors based on conducting polymers such as poly 3,4-ethylenedioxythiophene (PEDOT) [6], polypyrrole (PPy) [7] poly-o-phenylenediamine (P-o-PD) [8], polyanilines (PANI) [9] show promising biocompatibility and stability. Regarding carbon nanomaterials, carbon nanotubes (CNT) and graphene are used in most cases in electrocatalysis due to their stable physical and chemical properties, large specific surface area, good conductivity, biocompatibility and synergistic effect on catalytic activity. Thus, vitreous carbon electrodes modified with C_{60}

fullerenes were prepared followed by the constant potential deposition of platinum, which allowed the simultaneous detection of ascorbic acid, dopamine and uric acid, by separating their oxidation potentials [10]. The use of carbon paste electrodes modified with carbon nanotubes decorated with iron nanoparticles allowed the simultaneous detection of uric acid in the presence of interfering molecules such as ascorbic acid, dopamine and L-tyrosine [11]. Graphite-epoxy composites with synthetic zeolites have been successfully used for miniaturization of DA sensors [12]. Promising results have been obtained by modifying the electrodes with nanoparticles of noble metals, especially gold, due to its conductivity, catalytic activity and biocompatibility. For example, the electrochemical deposition of gold on the surface of reduced graphene oxide allowed the simultaneous, selective and sensitive detection of AA, DA and UA [13]. Also, the modification of carbon nanotubes with gold nanoparticles deposited by a chemical method had the effect of separating the oxidation potentials for AA, DA and UA [14]. Carbon nanotubes (multi-walled carbon nanotubes and single-walled carbon nanotubes) are nanomaterials with properties such as extraordinary tensile strength, excellent electrical conductivity and high chemical stability. The unique electronic properties of carbon nanotubes show better electron transfer rates when used as electrode materials and offer excellent prospects for the development of miniaturized electronic devices and electrochemical sensors [15]. Graphene is another carbon material, which presents excellent conductivity, stability, and low cost. The large surface area offered by the graphenes is useful for chemical detection [16]. Modified electrodes with reduced graphene oxide showed ultrasensitive detection of dopamine [17,18].

The aim of the present study is to reveal the effect of multi-walled carbon nanotube (CNT) and activated multi-walled carbon nanotube (CNT/ACT) toward DA oxidation and to evaluate the electrochemical response in the presence of AA and UA. Even though CNT in various forms have been extensively utilized for DA sensors, our goal was to identify at what extent the activation process of CNT contributes to the enhancement of electrocatalytic activity towards DA oxidation.

RESULTS AND DISCUSSION

Electrochemical detection of DA and AA on GC electrode

Firstly, the electrochemical behavior of GC electrode was investigated in 0.1 mol L^{-1} PBS electrolyte support (pH = 7.4). The square wave voltammograms (SWVs) recorded on GC for different dopamine concentrations

(**Figure 1a**) show the appearance of an oxidation peak of DA at 0.33 V whose intensity increases with increasing DA concentration. In addition, its position shifts slightly from 0.33 V to 0.36 V with increasing DA concentration. SWVs give a linear calibration curve for dopamine (**Figure 1b**). The kinetics of DA oxidation reaction was studied by cyclic voltammetry for the highest value of DA concentration, by recording cyclic voltammograms (CVs) at different scan rates (**Figure 1c**). A well-defined oxidation peak is observed at potential values of 0.25 V that slightly shifts to more positive values (0.27 V) as the scan rate increases. The effect of scan rate on the current peak density is presented and discussed in **Figure 4d** and Table 1 for the oxidation of DA and AA on GC and GC/CNT electrodes.

Figure 1. DA detection in 0.1 mol L^{-1} PBS (pH = 7.4) on GC electrode: (a) SWVs at different DA concentrations; (b) calibration curve and (c) CVs in 100 µM DA solution at different scan rates.

Square wave voltammograms recorded on GC for different concentrations of AA (**Figure 2a**) show that the intensity of the oxidation peak of AA is concentration dependent and its position shifts slightly from 0.40 V to 0.44 V with increasing concentration of AA. The obtained calibration line for AA on GC is

illustrated in **Figure 2b**. The kinetics of the AA oxidation reaction studied by cyclic voltammetry in 2 mM AA solution, at different scan rates reveal an irreversible oxidation peak around 0.61V (**Figure 2c)**. The position of this peak changes from 0.61 V to 0.68 V as the scan rate increases. Since the oxidation potentials of DA and AA differ by only 70 mV, their simultaneous detection on GC electrode is restricted, as proven by square wave and cyclic voltammograms given in **Figure 3** for a mixture of AA and DA.

Figure 2. AA detection in 0.1 M PBS (pH = 7.4) on GC electrode: (a) SWVs at different AA concentrations; (b) calibration curve and (c) CVs in 2 mM AA solution at different scan rates.

It is observed that when DA is added to the AA solution in PBS, the peak current intensity increases for both cyclic and square wave voltammogram, but there is no clear differentiation of the two-oxidation processes, these being overlapped due to the closed potentials at which they occur.
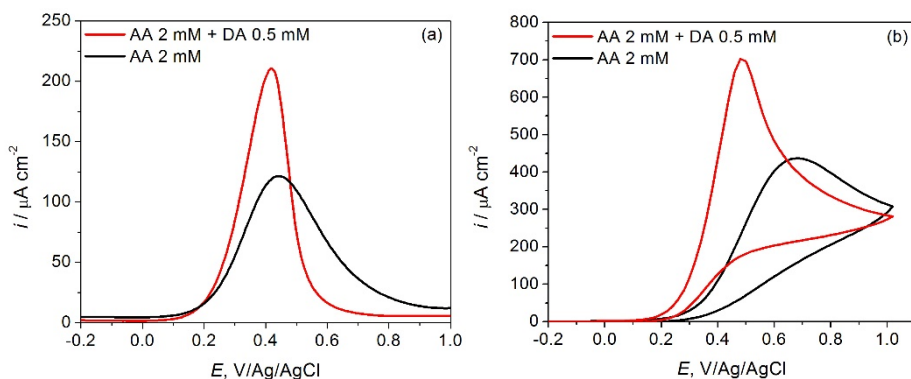
Figure 3. Simultaneous detection of AA and DA in 0.1 M PBS (pH = 7.4) on GC electrode: (a) square wave and (b) cyclic voltammograms.

Electrochemical detection of DA and AA on GC/CNT electrode

To improve the electrochemical response, the GC electrode was modified with carbon nanotubes. The SWVs recorded on GC/CNT for different DA concentrations (**Figure 4a)** reveal an oxidation peak situated at 0.13 V, whose intensity increases linearly with increasing DA concentration (**Figure 4b)**. The oxidation potential of DA on the GC/CNT electrode decreases compared to GC, which proves its increased activity for DA oxidation. The calibration line obtained is linear for concentrations between 1 - 100 µM. Cyclic voltammograms (**Figure 4c**) show a reversible oxidation peak at a potential value of 0.16 V, slightly shifting to more positive values as the scan rate increases.

Information about the kinetics of DA and AA oxidation on GC and GC/CNT electrodes are obtained from the slope of the linear dependence of log i_p versus log v, were i_p is the peak current density from the CVs and v is the scan rate (**Figure 4d**). The oxidation of DA and AA on GC electrode is a fast electron transfer reaction, controlled only by diffusion, as indicated by the slope close to 0.5, which is the theoretical value for a process controlled by diffusion (**Table 1**). On GC/CNT electrode, the linear dependence of log i_p versus log v for AA oxidation exhibits a slope close to 0.5, indicating that the reaction is still controlled by diffusion, whereas for DA oxidation the slope changes to 0.93, close to the theoretical value of 1, proving a surface adsorption-controlled kinetics.

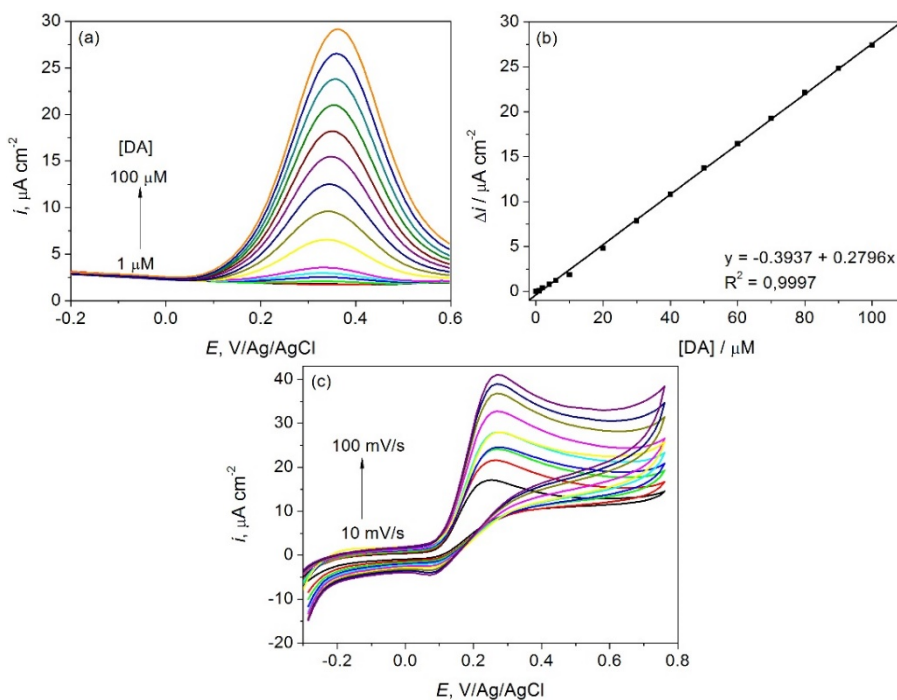**Figure 4.** DA detection in 0.1 M PBS (pH = 7.4) on GC/CNT electrode:
(a) SWVs at different DA concentrations; (b) calibration curve;
(c) CVs in 100 µM DA solution at different scan rates;
(d) plot of log i_p versus log v.

On GC/CNT electrode, the oxidation peak of AA is located at -0.056 V
(**Figure 5a**). The intensity of the oxidation peak increases with increasing
concentration of AA and its position shifts slightly from -0.056 V to -0.038 V
with increasing concentration of AA. The dependence between the
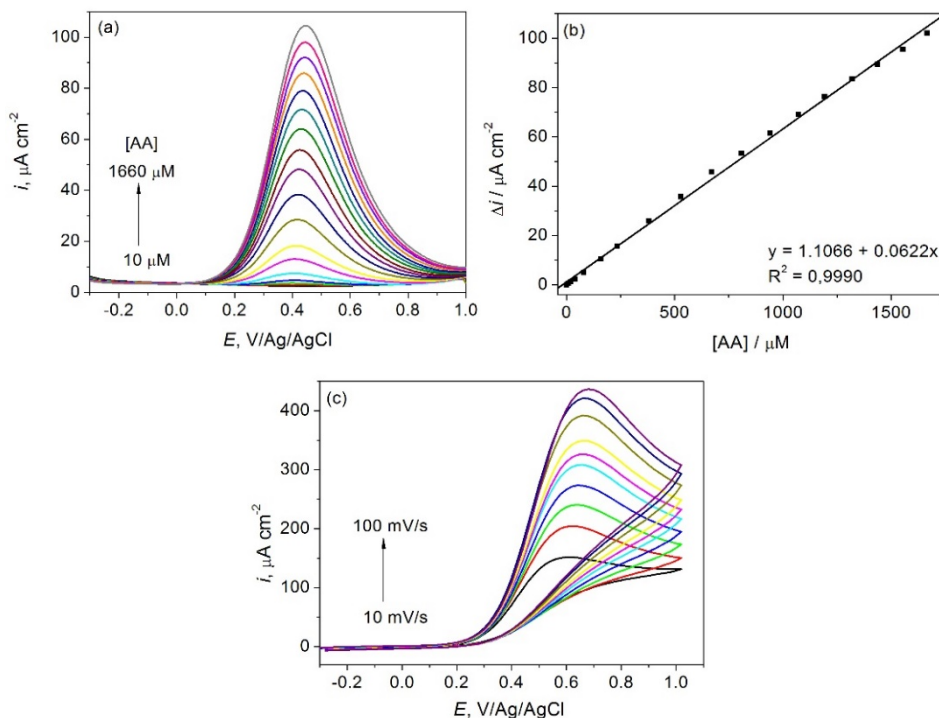intensity of the oxidation peak and AA concentration give a linear response
(**Figure 5b**).

Figure 5. AA detection in 0.1 M PBS (pH = 7.4) on GC/CNT electrode:
(a) SWVs at different AA concentrations and (b) calibration curve.

The oxidation potential of AA on GC/CNT electrode is shifted by 450 mV to more negative values than on GC, indicating its increased activity for AA oxidation. As a result, a sharp separation of the oxidation potentials of AA and DA is obtained, which allows the simultaneous detection of the two molecules.
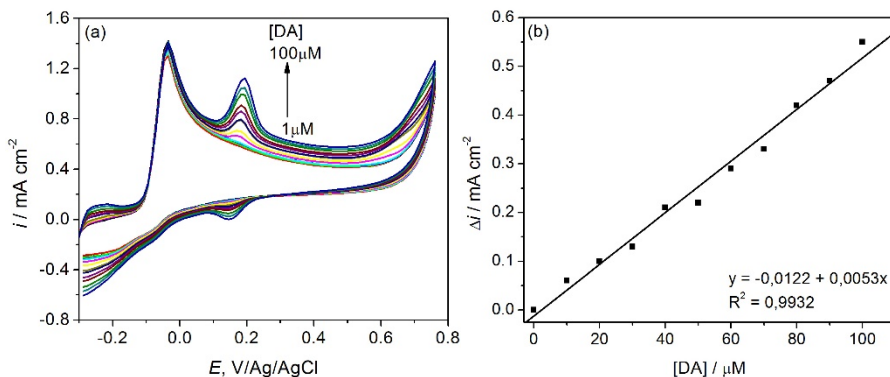
Figure 6. DA detection in the presence of 1.66 mM AA in 0.1 M PBS (pH = 7.4) on GC/CNT: (a) cyclic voltammograms and (b) calibration curve.

This is evidenced in **Figure 6**, which shows cyclic voltammograms recorded for DA oxidation in the presence of AA at constant concentration (1.66 mM). The first irreversible oxidation peak at -0.038 V corresponds to AA oxidation and the second reversible peak at 0.190 V to DA oxidation, with a separation of 225 mV between the two oxidation potentials.

The detection range of DA in the presence of AA (10 to 100 µM) is lower as compared to DA detection in the absence of AA (2 to 100 µM) using the GC/CNT electrode, however the sensitivity remains similar and it is 20-times higher than on GC electrode. The electroanalytical detection parameters are summarized in **Table 2**.

Electrochemical detection of DA and AA on activated GC/CNT/ACT electrode

A further improvement of the electrochemical detection parameters for DA detection was achieved by using activated CNT. By activation of the CNT (**Figure 7a)**, carbonyl and / or carboxyl type functional groups are introduced on their surface, which act as reactive centers in the interaction with various molecules. The presence of these functional groups was sustained by FTIR spectra before and after activation (**Figure 7b**).
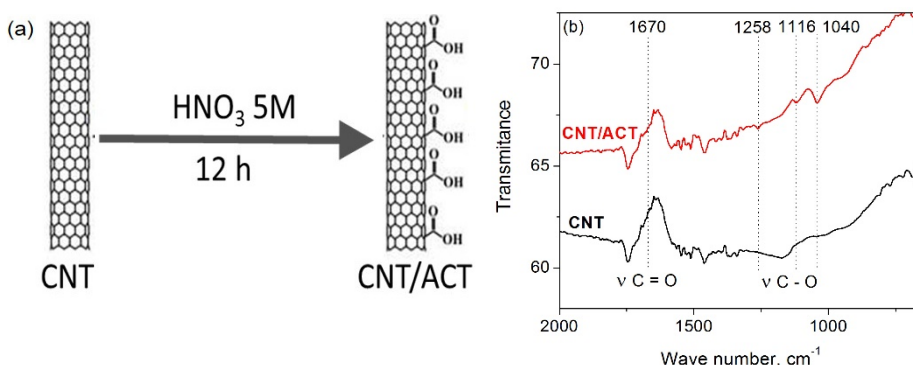
Figure 7. Activation of CNT: (a) Schematic representation and (b) FTIR spectra of pristine (CNT) and activated nanotubes (CNT/ACT).

The bands observed in the original CNT and CNT/ACT are assigned to the vibrations of carbon–oxygen groups from residual oxidation. The band at 1560 cm^{-1} is associated to C=C stretching vibrations of the aromatic carbon in non-graphitic domains [19]. The broad band at ~1130-1116 cm^{-1} has contributions from the skeletal C–C observed in other carbon materials, and from some C–O stretching vibrations of oxygen groups. A typical vibrational band of OH groups at 1340 cm^{-1}, due to the O–H bending mode. The shoulder at 1220 cm^{-1}, is significantly more intense in the spectra of the oxidized carbon materials, when compared with the CNT. The FTIR spectra also showed vibrational bands related to the C=O stretching of carboxylic acids, aldehydes, ketone and quinone groups at 1730 cm^{-1} and of ketones and quinones at

1670 cm^{-1}. The CNT/ACT spectrum showed the presence of higher relative intensity bands associated with v(C=O) and δ(O-H) vibrations of carboxylic acids (1730 and 1670 cm^{-1}, respectively). These distinctions indicate a higher percentage of acid groups on the surface of these samples when compared to CNT. In addition, activation increases important parameters as the specific surface area and capacity, and open up new possibility of application of the carbon nanotubes (i.e. in energy storage devices).

The SWVs recorded on the activated GC/CNT/ACT electrode for different concentrations of AA (**Figure 8a**) shows that the intensity of oxidation peak of AA increases and its position shifts slightly from -0.05 V to -0.022 V with increasing concentration of AA. Also, a linear dependence of peak intensity versus AA concentration is obtained (**Figure 8b**).
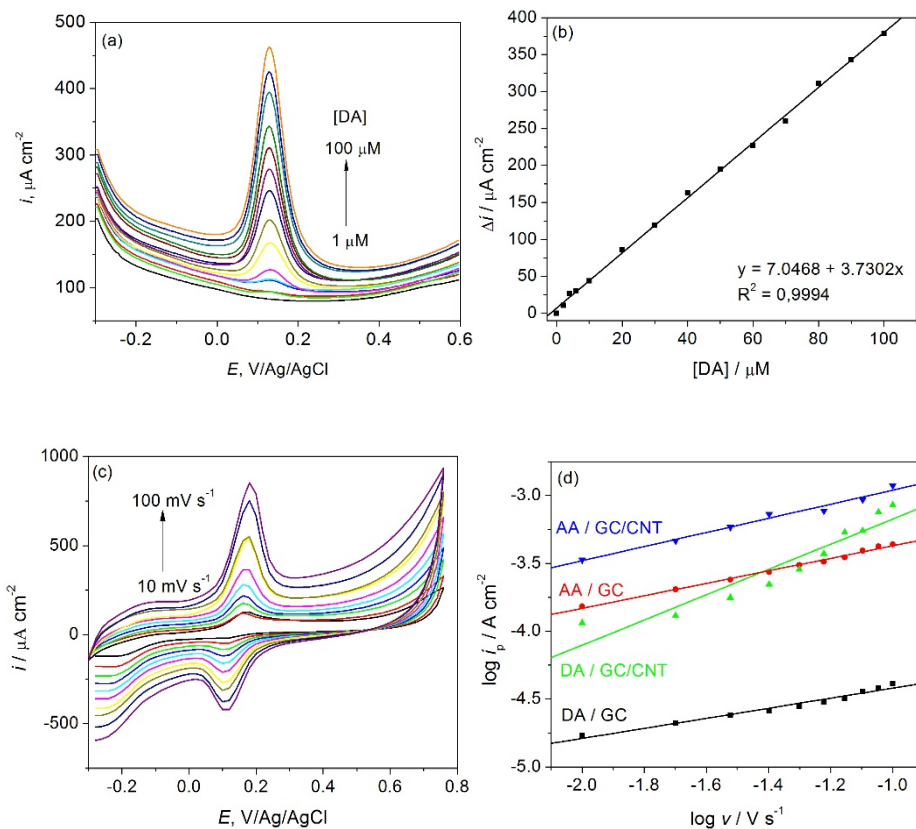

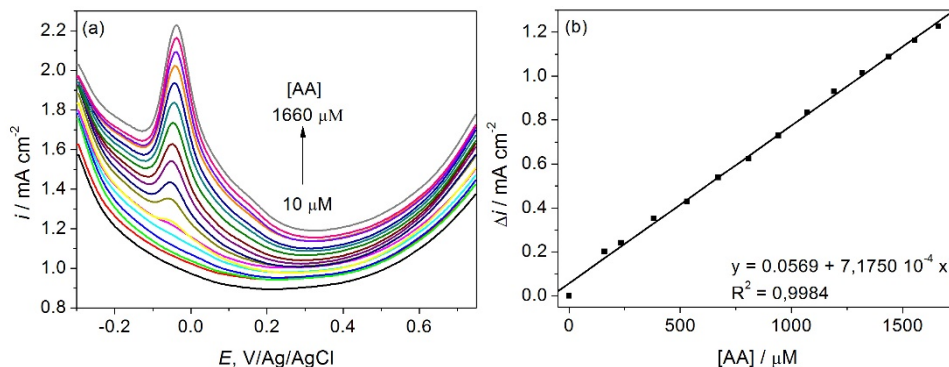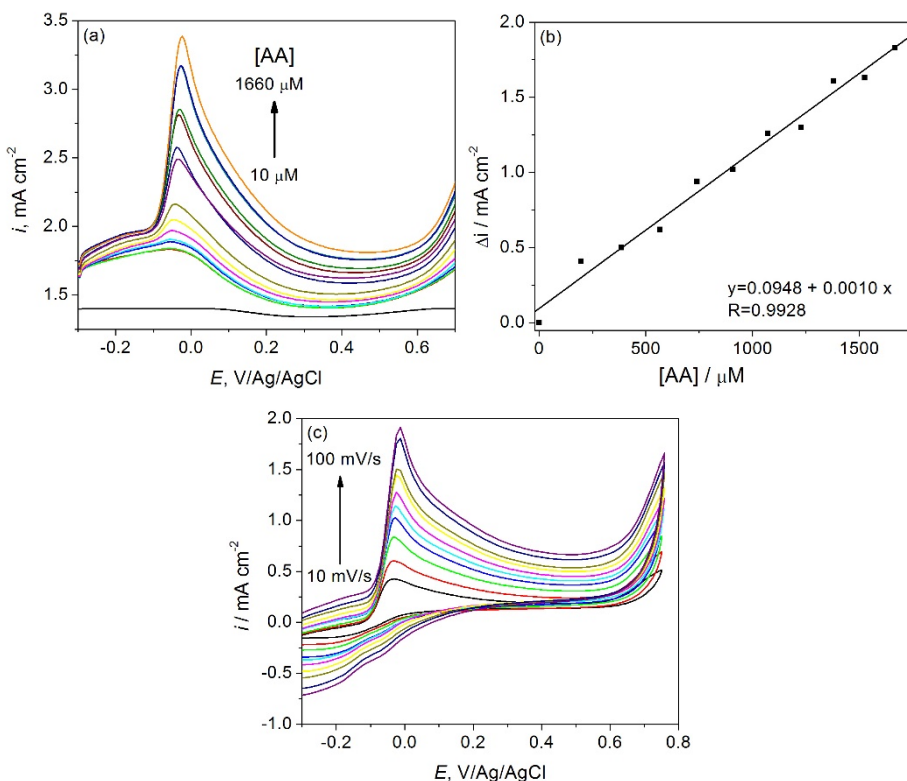**Figure 8.** AA detection in 0.1 M PBS (pH = 7.4) on GC/CNT/ACT electrode:
(a) SWVs at different AA concentrations; (b) calibration curve and
(c) CVs in 2 mM AA solution at different scan rates.

The AA oxidation reaction on GC/CNT/ACT electrode studied by cyclic voltammetry shows an irreversible oxidation peak that shifts from -0.03 V to -0.01 V as the scan rate increases (**Figure 8c**).

The SWVs recorded on the activated GC/CNT/ACT electrode for different DA concentrations are presented in **Figure 9a**.
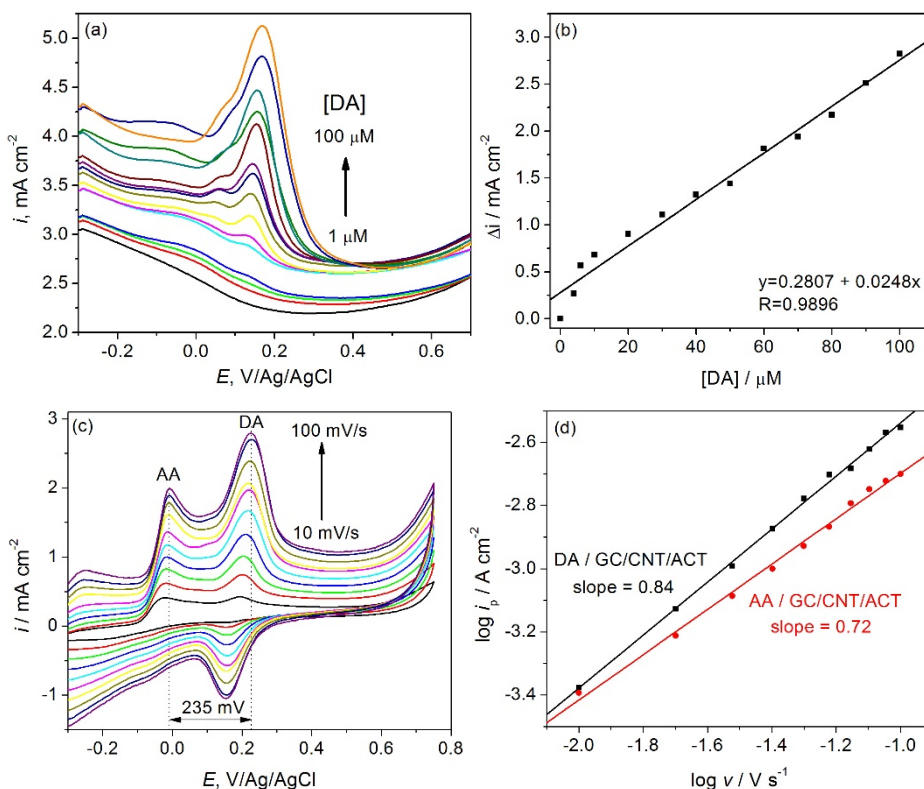
Figure 9. DA detection in 0.1 M PBS (pH = 7.4) on GC/CNT/ACT electrode:
(a) SWVs at different DA concentrations; (b) calibration curve
(c) CVs of 0.1 mM DA in the presence of 1.66 mM AA at different scan rates;
(d) plot of log i_p versus log v.

The intensity of the oxidation peak increases linearly (**Figure 9b**) and its position shifts slightly from 0.12 V to 0.16 V with increasing DA concentration. Cyclic voltammograms at different scan rates for a mixture of 1.66 mM AA and 0.1 mM DA are shown in **Figure 9c**. A peak separation of 235 mV between the oxidation potentials of AA and DA is observed, which makes possible their simultaneous detection. A single peak of AA oxidation is observed, without a correspondent in the cathodic branch, which is specific

to irreversible processes, while in the case of DA, two associated peaks are observed, indicating that DA oxidation is a reversible process. In addition, the peak current for DA oxidation shows a more pronounced increase with the scan rate compared to the peak current for AA oxidation, the peak current ratio being 1.4. The plot of log i_p versus log v given in **Figure 9d** also confirms this finding and shows different slopes for the oxidation of DA (0.840) and AA (0.716) on activated GC/CNT/ACT electrode, indicating an adsorption-controlled mechanism for DA oxidation and a mixed control of both diffusion and adsorption on AA oxidation. This behavior can be explained by enhanced attractive interactions between DA and the carbonyl and/or carboxyl type functional groups generated by CNT activation. DA presents an ortho-hydroxybenzene structure and an amino group in the side chain, protonated and positively charged at the working pH of 7.4 (pKa = 8.87 [20]). Also, the presence of benzene ring in the DA structure makes the oxidation of DA more facile due to the adsorption through π–π interactions of both its reduced and oxidized forms at sp^2 carbons of the CNT/ACT modified electrode [21].

Table 1. Effect of scan rate on the voltammetric response of GC, GC/CNT and GC/CNT/ACT electrodes for the oxidation of DA and AA, separately or in a mixture.

Electrode (Analyte)	Concentration	slope*	R^2 / n**
GC (DA)	100 µM	0.407	0.9835 / 9
GC/CNT (DA)	100 µM	0.930	0.9506 / 10
GC/CNT/ACT (DA+AA)	100 µM DA + 1.66 mM AA	0.840	0.9990 / 10
GC (AA)	1.66 mM	0.481	0.9958 / 9
GC/CNT (AA)	1.66 mM	0.520	0.9907 / 7
GC/CNT/ACT (AA+DA)	1.66 mM AA + 100 µM DA	0.716	0.9979 / 10

* slope of log i_p – log v dependence for the anodic process
** R^2 is the coefficient of determination and n the number of experimental points.

Square wave voltammetry measurements performed at constant AA concentration (1.660 mM), and at different DA concentration (2 to 100 µM) are shown in **Figure 10a**. It is observed that the separation between the oxidation potentials of AA and DA is maintained at 200 mV, which allows the detection of DA in the presence of AA. The linearity range of the calibration line for DA in the presence of AA (**Figure 10b**) is maintained within the same limits as in the case of the calibration line for DA in the absence of AA, being between 6 and 100 µM. There is a slight decrease in sensitivity from 24.6 µA / µM cm^2 in the absence of AA to 19.2 µA / µM cm^2 in the presence of AA, however DA can be detected selectively and sensitively using the activated GC/CNT/ACT electrode, even in the presence of concentrations of AA over 200 times higher.
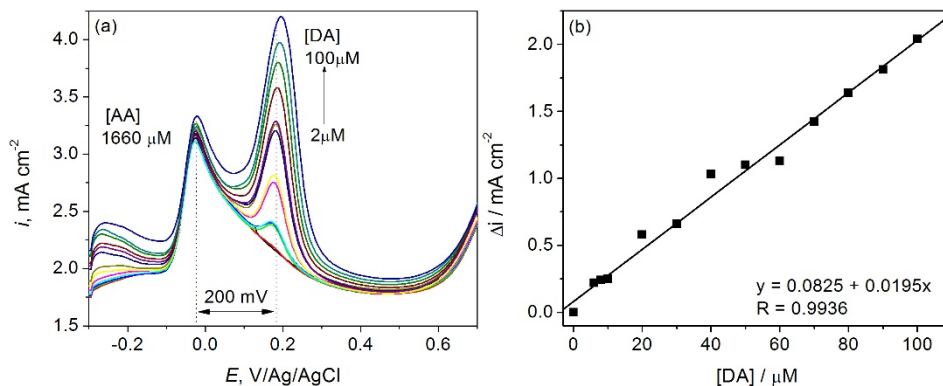
Figure 10. DA detection in the presence of 1.66 mM AA in 0.1 M PBS (pH = 7.4) on activated GC/CNT/ACT electrode: (a) SWVs at different DA concentrations; (b) Calibration line for DA detection in the presence of AA.

The result obtained for DA detection on GC/CNT and activated GC/CNT/ACT reveal comparable results with those reported for Polydopamine (PD) Copper(II) ions glassy carbon electrode (PD-Cu(II)h /GCE h Polydopamine) [20] or reduced graphene oxide and graphene oxide modified glassy carbon electrodes protected with a polymeric layer of Nafion or chitosan [24]. The detection parameters are better than those reported for Carbon fiber electrode (CFE) modified by graphene flowers (GEFi /CFE) [22]. Electrochemically pretreated pencil graphite electrode PGE [23] and nano-Au self-assembled modified electrode (nano-Au/CA/GC) [24] present lower detection limits than GC/CNT and GC/CNT/ACT.

The limit of detection (LOD) and limit of quantification (LOQ) were determined based on the standard deviation (S) and the slope of the calibration line (m), according to the following equations: LOD = 3S/m and LOQ = 10S/m. **Table 2** summarizes the electroanalytical detection parameters of DA, including relative standard deviation (RSD), determined in the absence and presence of AA for all the investigated electrodes.

Table 2. Electroanalytical detection parameters for DA on GC, GC/CNT and activated GC/CNT/ACT electrodes.

Electrode	Range, μM	Sensitivity μA/μM cm^2	R^2	RSD %	LOD μM	LOQ μM
GC (DA)	1…100	0.280	0.9997	0.019	16.08	53.59
GC/CNT(DA)	2…100	3.730	0.9995	0.027	1.76	5.87
GC/CNT (DA+AA)	10…100	5.300	0.9932	0.268	3.18	10.59
GC/CNT/ACT (DA)	4…100	24.79	0.9896	0.021	0.44	1.45
GC/CNT/ACT (DA+AA)	6…100	19.50	0.9936	0.023	0.64	2.14

Electrochemical detection of DA on CG/CNT/ACT electrode from synthetic biological samples in the presence of interferences

The performance of GC/CNT/ACT electrodes for DA detection from biological samples in the presence of potential interferences, was verified by recording SWVs for DA in the presence of AA and UA in 0.1 M PBS solution and by performing recovery measurement in a Ringer solution in the presence of AA and UA. **Figure 11** shows SWVs on activated GC/CNT/ACT for a solution containing 2 mM AA, 0.1 mM DA and 0.5 mM UA.
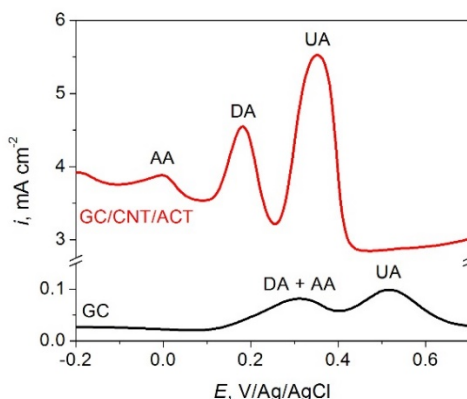
Figure 11. SWVs for a mixture of 2 mM AA, 0.1 mM DA and 0.5 mM UA on GC and activated GC/CNT/ACT electrode.

The electrochemical response of GC/CNT/ACT electrode is characterized by the appearance of three distinct oxidation peaks, corresponding to the oxidation of AA, DA and UA. The same measurements performed on the unmodified GC electrode indicate the appearance of only two oxidation peaks, the first one attributed to the simultaneous oxidation of AA and DA, and the second to the oxidation of UA. The peak potentials for the oxidation of DA, AA and UA on GC and GC/CNT/ACT are listed in **Table 3**. On the GC/CNT/ACT electrode, it is possible to detect DA in the presence of AA and UA, the differences between the peak potentials being of 0.20 mV and 0.17 mV, respectively.

Table 3. Peak potentials for simultaneous oxidation of DA, AA and UA on GC and activated GC/CNT/ACT electrodes in 0.1 M PBS.

Electrode	E_{AA} [V]	E_{DA} [V]	E_{UA} [V]
GC	0.32	0.32	0.52
GC/CNT/ACT	-0.02	0.18	0.35

For the recovery measurements, a Ringer's solution was used, with added AA and UA in order to obtain a concentration of 20 µM of each electroactive species. Then SWVs were recorded, with successive additions of DA to have increasing concentrations of 40, 50, 60, 70 and 80 µM. The obtained results are given in Table 4 and indicate satisfactory levels of recovery in the investigated concentration range.

Table 4. DA detection in Ringer's solution in the presence of AA and UA.

Added [µM]	Detected [µM]	Recovery [%]
40	31.8	79.5
50	49.3	98.5
60	59.0	98.4
70	65.9	94.2
80	75.3	94.1

CONCLUSIONS

The kinetics of DA and AA oxidation reaction was studied by cyclic voltammetry on GC, GC/CNT and activated GC/CNT/ACT electrodes. It has been found that DA oxidation on GC is a diffusion-controlled process, but it changes to an adsorption-controlled process on GC/CNT and GC/CNT/ACT electrodes.

The separate detection of DA and AA was carried out by square wave voltammetry, at concentrations between 1… 100 µM for DA and 10… 1660 µM for AA and the electroanalytical detection parameters were determined. The sensitivity of DA detection increased from 0.28 (GC) to 3,73 (GC/CNT) and 24.79 µA/µM cm^2 (GC/CNT/ACT). On GC electrode, the oxidation potentials of DA and AA are close, therefore DA detection in the presence of AA is not feasible. However, it has been found that modification of GC electrode with CNT and CNT/ACT induces a potential peak separation of 235 and 200 mV, respectively, which allows detection of DA even in the presence of AA, at more than 100 times higher concentrations. In the presence of 1.66 mM AA, the sensitivity slightly decreases to 19.50 µA/µM cm^2 on GC/CNT/ACT, compared to 24.79 µA/µM cm^2 in the absence of AA. In conclusion DA can be selectively and sensitively detected using GC modified with activated CNT.

GC/CNT/ACT electrodes also showed very good performance in the presence of both AA and UA, with well-resolved potential peak separation ($\Delta E_{AA–DA}$ = 200 mV, $\Delta E_{DA–UA}$ = 170 mV and $\Delta E_{AA–UA}$ = 370 mV).
Measurements of DA detection in synthetic solutions (Ringer's solution) in the presence of AA and UA showed that the method is reliable, obtaining recovery rates of 98% for added concentrations of DA of 50 and 60 µM,

respectively. In conclusion, our results showed the importance of activation step in the construction of CNT-based sensors for DA. The activated GC/CNT/ACT electrode can be successfully used for DA detection in the range of micromolar concentrations.

EXPERIMENTAL SECTION

Materials

Phosphate buffer (PBS) was prepared and used as the electrolyte solution, with the following composition: NaCl 0.8 g L^{-1}, KCl 0.2 g L^{-1}, Na$_2$HPO$_4$ 1.42 g L^{-1}, KH$_2$PO$_4$ 0.24 g L^{-1} and distilled water to 1L. All chemicals NaCl, KCl, Na$_2$HPO$_4$, KH$_2$PO$_4$ were purchased from Merck and used without purification. Stock solutions of 10^{-2} M dopamine (≥ 98.5% Fluka), 10^{-2} M L-ascorbic acid (≥ 99%, Sigma Aldrich) and 10^{-2} uric acid (≥ 99%, Sigma Aldrich) were freshly prepared in PBS buffer before use. A Ringer solution from B. Braun, with the composition NaCl 8.60 g L^{-1}, KCl 0.30 g L^{-1} and CaCl$_2$ 2H$_2$O 0.33 g L^{-1} was used. Multi-walled carbon nanotubes from Sigma Aldrich with an outer diameter of 6-9 nm and a length of 5 µm were used to modify the working electrode. As working electrode a glassy carbon electrode (GC) was used. Prior to each use, the electrode surface was prepared by polishing using diamond suspension with a particle size of 6 and 3 µm, respectively, followed by thoroughly rinsing with distilled water.

CNT activation and characterization

To activate the carbon nanotubes, 0.5 g of CNT were weighted and kept for 12 hours in 5M HNO$_3$ under magnetic stirring. The resulting product was then filtered and washed with abundant distilled water to neutral pH, followed by drying in an oven at 70 ° C for 12 hours. Samples are denoted as CNT/ACT. The structure of pristine and activated CNT was investigated by Fourier-transform infrared spectroscopy (FTIR), using an IR Prestige 21 Shimadzu spectrophotometer. FTIR spectra were recorded in KBr pellets, for wave numbers between 400 and 4000 cm^{-1}, where each spectrum consists of 20 interferograms with a resolution of 4 cm^{-1}.

GC/CNT and GC/CNT/ACT electrode preparation

A suspension of 4 mg CNT or CNT/ACT in 2 mL ethanol was subjected to ultrasonication for 60 minutes. The modified electrodes were prepared by drop casting 10 µL of the CNT or CNT/ACT suspension onto the previously cleaned surface of the GC, followed by solvent evaporation under nitrogen flow.

Electrochemical measurements

Cyclic voltammetry and square wave voltammetry measurements were performed in a three-electrode configuration electrochemical cell, using an AUTOLAB PGSTAT 302N. The electrochemical cell (50 mL) was equipped with a working glassy carbon electrode (GC, Φ = 3 mm, Metrohm A.G., Switzerland), a Pt wire electrode as a counter electrode and the reference electrode was a silver-silver chloride electrode, Ag/AgCl. Electrodes were immersed in 25 mL of PBS electrolyte solution and a SWV was recorded for the supporting electrolyte in the absence of DA and / or AA. SWV was carried with pulse amplitude of 20 mV, frequency of 10 Hz and step potential of 5 mV. CVs were recorded at increasing scan rates, from 10 to 100 mV s^{-1}, in steps of 10 mV s^{-1}. For the detection of DA and AA, SWV measurements were performed in the concentration range of 1 – 100 µM (DA) and 10 – 1660 µM (AA), respectively. Successive additions from the stock solutions were made of 2.5, 5, 10, 15, 25, 50, 75, 100, 125, 150, 175, 200, 225 and 250 µL for DA and 25, 50, 100, 200, 400, 600, 1000, 1400, 1800, 2200, 2600, 3000, 3400, 3800, 4200, 4600 and 5000 µL for AA. The corresponding concentration were calculated considering the volume change of the final solution. The calibration lines were obtained by representing Δi versus concentration of DA or AA, were Δi represents the difference between the current in the presence and absence of the analyte, at the same potential value.

REFERENCES

1. L. Yang, D. Liu, J. Huang, T. You, *Sensor. Actuat. B-Chem*, **2014**, *193*, 166-172
2. N.D. Oko, S. Garbarino, J. Zhang, Z. Xu, M. Chaker, D. Ma, D. Guay A.C. Tavares, *Electrochim. Acta,* **2015**, *159*, 174–183.
3. R.T. Kennedy, C.J. Watson, W.E. Haskins, D.H. Powell, R.E Strecker, *Curr. Opin. Chem. Biol.,* **2002**, *6*, 659–665.
4. B.J. Venton, R.M. Wightman, *Anal. Chem.*, **2003**, *75*, 414A–421A.
5. N.G. Tsierkezosa, S.H. Othman, U. Ritter, L. Hafermann, A. Knauer, J.M. Köhler, C. Downing, E.K. McCarthy, *Sensors Actuat. B-Chem.,* **2016**, *231*, 218–229.
6. N. Chauhan, S. Chawla, C.S. Pundir, U. Jain, *Biosens. Bioelectron.,* **2017**, *89*, 377–383.
7. A. Ramanavicius, A. Ramanaviciene, A. Malinauskas, *Electrochim. Acta* **2006**, *51*, 6025–6037.
8. D. Wu, H. Li, X. Xue, H. Fan, Q. Xin, Q. Wei, *Anal. Methods*., **2013**, *5*, 1469–1473.

9. N. Plesu, A. Kellenberger, I. Taranu, B.O Taranu, I. Popa, I., *React. Funct. Polym.,* **2013**, *73 (5)*, 772-778.
10. X. Zhang, L.-X. Ma, Y.-C. Zhang, *Electrochim. Acta,* **2015**, *177*, 118–127.
11. A.K. Bhakta, R.J. Mascarenhas, O.J. D'Souza, A.K. Satpati, S. Detriche, Z. Mekhalif, J. Dalhalle, *Mater. Sci. Eng.* C., **2015,** *57*, 328–337.
12. E.C. Ilinoiu, F. Manea, P.A. Serra, R. Pode, *Sensors*, **2013**, *13(6)*, 7296-7307.
13. C. Wang, J. Du, H. Wang, C. Zou, F. Jiang, P.Yang, Y. Du, *Sensor. Actuat. B –Chem.*, **2014**, *204*, 302–309.
14. F.R. Caetano, L.B. Felippe, A.J.G. Zarbin, M.F. Bergamini, L.H. Marcolino-Junior, *Sensor. Actuat. B-Chem.,* **2017**, *243*, 43–50.
15. I.V. Zaporotskova, N.P. Boroznina, Y.N. Parkhomenko, L.V. Kozhitov, *Mod. Electron. Mater.,* **2016**, *2*, 95-105.
16. M.J. Allen, V.C. Tung, R.B. Kaner, *Chem. Rev.,* **2010**, *110*, 132–145
17. Q. He, J. Liu, X. Liu, G. Li, P. Deng, J. Liang, *Sensors,* **2018**, *18*, 199;
18. Z. Hsine, S. Bizid, R. Mlika, H. Sauriat-Dorizon, A. Haj Said, H. Korri-Youssoufi, *Sensors* **2020**, *20*, 1256;
19. H. Gaspar, C. Pereira, S.L.H. Rebelo, M.F.R. Pereira, J.L. Figueiredo, C. Freire, *Carbon*, **2011**, *49*, 3441–3453.
20. J. Armstrong, R.B. Barlow, *Br. J. Pharmacol.,* **1976**, *57*, 501 – 516
21. R. Gusmão, M. Melle-Franco, D. Geraldo, F. Bento, M.C. Paiva, F. Proença, *Electrochem. Commun.*, **2015**, *57*, 22–26.
22. A. Liu, M.D. Wei, I. Honma, H. Zhou, *Adv. Funct. Mater.*, **2006**, *16*, 371 - 376.
23. L. Huang, S. Jiao, M. Li, *Electrochim. Acta*, **2014**, *121*, 233–239.
24. A.F. Szőke, G.L. Turdean, G. Katona, L. M. Muresan, *Studia UBB Chemia*, **2016**, *3*, 135-144.
25. J. Du, R. Yue, F. Ren, Z. Yao, F. Jiang, P. Yang, Y. Du, *Biosens. Bioelectron.,* **2014**, *53*, 220–224.
26. D.C. Stefanescu A.A. Ciucu, A.A. Rabinca, M. Buleandra, A.P. Stoian, R.C. Jecan, R. Hainarosie, *Rev.Chim.,* **2018**, *69(1)*, 277-281.
27. G.-Z. Hu, D.-P. Zhang, W.-L. Wu, Z.S. Yang, *Colloids Surf. B: Biointerfaces*, **2008**, *62*, 199–205.

SELECTION OF EFFECTIVE DEMULSIFYING AGENTS FOR OIL-WATER EMULSIONS BREAKDOWN

BAYAMIROVA RYSKOL[a], TOGASHEVA ALIYA[a], ZHOLBASSAROVA AKSHYRYN[a], BISSENGALIEV MAX[b], KUNAYEVA GAUKHAR[a], KULIYEV MURAD[a], BORIBEK SHYNGGYS[a]

ABSTRACT. Crude oil processing often requires the extraction of large amounts of water. Crude oil often mixes with water to form water-in-crude oil emulsions as a result of exposure such as high shear at the wellhead and natural surfactants in crude oil. These emulsions are undesirable and require demulsification to remove dispersed water and associated inorganic salts in order to meet production and shipping specifications. In addition, demulsifying these crude oil emulsions reduces corrosion and catalyst and consistently maximizes the overall profitability of crude oil production. The article looks into the results of tests on the selection of a demulsifier for the breakdown of water-in-oil emulsion mixtures at different settling times and temperatures depending on the specific consumption of the chemical agent, the effect of various demulsifiers on emulsions breakdown. The process of oil desalination with and without the addition of demulsifiers is considered. Desalination is carried out stepwise. Research results have shown that proxanol 305/50 is the most effective demulsifier.

Key words: oil-water emulsion; demulsifier; demulsification; residual water; dewatering.

INTRODUCTION

In the process of oil production and its joint movement with formation water, stable oil emulsions with high water content are formed. The reason for the formation of oil emulsions is the effective mixing of oil with formation water in the wellbore when it rises to the surface of the earth and during further movement along the field utilities. The most common emulsion in the

[a] *Yessenov University, Faculty of Engineering, 32 microdistrict, 130003 Aktau, Kazakhstan*
[b] *Atyrau University of Oil and Gas, Faculty of Oil and Gas, md.Railway station, st. Baimukhanova, 45A, Atyrau, Kazakhstan*
* *Corresponding autor: ainura_302015@mail.ru*

oil and gas industry is water in oil. The process of dispersing water droplets in oil is facilitated by the presence of surface acting agents (SAA) in the oil, such as asphaltenes, paraffins, resins and naphthenic acids. These SAAs are suspended in oil [1-3]. The concentration of these natural SAAa, which affect the stability of the oil-water emulsion, is higher in heavy oil than in light oil [4]. The quality of the oil produced, as is known, along with other indicators, is determined by its moisture content. The moisture content in the original product ranges from 90% to 0.1%. The quality of crude oil is also determined by the salt content, which ranges from a few mg/l to a few g/l. Water and salts present in oil cause a number of difficulties during transportation and processing. The effectiveness of the used demulsifying agent is the main factor in solving the problems of collecting and treating oil. Currently, the range of modern demulsifiers is wide. However, it is often impossible to achieve the required dewatering depth in the gathering system of oil wells and in the preparation process. With an increase in the share of high-viscosity oils and an increase in the average water-cut of oils this problem is acutely manifested in the total volume of production. The use of composites is several times more effective than the use of any compound in its pure form.

Oil treatment units (OTU) are used for dewatering and desalting oils. In addition, at these units measures are taken to reduce the ability of oil to evaporate (in order to reduce the loss of light hydrocarbons), i.e. oil stabilization is in progress.

It is most expedient to install OTU at points of maximum oil concentration in the field, for example, in tank farms. Taking into account the adopted scheme for gathering and transporting oil and gas, it is necessary to envisage the possibility of oil preparation at another field if an accident occurs at this field. Formation water produced with oil and with salts dissolved in it should be removed at the fields. In this case, the main processes are dewatering and desalination. Most of the salts are removed along with water during dewatering. However, in order to prevent corrosion of equipment, the formation of salt deposits and other disturbances in the process of oil refining, its deep desalination is required. Before desalination, fresh water is supplied to the oil as a result of which an artificial emulsion is formed which then undergoes destruction [5].

The process of breakdown of oil emulsions consists in merging of droplets of water dispersed in oil in the presence of a demulsifier and deposition of enlarged droplets.

Demulsifiers are surface acting agents that are adsorbed on the surface of water globules and form an adsorption layer with significantly lower mechanical strength, which facilitates droplet coalescence and contributes to the destruction of oil emulsions.

The following types of demulsifiers are used: diproxamine, proxamine, disolvan, separol, polyacrylamide, oxyethylated compound OC, etc. Demulsifier should meet the following requirements: be highly active at low specific consumption; dissolve well in water or oil; be cheap and transportable; do not deteriorate the quality of oil; do not change its properties with temperature changes. Demulsification effect depends on the intensity of mixing of the demulsifier with the emulsion and on the temperature of the mixture. Demulsifiers are supplied by dosing pumps [6].

RESULTS AND DISCUSSIONS

Table 1. Thermochemical breakdown of emulsions at consumption of 20 mg/l (n=1500 rpm

Demulsifier description	Amount of separated water at time, min		Residual water content, %
	60	120	
	Separated water, ml		
Without chemical agent	71	73	3.2
Diproxamine 157-65M	78	82	1.9
Reapon 4в	65	73	2.9
Proxanol 305*	25	82	2.1
Disolvan 4411	81	90	1.0

Note: * - 100 % chemical agent was used.

As follows from the experiments, the use of demulsifiers increases the depth of emulsion breakdown and reduces the residual water content in oil. However, the assumed consumption of 20 mg/l does not provide a reduction in residual water content below 1.0%. Therefore, in the next series of experiments the consumption of these demulsifiers was increased to 50 mg/l (see Table 2).

As can be seen from the Tables, with the increase in the consumption of demulsifiers (proxanol 305 and disolvan 4411), the residual water content in oil was below 1%. The most effective is disolvan 4411 (consumption up to 50 mg/l). Proxanol 305 is also acceptable.

Demulsifier consumption of 100 mg/l (at proxanol 305) is the initial one for the production of pilot tests and in the process of commissioning and testing of OTU mode can be reduced. The preferred point for demulsifier injection is before the gas separators of OTU and before the process pump of the oil dewatering stage.

Table 2. Thermochemical breakdown of emulsions at consumption of 50 mg/l
(n=1000 rpm)

Demulsifier description	Amount of separated water at time, min	Residual water content, %
	120	
	Separated water, ml	
Without chemical agent	90	2.3
Diproxamine 157-65M	90	2.1
Reapon 4в	85	3.8
Proxanol 305*	95	traces-0.5
Disolvan 4411	100	traces

Note: * - 100 % chemical agent was used.

The end of the mass transfer of the demulsifier with the emulsion stabilizer is carried out when passing through the heat exchanger. Thus, the following parameters can be recommended to arrange the process of dewatering of a mixture of oil and condensate at the Karachaganak field:

Oil-water emulsion heating temperature	60…70°C;
Settling temperature	60…70°C;
Demulsifier initial consumption	50…100 mg/l;
Demulsifier brand	proxanol 305, disolvan 4411;
Time in settling pit	up to 1 hour.

Compatibility of the demulsifier with wax inhibitors and corrosion inhibitors during dewatering

The compatibility of the inhibitors IKIG, Sever-1, Tyumen-2 and Neftekhim 3в and the effect on the demulsification process of oil-water-gas condensate emulsion when using the demulsifier proxanol 305-50 were studied. The studies were carried out according to the methodology presented above with the selected parameters.

In the course of the study the influence of the "aging" of the emulsion on the process of emulsion breakdown was also assessed.

The study results are given in the Table 3.

From the Table 3 it follows that aging significantly affects the depth of emulsion breakdown both with demulsifier and with the combined presence of demulsifier with a number of corrosion and wax inhibitors.

It is also seen from the experiments that the most preferred additives are inhibitors of the IKIPG type which practically do not affect the demulsifying activity of the selected demulsifier. The situation is somewhat worse with the compatibility of proxanol 305-50 and corrosion inhibitor such as imidozoline (Tyumen-2, Neftekhim 3в) and pyridones (Sever-1). However, it should be noted here that in the experiments we used a 2-fold reduction in the consumption of the demulsifier. This technique was used for a better manifestation of antagonism or synergy in the combined presence of demulsifier and inhibitor, and hence a more accurate assessment. With an increase in proxanol consumption the observed antagonism is suppressed due to its competing adsorption on globules of formation water in oil and peptization of the displaced asphaltene-paraffinic emulsion stabilizers.

Table 3. The amount of separated water

Chemical agent brand	Agent consumption, mg/l	"Fresh" emulsion		After its aging	
		Amount of separated water, %	Residual water content, %	Amount of separated water, %	Residual water content, %
1	2	3	4	5	6
Proxanol	50 100	100 -	traces -	75 95	2.5 0.5
Agent mixtures: Proxanol 305+ IKIPG	50 400	100	traces	100	traces
Proxanol 305+ IKIPG+ GKP-86	50 200 400	91	0,9	93	0.7
Proxanol 305+ Sever-1	50 200	97	0,3	67	3.3
Proxanol 305+ Tyumen-2	50 100	100	traces	82	1.8
Proxanol 305+ Neftekhim 3в	50 100	100	traces	85	1.5

Studies of the conditions of desalination were carried out taking into account the complicating factors, which include the formation of finely dispersed stabilized drops of formation water. The results of the study of emulsions "aging" are shown in the Table 4,5.

Table 4. Desalting of the base oil-condensate mixture of the Karachaganak field without demulsifiers

Stage 1					Stage 2		
Amount of flush water%	Type of water	Elimination in 2h, %		Salt content in oil, mg/l	Elimination in 2h, %		Salt content in oil, mg/l
		Water, ml	intermediate layer		Water, ml	intermediate layer	
15	B1	12.5	1.5	9.7	-	-	-
15	B2	13.0	2.0	20.0	-	-	-
15	B3	3.0	0.5	23.2	-	-	-
15	B1	13.0	2.0		14.0	-	4.0
15	B2	13.0	2,0		13.0	1.0	4.0
5	B3	4.0	1.0		4.0	1.0	7.2

Table 5. Desalting of the base oil-condensate mixture of the Karachaganak field using proxanol 305/50

Stage 1					Stage 2		
Amount of flush water %	Type of water	Elimination in 2h, %		Salt content in oil, mg/l	Elimination in 2h, %		Salt content in oil, mg/l
		Water, ml	Intermediate layer		Water, ml	intermediate layer	
15	B1	13.0	2.0	12.2	-	-	-
15	B2	14.0	1.0	11.0	-	-	-
15	B3	2.0	3.0	9.4	-	-	-
15	B1	13.5	2.0		14.0	Pit	3.0
15	B2	14.0	1.0		14.0	Pit	3.3
5	B3	2.5	2.5		3.0	0.8	8.8

Table 6. Desalting of the base oil-condensate mixture of the Karachaganak field using reapon 4в

Stage 1					Stage 2		
Amount of flush water, %	Type of water	Elimination in 2h, %		Salt content in oil, mg/l	Elimination in 2h, %		Salt content in oil, mg/l
		Water ,ml	intermediate layer		Water ,ml	intermediate layer	
15	B1	13.0	2.0	15.0	-	-	-
15	B2	12.0	3.0	15.4	-	-	-
15	B3	2.0	3.0	16.0	-	-	-
15	B1	13.0	2.0	-	15.0	Pit	4.0
15	B2	12.0	3.0	-	14.0	2.0	8.8
5	B3	2.0	2.0	-	3.0	2.0	9.2

Thus, the established demulsifier consumption should be dispersed along the process scheme in the direction of decreasing the emulsion aging time. In this, most of the demulsifier is used after the II stage separators (~ 60 mg/l), and a smaller part is fed to the intake of the process pump of the dewatering stage (40 mg/l). This recommendation has constitutive nature for assigning an initial consumption when commissioning a dewatering process.

CONCLUSIONS

Emulsions of oil condensate and water are relatively unstable and are destroyed by simple heating up to 60°C to 2 ... 5% by residual water content, however, as emulsions age, their stability increases, which requires special treatment with demulsifiers. Demulsifier injection should be dispersed along the process scheme in the direction of decreasing the aging time of the emulsion;

For successful demulsification of oil in the electric dehydrator, the rated power of the transformer should be greater than the rated active power required to maintain the electric field of the required strength. For oil from the Karachaganak field this condition is fulfilled, which makes it possible to use electric dehydrators for the preparation of oil and its mixture with condensate. In this case, the power of the standard transformer of the EG 200-10 electric dehydrator can be reduced substantially;

All investigated chemical agents used in oil production and collection (except for Sever-1) do not significantly affect the stability of emulsions.

Introduction of the optimal type of demulsifying agent in the amount not exceeding 50 mg/l is mandatory both for reasons of completeness of the dehydration process and in terms of desalination indicators.

- considering that a significant part of the KNGKM salts are in a difficult-to-recover form, the process temperature should be at least 70 ... 75°C;

- the required completeness of separation of the emulsion requires the use of intensifying factors. The simplest and most effective is the electric field. An additional factor for the intensification of desalination can be the addition of a salt inhibitor to the flush water.

EXPERIMENTAL SECTION

The study used the most stable emulsion with a water content of 10% and an oil-condensate ratio of 1: 2. The prepared emulsion after 16 hours of aging was heated to 60°C, and a demulsifier was added with stirring. The stirring time was 5 minutes, which, due to its low viscosity, turned out to be

sufficient to complete the processes of mass exchange of the demulsifier and stabilizer substances on the globules of dispersed water. After that, the emulsion was left to settle at the temperature of 60°C for 2 hours. At the end of the settling process, the amount of water released from the emulsion was measured and the residual water cut was calculated using the formula [7-9]

$$V = \frac{в - a}{c - в} \cdot 100\%,$$

where V – residual water content in oil, %;

c – emulsion volume, ml;

в – amount of water in original emulsion, ml;

a – amount of separated water in original emulsion, ml.

Demulsifiers of Kazan IA "Orgsintez" which are widely used in the field in the processing of light and paraffinic oils were taken as demulsifiers. These are diproxamine 157-65M, proxanol 305 and reapon 4в. For comparison, experiments were also carried out with an imported analogue of disolvan 4411 manufactured by Hoechst (Germany). Table 1 shows the results of the study of emulsion dewatering at the temperature of 60°C and the speed of mixing the emulsion with demulsifiers at 1500 rpm. The initial consumption of demulsifiers of all brands was constant (20 mg/l). Demulsifiers were introduced in the form of 1% aqueous solutions[10-13].

REFERENCES

1. Daniel-David, D.; Le Follotec, A.; Pezron, I.; Dalmazzone, C.; Noik, C.; Barre, L.; Komunjer, L. *Oil Gas Sci. Technol. Rev. L'IFP* **2008**, *63*, 165–173.
2. Kundu, P.; Paul, V.; Kumar, V.; Mishra, I.M. *Chem. Eng. Res. Des.* **2015**,*104*, P 773–790.
3. Martínez-Palou, R.; Reyes, J.; Cerón-Camacho, R.; Ramírez-de-Santiago, M.; Villanueva, D.; Vallejo, A.A.; Aburto, J. *Chem. Eng. Process. Process Intensif*. **2015**, *98*, 112–122.
4. Wong, S.; Lim, J.; Dol, S. *J. Pet. Sci. Eng.* **2015**,*135*, 498–504.
5. Dejam, M.; Hassanzadeh, H.; Chen, Z. *AIChE J.* **2015**, *61*, 3981–3995.
6. Abdulredha, M.M. *Arab. J. Chem.* **2018**, *52*, 258-264
7. Bayamirova R., Togasheva A., Zholbassarova A., Islamberdiyev Z., *Studia UBB Chemia*, **2020**, 65, 233-244.
8. Salam, K.; Alade, A.;Arinkoola, A.; Opawale, A. *J. Pet. Eng.* **2013**, P 793101.

9. Kang, W.; Yin, X.; Yang, H.; Zhao, Y.; Huang, Z.; Hou, X.; Sarsenbekuly, B.; Zhu, Z.; Wang, P.; Zhang, X.; et al. *Colloids Surf. A Physicochem. Eng. Asp*. **2018**, *545*, 197–204.
10. Ongarbayev Y., Golovko A., Krivtsov E., Tileuberdi E., Imanbayev Y., Tuleutayev B., Mansurov Z., *Studia UBB Chemia,* **2014**, 59, 57-64.
11. Mhatre, S.; Simon, S.; Sjöblom, J.; Xu, Z. Chem. Eng. Res. Des. **2018,** *134,* 117–129.
12. Imanbayev Y., Tileuberdi Y., Ongarbayev Y., Mansurov Z., Batyrbayev A., Akkazin Y., Krivtsov E., Golovko A., Rudyk S., *Eurasian Chemico-Technological Journal*, **2017**,19, 147-154
13. Bissembayeva K., Aissayeva T., Zholbassarova A., Islamberdiyev Z., Bayamirova R., Togasheva A.//*Inter.J. of Engineering and Technology(UAE)* **2018**, *7*, 376-379

NOVEL POLYDIOXANONE - PLURONIC 127 OXYTOCIN IMPREGNATED MESH, PRELIMINARY STUDY OF OXYTOCIN RELEASE IN VITRO

ANDREEA ELENA MIRON (LUNGU)[a], MARIOARA MOLDOVAN[b], DOINA PRODAN[b], MIHAELA VLASSA*[b], MĂDĂLINA MOLDOVAN[c], RAREȘ CĂLIN ROMAN[c], MÎNDRA EUGENIA BADEA[a]

ABSTRACT. Polymers represent a novel alternative in bone regeneration. Polydioxanone combined with Pluronic was used as a carrier for Oxytocin in form of an interfacial deposition obtained scaffold. The low rate of resorption of the scaffold follow the bone regeneration sequence assuring a constant and continuous release of Oxytocin. The Oxytocin release was monitored by RP-HPLC method. The separation was performed on a Phenomenex Luna 5μm C18 100A, 250x4.6mm, using isocratic elution with acetonitrile: phosphate buffer pH 7 (30:70 v/v) mobile phase. Flow rate 1 ml / min, column temperature 30°C, DAD, λ= 220nm. The surface morphology of polydioxanone - pluronic 127 - Oxytocin impregnated mesh was characterized by SEM.

The preliminary results show that the Polydioxanone combined with Pluronic is a promising polymer for bone regeneration engineering.

Keywords: polydioxanone, Oxytocin, bone reconstruction, biodegradable scaffolds, RP-HPLC, SEM

INTRODUCTION

First used as monofilament suture material, polydioxanone is a hydrophobic instable polymer with a low resorption rate expanding between 6 months to 2 years [1]. It can be manufactured as meshes, solid implants or membranes, making it suitable as a biological substitute [2]. Recently studied

[a] *University of Medicine and Farmacy Iuliu Hațieganu, Dental Medicine Department of Prevention in Dental Medicine, 31 Avram Iancu str., RO-400083, Cluj-Napoca, Romania*

[b] *Babeş-Bolyai University „Raluca Ripan" Institute for Researh in Chemistry, 30 Fântânele str., RO-400294, Cluj-Napoca, Romania*

[c] *University of Medicine and Farmacy Iuliu Hațieganu, Dental Medicine Department of Cranio-Maxilo-Facial Surgery, 33 Calea Moților str., RO-400001, Cluj-Napoca, Romania*

* *Corresponding author mihaela.vlassa@ubbcluj.ro*

ANDREEA ELENA MIRON (LUNGU), MARIOARA MOLDOVAN, DOINA PRODAN, MIHAELA VLASSA, MĂDĂLINA MOLDOVAN, RAREȘ CĂLIN ROMAN, MÎNDRA EUGENIA BADEA

in chest wall defects reconstruction, polydioxanone proved to sustain the needed resistance, flexural strength, and biocompatibility for a bone implant [3]. In large reconstructions of defects that extend the 6 cm limit of natural healing, the implant integration encounters several complications. Situs infection is the most common adverse outcome, followed by the pathological movement of the reconstructive segments, and abnormal scar tissue formation [4].

Absorbable graft materials present fewer healing complications when properly covered with soft tissue. In this context, adding Pluronic 127 to the polydioxanone mesh enriches the final compound hydrophilic behavior assuring a greater resorbable potency by hydrolysis [5]. Because of Pluronic 127 high hydrophilicity that compound was successfully used as cell carrier system in bone regeneration, maintaining cell viability and assuring the necessary permeability for bone growth mediators to reach the carried cells [6-9]. Pluronic 127 (poloxamer 407) is a synthetic hydrogel made of amphiphilic copolymers consisting of units of ethylene oxide (PEO) and polypropylene oxide (PPO) [9]. Due to its thermosensitivity it changes from solution to gel state at 37°C enabling the carrying matrix to withhold its charge stable in the bone defect [10].

Combining a slow resorbable polymer with a very fast one (small traces of pluronic were found after 3 weeks from its insertion in a bone defect) results in a controlled compound with superior mechanical strength and biocompatibility which may be used as a delivery system for cells, chemical mediators, proteins, growth factors, hormones, and drugs in bone tissue engineering.

Oxytocin is a hypophyseal hormone which plays an important role in labor, lactation and social relationships. Also, its role as a bone anabolic hormone is well known, local administration was yet avoided giving its short half-life and its lack of resistance to hydrolytic enzymes. Creating the optimal condition for Oxytocin release acquires a stable hydrophilic carrier with the right resistance, biodegradable rate and chemical bonds that allows Oxytocin to reach the bone tissue gradually, according to its healing sessions [11].

Oxytocin reaches osteoblast receptors and signals them to the bone defect stimulating new bone formation [12]. Its catabolic effect on adipocytes prevents enlargement of the fatty bone marrow, promoting dense trabecular bone with reduced marrow space. Oxytocin inhibits osteoclastic activity [13]. Oxytocin's osteoinductivity combined with its carrier polydioxanone-pluronic high biocompatibility and volumetric stability, assures the premises for optimal bone regeneration.

A wide range of analytical methods have been used to determine Oxytocin in different matrices. Radioimmunoassay (RIA) and Enzyme immunoassay (ELISA) was used to quantitative measurement of Oxytocin in biological sample because of its high sensitivity [14]. The chromatographic

methods were also used for determination of the Oxytocin in biological matrix by high performance liquid chromatography technique with different detectors (HPLC-UV) [15, 16], and LC plus tandem mass spectrometry (MS/MS) [17, - 20].

The aim of the work was to obtain the polymeric matrix (the mesh) for the Oxytocin impregnation and to monitor the release of this hormone by the HPLC technique. Also, the structure of polymeric mesh morphology was studied by SEM.

RESULTS AND DISCUSSION

For the quantitative determination of Oxytocin (see Figure 1) released from the polymeric mesh, a liquid chromatographic RP-HPLC method with isocratic elution was used. The validation of the present analytical method was done by the following parameters: selectivity, linearity, LOD (limit of detection), LOQ (limit of quantification) and precision [21].

Selectivity represent the ability to measure unequivocally the desired analyte in the presence of components such as excipients and impurities that may also be expected to be present. Thus, the selectivity was established by comparing the chromatogram of the Oxytocin standard solution with those of an Oxytocin sample extract (Figure 2). The retention time of Oxytocin were at 4.372 min both in standard solution and sample extract.

Linearity indicates the ability to obtain results that are directly proportional to the concentration of the analyte in samples and was established by plotting the analyte peak area against the analyte concentration. The obtained results proved an R^2 (correlation coefficient) of 0.9998 (Table 1).

Precision is the degree of agreement among individual results. The intra-day and inter-day precision were expressed as percentage of relative standard deviation (% RSD).
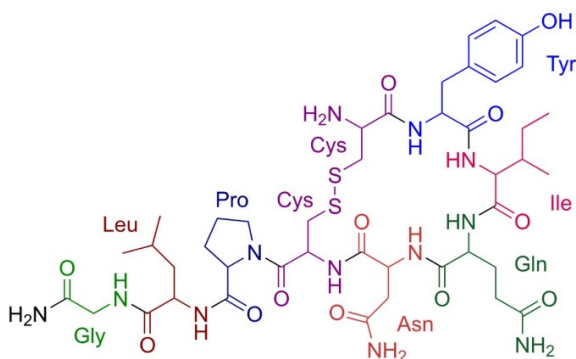
Figure 1. Chemical structure of the Oxytocin

The obtained results, 0.62 µg mL^{-1} value of LOD and 1.89 µg mL^{-1} for LOQ respectively, for Oxytocin determination, indicate a good sensitivity of the proposed method.

The parameters of the calibration curve are shown in Table 1 and the RP-HPLC chromatograms are presented in Figure 2.

Table 1. Linear regression data, LOD and LOQ of the Oxytocin standard solution

Parameters	Oxytocin
[a] RT [min]	4.37
[b] Regression coefficient R^2	0.9998
[c] Calibration curve	Y= 46.32309X- 14.93387
Linear range (µg mL^{-1})	1.563 - 100
[d] LOD (µg mL-1)	0.62
[e] LOQ (µg mL-1)	1,89

[a] RT the retention time; [b] R^2 regression coefficient of calibration curve (n=7, seven points); [c] Y, the peak area; X the concentration of standard compound; [d] LOD, the detection limit (3.3 S/σ); [e] LOQ, the quantification limit (10 S/σ); S= standard deviation of low concentration, σ= slope of the calibration line
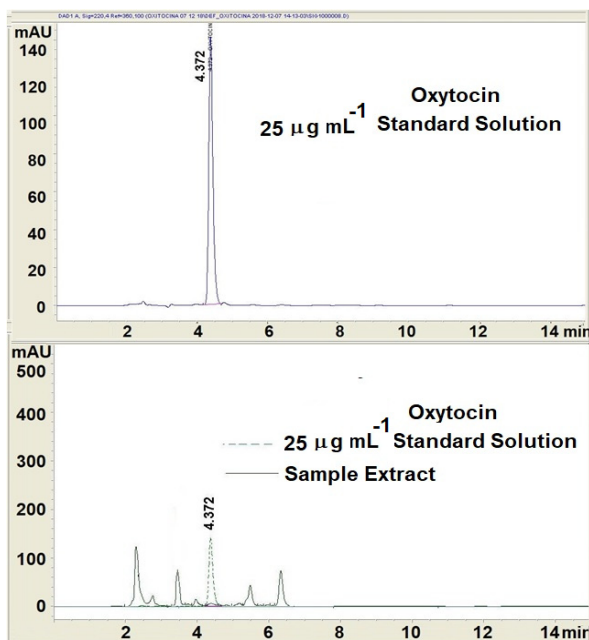
Figure 2. RP-HPLC chromatogram of 25 µg mL^{-1} Oxytocin standard solution and overlapped chromatograms of Oxytocin standard and sample solution.

The precision data are presented in Table 2 and the results show there were no significant differences between the test results. The method precision was satisfactory.

Table 2. Intra- and inter-day precision of Oxytocin

	Concentration ($\mu g \cdot mL^{-1}$)	Intra-Day Precision (n = 6)		Inter-Day Precision (n = 9)	
		Measured concentration Mean [a] ± SD [b],	RSD [c] (%)	Measured concentration Mean [a] ± SD [b],	RSD [c] (%)
Oxytocin	3.125	3.13±0.03	1.04	3.12±0.12	3.95
	12.5	12.48±0.14	1.15	12.37±0.56	4.56
	50	50.37±0.71	1.41	49.88±2.13	4.26

[a] Mean = Average of *n* determination; [b] SD = Standard deviation;
[c] RSD = Relative standard deviation;

The result of Oxytocin release from the polimer sample matrix from the first day shows a quantity of 1.97 $\mu g\ mL^{-1}$ Oxytocin extracted.

In the samples collected from the second, third and fourth day, the amount of Oxytocin released is below the detection limit of the method.

These results point out the strong bond betwen polydioxanone and Oxytocin, blocking the propper release of the hormone.

Preliminary results of Oxytocin release lead to hypotesis that to ensure a better release, probably an other compound like heparine, should be intercalated betwen this hormone and the polymer.

The surface morphology of polydioxanone - pluronic 127 - Oxytocin impregnated mesh was characterized by SEM and the results are shown in Figure 3.

SEM (Scanning Electron Microscopy) images shows a porous structure with specific geometric shapes and complex structures. Ceramic composite matrix, HA/TCP/Polymer, constitute the inorganic component of resorbable polymer/ceramic biocomposites. In this case, including calcium phosphates [e.g. calcium tetraphosphate ($Ca_4P_2O_9$) (CTP), tricalcium phosphate [$Ca_3(PO_4)_2$, TCP], hydroxyapatite [$Ca_{10}(PO_4)_6(OH)_2$, HA], and their derivatives and combinations]], that are the most popular ceramics used in bone tissue engineering and controlled drug delivery systems, is benefic.
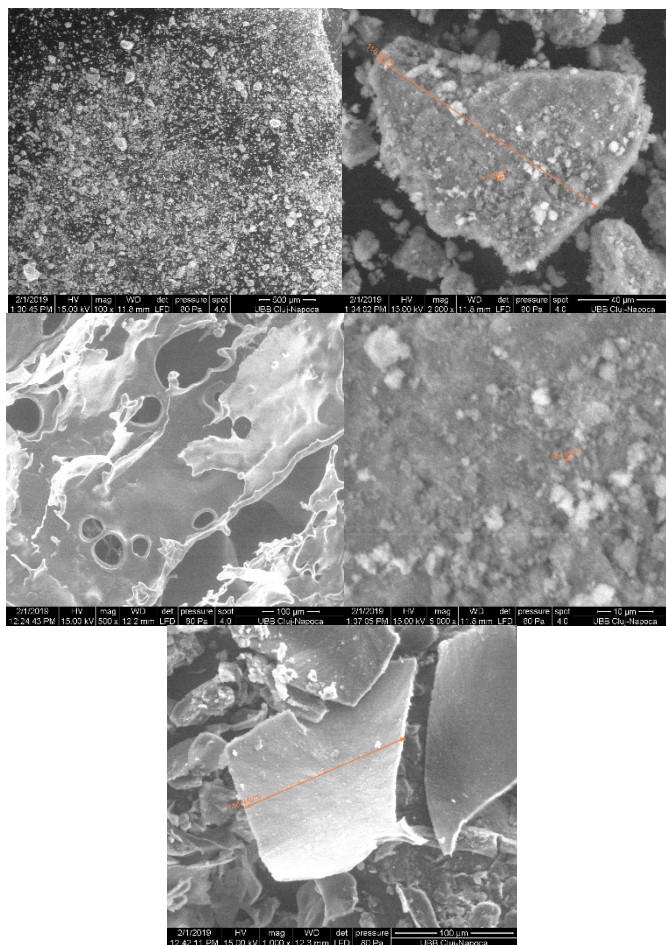
Figure 3. SEM imagine for polydioxanone - pluronic 127 mesh

CONCLUSIONS

Polydioxanone is a promising polymer for bone regeneration engineering. Its biocompatibility and polymorphism allow it to be fitted for every bone reconstruction need, from small defects characteristic for periodontal disease to large ones resulting from resective surgery or trauma.

To facilitate the continuous and controlled release of Oxytocin from the structure of new polymer, will be necessary to use (in future studies) a compound, like heparin, necessary to prevent the strong bonds with the other two primary components of the polymer.

Bioactive molecules play a critical role in bone gain by alloplastic grafts. Oxytocin presents a pleiade of metabolic effect that ensures osteoblastic activity boost and osteoclastic and bone adipocytes inhibition. The use of porous scaffolds is a potential method for repairing defects.

EXPERIMENTAL SECTION

Chemical and reagents

All reagents were of analytical grade. Analytical grade water was obtain from MilliQ Simplicity ultrapure water machine (Millipore, USA). Acetonitrile of HPLC grade and phosphoric acid were from (Optigrade Promochem, Germany). Oxytocin 1 mg solid (Sigma Aldrich, Germany), KH_2PO_4 (Roanal, Budapest, Hungary), KOH pellets (Sigma Aldrich, Germany). Pluronic F127 (Sigma-Aldrich, Germany), ethyl acetate (Sigma-Aldrich, Germany), polydioxanone (Merck, Germany), Miglyol (Caesar & Loretz, Hilden, Germany) hydroxyapatite and calcium triphosphate with chitosan (synthesis in ICCRR-UBB)

Pluronic – Polydioxanone mesh obtaining process: the preparation of the matrices was done by the interfacial deposition method. Two phases are prepared, the organic and the aqueous phase. The organic phase is composed of organic solvent (ethyl acetate) saturated with distilled water (2%), polymer (polydioxanone), oil (Miglyol or mineral oil), hydroxyapatite and calcium triphosphate with chitosan. The aqueous phase is composed of distilled water saturated with organic solvent (2% ethyl acetate) and surfactant (Pluronic F127).

For both phases, the solutions are mixed, in order to obtain clear and homogeneous solutions, then the other precursors are gradually introduced, each in turn, after the introduced precursor is dissolved (for example the polymer, only to then polymerize around the oil droplets). After the two phases are prepared, the organic phase is introduced into the aqueous phase, this time instantly, but the aqueous phase is in the presence of 8000 rpm rotation produced by Digital Dispenser T18-Agitator. Maintain the new solution for 10 minutes at this rotation, then add three or four times more water than the amount of solution resulting from the organic aqueous phase. This additional amount of water facilitates the diffusion of the respective surfactant of the organic solvent from the final solution.

These resulting solutions are then rotoevaporated and lyophilized, and the result are biocompatible mesh.

ANDREEA ELENA MIRON (LUNGU), MARIOARA MOLDOVAN, DOINA PRODAN, MIHAELA VLASSA, MĂDĂLINA MOLDOVAN, RAREȘ CĂLIN ROMAN, MÎNDRA EUGENIA BADEA

Oxytocin incorporation protocol and release determination

The obtained meshes of polymer are immersed in 3 ml Oxytocin saline solution and kept for 9 hours at 4°C. The Oxytocin concentration in saline solution was 2.5 mg mL^{-1}.

Monitoring the Oxytocin content released from the meshes

For the quantitative determination of Oxytocin released from the polymeric mesh, a liquid chromatographic RP-HPLC method with isocratic elution was used.

Instrumentation and chromatographic conditions

The Oxytocin determination were performed using an Agilent Technologies 1200 High Performance Liquid Chromatograph equipped with ALS G 1329 A autosampler, degasser G 1322 A, quaternary pump G 1311 A; thermostat TCC SL G 1316 B and diode array detector (DAD) G 1315 D. Data analyses were performed by ChemStation Software. The separation was achieved on a Phenomenex Luna 5u C18 100A, 250x4.6mm chromatographic column in isocratic conditions. The mobile phase was a mixture of acetonitrile: phosphate buffer pH 7 (30:70 v/v), at a flow rate 1 ml min^{-1} and 30°C temperature of column thermostat. The injected volume was 50 µL and chromatograms were collected at λ= 220 nm wavelength. The mobile phase is filtered and degassed through a 0.45 µm nylon membrane filter (Nordic Chemicals, Romania).

An analytical balance Ohaus (Switzerland) were used for samples weighing. The phosphate buffer pH was measured with a Hanna 211 pH-Metter (Hanna Instruments, United Kingdom). IKA Dispersers T 18 digital ULTRA-TURRAX (IKA. Germany) for stirring the samples.

Oxytocin standard solution preparation

Oxytocin stock solution (1mg mL^{-1}) were prepared by dissolving the Oxytocin in PBS (Phosphate Buffered Saline) with pH 7. The solution was kept in the refrigerator at 4°C for one month period. The working standard solutions for the calibrating curve were prepared by the dilution of the concentrated stock solution in PBS. The calibration curve was obtained in the range of 1. 563 – 100 µg mL^{-1} Oxytocin, each point on the curve being injected in triplicate.

HPLC sample preparation

The polymer pellets (polymeric mesh) with a diameter of 15 mm were placed in PVC vials with lids in 3 ml of PBS extraction solution with pH 7 and incubated at a temperature of 37°C for 24 h. The extraction solutions were collected every 24 hours. The collected solutions were stored in the freezer (-20°C) until their HPLC analysis, to determine the amount of Oxytocin released.

Method validation

For the quantitative determination of Oxytocin released from the polymeric mesh, were determined the following parameters: selectivity, linearity, LOD (limit of detection), LOQ (limit of quantification) and precision.

Selectivity was established by comparing the chromatogram of the Oxytocin standard solution with those of an Oxytocin sample extract. Linearity was established by plotting the analyte peak area against the analyte concentration. Calibration domain was between 1. 563 – 100 µg mL^{-1}

Parameter LOD was calculated based on Standard Deviation of the Response and the Slope of calibrating curve: 3.3XS/σ

Parameter LOQ was calculated based on the Standard Deviation of the Response and the Slope: The quantitation limit (QL) may be expressed as: 10XS/σ

The intra-day and inter-day precision were expressed as percentage of relative standard deviation (% RSD).

ACKNOWLEDGMENTS

REFERENCES

1. N. Goonoo, R. Jeetah, A. Bhaw-Luximon, D. Jhurry, *Eur. J. Pharm. Biopharm.*, **2015**, 97(Pt B), 371-391.
2. W.E. King III, Y. Gillespie, K. Gilbert, G.L. Bowlin, *Polymers,* **2019**, 12, 1-17.
3. H. Tang, Z. Xu, X. Qin, B. Wu, L. Wu, X.W. Zhao, Y. Li, *Biomaterials,* **2009**, 30, 3224-3233.
4. A. Ahmed, C. Gibson, P. Ayliffe, *Br. J. Oral Maxillofac. Surg.,* **2013**, 51,197-198.
5. T.H. Kim, S.H. Oh, S.Y. Chun, J.H. Lee, *J. Biomed. Mater. Res. A,* **2014**, 102, 1264-1274.
6. J.H. Lee, S.-W. Kim, U.-K. Kim, S.H. Oh, S. June-Kim, B.-W. Park, J.-H. Kim, Y.-S. Hah, D.R. Kim, G.-J. Rho, G.-H. Maeng, R.-H. Jeon, H.-C. Lee, J.-R. Kim, G.-C. Kim, J.-H. Byun, *J. Biomed. Mater. Res. A,* **2013**, 1, 942-953.
7. J.H. Lee, J.H. Kim, S.-H. Oh, S.-J. Kim, Y.-S. Hah, B.-W. Park, D.R. Kim, G.-J. Rho, G.-H. Maeng, R.-H. Jeon, H.-C. Lee, J.-R. Kim, G.-C. Kim, U.-K. Kim, J.-H. Byun, *Biomaterials,* **2011**, 32, 5033-5045.

8. J.H. Lee, Y.S. Hah, H.Y. Cho, J.H. Kim, S.H. Oh, B.W. Park, Y.H. Kang, M.J. Choi, J.K. Shin, G.J. Rho, R.H. Jeon, H.C. Lee, G.C. Kim, U.K. Kim, J.R. Kim, C.I. Lee, J.H. Byun, *Tissue Eng. Part A.,* **2014**, 20, 940-953.
9. I.M. Diniz, C. Chen, X. Xu, S. Ansari, H.H. Zadeh, M. M. Marques, S. Shi, A. Moshaverini, *J. Mater. Sci. Mater. Med.*, **2015**, 26,153.
10. H. Wu, Y. Deng, Y. Yan, D. Quan, Si M, *Sheng Wu Yi Xue Gong Cheng Xue Za Zhi.,* **2011**, 28, 1148-1153.
11. A.S. Akay, V. Arısan, E. Cevher, M. Sessevmez, B. Cam, *J. Orthop. Res., 2020, 38, 1676*-1687.
12. J.W. Park, J.M. Kim, H.J. Lee, S.H. Jeong, J.Y. Suh, T. Hanawa, *J. Clin. Periodontol.*, **2014**, 41,181-190.
13. M. Wang, L. Lan, T. Li, J. Li, Y. Li, *Connect. Tissue Res.*, **2016**, 57, 220-225.
14. A. Szeto, P.M. McCabe, D.A. Nation, B.A. Tabak, M.A. Rossetti, M.E. McCullough, N. Schneiderman, A.J. Mendez, *Psychosom. Med.*, **2011**, 73, 393-400.
15. D. Ashenafi, E. Van Hemelrijck, S. Chopra, J. Hoogmartens, E. Adams, *J. Pharm. Biomed. Anal.,* **2010**, 51, 24-29.
16. M. Mishra, S. Ali, M. Das, *Toxicol. Mech. Methods*, **2014**, 24, 342-346.
17. M.A. Kukucka, H.P. Misra, *J. Chromatogr. B*, **1994**, 653, 139-145.
18. G. Zhang, Y. Zhang, D.M. Fast, Z. Lin, R. Steenwyk, *Anal. Biochem*., **2011**, 416, 45-52.
19. O.S. Mabrouk, R.T. Kennedy, *J. Neurosci. Methods*, **2012**, 209, 127-133
20. E. Moriyama, H. Kataoka, *Chromatography*, **2015**, 2, 382-391.

COMPARATIVE FRAMEWORK OF CALCIUM PHOSPHATES-BASED PRODUCTS DERIVED FROM SUSTAINABLE MARINE AND TERRESTRIAL RESOURCES FOR BIOMEDICAL APPLICATIONS

**AURA-CĂTĂLINA MOCANU[a], MARIAN MICULESCU[a,*],
ROBERT-CĂTĂLIN CIOCOIU[a], TUDOR-MIHAI BUTTE[a],
ANA-IULIA BIȚĂ[a], CLAUDIA-GEORGIANA MILEA[a],
AURORA ANTONIAC[a], MARIUS VASILESCU[a], OCTAVIAN TRANTE[a],
CIPRIAN POP[a], LUCIAN-TOMA CIOCAN[b]**

ABSTRACT. Processing calcium and phosphor-rich natural resources, such as marble and seashells, and bovine and fish bones, envelops an environmentally friendly and eco-sustainable promising alternative for developing biomimetic products for various orthopaedic applications. In this regard, convenient, efficient, facile and completely reproducible technologies were involved in the fabrication process of biogenic calcium phosphates-based products through the conversion of the proposed resources. The aim of this research was to comparatively evaluate the morpho-compositional, structural and mechanical features of the developed products, subjected in advance to an air sintering program. The results revealed that the high temperature affects differently the morphological characteristics of the samples and facilitates the conservation of several elements, traced from their natural marine or terrestrial habitat. Moreover, the nature of the initial precursors clearly influenced the final composition of the samples: biphasic configuration for calcium carbonate derived products versus single phase for the calcium phosphate ones. The mechanical features are also a composed result of the resources type and sintering process, with significant recorded differences. Therefore, this study unveils the prospect for suitable strategies in terms of adequate natural precursor, fabrication technology and final properties of the biogenic products destined for a certain application in the biomedicine field.

Keywords: marble, seashells, bovine bone, fish bone, biogenic hydroxyapatite, compact products, comparative assessment

---

[a] *University Politehnica of Bucharest, Department of Metallic Materials Science, Physical Metallurgy, 313 Splaiul Independentei, 060042, J Building, District 6, Bucharest, Romania.*
[b] *„Carol Davila" University of Medicine and Pharmacy, Prosthetics Technology and Dental Materials Department, 37, Dionisie Lupu Street., District 1, 020022, Bucharest, Romania.*
* *Corresponding author: marian.miculescu@upb.ro, m_miculescu@yahoo.com*

A.-C. MOCANU, M. MICULESCU, R.-C. CIOCOIU, T.-M. BUTTE, A.-I. BIȚĂ,
C.-G. MILEA, A. ANTONIAC, M. VASILESCU, O. TRANTE, C. POP, L.-T. CIOCAN

INTRODUCTION

The production of daily waste materials by both private and public sectors of the population with defined activities in various industrial fields became an ongoing environmental problem of the current decade. The first negative outcomes were perceived by the end of the last century and awakened a great concern in terms of wastes disposal around the globe [1]. The sensibility towards environmental issues associated with the incremented aging facet of the population, often leading to multiple orthopaedic and dental incidents or reparatory surgeries, led to a continuous inter-connected development oriented for providing high class products and an enhanced healthcare system based on modern and efficient treatments [2-6].

In this light, the challenge arose in the fabrication area of eco-compatible and naturally-based bioproducts which responds to the task in hand by encouraging the exploitation of multiple marine and terrestrial raw resources (otherwise considered as a pollution or a bacterial growth factor) [7, 8], the energy saving and the substitution of chemical reagents for providing materials with improved qualities and features [9-11].

The emergence of such materials has been a motivating component for scientists worldwide and underscore the need for expanding the preparation and applicability of calcium phosphates (bulk/ceramic particles, 3D compact/ porous products, injectables or coatings), as targeted osseous treatment solutions used in biomedical applications (orthopaedic, dental or even plastic surgery) [12-18]. Native bones are composite materials made of ~70% mineral component and ~30% of organic matter and water [19-22]. Various types of calcium phosphates (CaPs) – hydroxyapatite (HA), β-tricalcium phosphate (β-TCP) or biphasic calcium phosphates (BCP) – are clinically studied and desired due to their close similarity with the mineral bone and teeth component's composition, biocompatibility, bioactivity and biodegradability [19, 20, 23-26]. An advantageous combination of biodegradability and mechanical features (high strength and toughness) is still out for quest, mainly because a high degree of biodegradable component rarely leads to strong mechanical bonds [24, 27-30].

To solve these challenges and to overcome the current flawed solutions for bone restoration (allografts, xenografts, autografts) [31-34], researchers looked for creative responses in the natural environment. Dedicated studies reported considerable knowledge regarding the involvement of marine and terrestrial resources of both calcium carbonate (invertebrates calcified structures: seashells, snails, etc., marble or eggshells) and calcium phosphate (vertebrates' bones: fish bones and mostly bovine bones) [7, 21, 27,

35-38]. Although seashells, marble or bovine bones were more intensively investigated in the last few years, fish bones have recently attracted real interest. Moreover, the incorporation of various chemical elements from their native habitat (e.g. Mg, Na, Si, F) [19, 39, 40] stands as a particular advantage against conventional commercial materials prepared mostly from synthetic reagents [41].

In terms of processing routes, regardless of the natural precursor and the synthesis method (wet chemical precipitation, sol-gel, hydrothermal procedures or thermal processing) [27, 37, 42, 43], the main focus is oriented towards the optimum variation of the processing parameters for fine-tuned features (morphological, compositional and mechanical). Given that new bone tissue was proved to grow into the pores of the implanted products, it was realized that even compact products comply best in vivo if a porous morphology is assured. Moreover, the pores could also assure a favourable surface for cells adhesion [44] and a better mechanical interlocking of the new grown tissue and positively influence the soluble character oh the synthesized ceramics (also dependent on the HA/β-TCP ratio) [14, 45].

Consequently, this study aims to expose and correlate the optimum natural resource and fabrication technology for the development of products based on biogenic calcium phosphates (mainly HA and/or β-TCP). The framework involved marine and terrestrial resources from two types of materials: calcium carbonate (marble and seashells) and calcium phosphate (bovine and fish bone) as initial source of calcium and/or phosphor. The proposed precursors are convenient candidates due to the highly promising researched area in terms of conversion procedures. Also, we advertise for the first time the comparison of prospect four natural precursors and two synthesis technologies. Moreover, the comparative investigation of the developed products features contributes to a significant advance for the adequate selection of bone reconstruction materials.

RESULTS AND DISCUSSION

1. Morpho-compositional evaluation

The morpho-compositional features of sintered products derived from two calcium carbonate resources (marble and seashell) and two calcium phosphates precursors (bovine bone and fish bone) are comparatively presented in Figure 1.
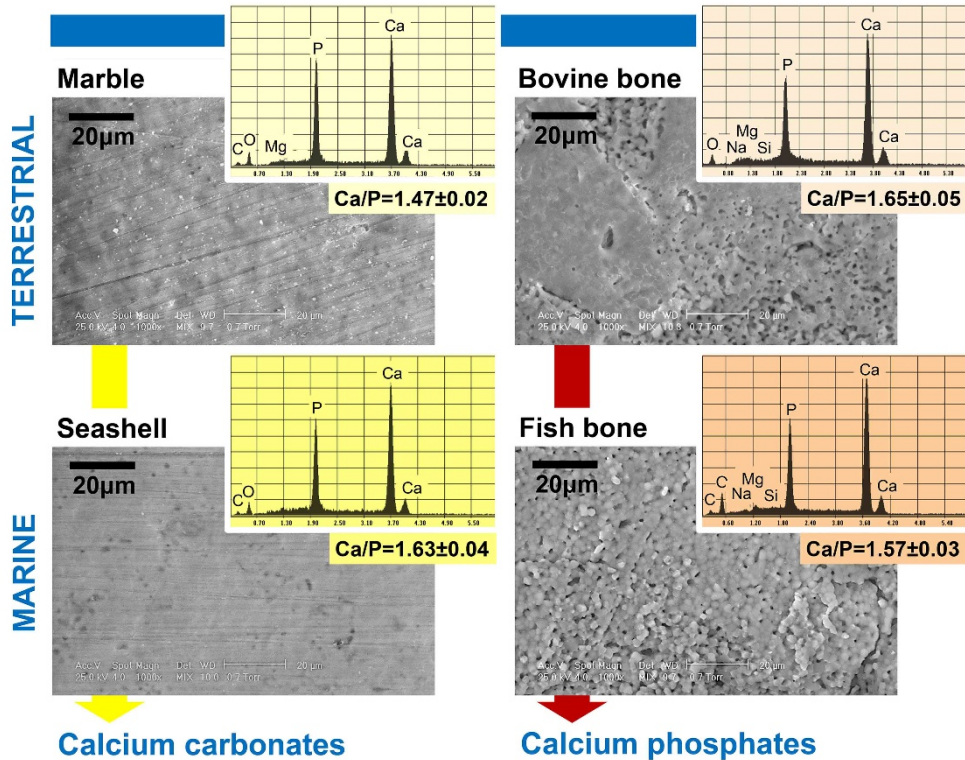
Figure 1. SEM-EDS results for bioceramic sintered products prepared from marble, seashell, bovine bone and fish bone precursors. Variation of Ca/P atomic ratio of the final bioceramic products (calculated as a mean of n=3 results ± standard deviation).

The results depict a clear difference in terms of compactness degree between the two types of products, which can be traced back to the particles shapes and sizes of all bioceramic powders derived from the four precursors. During the calcium carbonates conversion process, the obtained particles envelop a rounded and spherical aspect [36, 37, 42], while the calcium phosphates transformation leads to elongated/polyhedric particles with sharp edges [21, 27]. In this light, for marble and seashell derived products, the sintering stage led to highly compacted microstructures with few residual micropores unevenly dispersed on the samples surface and with variable sizes and grain shapes difficult to discriminate. In contrast, the sintered bovine bone and fish bone derived products revealed similar morphologies, with significantly induced densification of the bioceramic materials and strongly interconnected particles. However, the porosity and the pore sizes

and their distribution differ: for the bovine bone derived products, two areas were depicted – a mostly compact and uniform one, surrounded by areas with accentuated porosity and enlarged pore sizes distribution, while for the fish bone derived products, the microporous character is visible on the entire surface, with different distribution of the pore sizes.

The composition of the synthesized bioceramic products included Ca, P and O as major elements, specific to calcium phosphates materials, as revealed by the EDS spectra in Figure 1. Based on the natural origin of these products, variable quantities of other elements could be also traced. In the case of marble derived products, Mg was identified due to the dolomitic polymorphic form of the calcium carbonate, and its presence was preserved after chemical and thermal processing of the resource [36, 37]. Besides Mg, peaks of Na and Si were also present in the EDS spectra of bovine bone and fish bone derived products [21, 27, 47]. The compositional key indicator for naturally-derived products was the Ca/P atomic ratio (inset in Figure 1). The Ca/P ratio varied between 1.47 for marble derived samples and 1.65 for bovine bone-derived ones. Values close to the theoretical stoichiometric HA value of 1.67 [21], were found only for the samples derived from bovine bone and seashells [28].

2. Structural investigations

2.1. XRD

The XRD patterns of the sintered products are comparatively displayed in Figure 2. The phase transformation undergone by all samples was anticipated and consistent with our previously published results, demonstrating the reproducibility of both developed conversion technologies for both types of natural resources [21, 27, 28, 35, 36, 46].

The major diffraction maxima corresponding to hexagonal HA (ICDD: 00-009-0432) was identified for all sintered samples, with clear and sharp HA peaks, indicating that materials contain highly crystalline HA as major phase. The indirect synthesis route and the thermal treatment applied to the marble and seashell derived samples, facilitated the coexistence of HA and β-TCP (ICDD: 00-009-0169) in different ratios. This biphasic configuration appears to be specific to this type of materials [28, 36, 46]. For calcium phosphates derived samples, HA was consistently found as the single phase, due to the presence of stabilizing elements (e.g. magnesium) which prevent the decomposition of bovine and fish bones at 1200°C, and is preserved in the materials' structure [21, 27], as evidenced by the EDS results (Figure 1).

However, for bovine and fish bone derived products, traces of CaO phase (ICDD: 01-082-1690) were clearly spotted in the diffraction patterns.

These low limit traces were previously identified for samples prepared through repeated high temperature calcination and sintering processes and could be the result of the dehydroxylation of the material [27].

Figure 2. XRD patterns of bioceramic products derived from marble (M), seashell (S), bovine bone (B) and fish bone (F) precursors by chemical synthesis/calcination and sintering at 1200°C.

2.2. FTIR-ATR

The FTIR-ATR spectra of the sintered products are comparatively presented in Figure 3. A zoomed caption of the relevant functional groups in the final region of the spectra is displayed as inset-figure for a clear visualization.

The IR spectra of all investigated samples included bands specific to HA, corresponding to the characteristic vibrations of the orthophosphate functional groups ($(PO4)^{3-}$) [48, 49]: v_4 asymmetric bending (~552, ~557 and ~600 cm^{-1}), v_1 symmetric stretching (~945, ~961 and ~974 cm^{-1}) and v_3 asymmetric stretching (~1020 and ~1089 cm^{-1}). Additional bands were identified, corresponding to structural hydroxyl units [48, 49]: libration of $(OH)^-$ groups in HA (~633 cm^{-1}) – more prominent for bovine and fish bone derived products, and stretching of $(OH)^-$ groups in HA (~3572 and ~3640 cm^{-1}).

These results endorse the XRD findings and are in good agreement with previously reported studies in terms of sintered naturally-derived products, from either calcium carbonate or calcium phosphate resources. One could also notice that the high temperature treatments support the removal of carbonate groups usually present in the raw synthesized materials [21, 37, 50].

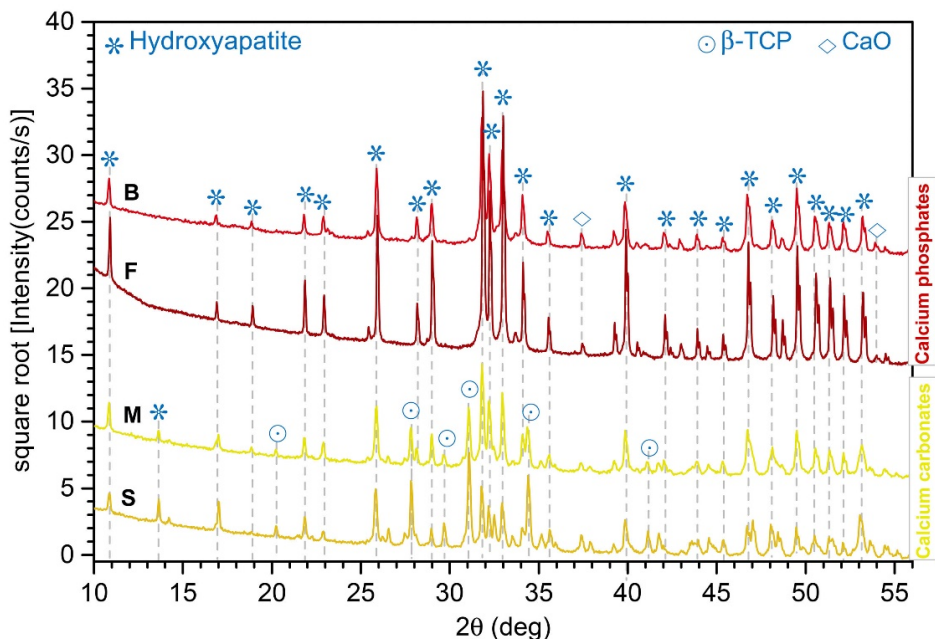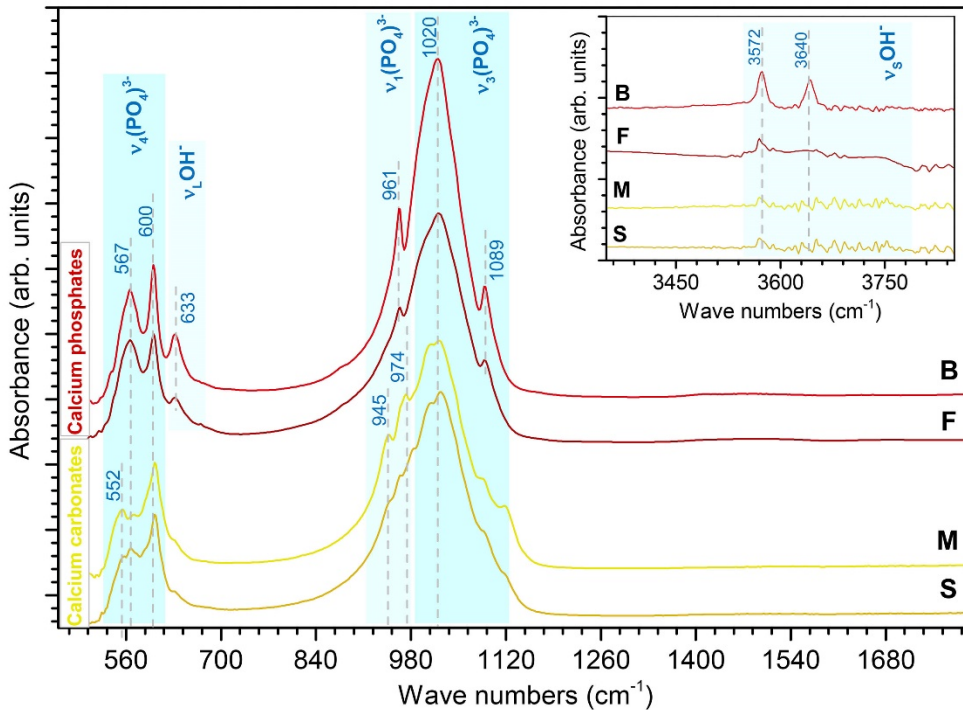**Figure 3.** Representative IR spectra of bioceramic products derived from marble (M), seashell (S), bovine bone (B) and fish bone (F) precursors by chemical synthesis/calcination and sintering at 1200°C.

3. Compressive strength

The mechanical performance of the developed products was evaluated by stress-strain curve measurements (Figure 4 – left) and compressive strength assays (Figure 4 – right). For all analysed samples, a fragile mechanical behaviour without any plastic deformations was depicted, typical for ceramic materials and accentuated in the case of calcium phosphates-derived ones.

Taking as a reference the corresponding compressive strength values for human bone, as host tissue in view of implantation (120 ÷ 180 MPa for the cortical bone type and 4 ÷ 12 MPa for the cancellous one) [51], the obtained

results resembles suitable outcomes. Moreover, the highest compressive strength values recorded for products derived from calcium phosphates sources are directly related to their phase composition – HA as single component (Figure 2), known for its increased mechanical resistance – and less influenced by their micro-porous character, as exposed by SEM micrographs (Figure 1). In contrast, as previously reported, marble and seashells lead to biphasic compositions even after the synthesis process, which is further converted through thermal treatment into the biphasic HA/β-TCP [36, 37]. The degree of β-TCP component is considerable for both types of products and is well known for both its high biodegradability and poor mechanical features [28].

Regardless of the compactness/porous level of the products, as exposed in Figure 1, the obtained results are justified due to the modulated composition of the samples, as function of high temperature processing.
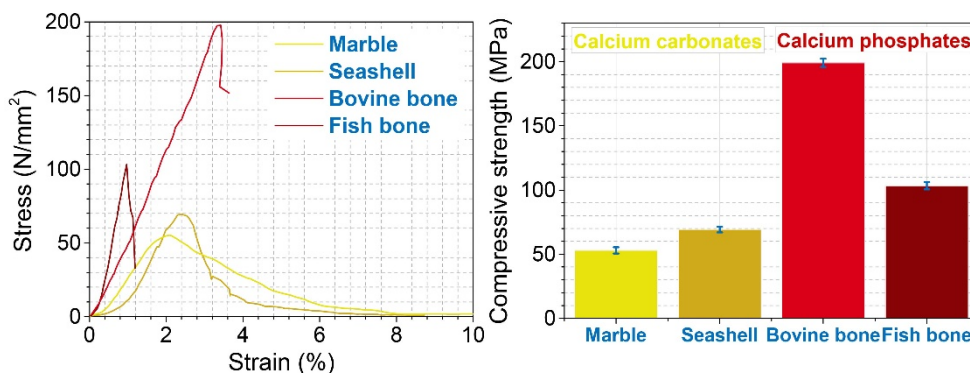
Figure 4. Comparative stress-strain curves (left) and compressive strength (right) for bioceramic products derived from marble, seashell, bovine bone and fish bone precursors by chemical synthesis/calcination and sintering at 1200°C.

CONCLUSIONS

This research provided an insightful investigation of four possible natural precursors – marble, seashells, bovine bone and fish bone – as raw resources for biogenic calcium phosphates synthesis. Accordingly, the two already developed technologies, completely parameterized and reproducible led to the fabrication of two types of ceramic products. The morpho-compositional, structural and mechanical investigations carried out in this regard, revealed that samples derived from marble and seashells consist of a biphasic calcium phosphate with different degree of HA/β-TCP ratio, while the bovine and fish bones promote the conservation of single HA counterpart,

without additional structural or compositional events. The sintering program also promoted the development of compact structures with accentuated porous character and mechanical resistance for products derived from the last two precursors.

Future perspectives are envisioned for the developed biogenic products in terms of optimal vascularization and osseointegration and prospect industrial fabrication based on further thoroughly examination.

EXPERIMENTAL SECTION

1. Naturally-derived products preparation

Experiments were performed on products prepared from calcium phosphates powders derived from four marine and terrestrial natural resources, two based on calcium carbonates (e.g. dolomitic marble and marine seashells) and the other two based on calcium phosphates (e.g. bovine bone and fish bone: carp bones (Cyprinus carpio)).

The initial bioceramic powders were synthesized through different conversion routes for each type of natural precursor. Mable and seashells followed an already established and reproducible indirect chemical precipitation route based on thermal dissociation of the calcium carbonate (air thermal treatment, 1300°C, 6h) and phosphoric acid treatment under stoichiometric conditions, as previously reported [28, 36, 37, 46]. For calcium phosphates-based precursors, the procedure involved initially the removal of soft tissue and organic components through mechanical removal of meat/soft tissue and boiling (in distilled water). Then, bone pieces were calcined in an electrical furnace at 500°C to 48 h followed by several heat treatments in air atmosphere for extended periods of time, as previously reported [21].

The compact products were obtained by isostatic pressing the synthesized bioceramic powders (grinded in advance with an agate mortar and pestle) in cylindrical moulds (Φ 10 mm) at 2.5 MPa, for 3 min, using a Bernardo WK 50 FH PRO work press. The pressed samples were further subjected to a conventional air sintering program in electrical furnace, at 1200°C, for 8 h. Samples were slowly cooled in the furnace, and deposited in sterile Petri dishes.

2. Experimental assessment

The morpho-compositional features of the sintered samples were studied with a scanning electron microscope (Philips XL 30 ESEM TMP) coupled with a microanalysis auxiliary system (EDAX Sapphire UTW). EDS

analyses were performed on three randomly chosen areas of each sample. The Ca/P atomic ratio was determined from the EDS results and will be expressed as a mean of the three independent results ± standard deviation.

The crystalline structure of the sintered samples was investigated using a Bruker D8 Advance X-ray diffractometer, with Cu Kα (λ = 1.5418 Å) radiation. The XRD analyses were performed in the 2θ = 9÷70° angular range, with a step size of 0.02° and 2 s acquisition time/ step.

The bonding architecture and functional groups presence in the sintered samples was evaluated after sintering by Fourier Transform Infrared spectroscopy (FTIR) in attenuated total reflectance (ATR) mode using a PerkinElmer Spectrum BX II spectrometer equipped with a Pike-MIRacle ATR head – diamond crystal. The FTIR-ATR spectra were recorded in the 500÷4000 cm^{-1} range at a spectral resolution of 4 cm^{-1}. A total of 32 scans/ experiment were performed.

Compressive testing was performed using a Walter + Bai LFV 300 universal testing machine, on smooth cylindrical samples (n = 5/sample precursor type), with a final diameter of 9.0±0.3 mm and a final height of 9.0±1.4 mm. The machine cross head speed was set to 1 mm/min with data acquisition time at 0.05 s.

REFERENCES

1. J.N.F. Holanda; *Springer International Publishing*; **2017**; 1-18.
2. A. Popa, G. Stan, M. Husanu, I. Mercioniu, L. Santos, H. Fernandes and J. Ferreira; *Int. J. Nanomedicine*; **2017**; *12*; 683.
3. B.W. Stuart, J.W. Murray and D.M. Grant; *Scientific reports*; **2018**; *8*;
4. I. Antoniac, D. Popescu, A. Zapciu, A. Antoniac, F. Miculescu and H. Moldovan; *Materials*; **2019**; *12*; 719.
5. H.R. Fernandes, A. Gaddam, A. Rebelo, D. Brazete, G.E. Stan and J.M. Ferreira; *Materials*; **2018**; *11*; 2530.
6. M. Ionita, L.E. Crica, S.I. Voicu, A.M. Pandele and H. Iovu; *Polym Adv Technol*; **2016**; *27*; 350-357.
7. F. Baino and M. Ferraris; *Int. J. Appl. Ceram. Technol.*; **2017**; *14*; 507-520.
8. F. Miculescu, M. Miculescu, L. Ciocan, A. Ernuteanu, I. Antoniac, I. Pencea and E. Matei; *Dig. J. Nanomater. Biostructures (DJNB)*; **2011**; *6*;
9. N. Stevulova, A. Estokova, J. Cigasova, I. Schwarzova, F. Kacik and A. Geffert; *J. Therm. Anal. Calorim.*; **2017**; *128*; 1649-1660.
10. T. Tite, A.-C. Popa, L. Balescu, I. Bogdan, I. Pasuk, J. Ferreira and G. Stan; *Materials*; **2018**; *11*; 2081.

11. Ö. Özmen, R. Sârbu, A. S. Săseanu and C. Toader; *Amfiteatru Econ.*; **2017**; *19*; 1064-1064.
12. M. Ebrahimi, M. G. Botelho and S. V. Dorozhkin; *Mater. Sci. Eng. C*; **2017**; *71*; 1293-1312.
13. Q. Zhang, W. Wu, C. Qian, W. Xiao, H. Zhu, J. Guo, Z. Meng, J. Zhu, Z. Ge and W. Cui; *Mater. Sci. Eng. C*; **2019**; *103*; 109858.
14. M. Castilho, C. Moseke, A. Ewald, U. Gbureck, J. Groll, I. Pires, J. Teßmar and E. Vorndran; *Biofabrication*; **2014**; *6*; 015006.
15. M. Garcés Villalá, J. Calvo Guirado, D. Granados, S. Limandri and V. Galván Josa; *X-Ray Spectrom.*; **2017**; *46*; 237-241.
16. C. Danoux, D. Pereira, N. Döbelin, C. Stähli, J. Barralet, C. van Blitterswijk and P. Habibovic; *Adv. Healthc. Mater.*; **2016**; *5*; 1775-1785.
17. G. Stan, A. Popa and D. Bojin; *Dig. J. Nanomater. Biostructures (DJNB)*; **2010**; *5*;
18. G. Armencea, C. Berce, M. Todea, A. Vulpoi, D. Leordean, S. Bran, C. Dinu, M. Lazar, O. Lucaciu and L. Crisan; *Studia UBB, Chemia*; **2019**; *64*;
19. M. Mucalo; *Hydroxyapatite (HAp) for biomedical applications*; **2015**; *307*.
20. F. Barrère, C.A. van Blitterswijk and K. de Groot; *Int. J. Nanomedicine*; **2006**; *1*; 317.
21. A. Maidaniuc, F. Miculescu, S. I. Voicu, C. Andronescu, M. Miculescu, E. Matei, A. C. Mocanu, I. Pencea, I. Csaki and T. Machedon-Pisu; *Appl. Surf. Sci.*; **2018**; *438*; 158-166.
22. C. Sarosi, A.R. Biris, A. Antoniac, S. Boboia, C. Alb, I. Antoniac and M. Moldovan; *J Adhes Sci Technol*; **2016**; *30*; 1779-1794.
23. S. Lala, M. Ghosh, P. Das, D. Das, T. Kar and S. Pradhan; *Mater. Chem. Phys.*; **2016**; *170*; 319-329.
24. L. Galea, D. Alexeev, M. Bohner, N. Doebelin, A.R. Studart, C.G. Aneziris and T. Graule; *Biomaterials*; **2015**; *67*; 93-103.
25. A. Vladescu, M. Badea, S.C. Padmanabhan, G. Paraschiv, L. Floroian, L. Gaman, M.A. Morris, J.-L. Marty and C.M. Cotrut; *Elsevier*; **2019**; 409-431.
26. L. Bizo, K. Sabo, R. Barabas, G. Katona, L. Barbu-Tudoran and A. Berar; *Studia UBB , Chemia*; **2020**; *65*;
27. A. Maidaniuc, F. Miculescu, R.C. Ciocoiu, T.M. Butte, I. Pasuk, G.E. Stan, S.I. Voicu and L.T. Ciocan; *Ceram. Int*; **2020**; *46*; 10159-10171.
28. A.-C. Mocanu, M. Miculescu, T. Machedon-Pisu, A. Maidaniuc, R.C. Ciocoiu, M. Ioniță, I. Pasuk, G.E. Stan and F. Miculescu; *Appl. Surf. Sci.*; **2019**; *489*; 226-238.
29. A.-I. Bita, G. Stan, M. Niculescu, I. Ciuca, E. Vasile and I. Antoniac; *J Adhes Sci Technol.*; **2016**; *30*; 1968-1983.
30. A. Moldoveanu, O.-M. Ferche, F. Moldoveanu, R.G. Lupu, D. Cinteză, D.C. Irimia and C. Toader; *IEEE Access*; **2019**; *7*; 8151-8171.
31. M. Montazerolghaem, M.K. Ott, H. Engqvist, H. Melhus and A. Rasmusson; *Mater. Sci. Eng. C*; **2015**; *52*; 212-218.
32. G. Cama, S. Nkhwa, B. Gharibi, A. Lagazzo, R. Cabella, C. Carbone, P. Dubruel, H. Haugen, L. Di Silvio and S. Deb; *Mater. Sci. Eng. C*; **2017**; *78*; 485-494.
33. M. O'Halloran; *Journal of Research&Practice in Dentistry*; **2014**; *2014*; 1-19.

34. M.K. Herliansyah, C. Muzafar and A.E. Tontowi; *Ind. Eng. Manag. Syst.*; **2012**; 1135-1145.
35. F. Miculescu, A. Maidaniuc, S. Voicu, M. Miculescu, A. Berbecaru, L. Ciocan, A. Purcaru, A. Semenescu and O. Preda; *J. Optoelectron. Adv. M.*; **2015**; *17*; 1361-1366.
36. F. Miculescu, A.C. Mocanu, G.E. Stan, M. Miculescu, A. Maidaniuc, A. Cîmpean, V. Mitran, S.I. Voicu, T. Machedon-Pisu and L.T. Ciocan; *Appl. Surf. Sci.*; **2018**; *438*; 147-157.
37. A.-C. Mocanu, G.E. Stan, A. Maidaniuc, M. Miculescu, I.V. Antoniac, R.-C. Ciocoiu, Ș.I. Voicu, V. Mitran, A. Cîmpean and F. Miculescu; *Materials*; **2019**; *12*; 381.
38. F. Miculescu, G. Stan, L. Ciocan, M. Miculescu, A. Berbecaru and I. Antoniac; *Dig. J. Nanomater. Biostructures (DJNB)*; **2012**; 7;
39. F. Heidari, M. Razavi, M. Ghaedi, M. Forooghi, M. Tahriri and L. Tayebi; *J. Alloys Compd.*; **2017**; *693*; 1150-1156.
40. A. Maidaniuc, M. Miculescu, S. Voicu, L. Ciocan, M. Niculescu, M. Corobea, M. Rada and F. Miculescu; *J Adhes Sci Technol.*; **2016**; *30*; 1829-1841.
41. M. Moldovan, D. Prodan, C. Sarosi, R. Carpa, C. Socaci, M.-C. Rosu and S. Pruneanu; *Mater. Chem. Phys.*; **2018**; *217*; 48-53.
42. F. Miculescu, A.-C. Mocanu, C.A. Dascălu, A. Maidaniuc, D. Batalu, A. Berbecaru, S.I. Voicu, M. Miculescu, V.K. Thakur and L.T. Ciocan; *Vacuum*; **2017**; *146*; 614-622.
43. C.M. Cotrut, A. Vladescu, M. Dinu and D.M. Vranceanu; *Ceram. Int*; **2018**; *44*; 669-677.
44. B. Cecen, L.D. Kozaci, M. Yuksel, O. Ustun, B.U. Ergur and H. Havitcioglu; *Mater. Sci. Eng. C*; **2016**; *69*; 437-446.
45. M. Vranceanu, I. Antoniac, F. Miculescu and R. Saban; *J. Optoelectron. Adv. Mater.*; **2012**; *14*; 671-677.
46. V. Mitran, R. Ion, F. Miculescu, M.G. Necula, A.-C. Mocanu, G.E. Stan, I.V. Antoniac and A. Cimpean; *Materials*; **2018**; *11*; 1097.
47. F. Miculescu, L. Ciocan, M. Miculescu and A. Ernuteanu; *Dig. J. Nanomater. Biostructures (DJNB)*; **2011**; *6*; 225-233.
48. M. Markovic, B.O. Fowler and M.S. Tung; *J Res Natl Inst Stand Technol*; **2004**; *109*; 553.
49. A. Rapacz-Kmita, C. Paluszkiewicz, A. Ślósarczyk and Z. Paszkiewicz; *J. Mol. Struct.*; **2005**; *744*; 653-656.
50. M. Lombardi, P. Palmero, K. Haberko, W. Pyda and L. Montanaro; *J. Eur. Ceram. Soc.*; **2011**; *31*; 2513-2518.
51. J.-Y. Rho, L. Kuhn-Spearing and P. Zioupos; *Med Eng Phys*; **1998**; *20*; 92-102.

DIELECTRIC BEHAVIOR OF SLUDGE FROM WASTEWATER TREATMENT

CSABA BARTHA[a], ALINA CARAMITU[b], MONICA JIPA[a]*, DANIELA MARIA IGNAT[a], ATTILA TÓKOS[a]

ABSTRACT. In the present study, dielectric spectroscopy was used to assess the influence of ELF (1-200 Hz) electromagnetic fields over protein relaxation from activated sludge (approx. 99% water content), sampled from the biological tank of a domestic wastewater treatment plant. Dielectric loss (*tg*δ) was determined for both activated sludge samples and autoclaved samples. Experimental data analysis shows that biological samples (activated sludge) have different dielectric behavior than the sterile samples (sterilized sludge). Unlike sterile samples in which the function *tg*δ vs. frequency is continuous, in the activated sludge samples, this function presents two discontinuities specific to electrical resonances around the frequencies of 26.5 Hz and 50.1 Hz. This behavior indicates that under the influence of the measuring signal of 26.5 Hz and 50.1 Hz, biochemical processes are stimulated in activated sludge. Also, the significant changes in the number of charge carriers suggest that, at these frequencies, changes occur in the mechanism and kinetics of biochemical processes.

Keywords: wastewater, activated sludge, dielectric spectroscopy, dielectric loss, electromagnetic fields, ELF

INTRODUCTION

From the perspective of sustainable development, streamlining the wastewater treatment process is a priority issue [1-3], theoretically complex, and with particular technical and economic implications.

[a] *Research-Development Institute for Environmental Protection Technologies and Equipment, Str. Parcului, Nr. 7, 420035, Bistrița, România*
[b] *National Institute for Research and Development in Electrical Engineering INCDIE ICPE-CA,313 Splaiul Unirii, RO-030138, Bucharest, Romania*
Corresponding author: monica.jipa@icpebn.ro

The theoretical complexity of the problem is mainly due to the unique diversity of organic [4-5] and inorganic [7-9] (sometimes radioactive [10]) pollutants contained in industrial and domestic wastewater.

Commonly, most wastewater treatment plants are provided with a biological treatment stage, where pollutant removal is carried out through biologically active sludge with high biodiversity [11-16].

Due to their specificity, the biochemical processes are relatively slow, representing the rate-determining step of the treatment processes. For this reason, the share of energy costs related to the microbiological stage is usually over 60% of the total treatment costs [11]. Given these considerations, research and developments upon streamlining the biological stages of water treatment are currently of great importance.

Attempts to accelerate the microbiological purification step by using bioactivators are reported [17]. Lingvay et al. [9], shows the ability of some plant extracts to activate the metabolism of microorganisms (bacteria and molds) even in environments with xenobiotic pollutants, usually present in domestic wastewater.

On the other hand, several studies show that extremely low-frequency electromagnetic fields (ELF-EMF) influence the mechanism and kinetics of natural electrochemical processes [18], effects of accelerating corrosion processes, and microbiological degradation of various materials used in construction and installations - both metallic and oxide [19-22] as well as polymeric ones [23-26], have been reported. Also, ELF influences on the living matter have been reported, such as stimulation of some biotechnological processes [27, 28], changes in circadian rhythm [29-31], etc.

It has been found experimentally, that intense electromagnetic fields, higher than 15 Vrms, lead to degradation by permeabilization of the cell membrane followed by leakage of the intracellular compounds [32, 33]. Also, in the study of the vacuolar H^+-ATPase (V-ATPase) rotary enzyme biocatalytic activity behavior in ELF, maximum changes were found around the frequency of 86 Hz, explainable by synchronisms in the ion-pumping steps in individual enzymes *via* a hold-and-release mechanism [34]. Recent studies have shown significant changes in the biocatalytic activity, selectivity, and growth of yeast cultures [35-38]. Through dielectric spectroscopy technique and specific biochemical techniques on *Aspergillus Niger* behavior, it was found that mold responds selectively only at certain discrete frequencies in the ELF field [39]-depending on the applied ELF frequency, the metabolites change [42], and upon exposure in the range of 10-15 Vrms of 50 Hz, the development (maturation) and multiplication rate (spore production) increase substantially [33].

Thus, in the current research, we aimed to assess activated sludge behavior in ELF (1-200 Hz) through the dielectric spectroscopy technique.

RESULTS AND DISCUSSION

According to [43], the results obtained, regarding the content of sedimentable suspended solids (activated sludge) in the investigated water sample are summarized in Table 1.

Table 1. Active sludge content of the investigated water sample

Method	Content of suspended solids [43]									
Sample	Volumetric [cm^3/dm^3]					Gravimetric [g/dm^3]				
	1	2	3	4	5	1	2	3	4	5
	235	250	240	260	255	4.8562	5.6008	5.5058	6.4012	6.0502
Average value	248					5.6828				

Results from Table 1 show that the average content of sedimentable suspended solids of the investigated water sample is 248 cm^3/dm^3, respectively 5.6828 g/dm^3 after drying at 105 ºC (approx. 99.4% water content).

The results obtained through the dielectric spectroscopy technique performed on the wet sediment of activated sludge, respectively, the evolution of dielectric loss (*tg*δ) depending on the applied frequency (in the range 1-200 Hz) are presented in Figure 1. Figure 1 shows that the evolution of dielectric loss depending on the applied frequency presents discontinuities at 26.5 Hz and 50.1 Hz.

The dielectric loss *tg*δ is the ratio between the real component ε' and the imaginary one ε" of the dielectric permittivity (1):

$$tg\delta = \frac{\varepsilon''}{\varepsilon'}$$
(1)

The imaginary component of the dielectric permittivity is determined by the electrical conductivity of the medium σ at a given frequency *f*, respectively (2):

$$\varepsilon'' = \frac{\sigma}{2\pi f}$$
(2)

Under these conditions, the discontinuities in Figure 1 indicates that under the influence of the electric field generated by the measuring signal, dynamic processes (1) occur near frequencies of 26.5 Hz and 50.1 Hz- such as protein condensation/hydrolysis- which suddenly changes the number of charge carriers (and implicitly of σ) in the investigated sample (biomass-activated sludge). Similar results have been reported on *Aspergillus Niger* cultures [39].
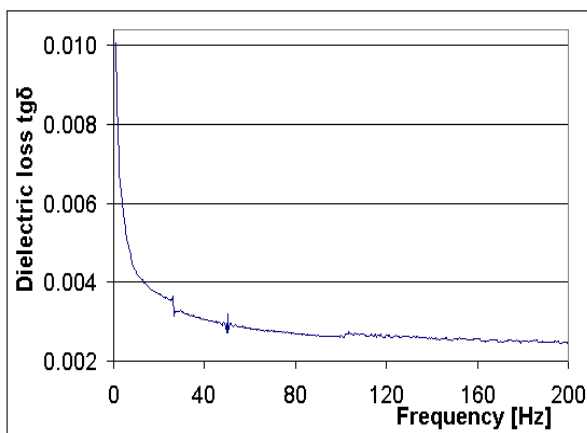
Figure 1. The evolution of dielectric loss *tg*δ in the
frequency range of 1- 200 Hz of activated sludge

It is noted that α amino acids with aliphatic groups R_1 and R_2- from (1)- depending on the size of these groups, have relaxation times and, consequently, different resonance frequencies. Under these conditions, following the application of an ELF field, depending on the frequency of the applied field, certain α amino acids resonate (depending on the volume and shape of the molecule, the dipole moment, the viscosity of the intracellular medium, etc.- there is practically a selective ″agitation″ at a given frequency of the polar molecule). Additionally, the observed dynamic processes near these frequencies may be due to the changes in charge distribution upon the interaction between the EMF fields with the cells' molecular system. Proteins present a specific amino acid sequence, formed by linking the α-carboxyl group of one amino acid to the α-amino group of another amino acid with a peptide bond (Scheme 1).
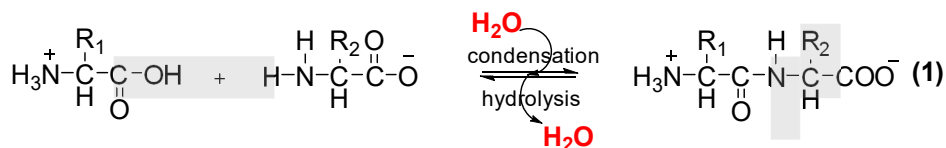
Scheme 1. Condensation of α amino acids

Because of the different charge distribution of the constituting polar and charged molecules, proteins are polarizable materials with specific electrostatic properties, contributing to the proteins electric and dielectric properties.

When an electrical field is applied, the randomly orientated polar molecules, including positive and negative charged molecules within the protein, rotate, move, align and polarize, triggering structural changes in proteins [40]. This displacement of charge distribution that drives such conformational changes plays an important role in membrane transport proteins and could explain the DNA's stimulation that initiates protein synthesis. Following the study of the electric and magnetic field influence on the Na^+/K^+ ATPase enzyme activity, results suggest that upon application of an electrical field, changes occur in the distribution of electrical charges, similar to the ion-binding activation mechanism. Studies also reveal that electric and magnetic fields act at different sites on the ATPase, changing the surface charge density and affecting ion transport across the membrane [41]. Thus, if certain frequencies stimulate the charge transfer process, previously reported results could be explained [23-26, 33, 35-38].

For a better highlighting of the electrical oscillations produced by the measurement signal applied to the investigated biomass (Figure 2), the evolution of derivative $\Delta tg\delta/\Delta f$ depending on frequency is presented.
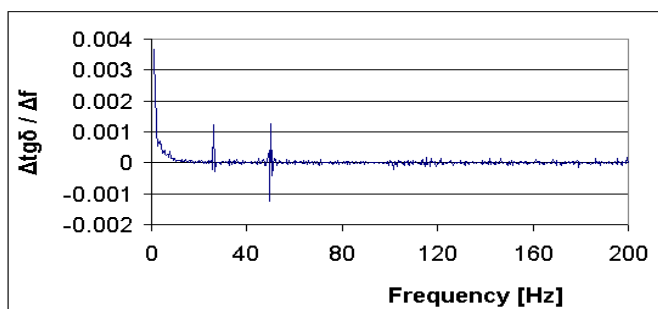
Figure 2. The evolution of $\Delta tg\delta/\Delta f$ as a function of the active sludge frequency

Figure 2 suggests that around frequencies of 26.5 Hz and 50.1 Hz electrical resonance phenomena occur, explainable by sudden changes in the concentration of charge carriers in the investigated samples.

In Figure 3, the evolution of dielectric loss ($tg\delta$) depending on the applied frequency in the range 1-200 Hz, obtained on the sterilized sludge sample by autoclaving at 105 °C for 30 minutes, is presented.

Figure 3 shows that the evolution of the dielectric losses depending on the applied frequency on the sterilized sludge is a continuous function without discontinuities/electrical resonances, as presented in Figure 1 and 2. This observation suggests that in the sterilized material (denatured proteins), under the influence of the measuring signal, there are no processes by which the number of carriers suddenly changes.

By comparing Figure 1 with Figure 3, it was found that the *tg*δ values of the sterilized material are systematically higher (up to 70 times) than of the activated sludge. This finding can be explained by the fact that after heat-based sterilization, cytoplasmic proteins are denatured, disturbing the natural balance (1) (hydrolysis no longer occurs), and the cell membranes disintegrate, discontinuing the activity of the ion pumps, which leads to the release of ionic species (charge carriers) from the cytoplasm and thus to the corresponding increase in conductivity σ.

These comparative results (activated sludge/sterilized sludge) suggest that dielectric relaxation is a specific feature of living matter, where the dynamic processes of hydrolysis/condensation of proteins, are not degenerated.
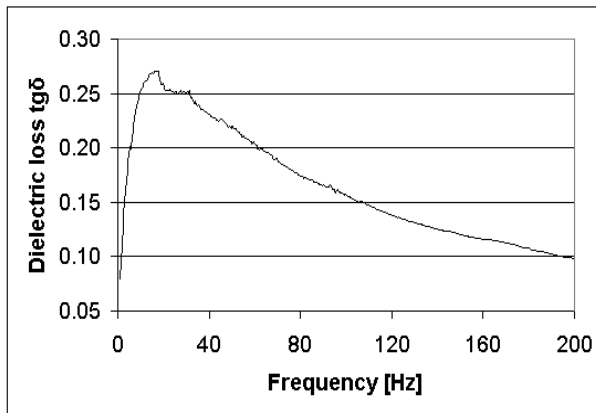
Figure 3. Dielectric losses on sterilized sludge suspension

Therefore, according to [33] and [39], it is considered that by applying an electric field of up to 15 Vrms/cm around the frequency of 26.5 Hz or 50.1 Hz, significant changes may occur in the activity/metabolism of the microorganisms from the activated sludge. These findings suggest that by applying an electric field in the ELF range, biological water purification processes can be controlled, both quantitatively (accelerating the process) and qualitatively (the share of metabolites formed - biogas [13], biohydrogen [12], etc.).

CONCLUSIONS

Through dielectric spectroscopy technique in the range 1-200 Hz, dielectric loss *tg*δ were determined for both activated sludge sediment sampled from a wastewater treatment plant and autoclaved sludge sediment.

After comparing the experimental results, it was found that living matter samples (activated sludge) have different dielectric behavior than the sterile samples (sterilized sludge), respectively:

- in sterile samples, the function *tg*δ vs. frequency is continuous, without discontinuities;

- in activated sludge samples, the function *tg*δ vs. frequency has two specific discontinuities specific to electrical resonances around the frequencies of 26.5 Hz and 50.1 Hz, respectively.

This behavior indicates that under the influence of the measurement signal of 26.5 Hz and 50.1 Hz, respectively, in activated sludge, biochemical processes are stimulated that take place through significant changes in the number of charge carriers- which suggests that at these frequencies, there are changes in the mechanism and kinetics of biochemical processes from the activated sludge.

EXPERIMENTAL SECTION

The investigated activated sludge was sampled from the biological treatment tank of the wastewater treatment plant located in Bistriţa-RO municipality.

The suspended solids content was determined according to [43]- both by the volumetric (sedimentation for 2 hours) and gravimetric method (drying at 105±3 °C).

Dielectric spectroscopy measurements were performed with specialized equipment AMTEK- 296 Dielectric interface (Solartron Analytical)- both on activated sludge sediment and autoclaved sediment for 30 minutes at 105±3 °C.

ACKNOWLEDGMENTS

REFERENCES

1. C. Staniloiu; C. Florescu; *Rev. Chim.*, **2014**, *65 (4)*, 502-505.
2. C.M. Dragomir Bălănică; C. Munteniță; A.G. Simionescu; I.G. Bîrsan; *Rev. Chim.*, **2020**, *71 (1)*, 266-272.
3. C. Muntenita; C.M. Dragomir Balanica; A.G. Simionescu; S. Stanciu; C.L. Popa; *Rev. Chim.*, **2019**, *70 (6)*, 1920-1923.
4. S. Gheorghe; G.G. Vasile; C. Stoica; M. Nita-Lazar; I. Lucaciu; A. Banciu; *Rev. Chim.*, **2016**, *67 (8)*, 1469-1473.
5. D. Cirtina; M.N. Mihut; *Rev. Chim.*, **2020**, *71 (2)*, 315-323.
6. C. Panaitescu; C. Jinescu; A.M. Mares; *Rev. Chim.*, **2016**, *67 (5)*, 925-928.
7. C.M. Dragomir Balanica; A.G. Simionescu; C.L. Popa; C.I. Bichescu; C. Muntenita; *Rev. Chim.*, **2019**, *70 (5)*, 1664-1666.
8. M. Mincu; M.I. Marcus; M.A. Mitiu; N.S. Raischi; *Rev. Chim.*, **2018**, *69 (12)*, 3553-3556.
9. I. Lingvay; D.I. Văireanu; K. Öllerer; C. Lingvay; *Environ. Eng. Manag. J.*, **2012**, *11 (4)*, 767-772.
10. N. Groza; A. Manescu; E. Panturu; A. Filcenco-Olteanu; R.I. Panturu; C. Jinescu; *Rev. Chim.*, **2010**, *61 (7)*, 680-684.
11. C. Bumbac; E. Manea; A. Banciu; C. Stoica; I. Ionescu; V. Badescu; M. Nita-Lazar; *Rev. Chim.*, **2019**, *70 (1)*, 275-277.
12. V.D. Gherman; P. Molnar; M. Motoc; A. Negrea; *Rev. Chim.,* **2018**, *69 (4)*, 806-808.
13. L.I. Dungan; A.E.Cioablă; V. Pode; *Rev. Chim.*, **2020**, *71 (1)*, 223-227.
14. C.G. Gheorghe; O. Pantea; V. Matei, D. Bombos; A.F. Borcea; *Rev. Chim.*, **2011**, *62 (10)*, 1023-1026.
15. E. Manea; C. Bumbac; A. Banciu; C. Stoica; M. Nita-Lazar; *Rev. Chim.*, **2020**, *71 (1)*, 88-92.
16. E.S. Biris-Dorhoi; M. Tofana; S.M. Chis; C.E. Lupu; T. Negreanu-Pirjol; *Rev. Chim.,* **2018**, *69 (5)*, 1089-1098.
17. D.E. Pascu; C. Modrogan; A.R. Miron; P. C. Albu; D.D. Clej; M. Pascu (Neagu); S. Caprarescu; *Rev. Chim.,* **2015**, *66 (12)*, 1950-1955.
18. I. Lingvay; C. Lingvay; A. Voina; *Rev. Roum. Sci. Tech. El.*, **2008**, *53 (2)*, 85-94.
19. C. Lingvay; A. Cojocaru; T. Vişan; I. Lingvay; *U.P.B. Sci. Bull. Series B*, **2011**, *73 (4)*, 143-152.
20. I. Lingvay; M. Gabor; C. Lingvay; *Rev. Chim.,* **2006**, 57 (2), 180-183.
21. I. Lingvay; C. Lingvay; C. Homan; O. Ciogescu; *Rev. Chim.,* **2006**, *57 (12),* 1279-1282.
22. I. Lingvay; A.M. Bors; D. Lingvay; L. Radermacher; V. Neagu; *Rev. Chim.*, **2018**, *69 (12),* 3593-3599.
23. A.M. Bors; N. Butoi; A.R. Caramitu; V. Marinescu; I. Lingvay; *Mat. Plast.*, **2017**, *54 (3)*, 447-452.
24. A. Caramitu; N. Butoi; T. Rus; A.M. Luchian; S. Mitrea; *Mat. Plast.,* **2017**, *54 (2),* 331-337.

25. I. Szatmari; M. Lingvay; L. Tudosie; A. Cojocaru; I. Lingvay; *Rev. Chim.,* **2015**, *66 (3),* 304-311.
26. T. Rus; E. Radu; I. Lingvay; M. Lingvay; O.C. Ciobotea-Barbu; C. Campureanu; F.M. Benga; G.C. Lazar; D.I. Vaireanu; *U.P.B. Sci. Bull.*, **2017**, *79 (4),* 167-180.
27. J. Filipič; B. Kraigher; B. Tepuš; V. Kokol; I. Mandic-Mulec; *Bioresour Technol*. **2012**, *120,* 225-232.
28. R.W. Hunt; A. Zavalinl; A. Bhatnagar; S. Chinnasamy; K.C. Das; *Int. J. Mol. Sci.*, **2009**, *10*, 4515-4558.
29. B. Lewczuk; G. Redlarski; A. Żak; N. Ziółkowska; B. Przybylska-Gornowicz; M. Krawczuk; *BioMed Res. Int.*, **2014**, ID 169459
30. O. Hiwaki; *Engineering in Medicine and Biology Society*, *Proceedings of the 20th Annual International Conference of the IEEE*, **1998**.
31. Y. Touitou; B. Selmaoui; *Dialogues Clin Neurosci.*, **2012**, *14 (4)*, 381-399.
32. K. Aronsson; U. Rfnner, E. Borch; *Int. J. Food Microbiol.,* **2005**, *99*, 19-32.
33. E. Radu; D. Lipcinski; N. Tănase; I. Lingvay; *Electroteh. Electron. Autom.*, **2015**, *63 (3)*, 68-74.
34. C.M. Ferencz; P. Petrovszki; A. Dér; K. Sebők-Nagy; Z. Kóta; T. Páli; *Sci. Rep.,* **2017**, *7*, 45309.
35. C. Stancu; M. Lingvay; I. Szatmári; I. Lingvay; *The 8th Int. Symp. on ATEE, Bucharest, Romania*, May 23-25, **2013**, 1-4.
36. D. Sandu; I. Lingvay; S. Lányi; D.D. Micu; C.L. Popescu; J. Brem; L.C. Bencze; C. Paizs; *Studia UBB Chemia*, **2009**, *54* (*4*), 195-201.
37. M. Lingvay; L. Czumbil; *Electroteh. Electron. Autom.*, **2014,** *62 (3),* 84-89.
38. M. Lingvay; C. Stancu; I. Szatmári; I. Lingvay; *Electroteh. Electron. Autom.*, **2013**, *61 (1),* 43-47.
39. M. Lingvay; A.R. Caramitu; A.M. Borș; I. Lingvay; *Studia UBB Chemia*, **2019,** *64 (2)*, 279-288.
40. I.A.A. Al-Darkazly; S.M.R. Hasan; *IEEE J. Transl. Eng. Health Med.,* **2020,** *8,* 1–13.
41. M. Blank; *Electromagn. Biol. Med.,* **2008**, *27(1),* 3–23.
42. M. Gao; J. Zhang; H. Feng; *Bioelectromagnetics*, **2011**, *32*, 73-78.
43. STAS 6953-81 – Surface water and wastewater. Determination of suspended solids content, calcination loss and calcination residue.

RESEARCH ON THE HEAVY METALS IN SURFACE SEDIMENTS, IN STRÂMTORI-FIRIZA RESERVOIR, SITUATED IN N-W OF ROMANIA

IRINA SMICAL[a,*], ADRIANA MUNTEAN[b], DAN CIURTE[b], VALER MICLE[c]

ABSTRACT. In this study referring to the surface sediments quality of Strâmtori-Firiza reservoir, a series of heavy metals like arsenic, cadmium, copper, lead and zinc were investigated from 2017 to 2019. The samples analysis and interpretation of the results for 18 samples taken from surface sediments indicated that the correlation coefficients calculated for the metallic elements showed a significant correlation between them. Thus, highlighting their same origin in the composition of the studied surface sediments, only the value of the coefficient between As and Pb implies a statistically significant correlation. Pollution indices, calculated for each sampling site, indicated anthropogenic unpolluted surface sediments. The potential ecological risk (RI), calculated for assessing the toxicity risk related to surface benthic biomass, showed that the potential ecological risk for biological life in surface sediments was low.

Keywords: surface sediment, heavy metals, risk, pollution indices

INTRODUCTION

The development of the non-ferrous ore exploitation and processing industry between 1950s and 1960s in Baia Mare area, coupled with the migration of the labor force from the villages to the city, led to the review of water needs and the design of engineering schemes for hydro-technical planning [1]. At the Somes-Tisa basin, this planning management water

---

[a] *North University Centre of Baia Mare, Technical University of Cluj-Napoca, Engineering of Mineral Resources, Materials and Environment Department, 62A Victor Babes str., 430083, Baia Mare, Romania*
[b] *Maramureş Water Management System, Someş-Tisa Basinal Water Administration, no. 2, Hortensiei Street, 430294, Baia Mare, Romania*
[c] *Technical University of Cluj-Napoca, Faculty of Materials and Environmental Engineering, 28, Memorandumului Street, 400114 Cluj-Napoca, Romania*
* *Corresponding author: irina.smical@cunbm.utcluj.ro*

needs includes, after the main use - the drinking water supply of the localities, other uses as: raw water for industry, hydropower potential, flood protection, irrigation, fishing and even recreational activities.

In this context, during the period 1960-1964, the works for the construction of the Strâmtori reservoir on the Firiza River and the Berdu compensatory lake were executed, which had as main use the supply of raw water for industry, as well as drinking water for the downstream population. The energy potential of the dam is also used, with an installed power of 4.2 MW [1].

The Strâmtori accumulation is located on the Firiza River, about 10 km upstream of Baia Mare. The accumulation dam is built in concrete counterweight, with a useful volume (at commissioning in 1964) of 14.5 million m^3, the annual average clogging being less than 20 000 m^3, holding a reception pool with an area of 130 km^2 [1-2].

After 1997, when the mining activity was ceased, the Strâmtori-Firiza reservoir has served mainly for supplying of raw water for drinking in Baia Mare area.

Elaborated as a result of recent studies on the status of the caging of the reservoir [2], the present study highlights the current state of pollution with characteristic metals of the area: arsenic, cadmium, copper, lead and zinc, by analyzing the water, the surface sediment layer and calculating the pollution indices.

To assess the environmental risks associated with the heavy metals (Cr, Mn, Cu, Zn, Cd, Hg and Pb) migration in sediments in various water reservoirs or accumulations, a lot of research has been made all over the world [3-7].

The influence of human activities like agriculture, waterborne transport, industry and especially mining industry was highlighted by Bing et al., (2016) [5] in their research regarding the heavy metal contamination of sediments of Three Gorges Reservoir (TGR) from China. More recently studies on heavy metal contamination of surface water of the Three Gorges Reservoir (TGR) showed that heavy metals did not exceed the first grade water quality threshold values, excepting Zn. The main risk for human health was due to the presence of Cr and As [8].

The research of Pratap et al., (2020) [9] to assess the influence of wastewater discharging from Kinoya Wastewater Treatment Plant into Laucala Bay sediments, showed an important increase of the concentration of studied metals in the place around the discharging effluent sites. This indicated the negative anthropic influence on the sediments quality. The results of research made by Zhou et al., (2017) [10] for a drinking water reservoir in China showed an increasing of the organic carbon (OC), total nitrogen (TN), and total phosphorus (TP) in sediments. As well, the concentration of Fe and Mn posed high to very high risk [10].

The aim of this study was to assess the surface sediments quality of Strâmtori-Firiza reservoir related to a series of heavy metals like arsenic, cadmium, copper, lead and zinc. For this, the following indices were calculated: (1) Single pollution index, (2) Geo-accumulation index, (3) Contamination factor, (4) Pollution Load Index and (5) Multi-element contamination.

RESULTS AND DISCUSSION

Trace elements in water

In the monitoring period (2017-2019) the obtained results for the investigated elements (As, Cd, Cu, Pb and Zn) were compared with the maximum allowed concentrations, expressed as quality standards (QS) by the Romanian legislation [11] and the lake water was within the first class of quality, as shown in Table 1.

Table 1. Basic statistics of metal concentrations in water samples

Metal	As	Cd	Cu	Pb	Zn
*QS, µg L^{-1}	10.000	0.500	20.000	5.000	100.000
Basic statistics of metal concentrations in 18 water samples collected from 6 locations, in 3 sampling campaigns during 2017-2019 period					
Minimum, µg L^{-1}	0.360	0.120	0.750	1.040	7.902
Maximum, µg L^{-1}	1.080	0.260	20.004	1.460	58.101
Average, µg L^{-1}	0.724	0.179	10.422	1.205	26.713
Standard deviation, µg l^{-1}	0.202	0.041	9.631	0.124	11.504
Detection limit, µg L-1	0.300	0.075	0.500	1.000	5.000
* Quality Standards (QS) for the elements of the first class, according to the Romanian legislation [11]					

Trace elements in surface sediment

Because there were no data for the natural background of sediments in this area, the obtained concentration values were compared with the quality standard (QS) values, provided by Romanian legislation as maximum allowed values [11].

As outlined in Table 2, no obtained value exceeded the maximum allowed values provided by Romanian normative [11]. Zn concentrations were approaching its corresponding QS (concentration determined as 89.33% of QS), in sampling campaign of 2019, in the sampling point 3.

Table 2. Basic statistics of metal concentrations in 18 sediment samples collected from 6 locations, in 3 sampling campaigns, from 2017 to 2019

Metal	*QS, mg kg^{-1}, (**d.w.)	Minimum, mg kg^{-1}	Maximum, mg kg^{-1}	Average, mg kg^{-1}	Standard deviation, mg kg^{-1}
As	29.000	0.980 (in 2018, in P1)	3.670 (in 2019, in P3)	2.001	0.761
Cd	0.800	0.590 (in 2018, in P1)	1.650 (in 2018, in P3)	0.990	0.261
Cu	40.000	5.221 (in 2017, in P1)	34.103 (in 2018, in P3)	16.402	7.903
Pb	85.000	10.404 (in 2018, in P6)	35.201 (in 2019, in P3)	19.172	6.264
Zn	150.000	51.504 (in 2018, in P1)	134.003 (in 2019, in P3)	76.195	23.174
* Quality Standards (QS) for the elements, according to the Romanian legislation for sediments, fraction <63 μm [11]					
** dry weight					

Although the correlation coefficients calculated for the studied metals showed a good correlation between them, thus highlighting their same origin in the composition of the studied surface sediments, only the value of the correlation coefficient between As and Pb implied a statistically significant correlation (Table 3).

Table 3. Correlation coefficients between heavy metals analyzed form surface sediment

	As	Cd	Cu	Pb	Zn
As	1.000				
Cd	0.822	1.000			
Cu	0.870	0.840	1.000		
Pb	0.891*	0. 712	0.869	1.000	
Zn	0.773	0.861	0.734	0.679	1.000
* significant correlation (the critical value for p=5% is 0.880)					

The Single Pollution Index was calculated with the mean of all obtained values in the sampling campaigns and was presented in Table 2. According to values of the Single Pollution Index in Figure 1, the level of contamination

for each site and metal was established (Figure 1). The results for the sampling sites do not show any contamination with As, Cu, Pb and Zn. There was one exception for Cd, for which the calculated pollution index showed a low pollution in P1, P2, P3, P4, P5 and P6 sampling sites.
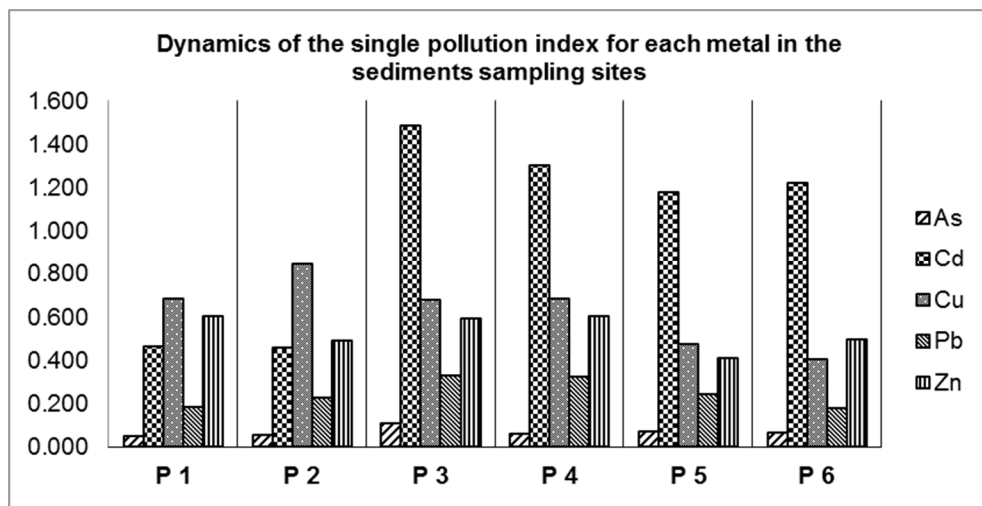
Figure 1. Single pollution Index for each metal from sediments in the 6 sampling sites

The maximum value of the pollution index (1.488) was calculated in P3 sampling site, closest to the potential anthropic impact. Also, the calculated PLI indicated a low pollution of the surface sediments with Cd in all sites, through accumulation in the surface sediment layer, most likely, due to various anthropic activities (upstream urban agglomerations or relaxing activities allowed near the lake perimeter).

The obtained values for the geo-accumulation index – Table 4 reflect the non-pollution of the area, from the point of view of the studied elements.

Table 4. Basic statistic of the I_{ga}

I_{ga}	Minimum	Maximum	Mean
As	-3.957	-2.858	-3.593
Cd	-0.936	-0.401	-0.645
Cu	-3.618	-1.489	-2.370
Pb	-1.464	-0.543	-1.149
Zn	-1.887	-1.325	-1.663

The **contamination factor,** calculated with equation 3, shows the moderate contamination with cadmium, mostly in the P3 sampling point, where the single pollution index also indicated a slight pollution (Figure 2).
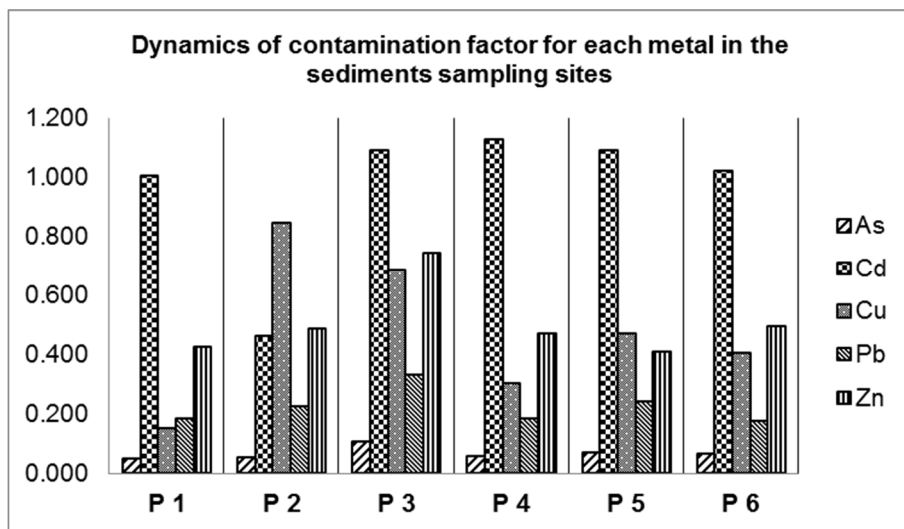
Figure 2. Dynamics of the contamination factor for each metal

The sum of the contamination factors calculated for each sampling site, allowed to highlight the degree of contamination corresponding to the entire studied area, for each investigated metal: As=0.793; Cd=5.94; Cu=1.97; Pb=1.64; Zn=2.91. In accordance with the values, it can be concluded that the surface sediments in this area are not contaminated with As, Cd, Cu, Pb or Zn, and the global degree of contamination was low.

To evaluate the total degree of contamination due to the accumulation of heavy metals in surface sediments the pollution load Index (PLI) = 0.328 was calculated. The obtained value indicated non-pollution of the study area.

The source of heavy metals was identified after calculating the multi-element contamination index (MEC), in accordance to equation 5. The value of the MEC=0.428, certifies that there was not anthropogenic impact on the analyzed surface sediments of the reservoir Strâmtori-Firiza.

The potential ecological risk (RI) was also calculated for assessing the toxicity risk related at surface benthonic biomass, in accordance with equations 6 and 7 (RI=43.7). The result showed that the potential ecological risk for biological life in surface sediments was low.

CONCLUSIONS

In accordance with the results obtained during the entire monitoring period it could be said that the correlation factors calculated for the studied metals, indicated a direct connection and distinctly significant correlations factor between As and Pb. This is due to the same provenience of the metals from non-ferrous ores. Correlation factors between Pb and Cd, Zn and As, Zn and Cu, or Zn and Pb were calculated, without statistically importance. As a consequence, the pollution indices calculated for each sampling site indicated unpolluted anthropic surface sediment.

There was highlighted an absent level of pollution with As, Cu, Pb and Zn; except for Cd, for which the calculated pollution index showed a low pollution in P1, P2, P3, P4, P5 and P6 sampling sites.

A low pollution of the surface sediments with Cd was determined in all sites, through accumulation in the surface sediment layer, most likely, due to anthropic activities.

The source of heavy metals, identified after calculating the multi-element contamination index (MEC), indicated that there was not anthropogenic impact on the analyzed surface sediments of the reservoir Stramtori-Firiza.

The potential ecological risk (RI) calculated for assessing the toxicity risk related at surface benthonic biomass showed that the potential ecological risk for biological life in surface sediments was low.

EXPERIMENTAL SECTION

In the studied period 2017-2019, the sampling campaigns started at 15th of June, depending on climatic conditions. Also, the sampling sections of water and surface sediment were the same in each investigated year. Studied area is shown in Figure 3.
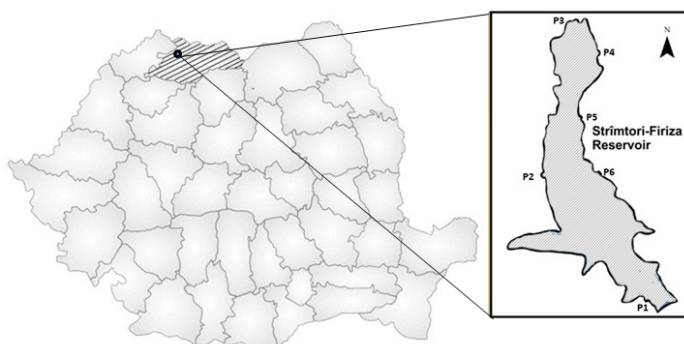

Figure 3. Sampling points on the Strâmtori-Firiza reservoir

Sampling and conservation the samples

In the studied period of time (2017-2019), the sampling campaigns were held in June, after 15th, depending on climatic conditions. Both the sampling sections of water and surface sediment were the same in each investigated year.

Water sampling was carried out from the foothills of the lake, in 6 sites, using a 1.5 m long telescopic rod, with a 1 L plastic container. From each sampling point, three samples were collected, then they were homogenized in a bucket, from which a 1 L sample was collected in a glass container. The water samples thus obtained were preserved with HNO3 (65%, p.a., Merck, Darmstadt, Germany) [12]) and transported to the laboratory.

For surface sediment sampling, a Draga-Ponar sampler was used; from each of the 6 sampling points. Three independent replicates were collected, which constituted, after homogenization, the sample from that sampling point. For the present study, the sieving of the collected sediment samples was performed in order to collect the sediment fraction <63 µm, in wet environment, immediately after sampling [13,14]. The sediment fractions (<63 µm), each of at least 50 g, were collected in glass containers, transported in the laboratory and air-dried (far from the direct sun rays). After the complete drying (about 2 days) to the constant mass the part of it, 0.2 g of sediment, applying the quartering method, was subjected to the mineralization, in order to determine the concentrations of metals [15].

The concentrations of heavy metals in water samples were interpreted in accordance with Romanian legislation in force [11], for the first class of quality.

In order to assess the heavy metals pollution of surface sediment, different indices were used [16-20].

Single Pollution Index (PI) – used in order to provide a measure of the contamination degree of the sampling site with individual studied element. Pollution Index was calculated using the equation 1 [20]:

$$Pl_i = \frac{C_i}{S_i} \tag{1}$$

where: Pl_i – pollution index for metal *i*; C_i – mean concentration of metal in surface sediment; S_i – references values, provided by national legislation, as ca maximum allowed values [11].

Geo-accumulation index (I_{ga}) – used to complete the previous data and information to establish the pollution degree [21] and then other researchers calculated the geo-accumulation index [16-17] [21-23] using equation 2:

$$I_{ga} = \log_2\left(\frac{C_n}{K \times C_{fn}}\right)$$ (2)

where: I_{ga} - geo-accumulation index; C_n – the n element concentration in 0.63 μm sediment fraction; K – correction factor for element required by the geochemical background and lithological conditions variation, K =1.5; C_{fn} – natural geochemical background of the n element in sediment (As=15; Cd=1.0; Cu=50; Pb=70; Zn=175, all expressed in mg kg^{-1} dry weight) [20].

The obtained results for the two indices were compared with the values shown in Table 5.

Table 5. Assessment of the potential ecological risk with pollution indices

Single Pollution index (PI) * highlights the contamination level		Geo-accumulation index (I$_{ga}$)* highlights the pollution degree	
PI≤1	absent	≤ 0	unpolluted
1< PI< 2	low	0 - 1	unpolluted to moderately
2< PI< 3	moderate	1 -2	moderately
3< PI< 5	strong	2 - 3	moderately to highly
PI >5	very strong	3 - 4	highly
		4 - 5	highly to extremely high
		>5	extremely high

*after Kowalska et al., 2018 [16]

Contamination factor (C$_f$) – illustrates the difference between sample and reference values of each heavy metal. It is calculated with equation 3 [20]:

$$C_f = \frac{C_m}{C_{p-i}} \times C_f$$ (3)

where:

C_m – mean of content of the heavy metal, of the individual sampling point, in mg kg^{-1};

C_{p-i} – pre-industrial reference value for the heavy metals [20].

The sum of the contamination factors for the each metal, illustrated de degree of contamination. The contamination factor and the degree contamination were interpreted according to the values provided in Table 6 [16].

Table 6. Contamination Factor (C_f) and Degree of Contamination (C_{deg}) interpretation (Kowalska et al., 2018 [16])

C_f value	Contamination	C_{deg} value	Degree of contamination
< 1	low	< 8	low
1 - 3	moderate	8 - 16	moderate
3 - 6	considerable	16 - 32	considerable
> 6	very high	> 32	very high

The degree of total pollution was evaluated with the **Pollution Load Index (PLI) –** calculated with equation 4, indicated the total degree of contamination and demonstrates deterioration of the conditions due to the accumulation of heavy metals in surface sediments [16-17]:

$$PLI = \left(PI_1 \times \ldots \times PI_i \right)^{1/n} \tag{4}$$

where:

$PI_{1\ldots i}$ – pollution index for each metal i; n- number of metals taken into consideration (for this study n=5).

In Table 7 the interpretation of the contamination categories of the pollution load index is presented.

Table 7. Contamination categories of Pollution Load Index (PLI) [16-17]:

Value of *PLI*	Pollution status
< 1	denote perfection
1	between the acceptable limits of pollution
> 1	deterioration of soil quality

The source (natural or anthropogenic) of heavy metals was identified after calculating the **multi-element contamination (MEC) index** [16] [20]. This is a measure of contamination assessment on the surface sediment with the tolerable levels given. It was calculated with equation 5:

$$MEC = \frac{\left(\dfrac{C_1}{T_1} + \cdots + \dfrac{C_i}{T_i} \right)}{n} \tag{5}$$

where:

$C_{1\ldots i}$ – content of the heavy metal;

T_i – tolerable levels

Higher values than 1 of the MEC index certify the presence of the anthropogenic impact in the analyzed surface sediments.

According to Hakanson, (2011) [20], the **Potential Ecological Risk (RI)** was calculated for assessing the degree of the ecological risk related to the presence of the heavy metals in analyzed surface sediment. The calculation of this index was in accordance with equation 6 and 7 [20]**.**

$$RI = \sum_{i=1}^{n} E_f^i \tag{6}$$

where: RI – pollution index; E_f^i – pollution coefficient of a single metal.

The pollution coefficient of a single metal was calculated with the equation:

$$E_f^i = T_f^i \times PI_i \tag{7}$$

where:

E_f^i – pollution coefficient of a single metal;

T_f^i – factor of the biological (surface benthic) toxicity for each metal: As=10, Cd=30, Cu=Pb=5 and Zn=2, all in mg kg^{-1} dry weight [24]

PI_i – pollution index for each metal, calculated with equation 1.

Applying these calculations was possible to highlight the level of pollution based on data presented by Kowalska, 2018 [16]: <90 – low pollution ecological risk, 90-180 – moderate pollution ecological risk, 180-360 strong pollution ecological risk, 360-720 very strong pollution ecological risk, ≥ 720 highly-strong pollution ecological risk.

Chemical analysis

Metal concentrations in water and sediment samples were analyzed using graphite furnace atomic absorption spectrometry (GF-AAS) and comprised of two stages: sample digestion, and quantitative analysis of metals in digested samples using a Perkin-Elmer AAS, type AAnalyst 700, metrological verified and provided with a calibration certificate.

Each result was obtained as an average of three individual sample readings and validated using relative standard deviation, using the software WinChemLab. The calibration curves used were validated based on the determination coefficient (R^2), only values of ≥0,990 being accepted. For each processed samples batch, in lab, was run a blank sample consisting in

ultrapure water, sample for intern control: Shewhart diagrams, replicated and CRM (for water sample: TM-24.4 - „A low level fortified sample for trace elements", Environment and Climate Change Canada; for sediments: BCR-320R „Channel sediment (trace element)", LGC-Standards). The measured mean and standard deviation of elemental values for CRM were compared with the certified values. In both cases it was confirmed that the sample preparation and instrumentation conditions provided good levels of accuracy, precision and degree of recovery (90-110%).

Samples digestion was performed in Teflon vessels of a microwave digestion system, Millestone Ethos D, according to producer operating instructions, namely DG-EN-30 and DG-EN-08 for sediment and water, respectively. Thus, 0.2 g dried sediment sample were digested with acids (4 ml of 96% H_2SO_4 in the first step, then in second step, 6 ml of 65% HNO_3, analytical purity, provided by Merck, Darmstadt, Germany), at 220 °C, 20 minutes, at 800 W microwave power [25].

The residue obtained after mineralization was brought into 50 ml volumetric flasks with 0.02 M HNO_3 solution, which, after filtration, subjected to metal determination using GF-AAS technique.

REFERENCES

1. C. Sofronie, *Amenajări Hidrotehnice în Bazinul Hidrografic Someş-Tisa*, Gloria Home Press, Cluj-Napoca, Romania, **2000**, pp. 20-65.
2. D.L. Ciurte, A. Mihu-Pintilie, L.E. Paveluc, C.C. Stoleriu, *Proceeding of the 5TH Jubilee International Scientific Conference & Expo, Geobalcanica (13-14 June 2019, Sofia, Bulgaria)*, **2019**, 591-597.
3. M. Deng, X. Yang, X. Dai, Q. Zhang, A. Malik, A. Sadeghpour, *Ecol. Indic.*, **2020**, *112*, 106-166.
4. M. Kijowska-Strugala, L. Wiejaczka, R. Kozlowski, J. Lekach, *Int. J. Sediment Res.*, **2020**, *35*, 269-277.
5. H. Bing, J. Zhou, Y. Wu, X. Wang, H. Sun, R. Li, *Environ. Pollut.*, **2016**, *214*, 485-496.
6. P. Palma, L. Ledo, P. Alvarenga, *Catena (Amst)*, **2015**, *128*, 174–184.
7. A. Zahra, M.Z. Hashmi, R.N. Malik, Z. Ahmed, *Sci. Total Environ.,* **2014**, 470–471, 925–933.
8. L. Zhao, D. Gong, W. Zhao, L. Lin, W. Yang, W. Guo, X. Tang, Q. Li, *Sci. Total Environ.,* **2020,** *704*, 134883.
9. A. Pratap, F.S. Mani, S. Prasad, *Mar. Pollut. Bull.*, **2020**, *156*, 111238.
10. Z. Zhou, T. Huang, Y. Li, W. Ma, S. Zhou, S. Long, *J Environ Sci (China),* **2017**, *52,* 223–231.

11. Order no. 161/2006 for the approval of Normative on the surface water classification in view of establishing ecological status of water bodies, published in OG no. 511/13 June **2006**.
12. SR EN ISO 5667-6:2017 – Water quality - Sampling - Part 6: Guidance on sampling of rivers and streams.
13. SR ISO 5667-12:2001 – Water quality. Sampling. Part 12: Guidance on sampling of bottom sediments.
14. SR EN ISO 5667-15:2010 – Water quality. Sampling. Part 15: Guidance on preservation and handling of sludge and sediment samples.
15. A. Cernatoni, V. Cușa, Institute of Research and Environmental Engineering, Ministry of Waters, Forests and Environmental Protection Press, Romania, **1996**, pp. 40-52.
16. J.B. Kowalska, R. Mazurek, M. Gasiorek, T. Zaleski, *Environ. Geochem. Health*, **2018***, 40*, 2395-2420.
17. M. Varol, *J. Hazard. Mater.*, **2011**, *195*, 355-364.
18. S.A. El-Sayed, E.M.M. Moussa, M.E.I El-Sabagh, *J. Radiat. Res. Appl. Sci.*, **2015**, *8*, 276-285.
19. M.E. Goher, H.I. Farhat, M.H. Abdo, S.G. Salem, *Egypt J Aquat Res*, **2014**, *40*, 213-224.
20. L. Håkanson, *Water Res.*, **2011**, *14*, 975 – 1001.
21. G. Müller, *Veränderungen seit*, **1979**, *1971*, 107-126.
22. U. Förstner, W. Ahlf, W. Calmano, M. Kersten,**1990**, Sediment Criteria Development. In: Heling D., Rothe P., Förstner U., Stoffers P. (eds) Sediments and Environmental Geochemistry. Springer, Berlin, Heidelberg. https://doi.org/10.1007/978-3-642-75097-7_18.
23. M. Singh, A.A. Ansari, G. Müller, et al., *Environ. Geol.*, **2013**, *29 (3/4),* 246-252.
24. A. Kloke, Tolerable amount of heavy metals in soil and their accumulation in plants, Environmental Effects of Organic and Inorganic Contaminants in Sewage Sludge Press, **1983**, 171-175.
25. DG-EN-30 protocol. Technical Book DIGESTOR (microwaves oven) Milestone. type ETHOS - Application: Environment - River sediment. Digestion Application Note: DG-EN-30. Rev. 03_04.

AN ALTERNATIVE USAGE OF *URTICA DIOICA* AS ADSORBENT FOR MALACHITE GREEN: OPTIMIZATION STUDY

BENGÜ ERTAN[a*], SUMEYRA GURKOK[b], DERYA EFE[a]

ABSTRACT. The adsorption of malachite green (MG) by the use of an eco-friendly adsorbent *Urtica dioica (U. dioica)* has been reported in the present study. The effects of different parameters were tested on MG adsorption and optimization of the effective parameters (pH, temperature and initial dye concentration) were performed by response surface methodology (RSM). Maximal adsorption yield of 91.67% was achieved at pH 6.5 and 50 °C with 200 mgL^{-1} initial dye concentration. The isotherm and kinetic studies were employed to describe the adsorption process. The experimental data fitted better on the Freundlich model and the adsorption process followed by the pseudo-second order model.

Keywords: Urtica dioica, Malachite Green, Adsorption, Response Surface Methodology

INTRODUCTION

The environmental pollution is a global problem as a result of rapid industrialization. Waste water discharged into natural water sources is mostly contaminated with synthetic dyes, which are the main water pollutants with an annual production of more than 700,000 tons and more than 10000 varieties. [1]. One of the most hazardous coloring agents is malachite green (MG). It is an organic cationic dye widely used in different industries such as textile, rubber, paper, plastic, leather, cosmetic, food and printing [2,3]. MG is also used as an antimicrobial agent in aquaculture and for staining bacterial endospores and tissue samples. MG is known as a mutagenic and carcinogenic multi-organ toxin causing serious damages in liver, spleen, heart, and lungs. In

---

[a] *Giresun University, Espiye Vocational School, Adabük, 28500/Düzköy, Espiye, Giresun, Turkey*
[b] *Ataturk University, Faculty of Science, Department of Biology, 25240, Erzurum, Turkey*
* *Corresponding author: bengu.ertan@giresun.edu.tr*

addition, like other synthetic dyes, the widespread use of MG causes significant environmental problems by preventing sunlight from penetrating into the water, thereby reducing the effectiveness of photosynthesis. [4,5]. Since MG is defined as a Class II Health Hazard in the United States, its use in aquaculture is prohibited by the Food and Drug Administration. Serious health problems have been reported in many countries as a result of eating aquatic fish contaminated with MG [6,7]. However, millions of kilograms of MG are still produced annually and are used as dyes due to their low prices, easy availability, effectiveness and lack of a suitable alternative [8].

MG has a complex, stable and non-biodegradable structure, therefore, it should be removed using an effective treatment method before being released into the media [9]. Recently, the adsorption with various adsorbents has gained importance and great demand due to its efficiency and simplicity [10,11]. The use of biomaterials for adsorption has many advantages in terms of low cost, efficiency, availability and being environmentally friendly [12,13]. Although many studies have been carried out on the adsorption potential of different biomaterials such as oil palm [14], de-oiled soya [15], rice straw [16], corn stalks [13], etc. [17,18], there is still a great interest and demand to evaluate adsorption potential of novel and alternative materials.

U. dioica, belonging to *Urticaceaea* family, is a perennial plant with the ability to grow 2 to 4 meters high [19,20]. It has upstanding green stem, opposite and finely toothed leaves with dark green above and paler beneath and dioecious flowers in reddish-brown to greenish-white color [21]. Although it origins from colder region of Northern Europe and Asia, it spreads all over the world especially temperate zones of the world. *U. dioica*, generally an under storey plant, is called as nettle or stinging nettle because of its stinging hairs on the leaves [22]. It is known as a medical plant because of its antimicrobial, antioxidant, antiulcer, analgesic, antidiabetic, and anticancer properties [23]. Likewise, *U. dioica* has a significant adsorption potential, as it has soft, resistant and low specific weight fibers which possess non-lignified cell walls [24]. In several studies, it has been reported as adsorbent for the heavy metals such as Cu, Pb, and Cd [25].

Various factors such as temperature, initial dye concentrations, amount of adsorbent, pH, contact time and particle size of adsorbent determine the efficiency of dye adsorption process. In order to achieve an effective MG adsorption, it is essential to analyze their effects and optimize them. Evaluating these variables individually and finding their optimum values takes a lot of time and ignores the interaction between the parameters. Instead of traditional optimization techniques, statistical techniques [26] have been widely used to improve a wide range of bioprocesses in recent publications [27,28]. Statistical approaches, such as response surface methodology (RSM), provide

comprehensive information about the processes and reduce time and expense by ensuring fewer experiments. RSM is a highly accepted mathematical and statistical technique that is used in determining optimum conditions and clarifying the interactions of the parameters, especially in processes where several parameters affect the response. In order to determine the optimal conditions for maximal yield, RSM creates empirical models and designs experiments. Response surface designs have two basic types, central composite design (CCD) and Box–Behnken design (BBD). BBD has less design points and requires fewer experiments than CCD and therefore, it is less expensive to run with the same number of factors.

Therefore, the present study aimed to determine the adsorption potential of *U. dioica* grown in Giresun and to optimize the operation conditions of MG adsorption. BBD of RSM was applied for analyzing the effects of temperature, pH and initial dye concentration on MG adsorption. The use of *U. dioica* for the adsorption of MG and optimization of the operation conditions has been reported for the first time in this study.

RESULTS AND DISCUSSION

The adsorption parameters of the MG removal

Several factors are known to affect the adsorption process. Among them, significant variables (pH, initial dye concentration, adsorbent amount, contact time) have been tested in this study.

Effect of pH

The pH of the media determines the ionization degree of the adsorbent and the dissociation of functional groups [29]. The effect of pH was evaluated in the pH range of 2–8 as seen from Fig. 1a. At the initial pH, the number of negatively charged groups on the surface of adsorbent was decreased. As the pH increased, the negatively charged groups on the surface of the adsorbent and MG adsorption increased (max. adsorption 84.88% at pH 6). This can be explained as a result of the electrostatic attraction between positively charged MG molecules and negatively charged *U. dioica*. pH values above 8 have not been investigated due to the instability of MG color.
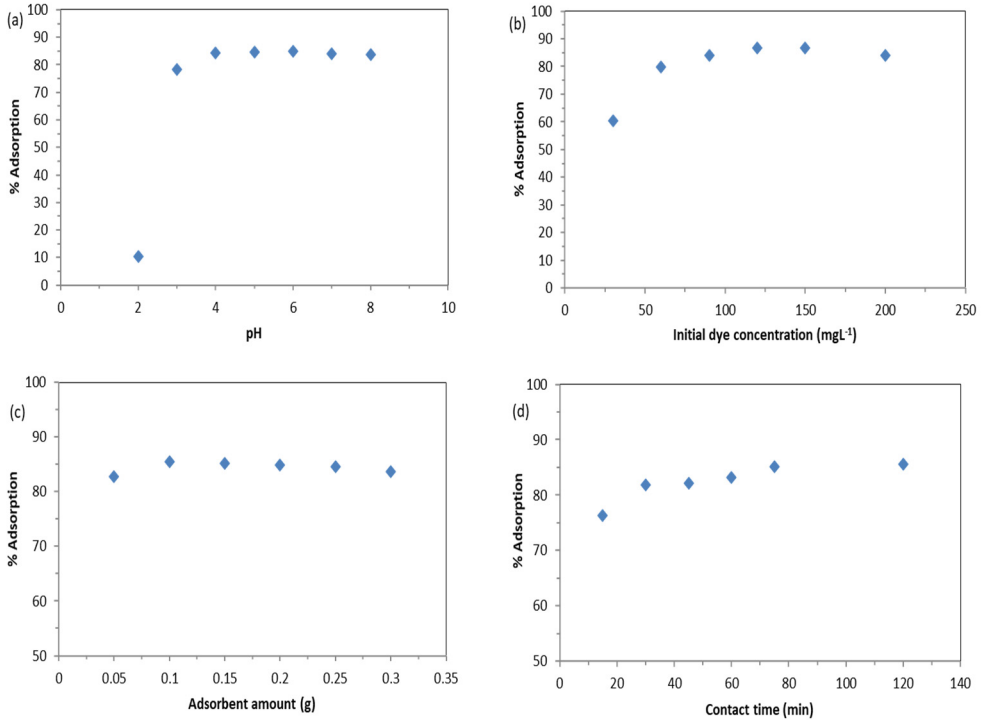
Figure 1. The effect of (a) pH (150 mgL^{-1} initial dye concentration, 0.1 g adsorbent amount at room temperature); (b) initial dye concentration (pH:6, 0.1 g adsorbent amount at room temperature); (c) adsorbent amount (150 mgL^{-1} initial dye concentration, pH:6, at room temperature); (d) contact time (150 mgL^{-1} initial dye concentration, pH:6, 0.1 g adsorbent amount at room temperature) on the adsorption of *U. dioica*

Effect of initial dye concentration

The influence of the initial MG concentration on adsorption was performed at fixed values of pH (6), adsorbent amount (0.1 g) and contact time (2 h). As shown in Fig. 1b, adsorption (%) increased with the increasing initial dye concentration depending on the available binding sites. Adsorption (%) did not changed above 150 mgL^{-1} of MG concentration as the adsorption sites of the adsorbent were almost completely occupied or reached saturation.

Effect of adsorbent amount

Effect of adsorbent amount on the adsorption was studied in the range of 0.05–0.3 g. As the quantity of adsorbent increases, an increase in the number of suitable sites and surface area occurs. Even the use of a small amount of *U. dioica* was effective in MG removal, as seen in Fig. 1c.

Effect of contact time

In the first 15 min, the adsorption rapidly increased by 77%, then increased more slowly. Equilibrium was reached with an adsorption rate of 85% in 75 min and this value did not change in the following periods as seen in Fig. 1d [30].

Statistical optimization of dye adsorption conditions by BBD of RSM

The effects of three parameters pH, initial MG concentration and temperature on % adsorption of *U. dioica* on MG were studied and interactive effects of the variables on the adsorption yields were presented in Fig. 2. Fig. 2a shows the interactive effect of pH and temperature on the adsorption of MG. According to this figure, adsorption efficiency (%) increased significantly with increasing pH, but less affected by increasing temperature.

Figure 2. Response surface plots presenting the interactive effects of pH and temperature (a), initial dye concentration and temperature (b), and initial dye concentration and pH (c) on MG adsorption. In all cases, the third factor was fixed at the middle point.

The combined effect of initial dye concentration and temperature is seen in Fig. 2b. Likewise, adsorption efficiency increased with increasing initial MG concentration and temperature, but it can be seen from this figure that initial MG concentration is more effective than temperature. The positive effect of combined initial MG concentration and pH on the adsorption yield of MG is given in Fig. 2c. It is deduced from the figures that the most dominant parameter is pH, then the initial MG concentration and temperature, respectively.

Response surface plots (Fig. 2) and contour plots (Fig. 3) show maximal adsorption efficiency around 80–90% which was obtained when the temperature, pH, and initial dye concentration reached slightly beyond the 50 °C, pH 6, and 180 mgL^{-1}, respectively.
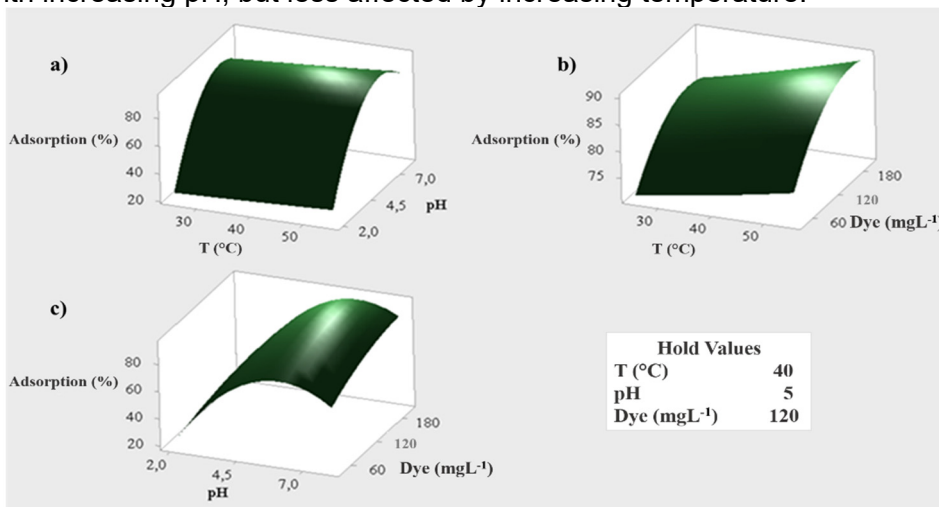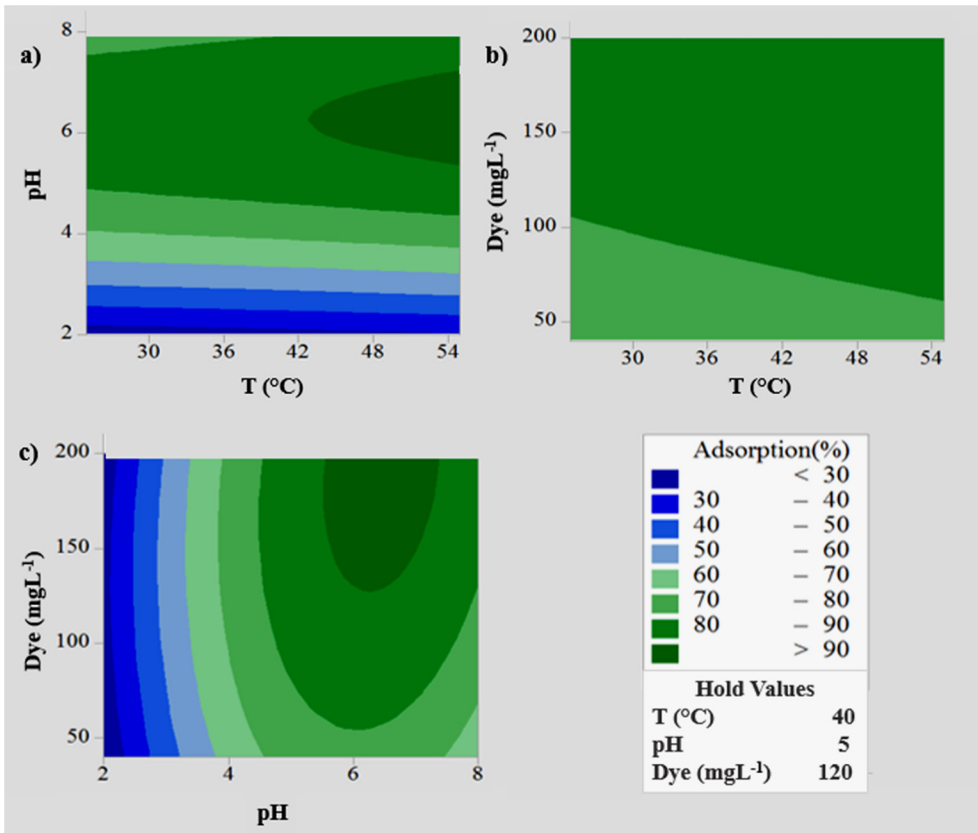

Figure 3. Contour plots presenting the interactive effects of pH and temperature (a), initial dye concentration and temperature (b), and initial dye concentration and pH (c) on MG adsorption. In all cases, the third factor was fixed at the middle point.

The regression analysis for the dye adsorption model is given in Table 1. As it is seen from the regression analysis and also from the surface plots, the temperature is the less effective factor on the adsorption efficiency. When the temperature increased, the efficiency increased slightly. However, increase in pH and initial dye concentration effectively increased the efficiency. Beyond these levels, increase either caused adverse effect on responses or did not affect.

In Fig. 3, contour plots of T*pH (p:0.407) and T*Dye concentration (p:0.532) interactions resulted in orbicular shape, which means there are negligible interaction between the variables. Elliptical shape in contour plot of pH*Dye concentration (p <0.0001) indicated significant interaction between the variables [27].

Table 1. Predicted coefficients of regression analysis for dye adsorption

Term	Coef	SE Coef	T-Value	p-Value
Constant	83.920	1.280	65.510	p<0.0001
A-T(°C)	3.096	0.785	3.950	0.001
B-pH	25.943	0.785	33.070	p<0.0001
C-Dye (mgL^{-1})	5.877	0.785	7.490	p<0.0001
A^2-T(°C)* T(°C)	0.240	1.150	0.210	0.835
B^2-pH*pH	-31.150	1.150	-26.970	p<0.0001
C^2-Dye (mgL^{-1})*Dye (mgL^{-1})	-4.470	1.150	-3.870	0.001
AB-T(°C)*pH	0.940	1.110	0.850	0.407
AC-T(°C)*Dye (mgL^{-1})	0.710	1.110	0.640	0.532
BC-pH*Dye (mgL^{-1})	4.730	1.110	4.270	p<0.0001

SE: Standard Error; Coef: Coefficient; T: Student's t-Test; p: Probability

Optimization of adsorption process was performed by applying second order polynomial equation and the generalized polynomial model equation Eq. 1 for three factors was as follows;

$$Y= b_0+b_1A+b_2B+b_3C+b_{11}A^2+b_{22}B^2+b_{33}C^2+b_{12}AB+b_{13}AC+b_{23}BC \qquad (1)$$

In Eq. 1, Y is the predicted response (adsorption yield), A, B, C are independent variables [(temperature (A), pH (B) and initial dye concentration (C)], b_0 is the intercept (constant), b_1, b_2, b_3 are linear coefficients, b_{11}, b_{22}, b_{33} are the squared coefficients and b_{12}, b_{13}, b_{23} are the interaction coefficients.

According to the regression analysis, A, B, C, B^2, C^2, BC, are significant terms for the model ($p<0.05$). Other terms can be considered as insignificant ($p>0.05$) and deduced from the equation for the improvement of the model. Therefore, the final reduced empirical formula to predict the adsorption yield (Y) is shown as Eq. 2.

$$Y = 83.92+3.09A+25.94B+5.88C-31.15\,B^2-4.47C^2+4.73BC \qquad (2)$$

where Y is predicted response which stands for adsorption yield, A, B, and C stands for coded value of temperature, pH and initial dye concentration, respectively.

The magnitute of model coefficients in Table 1 indicate that pH (25.943) had a more prominent effect on adsorption efficiency than initial dye concentration (5.877) and temperature (3.096).

The ANOVA of the quadratic polynomial model for adsorption efficiency was shown in Table 2. The F-value of 213.46 and p-value of 0.000 verify the model is statistically highly significant. The p-value of Lack-of-Fit (0.882) indicates the model successfully predicted the dye adsorption efficiency and the experimental data fitted well on the model. The R^2 value of 0.99 revealed that the results of the experiments adequately fit to the regression model equation. The predicted R^2 of 0.97 is in acceptable agreement with the adjusted R^2 of 0.98 (Table 2).

Table 2. ANOVA of quadratic polynomial model for adsorption efficiency

Source	DF	Adj SS	Adj MS	F-Value	p-Value
Model	9	18920.1	2102.2	213.46	$p<0.0001$
Linear	3	11475.0	3825.0	388.38	$p<0.0001$
Square	3	7254.7	2418.2	245.54	$p<0.0001$
2-Way Interaction	3	190.4	63.5	6.44	0.003
Error	20	197.0	9.8		
Lack-of-Fit	3	7.3	2.4	0.22	**0.882**
Pure Error	17	189.6	11.2		
Total	29	19117.1			

R^2: 0.99 R^2(Adj): 0.98 R^2(Pred): 0.97
DF: Degree of freedom; Adj: Adjusted; SS: Sum of squares; MS: Mean square;

Multiple response prediction for dye adsorption under the optimized condition (50 °C, pH 6.5 and 200 mgL^{-1} initial dye concentration) determined by MINITAB program was performed in triplicate. Adequate agreement was achieved between the statistically estimated adsorption yield (90%) and measured (experimental) adsorption yield (91.67%).

Adsorption isotherms

The isotherm models were used to define the equilibrium data and the Freundlich isotherm model had a higher R^2 value with 0.9912 than the Langmuir model. In this model, it is suggested that the sorbent has a surface with a nonuniform distribution and the adsorbent surface is heterogeneous [31]. The n value of 0.918 obtained from the Freundlich isotherm showed that the interaction forces between the dyes and adsorbent were strong. The results are presented in Table 3.

Table 3. Isotherm constants for the adsorption of MG onto *U. dioica*

Langmuir	q_{max}(mgg^{-1})	K_L (Lmg^{-1})	R^2
	24.631	0.026	0.987
Freundlich	n	K_F (Lmg^{-1})	R^2
	0.918	2.312	0.991

Adsorption kinetics

Adsorption kinetics were used to test the experimental data, to examine the mechanism of the adsorption process and to predict the adsorption rate quantitatively. The pseudo-first order and the pseudo-second order kinetic models were applied [32]. According to the R^2 values in Table 4, The pseudo-second kinetic model was the most ideal to describe adsorption kinetic with the R^2 value (0.999) and q_e value calculated from model (58.823 mgg^{-1}) was also very close the experimental q_e value (56.16 mgg^{-1}). It has been elucidated that the rate-limiting step can be chemisorption involving valence forces with sharing or exchange of electrons between adsorbent and dye [33].

Table 4. Kinetic parameters for the adsorption of MG onto *U. dioica*

Pseudo-first order kinetic model	k_1(min^{-1})	q_e(mgg^{-1})	R^2
	0.205	39.415	0.966
Pseudo-second order kinetic model	k_2(mgg^{-1}min^{-1})	q_e(mgg^{-1})	R^2
	9.960	58.823	0.999

CONCLUSIONS

U. dioica is essentially a lignocellulosic, non-toxic, cheap and easy-to-access plant worldwide. In the present study, the use of *U. dioica* has been reported as adsorbent for the adsorption of MG. The improvement of dye adsorption was achieved through the use of statistical optimization of process parameters. Optimized conditions were found as pH 6.5, 50 °C and the initial dye concentration of 200 mgL^{-1}. Despite being applied directly without any chemical pretreatment processes, *U. dioica* proved to be an effective adsorbent with up to 91.67% dye removal under the optimized conditions.

EXPERIMENTAL SECTION

Preparation of materials

U. dioica collected from Giresun in Black Sea Region was washed several times with deionized water and dried firstly at ambient temperature then at 80 °C for 48 h in oven to remove the moisture. The samples were ground and passed through a 0.5 mm sieve. The adsorbent was stored in a dark bottle during the adsorption experiments.

The stock solution of malachite green (chemical formula $C_{23}H_{25}N_2.C_2HO_4.0.5C_2H_2O_4$, molecular weight: 463.50 gmol^{-1}, λ_{max}: 618 nm) was prepared 1 gL^{-1} with double distilled water using malachite green oxalate. The stock solution was diluted to prepare the desired concentrations. The pH of the solutions was adjusted with HCl (0.1 M) and NaOH (0.1 M). The chemicals were analytical grade and supplied from Sigma Aldrich.

Adsorption studies

The batch model was applied for adsorption studies. In the batch model, 50 mL of dye solution at various pH values and current amount of adsorbent were stirred at 200 rpm at 25 °C for 2 h, and then centrifuged at 3000 rpm to separate the liquid phase. The dye concentrations were determined by UV-visible spectrophotometer (Mapada-UV6100PCS Double Beam Spectrophotometer) at 618 nm. The adsorption studies were performed to determine the effects of parameters such as pH (2–8), initial dye concentration (30-200 mgL^{-1}), adsorbent amount (0.05–0.3 g) and contact time (15–120 min) and temperature (25-55°C). The effect of pH was studied the range of 2-8 that was adjusted using 0.1 M HCl and 0.1 M NaOH. To determine the effect of contact time, 0.1 g adsorbent was added to a 150 ppm MG solution at the pH: 6

for 15, 30, 45, 60, 75, 90 and 120 min. Adsorption isotherm was performed by shaking different initial dye concentration (30-200 mgL^{-1}) with the fixed adsorbent amount (0.1 g) until equilibrium. Adsorption kinetics were determined by analyzing dye removal at different time intervals (15-120 min).

The percentage of dye adsorption and the amount of dye uptake at the equilibrium time were calculated using Eq. (3) and Eq. (4).

$$\% \ Dye \ Adsorption = \frac{c_0 - c_e}{c_o} \times 100 \tag{3}$$

$$q_e = \frac{c_0 - c_e}{W} \times V \tag{4}$$

c_0: the initial dye concentration (mgL^{-1}), c_e: the equilibrium dye concentration (mgL^{-1}), q_e: the adsorbed dye per gram of adsorbent at equilibrium time (mgg^{-1}), V: the dye solution volume (L) and W: the adsorbent mass (g). All experiments were carried out in triplicates and the results were used in data analysis.

Adsorption isotherms

Adsorption isotherms describe interactions between adsorbates and adsorbents. Isotherm models for the single component systems that express the adsorption isotherms mathematically are Langmuir, Freundlich, Redlich-Peterson, BET, Tempkin and Koble-Corrigan [34,35]. There are also multicomponent isotherm models derived from these single component system isotherms. Multicomponent isotherm models are also used for the adsorption of wastewater containing multiple pollutants [31,36]. The data obtained from these isotherm models provide important information about the adsorption mechanisms and the surface activities of the adsorbent.

The Langmuir isotherm model assumes that the surface is homogenous and covered by a monolayer of adsorbate. The linear Langmuir equation is as follows;

$$\frac{1}{q_e} = \frac{1}{q_{max}} + \left(\frac{1}{q_{max} K_L}\right) \frac{1}{C_e} \tag{5}$$

c_e: equilibrium dye concentration (mgL^{-1}), q_e: adsorption capacity at equilibrium (mgg^{-1}), q_{max}: maximum adsorption capacity (mgg^{-1}) and K_L: the Langmuir constant (Lmg^{-1}).

The $1/q_e$ versus $1/c_e$ give straight line. The value of q_{max} and K_L were calculated from the slope and intercept of this plot [37] and are exhibited in Table 3.

The Freundlich isotherm equation is as follows;

$$\ln q_e = \ln K_F + \frac{1}{n}\ln c_e \qquad (6)$$

K_F: the Freundlich constant, n: the heterogeneity factor related to the adsorption intensity (mgL^{-1}).

Adsorption kinetics

Two adsorption kinetic models, pseudo-first order and second-order models have been carried out to explain the adsorption kinetics.

The Lagergren pseudo-first order rate expression can be given as;

$$\ln(q_e - q_t) = \ln q_e - k_1 t \qquad (7)$$

q_e and q_t: the amount of dye uptake at equilibrium and at time t (mgg^{-1}), respectively, and k_1: rate constant of adsorption (min^{-1}). It is calculated k_1(slope) and intercepts ($\ln q_e$) from the linear plots of $\ln(q_e-q_t)$ versus t.

The pseudo-second order kinetic model is shown in Eq. 8. k_2: the rate constant of adsorption (gmg^{-1}min^{-1}), q_e and q_t: the amount of dye uptake (mgg^{-1}) at equilibrium and at time t (mgg^{-1}), respectively. k_2 and q_{cale} were calculated from the intercepts ($1/k_2q_e^2$) and slopes ($1/q_e$) of the plots of t/qt vs. t [31], respectively, and are presented in Table 4.

$$\frac{1}{q_t} = \frac{1}{k_2 q_e^2} + \frac{t}{q_e} \qquad (8)$$

Optimization of adsorption conditions by RSM

Design of experiments

The outcomes of the experiments conducted to reveal the impacts of temperature, pH and initial dye concentration on MG adsorption yields of *U. dioica* were given in Table 5. These parameters were analyzed at 3 levels [-1 (low), 0 (medium), +1 (high)] for the optimization of adsorption yield. The limits of these independent variables were 25–55 °C for temperature, 2–8 for pH and 40–200 mgL^{-1} for initial dye concentration. Adsorption assays were performed in 100 mL Erlenmeyer flasks containing 50 mL of dye solution. The statistical and graphical software Minitab® Version 17 (State College, PA) was utilized for the experimental design and analysis of RSM.

In regression analysis, the confidence level is 95% and significance level alpha (α) is considered as 0.05. A p (probability) value less than α (typically ≤ 0.05) is regarded as statistically significant.

Table 5. BBD of parameters (temperature, pH, and initial dye concentration) and experimental responses (adsorption) using RSM

Run	Variables			Response
	A (Temperature, °C)	B (pH)	C (Dye, mgL^{-1})	Y (Adsorption, %)
1	55	5	40	75.66
2	25	5	40	66.63
3	40	2	40	22.00
4	25	8	120	81.68
5	40	5	120	82.96
6	55	5	200	90.07
7	25	5	40	75.46
8	25	5	200	82.71
9	40	5	120	84.46
10	40	2	200	18.83
11	25	5	200	79.76
12	55	5	40	77.86
13	55	8	120	82.60
14	40	5	120	83.11
15	55	2	120	26.55
16	40	8	40	63.08
17	55	5	200	89.47
18	25	2	120	26.80
19	40	8	40	63.08
20	40	5	120	82.96
21	40	2	200	29.30
22	25	8	120	74.08
23	40	5	120	84.99
24	25	2	120	23.02
25	40	8	200	83.33
26	40	5	120	85.06
27	40	8	200	85.59
28	55	2	120	30.00
29	55	8	120	83.43
30	40	2	40	21.25

ACKNOWLEDGMENTS

REFERENCES

1. V.K. Garg; R. Kumar; R. Gupta; *Dyes Pigm.*, **2004**, *62*, 1–10.
2. N. Gupta; A.K. Kushwaha; M.C. Chattopadhyaya; *J. Chem. Pharm. Res.*, **2011**, *3*, 284–296.
3. A. Raducan; A. Olteanu; M. Puiu; D. Oancea; *Cent. Eur. J. Chem.*, **2008**, *6*, 89–92.
4. E. Sudova; J. Machova; Z. Svobodova; *Vet. Med.*, **2007**, *52*, 527-539.
5. U.U. Tezcan; F. Ates; N. Erginel; O. Ozcan; E. Oduncu; *J. Environ. Manag.*, **2015**, *15*, 89–96.
6. D.J. Alderman; R.S. Clifton-Hadley; *J. Fish Dis.*, **1993**, *16*, 297–311.
7. A.S. Sartape; A.M. Mandhare; V.V. Jadhav; P.D. Raut; M.A. Anuse; S. S. Kolekar; *Arab. J. Chem.*, **2017**, *10*, 3229–3238.
8. W.C. Andersen; S.B. Turnipseed; J.E. Roybal; *J. Agric. Food Chem.*, **2006**, *54*, 4517–4523.
9. M. Dastkhoon; M. Ghaedi; A. Asfaram; MH.A. Azqhandi; M.K.A. Purkait; *Chem. Eng. Res. Des.*, **2017**, *124*, 222–237.
10. S. Ben-Ali; I. Jaouali; S. Souissi-Najar; A. Ouederni; *J. Clean. Prod.*, **2017**, *142*, 3809–3821.
11. V.K. Gupta; C.K. Jain; S. Chandra; S. Agarwal; *Water Res.,* **2002**, *36*, 2483–2490.
12. S.M. Bowman; S.J. Free; *Bioassays*, **2006**, *28*, 799–808.
13. MR. Fathi; A. Asfaram; A. Farhangi; *Spectrochim Acta A Mol Biomol. Spectrosc.*, **2015**, *135*, 364–372.
14. I.A.V. Tan; B.H. Hameed; A.L. Ahmad; *Chem. Eng. J.*, 2007, *127*, 111–119.
15. A. Mittal; L. Krishnan; V.K. Gupta; *Sep. Purif. Technol.*, **2005**, *43*, 125–133.
16. R. Gong; K. Zhong; Y. Hu; J. Chen; G. Zhu; *J. Environ. Manage.*, **2008**, *88*, 875–880.
17. R. Jain; M. Mathur; S. Sikarwar; A. Mittal; *J. Environ. Manage.*, **2006**, *85*, 956–964.
18. A.S. Ozcan; S. Tetik; A. Ozcan; *Sep. Sci. Technol.*, **2004**, *39*, 301–320.
19. T. Baytop; *Therapy with Plant in Turkey*, Istanbul University, Faculty of Pharmacy (2nd press), Nobel Medicine Bookstores; Istanbul, Turkey, **1989**.
20. K.K. Mueen Ahmed; S. Parsuraman; *Sys. Rev. Pharm.*, **2014**, *5*, 6–8.
21. I. Gülçin; O.I. Küfrevioglu; M. Oktay; M. E. Büyükokuoglu; *J. Ethnopharmacol.*, **2004**, *90*, 205–215.
22. J. Viktorova; Z. Jandova; M. Madlenakova; P. Prouzova; V. Bartunek; B. Vrchotova; P. Lovecka; L. Musilova; T. Macek; *Plos One*, **2016**, *12*, 1–12.
23. S. Hoşbaş; M. Aslan; E. Sezik; *Turk. J. Pharm. Sci.*, **2014**, *11*, 223–230.

24. N. Di Virgilioa; E.G. Papazogloub; Z. Jankauskienec; S. Di Lonardod; M. Praczyke; K. Wielgusze; *Ind. Crops Prod*., **2015**, *68*, 42–49.
25. V.D. Dimitrijević; M.N. Stanković; D.M. Đorđević; I.M. Krstić; M.G. Nikoli;, A. L.J. Bojić; N. S. Krstić; *Studia UBB Chemia*, **2019**, 1, 19-39
26. G.E.P. Box; D.W. Behnken; *Technometrics*, **1960**, *2*, 455–475.
27. S. Gurkok; D. Cekmecelioglu; Z.B. Ogel; *Bioresour. Technol*., **2011**, *102*, 4925–4929.
28. M. Ozdal; S. Gurkok; O.G. Ozdal; *3 Biotech*., **2017**, *7*, 117.
29. Y. Sağ; T. Kutsal; *Process Biochem*., **1997**, *32*, 591–597.
30. B. Ertan; D. Efe; D; *Adsorption properties of U. dioica on colour removal of Malachite Green*, In:1 st international technological sciences and design symposium, Giresun, Turkey, **27-29 June 2018**, pp. 107–115.
31. D.O. Hayward; B.M.W. Trapnell; W. Garden; *Chemisorption*, Butterworths, London, **1964**, pp. 67–159.
32. S. Lagergren; *Zurtheorie der sogenannten adsorption gelosterstoffe*, Kungliga Svenska Vetenskaps akademiens, Handlingar, **1898**, pp. 1–39.
33. Y.S. Ho; G. McKay; *Process Saf. Environ. Prot*., **1998**, *76*, 183–191.
34. H.M.F. Freundlich; *Uber die adsorption in Losungen*. In: Zeitschrift fur Physikalische Chemie, Leipzig, **1906**, pp. 385-470.
35. I. Langmuir; *J. Am. Chem. Soc*., **1918**, *40*, 1361–1403.
36. Y. Tian; C. Ji; M. Zhao; *Chem. Eng. J*., **2010**, *165*, 474–481.
37. Z. Aksu; H. Gülen; *Process Biochem*., **2002**, *38*, 161–173.

COMPARATIVE STUDIES BETWEEN ALUM SYNTHESIZED FROM ALUMINUM CANS AND NATURAL COAGULANT SYNTHESIZED FROM WATERMELON SEED

MUHAMMAD SULAIMAN RAHAMA[a]*, AHMED LAWAL MASHI[a] and ABUBAKAR SANI MUHAMMAD[a]

ABSTRACT. This study focused on the comparative analyses between the alum synthesized from aluminum can and natural coagulant synthesized from watermelon seed in water treatment. It also involved the identification of phytochemical groups of watermelon seed cake. The two different synthesized coagulants were used in jar test analysis; the result obtained showed a good elimination of turbidity and suspended solid particles. The pH of the natural coagulant of the treated water falls within the range of 6.9 to 7.2. Alkaloid tannins, saponin, anthracene and flavonoid were found present in the watermelon seed cake. Moreover, the result from the research showed that both the natural coagulant synthesized from watermelon seed and the one synthesized from aluminum cans could be used as good flocculant in surface water treatment.

Keywords: Watermelon seed cake, Alum, Aluminum can, Coagulation, Phytochemical

INTRODUCTION

Natural coagulants have been increasingly popular in the past few years due to its benefits and the fact that it resolves most of the associated problems when using chemical coagulants. Plant-based natural coagulants perform coagulation either by polymer bridging or charge neutralization; it can be extracted from various plant components. Coagulation and flocculation processes are widely used in water and wastewater treatment. Its main objective is to remove suspended colloidal particles and to reduce turbidity in water body [1]. The process usually takes place in a chemical reactor in which

---

[a] *Umaru Musa Yaradua University, Faculty of Natural and Applied Sciences, Department of Pure and Industrial Chemistry, Katsina, Nigeria*
* *Corresponding author: muhammad.sulaimanr@umyu.edu.ng*

the influent water or wastewater enter the basin and it is mixed with coagulant agents using a mechanical mixer, followed by sedimentation process to remove the particulate through gravity settling [2]. There are many types of coagulants available. The most often used are the chemical-based coagulants such as alum and ferric salts [3].

A number of studies have pointed out that the introduction of natural coagulants as a substitute for metal salts may ease the problems associated with chemical coagulants. Using natural coagulants instead of aluminium salts might give advantages, such as lower costs of water production, less sludge production and ready availability of reagents. There are also some disadvantages such as increased concentration of nutrients and chemical oxygen demand (COD) in the treated water due to the organic nature of this type of coagulants [4]. Among plant materials that have been tested over the years, the seeds from *Moringa oleifera* have been shown to be one of the most effective primary coagulant in water treatment or purification. *Moringa oleifera* is the best natural coagulant discovered so far that can replace aluminium sulphate (alum), which is used widely for water treatment around the world [5]. Coagulants are formulated to assist in the solids/liquid separation of suspended particles in a solution. Such particles are characteristically very small and the suspended stability of such particles (colloidal complex) is due to both their small size and to the electrical charge between particles [6],[7].

Recently, however, there has been a resurgence of interest in natural coagulants for water treatment in developing countries. For this purpose the greatest degree of attention has been focused on the seed of *Moringa oleifera* from Sudan, Nirmali seed in India, mesquite bean and in Venezuela, red bean and common bean, sweet corn and so on. These natural coagulants can be used alone or as a substitution for chemical coagulants and flocculants. They can be used for reducing turbidity and microorganisms in water, for water softening and for dewatering sludge [8]. Some of the plants are able to be a coagulant because they are able to conduct some of the coagulation mechanisms which are neutralizing the charge in colloidal particles and perform polymer bridging [9].

Watermelons (*Citrullus Lanatus*) are a popular seasonal plant in the sub-Sahara and their seeds can be used as effective water purifiers because of their adsorbent properties like most indigenous seeds [10].

Water supply is a basic need required for living creatures and human being specifically. Developing countries and third world countries are facing potable water supply problems because of inadequate financial resources. The cost of water treatment is increasing and the quality of river water is not stable due to suspended and colloidal particle load caused by land development and high storm runoff during the rainy seasons [11]. During the rainy seasons

the turbidity level increases and the need for water treatment chemicals increase as well, which leads to high cost of treatment which the water treatment companies cannot sustain. As a result, the drinking water that reaches the consumer is not properly treated [5].

Aluminum is one of the most important metals used by modern societies. The combination of the physical properties of aluminium results in its use in a wide variety of products, many of which are indispensable to modern life [12].

In this study, instead of recycling aluminum in to new metal cans, a chemical process will be used to transform the scrap aluminum into a useful chemical compound, potassium aluminum sulfate dodecahydrate, $KAl(SO_4)_2 \cdot 12H_2O$, commonly called "alum", then its properties will be compared with a natural coagulant that will be synthesized from watermelon seed; likewise, their effect in water treatment.

RESULTS AND DISCUSSION

The results of the jar test analysis of the synthesized alum and watermelon seed are highlighted below, likewise phytochemical screening of the watermelon seed and the qualitative analysis of the synthesized alum are shown below.

Table 1. Results of jar test analysis of the synthetic alum

Mass of Synthetic Alum (g)	pH	Turbidity (NTU)	TDS (mg/L)	Colour (Hazen)
0.5	6.6	5.6	44	5
1.0	6.4	4.9	44	5
1.5	6.2	4.3	41	5
2.0	5.9	3.1	38	5
2.5	5.8	2.9	36	5
3.0	5.3	2.3	36	5
WHO standard	6.5-8.5	5 max.	500	15 max.
Raw water	7.8	734.60	325.0	73.0

Table 1 above showed the results for jar test analysis using synthetic alum crystals. The values of pH, turbidity, TDS and color were analyzed and recorded. The results indicated that the values of the pH at varying alum dosage kept increasing to acidic level insignificantly. However, the turbidity also decreases from 5.6 NTU at 0.5 g to 2.3 NTU at 3.0 g alum dosages.

These observations were in accordance with previous studies on coagulation ability of recycled aluminum cans as reported by Birnin-Yauri and Musa [13]. The results for the TDS were also recorded; there is decrease in the TDS values as the concentration of alum dose increases. The secondary standard value for the TDS of drinking water by WHO is 500 mg/L, therefore, the synthetic alum powder has the potential to reduce TDS.

Table 2. Results of jar test analysis of the watermelon seed cake

Watermelon seed cake (g)	pH	Turbidity (NTU)	TDS (mg/L)	Colour (Hazen)
0.5	6.9	28.3	83	15
1.0	6.9	30.1	83	15
1.5	7.0	32.6	79	10
2.0	7.1	33.2	76	10
2.5	7.1	35.5	75	5
3.0	7.2	37.2	75	5
WHO standard	6.5-8.5	5 max	500	15 max
Raw water	7.8	734.60	325.0	73.0

Table 2 above showed the results for jar test analysis using watermelon seed cake. The values for pH, turbidity, TDS and colour were analysed and recorded. The use of watermelon seed cake as a coagulant to treat water resulted in portable water that met the World Health Organisation (WHO) standards for portable water [14]. The results indicated that the results of pH showed insignificant decrease as the mass of the watermelon seed cake increases. This was observed at 0.5 g of the seeds powder where 6.9 were recorded as pH value and 3.0 g of the seed powder where 7.2 was recorded as pH value. This observation was in accordance with previous studies on watermelon seed cake as reported by Muhammad *et al.,* [11]. The values of the turbidity observed indicated that the watermelon seed cake is somehow effective in the removal of turbidity. The greatest decrease was seen at the dose of 0.5 g/L of raw water which had a turbidity of 28.3 NTU. This value is still above the WHO recommended level of 5 NTU. However, according to Muhammad et al., [11] the optimal dosage for a specific water is defined as the dosage which gives the lowest turbidity in the treated water therefore the optimum dosage is 0.5 g/L. The results for the TDS were also recorded; there is decrease in the TDS values as the concentration of the watermelon seed cake increases. The secondary standard value for the TDS of drinking water by WHO is 500 mg/L, therefore, the watermelon seed cake has the potential to reduce TDS.

Table 3. Results of phytochemical screening of the watermelon seed

S/NO	PHYTOCHEMICALS	COMFIRMATION
1.	Alkaloid	+
2.	Tannins	+
3.	Saponin	+
4.	Anthracene	+
5.	Flavonoids	+

Key:
+ Presence
_ Absence

Table 3 presents the phytochemical analysis of the extracted watermelon seed cake. The extracted seed found to contain the following; component: Alkaloid, Tanins, Saponin, Anthracene and flavonoids.

Table 4. Results of qualitative analysis of the synthesized alum

Test	Observation	Inference
Alum solution + Aqueous $BaCl_2$ Solution	White Precipitate formed, and insoluble (After 20 hours)	SO_4^{2-} Confirmed
Solid Alum Crystal+ heat (10 minutes)	Red flame turned to Pale purple flame color	K^+ Confirmed
Alum Solution + H_2SO_4(aq) in drop and in Excess	Thick, white gelatinous precipitate formed insoluble in drop but soluble in excess	Al^{3+} Confirmed

Table 4 presents the qualitative analysis of the synthesized alum crystals, the aluminum, potassium and sulfate ions were positively tested as expected. This is an indication that the synthesized alum crystal possesses all necessary chemical properties expected of any alum crystal. This was also contained in the research made by Birnin-Yauri and Musa [13].

CONCLUSIONS

From the results obtained in this research, it shows that the use of natural coagulant in water treatment is more effective than the chemical coagulants in terms of pH, because the natural coagulant has a pH that is neither acidic nor basic, hence neutral which falls within the range of 6.9 to 7.2, but in terms of turbidity and TDS, the chemical coagulant is more effective than the natural coagulant, it can be concluded that the watermelon seed can be used as natural coagulant for water treatment.

EXPERIMENTAL SECTION

Procedure for the synthesis of alum from aluminum can

The method of Birni-Yauri and Musa [13] was adopted for the synthesis of the alum. Empty aluminum cans were obtained and brought in to the lab, sand paper was used to scrape off paint and plastic coating from both sides as completely as possible. It was then cut at approximately 5 cm x 7.5 cm by the use of scissor. 1.0g of aluminum pieces was weighted and put into 250 cm^3 beaker. 50 cm^3 of 1.4M potassium hydroxide was added to the 250 cm^3 beaker containing the aluminum pieces. The beaker was then placed on a hotplate, in a fume hood and heated. Bubbles of hydrogen formed from the reaction between aluminum and aqueous potassium hydroxide was observed. The reaction was complete as the hydrogen evolution ceases and there were no visible pieces of aluminum metal. While the reaction was taking place, the initial colorless mixture turns to black. The hot solution was filtered to remove solid residue and black substances in the solution. The clear filtrate solution was transferred into a clean 250 cm^3 beaker. As the solution is cooled, 20 cm^3 of 9.0M H$_2$SO$_4$ was added to the solution and stirred gently, the final solution contained potassium ions (from the KOH used), aluminum ions, and sulfate ions. The solution was also filtered using filter paper. An ice water bath was prepared and the beaker containing the solution was placed in to the ice water bath and the mixture was allowed to chill. Cold water was added to cover the ice. The reaction beaker was set into the ice-water bath to chill for about 20 minutes. Crystals of the alum began to form in few minutes. The alum crystal formed was filtered from the chilled solution.

Synthesis of coagulant from watermelon seed

Fresh seed of watermelon were obtained, the seed were washed severally with water and it was allowed to dry for about one week, the dried seed were sorted and the bad ones were removed, it was then ground to powder. 150g of the powdered watermelon seed were weighed and placed in a thimble, 500 cm^3 of n-hexane was added, the thimble was then placed in a soxhlet extractor, it was then allowed to stand for 6hrs, the set up was stopped as the extraction was completed. The powdered seed were washed with distilled water to remove the residual n-hexane, the residue was then dried in an oven till constant weight was obtained. The finer particle finally obtained was termed as coagulant [11].

Procedure of Jar Test Analysis

The procedure of Katsina State Water Board manual for water treatment and analyses, 2019 was used. The jar test machine was switched on and set at low speed. The raw water sample was put in 6 different beakers of 1000 cm^3, where different grams of 0.5g, 1g, 1.5g, 2g, 2.5g and 3g were used for the synthesized alum. The raw water sample was then added to make up the 1000 cm^3 mark and the jars were then placed in the jar test kit and the stirrers lowered into each. The speed of the jar test machine was then set at 400rpm for 10 minutes; which was later set at low speed again. This is to allow the merging of the smaller flocs formed to larger one. The procedure was repeated for watermelon seed cake.

Determination of pH

The 2 water samples (100 cm^3 each) were transferred into a clean dried glass beaker, then the electrodes of standardized pH meter was immersed and the meter was allowed to standardized, after which the reading was taken. The electrode was rinsed well with distilled water and tabbed slightly with tissue paper after each test as described by Geotechnical Engineering Bureau, 2007.

Determination of Turbidity

The 2 samples of the water were transferred into the sample cell turbidity meter up to the horizontal mark, then wiped with tissue paper and subsequently placed in the turbidity meter such that the vertical mark in the sample cell coincide with the mark in the turbidity meter, after which it was covered. The readings displayed on the screen and were recorded, as described by Manual of Water Treatment and Analysis, Katsina State Water Board, 2009.

Determination of TDS

The TDS of the samples were analyzed using TDS meter. The samples were put in a clean beakers and the head of the TDS meter was immersed in the beakers. Readings were taken for each sample separately, as described by Manual of Water Treatment and Analysis, Katsina State Water Board 2009.

Determination of Color

The color of the 2 water samples was analyzed using comparator and Disc, where the samples were put in different tubes of 10 cm^3, and then inserted in the hole of the comparator. The disc was then scroll until a suitable

and matching color was observed for each sample. The reading of the corresponding color for each was recorded, as described by Manual of Water Treatment and Analysis, Katsina State Water Board 2009.

Procedure for the phytochemical analysis

Alkaloid: 1 cm^3 of the extract was stirred with 5 cm^3 of 10% aqueous hydrochloric acid on a steam bath for 20 minutes, cooled and filtered. 1 cm^3 of the filtrate was treated with few drops of Mayer's reagent. A creamy precipitate was observed which indicated the presence of alkaloids [15].

Tannins: 3 cm^3 of the diluted extract was pipetted into a clean test tube; ferric acid chloride solution was added dropwise into the extract. Blue black colouration was observed which indicated the presence of tannin [16].

Saponins: 5 cm^3 of the diluted extract was pipetted into a clean test tube and corked with cotton wool and shaken for about 3 minutes. Persistent froth was o0bserved which indicated the presence of saponin [16].

Anthracene: 4 cm^3 of the diluted extract was pipetted into a clean test tube; equal volume of chloroform was added and shaken. The mixture was allowed to separate into two layers. The chloroform layer was collected and 1 cm^3 of 10% ammonia solution was added and shaken, a brick red precipitate was observed which indicated the presence of anthracene [16].

Flavonoids: 3 cm^3 of the exract was placed in a test tube, 3 cm^3 of 0.1M HCl was added, 0.5 cm^3 0f 0.5M NaCl was added. A yellow colour was observed which indicated the presence of flavonoids [16],[17].

ACKNOWLEDGMENTS

REFERENCES

1. S.Y. Choy; K.M.N. Prasad; T.Y. Wu; M.E Raghunandan; R.N. Ramanan; *Journal of Env. Sci.,* **2014**, *26***,** 2178–2189.
2. M.J. Hammer; Jr. M.J. Hammer; *Int. J. App. Env. Sci.,* **2004**, *3*, 469-487.
3. I.N. Fathinatu; R. Nithyanandam; *Int. J. Eng. &Tech.,* **2014**, *7*, 34-37.
4. Y.S. Daniyan; A.M. Enemaduku; E.O. Eru; *Int. J. Res. in Ayurveda & pharm.,* **2011**, *2*, 1265-1270.

5. S.A. Muyibi; E.N. Ali; H.M. Salleh; *Thirteenth Int. Water Tech. Conf.,* **2009**, *13*, 1-10.

6. C. Deepika; S. Dipak; P. Anjani; *Eur. Chem. Bull.,* **2013,** *2*, 880-886.

7. E.S. Salem; J. Bakir; M.E. Ahmed; A.E. Ahmed; *Int. J. Eng. App. Sci.*, **2014**, *1*, 19-24.

8. A.G. Mirjana; S. Marina; P. Nada; *Bioresource tech.,* **2010**, *10*, 2167-2172.

9. H. Kristiano; *J. of Water Cons. of Sci. and Eng.,* **2017**, *2*, 51–60.

10. S. Malunjkar; K.R. Ambekar; *Int. J. of Eng. and Tech. Res.*, **2015**, *3*, 263-266.

11. I.M. Muhammad; S. Abdulsalam; A. Abdulkarim; A.A. Bello; *Global J. of Res. in Eng.: Chem. Eng.,* **2015**, *15*, 17-24.

12. A.L. Adejumo; R.U. Owolabi; S.A. Adebisi; W.A. Agbaje; M.A. Usman; *J. Eng. App. Sci.,* **2016**, 3, 8-13.

13. A.U Birnin-Yauri; A. Musa; *Int. J. of Adv. Res. in Chem. Sci., (IJARCS)* **2014**, *1*, 1-6.

14. M.M. Musaida; C. Tawanda; *Int. Conf. on P. and App. Chem., ICPAC: Emerging Trends in Chemical Sciences*. **2016**, *1*, 1-6.

15. E.A. Sofowora; *Medical plants and Traditional plants in Africa*; John Willey and Sons, New York; **1982**, Pp 1-20.

16. M.M. El-olemy; F.J. Al-muhtadi; A.A. Afifi; *Experimental phytochemistry: A laboratory manual,* King Fahad University Press; Saudi Arabia, **1994**, pp. 3-19.

17. J.B. Harbone, Examination of Flavonoid Aglycones in Hydrolysed Plant Extracts, in *Phytochemical methods*, Chapman and Hall, London: **1973**, pp. 1-32.

SYNTHESIS AND MESOMORPHIC PROPERTIES OF NEW ROD-LIKE HETEROCYCLIC LIQUID CRYSTALS

KOK-LEEI FOO[a], SIE-TIONG HA[a,*], GUAN-YEOW YEAP[b] and HONG-CHEU LIN[c]

ABSTRACT. Structure-property relationship is one of the most important research areas in the liquid crystals. Therefore, in the present work, we studied a new series of rod-like heterocyclic liquid crystals, 6-methyl-2-[4-(4-alkoxybenzoyloxy)benzylideneamino]benzothiazoles. The rod-like molecules having heterocyclic and two phenyl rings as core system, imine and ester as linking units, long alkoxy chain at the terminal position. There are six members in the series with different length of alkoxy chain ($C_nH_{2n+1}O-$, where n = 6, 8, 10, 12, 14, 16). The structures of the compounds were elucidated using spectroscopic techniques. Their mesomorphic behaviours were determined by differential scanning calorimetry, polarizing optical microscopic and powder X-ray diffraction techniques. Members with shorter alkoxy chain (n = 6, 8, 10) exhibited single mesophase (nematic). As the alkoxy chain increased to n = 12, 14, 16, the nematic phase appeared together with an additional mesophase (smectic). The phase width was dependent on the alkoxy chain length. The incorporation of the methyl substituent at the sixth position (lateral) of the benzothiazole able to increase the clearing point and widen the mesophase width of the compounds.

Keywords: benzothiazole, Schiff base, nematic, smectic A

INTRODUCTION

Heterocyclic-based liquid crystal (LC) is of current interest due to its potential applications as photoconductive materials, fluorescent compounds and thin-film organic-field-effect transistors [1-4]. Earlier work on rod-like or

---

[a] *Faculty of Science, Universiti Tunku Abdul Rahman, Jln Universiti, Bandar Barat, 31900 Kampar, Perak, Malaysia.*

[b] *Liquid Crystal Research Laboratory, School of Chemical Sciences, Universiti Sains Malaysia, 11800 Minden, Penang, Malaysia.*

[c] *Department of Materials Science & Engineering, National Chiao Tung University, 1001 Ta-Hsueh Road, Hsinchu 300, Taiwan, ROC.*

* *Corresponding author: hast_utar@yahoo.com, hast@utar.edu.my*

calamitic LCs has been focused on low-molar mass liquid crystals possessing only phenyl rings and the current trend is shifted to the phenyl structures with inclusion of heterocycles. This is not only due to the better potential with heterocycles for the formation of new mesogens, but also because the addition of heteretoatoms strongly affects the mesophase formation [5-7]. The presence of heteroatoms (S, O and N) can greatly alter the polarity, polarizability and sometimes the geometric shape of the molecule, thus controlling the type of mesophase, phase transition temperatures, dielectric and other properties of the mesogenic molecules [8]. A few examples of heterocyclic rings used as a core system include benzothiazole [9], 1,3,4-thiadiazole [10,11] and pyridine [12-14].

Mesomorphic behavior can be varied by modifying its molecular structure including linking, terminal and core groups. Imine (or Schiff base), a linking group is usually incorporated into the molecular structure to increase the length and polarisability anisotropy of the molecular core in order to enhance the phase stability [15]. Other linking groups such as ester [16-20], cinnamate [21-23], or chalcone [24] which was incorporated together with the imine linker has received much attentions owing to interesting properties and substantial temperature range.
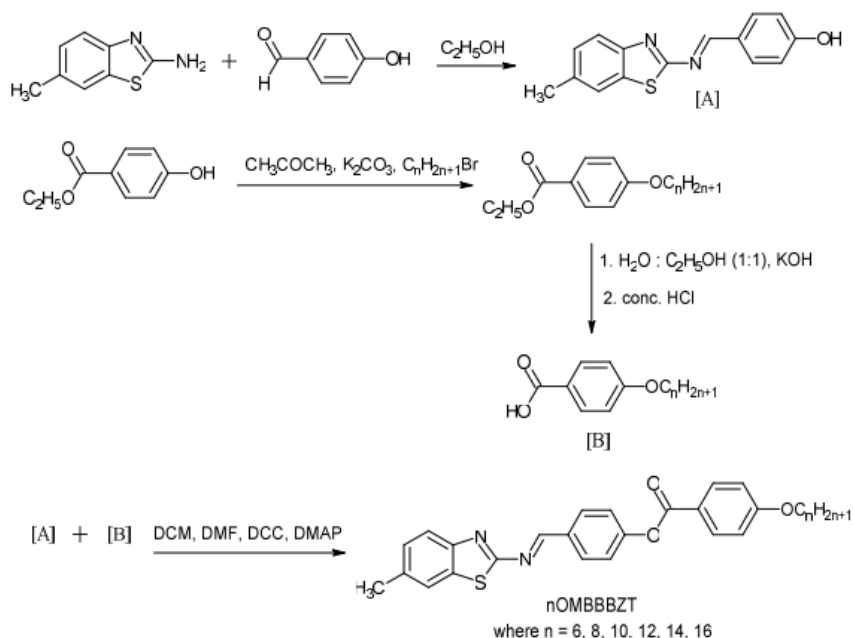
Scheme 1. Synthetic of heterocyclic liquid crystals, nOMBBBZT. Yield: n = 6 (40%), n = 8 (46%), n = 10 (51%), n = 12 (46%), n = 14 (59%), n = 16 (63%).

In this paper, we report another new homologous series of heterocyclic benzothiazole-imine-ester based liquid crystals (Scheme 1). The current structure is closely related to the structures (compounds **D** and **E** in Table 3) reported in our previous works [25,26]. Structure modification at the benzothiazole ring with the incorporation of a methyl substituent in the current compound can increase the clearing point and nematic phase width of the compounds. Although it is a minor modification in its molecular geometry, it has brought significant changes to its mesomorphic properties.

RESULTS AND DISCUSSION

EI-MS Data

EI-MS analysis were carried out on two representative compounds, 12OMBBBZT and 16OMBBBZT. The prominent molecular ion peaks at m/z 556.4 (Fig. 1a) and 612.4 (Fig. 1b) established its molecular formula as $C_{34}H_{40}N_2O_3S$ and $C_{38}H_{48}N_2O_3S$ supporting the proposed structure of 12OMBBBZT and 16OMBBBZT, respectively. Both compounds showed base peak of phenyl acylium ion at m/z 289.2 and 345.3, respectively.
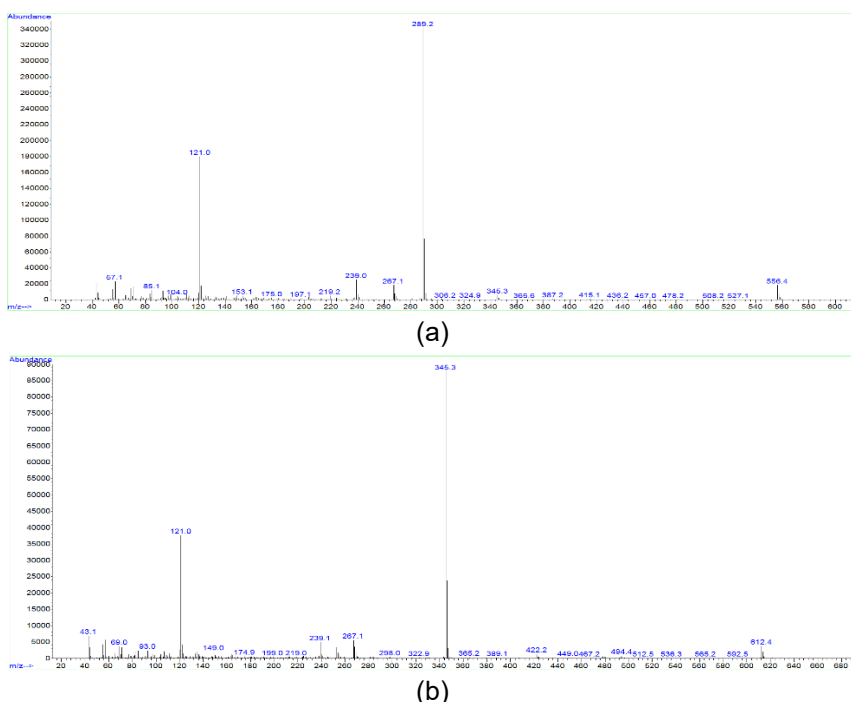

(a)

(b)

Figure 1. EI mass spectra of (a) 12OMBBBZT and (b) 16OMBBBZT.

IR and NMR Spectral Data

Based on FT-IR spectral data of 14OMBBBZT, the presence of two strong peaks at the frequencies of 2921 and 2851 cm^{-1} can be attributed to the long alkoxy groups. This indicates that the terminal phenolic hydroxy group (-OH) attached at one end of the intermediate was replaced by terminal alkoxy chain (-OC$_n$H$_{2n+1}$). The presence of C=N bond of imine is confirmed based on the band with strong intensity at 1601 cm^{-1}. This absorption band is overlapped with the band arising from the C=N of the benzothiazole ring, therefore, it resulted in a sharp and strong absorption band [27]. Aromatic C=C functional group showed its band at 1576 cm^{-1} with medium intensity. Another strong absorption band at 1726 cm^{-1} is ascribed to the ester functional group that connected between two aromatic rings. Band due to the stretching of ether, C-O-C bond can be found as strong band at 1252 cm^{-1}.
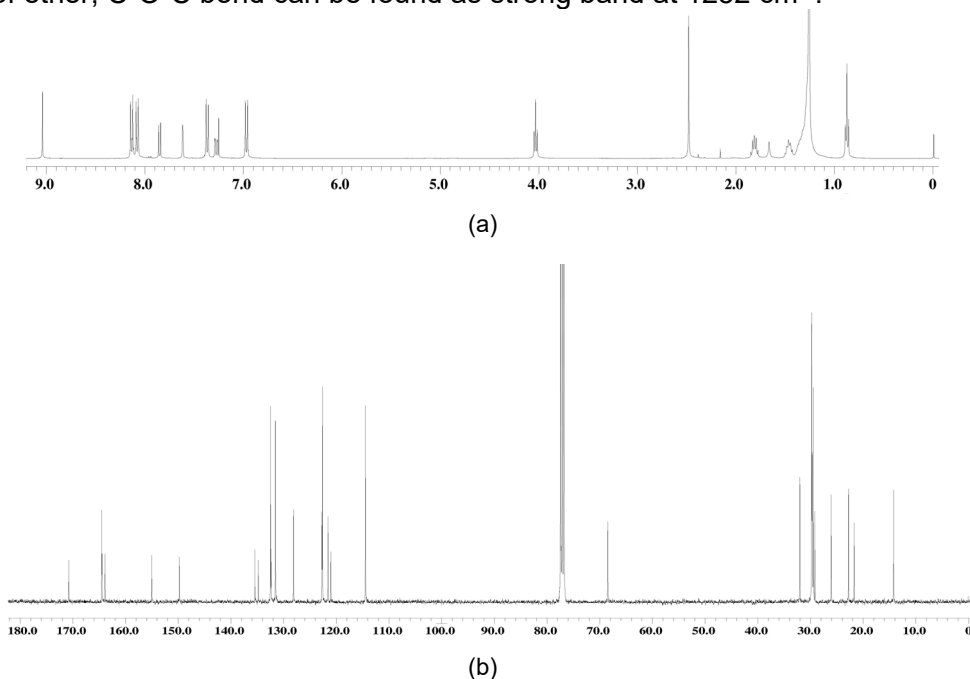

(a)

(b)

Figure 2. ^{1}H NMR (a) and ^{13}C NMR (b) spectra of 14OMBBBZT.

In the ^{1}H NMR spectrum (Fig. 2a) of 14OMBBBZT, two triplets at δ 0.88 and δ 4.03, were respectively belonged to the methyl (C$\underline{H}_3$) protons and methylene protons that directly bonded to oxygen atom (-C$\underline{H}_2$O-Ar). Another methylene protons (-CH$_2$-C$\underline{H}_2$-CH$_2$-O-) showed its presence as quintet signal at δ 1.81. Balance of protons of the long alkoxy chain showed multiplet signal

at chemical shifts range of 1.26-1.50 ppm. A singlet signal at δ 2.48 is belonged to the methyl group that attached to the aromatic ring. Four doublet signals with each integration of two protons appeared at δ 6.97, 7.37, 8.09 and 8.14 were assigned to the two *para*-substituted aromatic rings. Three protons at the benzene ring that fused to thiazole ring showed three distinct signals at δ 7.28, 7.62 and 7.85 with doublet, singlet and doublet splittings, respectively. A singlet signal at the most downfield region, δ 9.04, confirmed the presence of the imine linking group [28].

The molecular structure of 14OMBBBZT was further verified by using ^{13}C NMR spectroscopy (Fig. 2b). The peak at δ 14.25 was belonged to the methyl carbon of the alkoxy chain while the peaks between δ 22.80-68.48 was assigned to the methylene carbons of the long alkoxy chain. The methyl carbon that attached to the benzene ring is appeared at δ 21.72. Fourteen aromatic carbons are resonated between δ 114.49 and 163.90. The presence of C=N of thiazole and C=N of azomethine groups are confirmed based on the peaks appeared at δ 164.47 and 164.53. Another important signal resonated at δ 170.78 is belonged to the C=O of ester.

Mesomorphic Properties

The mesophases of the compounds were identified using an polarizing optical microscope during heating cycle. The optical photomicrographs of 8OMBBBZT and 16OMBBBZT are shown in Fig. 3 as representative illustrations. Observation of 8OMBBBZT upon heating it from its crystal phase, showed the presence of single mesophase. The droplets texture (Fig. 3a) is identified as nematic phase. As for 16OMBBBZT, it exhibited two types of mesophases. On heating, fan-shaped texture of smectic A (SmA) phase (Fig. 3b) was first observed. The SmA phase has been identified based on the optical textures in which regions of fan-shaped and homeotropic (dark area) textures coexist [29]. On further heating of 16OMBBBZT, it turned into nematic phase with Schlieren texture (Fig. 3c) on further heating. All observed textures are typical according to the literature [30,31].

The phase transition temperatures and associated enthalpy changes of nOMBBBZT were obtained using a differential scanning calorimeter. Fig. 4 shows the DSC thermograms of representative compounds, 10OMBBBZT and 12OMBBBZT. The data are summarized in Table 1. All the compounds exhibited enantiotropic properties. Their endotherms were characterized by the crystal-mesophase-isotropic transitions occurring above the melting temperatures recorded during the heating cycle. Such transitions were also supported by the enthalpy values of the respective compounds.
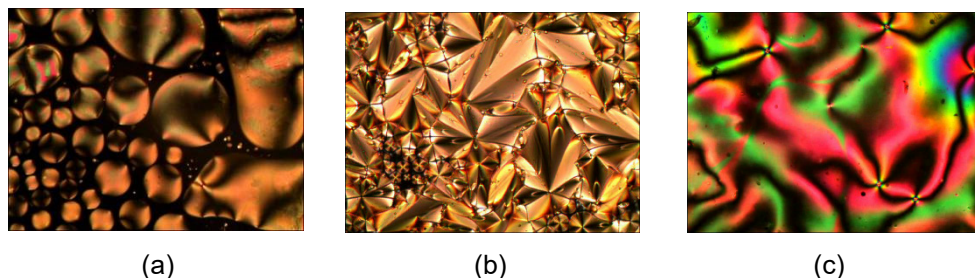
(a) (b) (c)

Figure 3. (a) Optical photomicrograph of 8OMBBBZT exhibiting droplets texture of nematic phase. (b) Optical photomicrograph of 16OMBBBZT exhibiting fan-shaped texture of SmA phase. (c) On further heating of 16OMBBBZT, it turned into *Schlieren* texture of nematic phase

Table 1. Transition temperatures and associated enthalpy changes of nOMBBBZT

| Compound	Transition Temperatures, ºC (ΔH, kJ mol^{-1})
6OMBBBZT	Cr$_1$ 121.7 (30.0) Cr$_2$ 140.8 (35.2) N 255.1 (27.0) I
8OMBBBZT	Cr 130.5 (33.3) N 215.2 (1.7) I
10OMBBBZT	Cr$_1$ 93.7 (17.9) Cr$_2$ 123.8 (26.8) N 221.9 (0.6) I
12OMBBBZT	Cr$_1$ 81.3 (8.2) Cr$_2$ 110.6 (29.1) SmA 161.8 (0.7) N 217.9 (1.2) I
14OMBBBZT	Cr$_1$ 96.7 (12.4) Cr$_2$ 109.7 (25.4) SmA 179.2 (0.4) N 216.5 (0.9) I
16OMBBBZT	Cr$_1$ 86.5 (27.3) Cr$_2$ 104.1 (32.5) SmA 179.2 (1.3) N 198.7 (1.2) I

Notes: Cr = crystal; I = isotropic liquid; N = nematic; SmA = smectic A.

Two types of phase transition sequences were observed. First, a single mesophase (nematic) was observed for the early three member of the series (n = 6, 8, 10). The phase sequence of Cr-to-N-to-I is well reflected in the DSC thermogram of 10OMBBBZT (Fig. 4a). The second type of phase transition sequence was observed for the later members. The SmA phase started to emerge in the later members (n = 12, 14, 16) along with the nematic phase. The phase sequence of Cr-to-SmA-to-N-to-I is illustrated in the DSC thermogram of 12OMBBBZT (Fig. 4b).
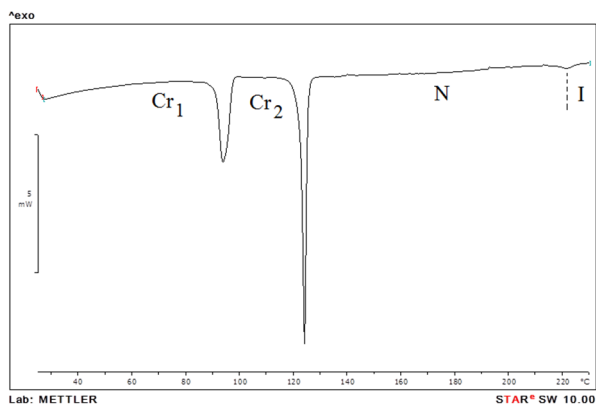
(a)
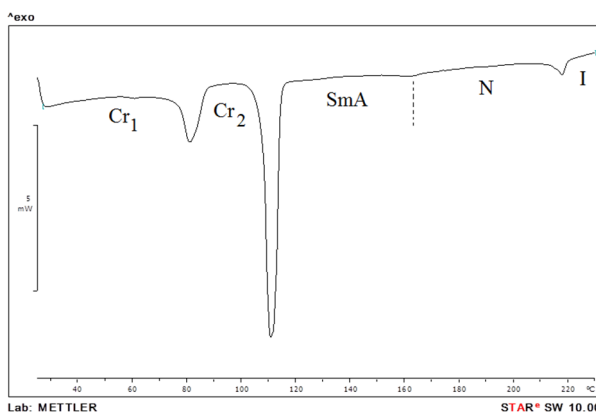
(b)

Figure 4. DSC thermograms of (a) 10OMBBBZT and
(b) 12OMBBBZT during heating scan.

X-Ray Diffraction Analysis

The SmA phase has been further verified on the representative compound 16OMBBBZT via XRD analysis. The XRD diffractogram of 16OMBBBZT is shown in Fig. 5 whereas the XRD data is tabulated in Table 2. For a smectic phase, it is basically known that a sharp and strong peak appears at low angle ($1^\circ < 2\theta < 4^\circ$) in small-angle X-ray scattering curve and a broad peak associated with lateral packing at $2\theta \approx 20^\circ$ can be spotted in wide-angle X-ray diffraction curve. On the other hand, for the nematic phase, there will be no peak appeared at low angle and a broad peak at $2\theta \approx 20^\circ$ can be observed in the XRD diffractogram [32].

141

As from XRD pattern of the current compound, 16OMBBBZT, it can be seen that a single sharp diffraction peak appeared at 2θ = 1.35° together with a broad peak at wide angle (2θ ≈ 13°). This typical XRD pattern indicates the presence of a lamellar structure (smectic layered arrangement) for liquid crystal phase [33,34].

Table 2. Powder X-ray diffraction data of 16OMBBBZT

2 theta (°)	1.35
d-spacing	43.1 Å
L	40.75 Å
d/L	1.06
Phase	SmA
Arrangement	Monolayer

Combining the data from POM and XRD, types of smectic phase can be confirmed. Based on the XRD data, the *d*-layer spacing was found to be 43.1 Å whereas the molecular length (*L*) obtained from the MM2 molecular calculation is 40.75 Å, where *d* is the layer spacing and *L* is the molecular length. Hence, the *d/L* ratio was calculated to be 1.06 which is approximate to 1. As a general rule, when the layer spacing is approximate to the molecular length (*d*~*L*), the SmA phase is identified as monolayer type [35]. Thus, the SmA phase exhibited in 16OMBBBZT was said to be monolayer arrangement. Similar results were obtained for azine-type mesogens reported by Wei and coworkers [36].
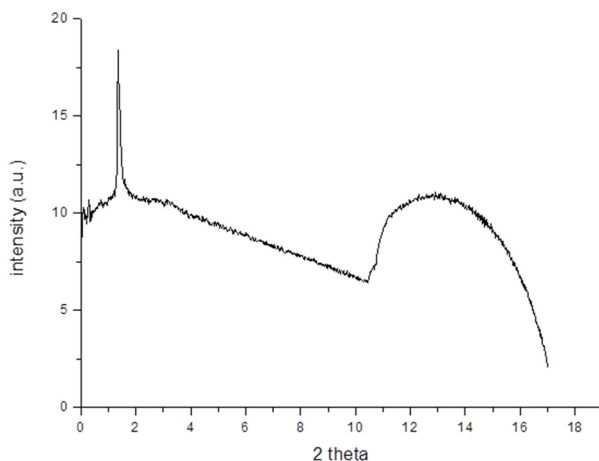

Figure 5. X-ray diffractogram of 16OMBBBZT.

Structure-Mesomorphic Property Relationships

Influence of the length of alkoxy chain on the mesomorphic properties can be established based on the graph of the phase transition temperature against the number of carbons in the alkoxy chain (Fig. 6). As the alkoxy chain lengthens, the melting and clearing temperatures exhibited a gradual descending trend. It was due to the dilution of the mesogenic core by the long carbon chain [37,38]. Suitable ratio between length and width of the molecule is an important factor for the molecules to display mesophase. All the members of the current homologue series exhibited enantiotropic phases, even the compounds with the shortest alkoxy chain (n = 6) where the nematic phase appeared. Hence, it indicates that the current molecule is a potential mesogenic core that worth to be further explored for design of new liquid crystalline molecules.

Smectic phase is generally observed for higher members of a series as the longer alkoxy chain is able to intertwine and facilitate the smectic phase formation [39]. In addition, the ester linking group that provided greater dipole-dipole interaction and subsequently encouraged the lateral packing and arranged themselves in the smectic phase. As the number of carbons at the alkoxy chain reached n = 12, an additional phase (SmA) emerged together with the nematic phase. It can therefore be suggested that in order to generate the smectic phase in the analogous substituted $C_6H_4COOC_6H_4C(H)=NC_7H_4NS$ compounds, the number of carbons in the alkoxy chain must be at least 12 (n ≥12) [40].
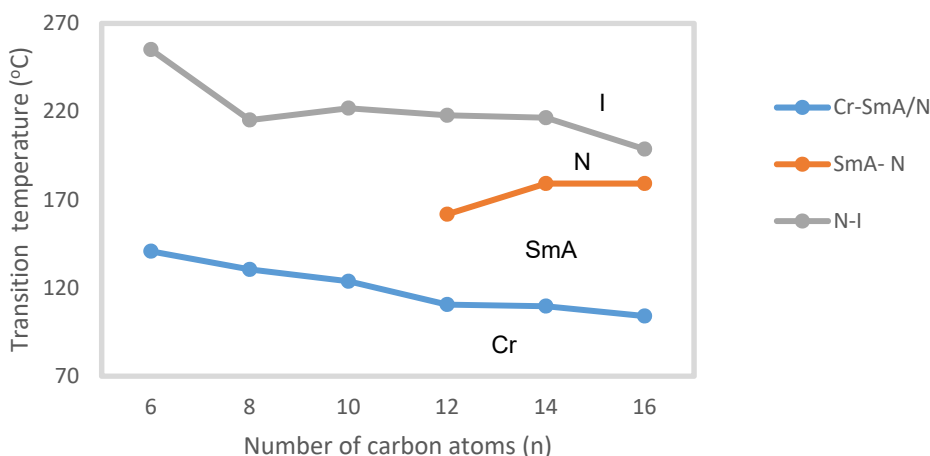

Figure 6. Graph of phase transition temperature against the number of carbon atoms (n) in alkoxy chain.

Phase width of liquid crystals can also be controlled by the length of terminal chain. The plot of phase width against the number of carbons in the alkoxy chain is depicted in Fig. 7. It is clearly shown that the nematic phase width decreased while the smectic phase width increased as the alkoxy chain lengthened. The last member of the series, 16OMBBBZT with the longest alkoxy chain possessed the narrowest nematic phase width (ΔN = 19.5 °C) and the largest smectic phase width (ΔSmA = 75.1 °C). Therefore, for the current molecular core structure, it can be proposed that the suitable terminal chain length that give the widest SmA phase is C16, while the widest nematic phase was possessed by the member with the shortest alkyl chain length (C6, ΔN = 114.3 °C).
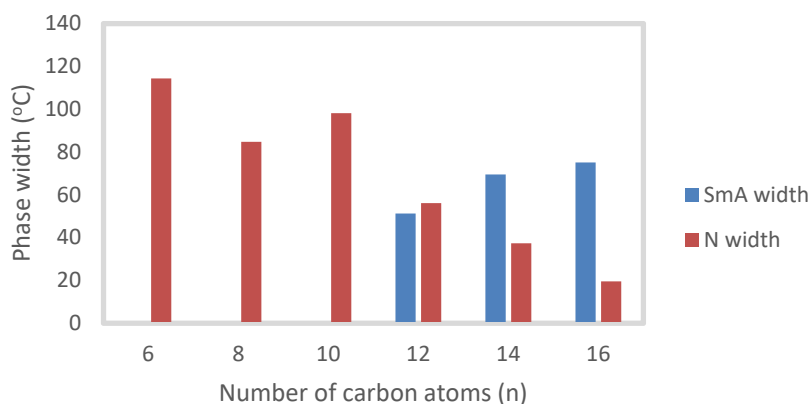

Figure 7. Plot of mesophase width against the number of carbons in alkoxy chain.

Comparison with Related Compounds

The reported examples revealing the influence of molecular geometry on the mesomorphic property usually involve contribution from molecular packing effects. The model system that will give a clear illustration on how molecular geometry affects the mesomorphic property will usually attract much attention. Table 3 shows the comparison of mesomorphic properties between the reported compounds **A** [41], **B** [27], **C** [42], **D** [26] and **E** [25] with the present compound, 12OMBBBZT. Molecules with two rings, compounds **A** and **B** with an aromatic ring connected to a benzothiazole ring via Schiff base linker exhibited SmA phase with lower clearing point compare to molecules with three rings (12OMBBBZT, **C**, **D** and **E**). Among the molecules with two rings, it was found that the different linking groups that attached to the alkyl chain (ether group in compound **A** and ester group in compound **B**) between the phenyl ring and the alkyl chain can change the mesomorphic behaviours.
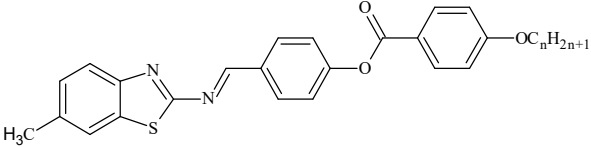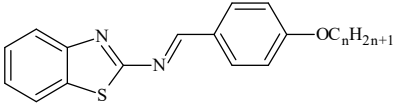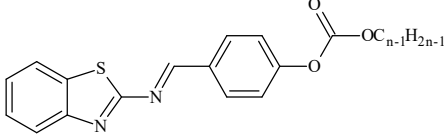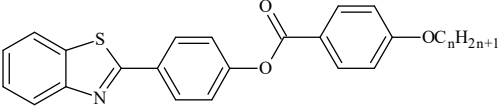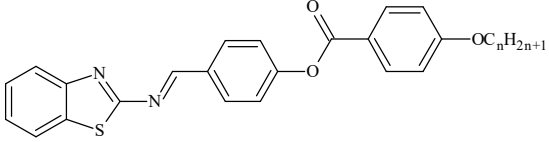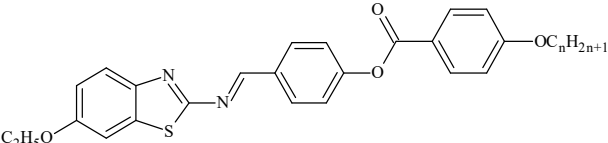
144

The ether linking group provides greater linearity to molecules rather than the ester group, thus resulting in the higher clearing point in compound **A** (T_c = 90.1 °C) compared to compound **B** (T_c = 85.6 °C). This in turn results in wider larger phase width of SmA phase being observed in compound **A** (ΔSmA = 8.2 °C) compared to compound **B** (ΔSmA = 4.8 °C). Therefore, the ether linkage at the terminal position is more favorable to mesomorphism than the ester linkage. Subsequently, benzothiazole liquid crystals (12OMBBBZT, **C**, **D** and **E**) were built up with the ether linked to the terminal alkyl chain.

As a phenyl ring is added to the existing molecular structure of compound **A**, this has resulted an extended core system with three ring molecule. It increased the clearing point of 12OMBBBZT to 217.9 °C. In addition, this extended core system is more adequate to generate mesophase because the SmA phase width increased dramatically from 8.2 °C in compound **A** to 51.2 °C in 12OMBBBZT. Additionally, nematic phase was detected in 12OMBBBZT but not in the case of compound **A**.

The dissimilarity between the molecules with three rings (12OMBBBZT and compound **C**) is the linking unit that connected benzothiazole and aromatic rings. 12OMBBBZT possessed Schiff base linking group whereas compound **C** was without any linking group. 12OMBBBZT showed lower melting point (110.6 °C) and larger SmA phase width (ΔSmA = 51.2 °C) compared to compound **C** (m.p. = 127.7 °C; ΔSmA = 14.8 °C). Although Schiff base provides a stepped core structure, it maintains molecular linearity, therefore providing higher stability and enhancing formation of mesophase. Therefore, it can be assumed that Schiff base linking unit played an important role at suppressing the melting temperature and then, it widens the existing mesophase width.

Compounds **D**, **E** and 12OMBBBZT are having similar structure except for the additional substituent (methyl and ethoxy) at the sixth position of the benzothiazole ring for compound **E** and 12OMBBBZT. Compound **D** without the lateral substituent possessed lower clearing point (179.6 °C) compared to compounds with lateral substituent, 12OMBBBZT (with methyl substituent, 217.9 °C) and compound **E** (with ethoxy substituent, 223.2 °C). This indicates that the incorporation of a small alkyl/alkoxy group at the lateral position of the benzothiazole ring can increase the clearing point of the molecule. This has also caused the nematic phase width increased from 15.0 °C in compound **D** to 56.1 °C in 12OMBBBZT, to 64.7 °C in compound **E**. Therefore, it suggests that the lateral substituent at the benzothiazole ring able to widen the nematic phase width. Taking into account with the higher clearing point and broader nematic phase width in 12OMBBBZT and compound **E**, it can be assumed that alkyl/alkoxy substituent at the lateral position of the current system, $C_6H_4COOC_6H_4C(H)=NC_7H_4NS$ can greatly enhance the mesomorphic properties.

Table 3. Comparison of present series with reported liquid crystalline compounds
(denotes as **A**, **B**, **C**, **D** and **E**) (where n = 12)

Compound	Phase transition (ºC) Phase range (ºC)
12OMBBBZT [Current study]	Cr$_1$ 81.3 Cr$_2$ 110.6 SmA 161.8 N 217.9 I $\Delta SmA = 51.2$; $\Delta N = 56.1$
A [41]	Cr 81.9 SmA 90.1 I $\Delta SmA = 8.2$
B [27]	Cr 80.8 SmA 85.6 I $\Delta SmA = 4.8$
C [42]	Cr 127.7 SmA 142.5 N 176.1 I $\Delta SmA = 14.8$; $\Delta N = 33.6$
D [26]	Cr 95.8 SmA 164.6 N 179.6 I $\Delta SmA = 68.8$; $\Delta N = 15.0$
E [25]	Cr 91.0 SmC 158.5 N 223.2 I $\Delta SmC = 67.5$; $\Delta N = 64.7$

CONCLUSIONS

In this article, a new series of heterocyclic liquid crystals, 6-methyl-2-[4-(4-alkoxybenzoyloxy)benzylideneamino]benzothiazoles is reported. The lowest member (*n*-hexyloxy, C6) possesses the largest nematic phase width indicates that the current structure has a good mesogenic system for mesophase formation. The smectic phase was emerged from the *n*-dodecyloxy (C12) to *n*-hexadecyloxy (C16) derivatives. Hence, it can be concluded the current core system needs a specific alkoxy chain length (n ≥ 12) in order to produce SmA phase. Among these members (C6-C16), member with the longest terminal chain (C16) possessed the largest SmA phase width. The current finding considerably influence our future direction by using the current core system for producing new liquid crystal molecules.

EXPERIMENTAL SECTION

Characterization

Fourier-Transform Infrared (FT-IR) spectra of the synthesized compounds were collected using a Perkin-Elmer System 2000 FT-IR Spectrometer. All compounds were prepared as KBr pellets and analyzed with a measurement range of 4000-400 cm^{-1}. ^{1}H NMR (400 MHz), ^{13}C NMR (100 MHz) and 2D HMQC spectra were recorded in CDCl$_3$ solvent using a JEOL LA-400 MHz NMR spectrometer. Electron-ionization mass spectrometry, EI-MS (70 eV) was performed using a Mass Spectrometer Finnigan MAT95XL-T at a source temperature of 200 °C.

Mettler Toledo DSC823^e differential scanning calorimeter was used to determine the phase transition temperatures and associated enthalpy changes at heating rate of 10 °C/min. Carl Zeiss polarizing optical microscope attached to a Linkam hotstage was utilized for temperature dependent studies of the mesophase textures. A video camera (Video Master coomo20P) installed on the microscope was connected to a video capture card (Video Master coomo600), allowing real-time video capture and image saving. The texture of liquid crystals exhibited by the compounds was observed using polarized light with crossed polarizers. Samples were prepared as thin films sandwiched between a glass slide and a cover slip. Phase identification was made by comparing the observed textures with those reported in the literature [21,22].

Synchrotron powder X-ray diffraction (XRD) measurements were recorded using a beamline BL17A at the National Synchrotron Radiation Research Center (NSRRC) in Taiwan. The X-ray wavelength used was 1.32633 Å. The XRD data

were collected using imaging plates (IP, of an area = 20 × 40 cm^2 and a pixel resolution of 100) curved with a radius equivalent to the sample-to-image plate distance of 280 mm, and the diffraction signals were accumulated for three minutes. The powder samples were packed into a capillary tube and heated by a heat gun, where the temperature controller was programmed by a PC with a PID feedback system. The scattering angle theta was calibrated by a mixture of silver behenate and silicon.

Synthesis

All solvents and reagents were purchased commercially and used without any further purification. 4-Dimethylaminopyridine (DMAP), 4-hydroxy-benzaldehyde, 1-bromoalkanes ($C_nH_{2n+1}Br$ where n = 6, 8, 10, 12, 14, 16), potassium hydroxide and potassium carbonate were purchased from Merck (Germany). Ethyl 4-hydroxybenzoate, 2-amino-6-methylbenzothiazole and *N,N'*-dicyclohexylcarbodiimide (DCC) were supplied by Acros Organics (USA).

The synthetic route used for the preparation of nOMBBBZT is shown in Scheme 1. Steglich esterification between intermediate compounds, 6-methyl-2-(4-hydroxybenzylideneamino)benzothiazole and 4-alkoxybenzoic acid were carried out according to methods described by Foo *et al.* [41] and Kadkin *et al.* [43], respectively. In the Steglich esterification, DCC is used as coupling agent and DMAP as catalyst. The water from this esterification is removed in dicyclohexylurea form [44].

Synthesis of heterocyclic liquid crystals

6-Methyl-2-(4-hydroxybenzylideneamino)benzothiazole (5 mmol, 1.94 g), appropriate 4-alkoxybenzoic acid (5 mmol) and DMAP (1 mmol, 0.12 g) were dissolved in 40 mL mixture of dichloromethane (DCM) and dimethylformamide (DMF), and the solution was stirred at 0 °C. DCC (5 mmol, 1.03 g) dissolved in 10 mL of DCM was added into the mixture dropwise and the solution was continuously stirred for an hour at 0 °C. The mixture was then stirred at room temperature for another five hours. Then, the mixture was filtered and the solvent was removed by evaporation. The obtained solid was repeatedly recrystallized from hexane and ethanol until the transition temperatures remained constant. The purity of all compounds was checked by thin layer chromatography (Merck 60 F_{254}) and visualized under short-wave UV light. The IR and NMR (^{1}H, ^{13}C) for the representative compound, 14OMBBBZT, are summarized as follows.

IR v_{max} (KBr, cm^{-1}): 3017 (*v* C-H aromatic), 2921, 2851 (*v* C-H aliphatic), 1726 (*v* C=O ester), 1601 (*v* C=N Schiff base, C=N thiazole), 1576 (*v* C=C aromatic), 1252 (*v* C-O, aromatic ether); ^{1}H NMR (400 MHz, CDCl$_3$): 0.88 (*t*, 3H, *J* = 6.9 Hz, CH$_3$-), 1.26-1.50 (*m*, 22H, CH$_3$-(C<u>H$_2$</u>)$_{11}$-(CH$_2$)$_2$-O-), 1.81 (*quint*, 2H,

J = 7.0 Hz, -C$\underline{H}_2$-CH$_2$-O-), 2.48 (s, 3H, Ar-C$\underline{H}_3$), 4.03 (t, 2H, J = 6.9 Hz, -C$\underline{H}_2$-O-), 6.97 (d, 2H, J = 9.2 Hz, Ar-H), 7.28 (d, 1H, J = 8.2 Hz, Ar-H), 7.37 (d, 2H, J = 8.7 Hz, Ar-H), 7.62 (s, 1H, Ar-H), 7.85 (d, 1H, J = 8.2 Hz, Ar-H), 8.09 (d, 2H, J = 9.2 Hz, Ar-H), 8.14 (d, 2H, J = 8.7 Hz, Ar-H), 9.04 (s, 1H, CH=N); ^{13}C NMR (100 MHz, CDCl$_3$): δ 14.25 (C̲H$_3$-), 22.80, 26.08, 29.18, 29.47, 29.66, 29.70, 29.77, 32.03 for methylene carbons (CH$_3$-(C̲H$_2$)$_{12}$-), 21.72 (Ar-C̲H$_3$), 68.48 (-C̲H$_2$O-), 114.49, 121.04, 121.58, 122.65, 122.75, 128.14, 131.57, 132.38, 132.50, 134.81, 135.45, 149.82, 155.02, 163.90 for aromatic carbons, 164.47 (C=N thiazole), 164.53 (C=N Schiff base), 170.78 (-C̲OO-).

ACKNOWLEDGMENTS

REFERENCES

1. K.C. Zhao; J.Q. Du; H.F. Wang; K.Q. Zhao; P. Hu; B.Q. Wang; H. Monobe; B. Heinrich; B. Donnio; *Chem. Asian J.*, **2019**, *14(3)*, 462-470.
2. W. Zhang; T. Sakurai; M. Aotani; G. Watanabe; H. Yoshida; V.S. Padalkar; Y. Tsutsui; D. Sakamaki; M. Ozaki; S. Seki; *Adv. Opt. Mater.*; **2019**, article number 1801349.
3. B.B. Chakraborty; S. Anwar; S. Das; S.B. Paul; G. Mohiuddin; J. De; S. Choudhury; *Liq. Cryst.*; **2018**, *45(11)*, 1644-1653.
4. F.N. da Silva; A.S. da Silva; I.H. Bechtold; E. Zapp; A.A. Vieira; *Liq. Cryst.*, **2019**, *46(11)*, 1707-1717.
5. A.J. Seed; P. Sampson; *Liq. Cryst.*, **2017**, *44(12-13)*, 1894-1910.
6. E. Girotto, I.H. Bechtold, H. Gallardo; *Liq. Cryst.*, **2016**, *43(12)*, 1768-1777.
7. D. Shi, K. Hu; P. Chen; W. Du; A. Gao; R. Chen; X. Chen; Z. An; *Liq. Cryst.*, **2016**, *43(10)*, 1397-1407.
8. L.L. Lai; C.H. Wang; W.P. Hsien; H.C. Lin; *Mol. Cryst. Liq. Cryst.*, **1996**, *287*, 177-181.
9. B.B. Chakraborthy; S. Anwar; S. Das; S.B. Paul; G. Mohiuddin; J. De; S. Choudhury; *Liq. Cryst.*; **2018**, *45*, 1644-1653.
10. M.L. Parra; E.Y. Qlgueta; J.A. Ulloa; J.M. Vergara; Al. Sanchez; *Liq. Cryst.*, **2012**, *39(8)*, 917-925.
11. J. Seltmann; M. Lehmann; *Liq. Cryst.*, **2011**, *38(4)*, 407-422.
12. W.L. Chia; C.W. Lin; *Liq. Cryst.*, **2013**, *40*, 922–931.
13. M.Z. Shafikov, A.M. Prokhorov; D.W. Bruce; *Liq. Cryst.*, **2017**, *44(4)*, 705-712.
14. M. Hagar; H. Ahmed; O. Alhaddad; *Liq. Cryst.*, **2019**, *46(9)*, 1440-1451.

15. P.J. Collings; M. Hird M; *Introduction to Liquid Crystals: Chemistry and Physics*, Taylor & Francis Ltd., UK, **1998**.
16. G. Karanlik; H. Ocak; B. Bilgin Eran; *J. Mol. Liq.*, **2019**, *275*, 567-577.
17. M. Hagar; H.A. Ahmed; G.R. Saad; *Liq. Cryst.*, **2018**, *45(9)*, 1324-1332.
18. H.A. Ahmed; M. Hagar; T.H. El-Sayed; R.B. Alnoman; *Liq. Cryst.*, **2019**, *46(7)*, 1156-1166.
19. M. Hagar; H.A. Ahmed; G.R. Saad; *J. Mol. Liq.*, **2019**, *273*, 266-273.
20. V.S. Sharma; R.B. Patel; *Mol. Cryst. Liq. Cryst.*, **2017**, *648(1)*, 53-65.
21. C. Selvarasu; P. Kannan; *Mol. Cryst. Liq Cryst.*, **2017**, *648(1)*, 77-87.
22. C. Selvarasu; P. Kannan; *J. Mol Liq.*, **2016**, *1125*, 234-240.
23. B.T. Thaker; D.B. Solanki; B.S. Patel; N.B. Patel; *Liq. Cryst.*, **2013**, *40(9)*, 1296-1309.
24. V.S. Sharma; R.B. Patel; *Mol. Cryst. Liq. Cryst.*, **2017**, *643(1)*, 141-158.
25. T.M. Koh; S.T. Ha; G.Y. Yeap; H.C. Lin; *Chin. Chem. Lett.*, **2013**, *24*, 926-928.
26. K.L. Foo; S.T. Ha; G.Y. Yeap; H.C. Lin; *Phase Trans.*, **2019**, *92(1)*, 87-99.
27. S.T. Ha; T.M. Koh; H.C. Lin; G.Y. Yeap; Y.F. Win; S.T. Ong; Y. Sivasothy; L.K. Ong; *Liq. Cryst.*, **2009**, *36(9)*, 917-925.
28. G.Y. Yeap; T.C. Hng; D. Takeuchi; K. Osakada; W.A.K. Mahmood; M.M. Ito; *Mol. Cryst. Liq. Cryst.*, **2009**, *506*, 134-149.
29. G.M. Paterno; V. Robbiano; K.J. Fraser; C. Frost; V. Garcia Sakai; F. Cacialli; *Sci. Rep.*, **2017**, *7*, 41013.
30. D. Demus; L. Richter; *Textures of Liquid Crystals*, Verlag Chemie, New York, **1978**.
31. I. Dierking, *Textures of Liquid Crystals*, Wiley-VCH, Weinheim, **2003**.
32. B.Y. Zhang; Y.G. Jia; D.S. Yao; X.W. Dong; *Liq. Cryst.*, **2004**, *31*, 339-345.
33. D. Pociecha; D. Kardas; E. Gorecka; J. Szydlowska; J. Mieczkowski; D. Guillon; *J. Mater. Chem.*, **2003**, *13*, 34-37.
34. R.A. Reddy; B.K. Sadashiva; *J. Mater. Chem.*, **2004**, *14*, 310-319.
35. K.C. Majumdar; S. Mondal; N. Pal; P.K. Sinha; *Tetrahedron Lett.*, **2009**, *50*, 1992-1995.
36. Q. Wei; L. Shi; H. Cao; L.P. Wang; H. Yang; Y.B. Wang; *Liq. Cryst.*, **2008**, *35*, 581-585.
37. G.W. Gray; *Molecular Structure and the Properties of Liquid Crystals*, Academic Press, London, **1962**.
38. P. Berdague; J.P. Bayle; M.S. Ho; B.M. Fung; *Liq. Cryst.*, **1993**, *14*, 667-674.
39. P.J. Collings; M. Hird; *Introduction to Liquid Crystals: Chemistry and Physics*, Taylor & Francis Ltd., UK, **1998**.
40. G.Y. Yeap; S.T. Ha; P.L. Lim; P.L. Boey; M.M. Ito; S. Sanehisa; Y. Youhei; *Liq. Cryst.*, **2006**, *33(2)*, 205-211.
41. K.L. Foo; S.T. Ha; F.W. Yip; G.Y. Yeap; H.C. Lin; S.S. Sastry; *Liq. Cryst.*, **2014**, *41(11)*, 1516-1525.
42. S.T. Ha; T.M. Koh; F.W. Yip; S.S. Sastry; *Liq. Cryst.*, **2013**, *40(8)*, 1016-1023.
43. O.N. Kadkin; H. Han; Y.G. Galyametdinov; *J. Organomet. Chem.*, **2007**, *692*, 5571-5582.
44. A.B. Lutjen, M.A. Quirk, A.M. Barbera, E.M. Kolonko; *Bioorg. Med. Chem.*, **2018**, *26*, 5291-5298.

RADIOCARBON DATING OF A VERY LARGE GRANDIDIER BAOBAB, THE GIANT OF BEVOAY

**ADRIAN PATRUT[a,b]*, ROXANA T. PATRUT[c],
JEAN-MICHEL LEONG POCK-TSY[d], STEPHAN WOODBORNE[e],
LASZLO RAKOSY[c], ILEANA-ANDREEA RATIU[b],
JENŐ BODIS[b], PASCAL DANTHU[f]**

ABSTRACT. The article presents the AMS (accelerator mass spectrometry) radiocarbon dating results of the Giant of Bevoay, which is a very large Grandidier baobab (*Adansonia grandidieri* Baill.) of Madagascar. The investigation of this baobab shows that it has a cluster structure, which consists of 3 perfectly fused stems. The calculated wood volume of the tree is 520 m^3, which makes it the third largest Grandidier baobab and also the third largest individual of all *Adansonia* species**.** Two samples were collected from the outer part of the stems. The oldest dated sample segment had a radiocarbon date of 525 ± 23 BP, which corresponds to a calibrated age of 585 ± 10 years. According to this value, the Giant of Bevoay is 825 ± 50 years old.

Keywords: AMS radiocarbon dating, Adansonia grandidieri, tropical trees, age determination.

INTRODUCTION

The *Adansonia* genus, that belongs to the Bombacoideae, a subfamily of Malvaceae, contains eight or nine species. One or two species originate from the tropical savanna of Africa, six species are endemic to Madagascar and one species grows only in Australia [1-6].

---

[a] *Babeş-Bolyai University, Faculty of Chemistry and Chemical Engineering, 11 Arany Janos, RO-400028, Cluj-Napoca, Romania.*
[b] *Babeş-Bolyai University, Raluca Ripan Institute for Research in Chemistry, 30 Fantanele, RO-400294 Cluj-Napoca, Romania.*
[c] *Babeş-Bolyai University, Faculty of Biology and Geology, 44 Republicii, RO-400015, Cluj-Napoca, Romania.*
[d] *Drfgrn-fofifa, Antananarivo, Madagascar.*
[e] *iThemba LABS, Private Bag 11, WITS 2050, South Africa.*
[f] *Cirad, UPR HortSys, Montpellier, France.*
* Corresponding author: apatrut@gmail.com

ADRIAN PATRUT, ROXANA T. PATRUT, JEAN-MICHEL LEONG POCK-TSY, STEPHAN WOODBORNE, LASZLO RAKOSY, ILEANA-ANDREEA RATIU, JENŐ BODIS, PASCAL DANTHU

In 2005, we initiated an extensive research project for elucidating several controversial or poorly understood aspects related to the architecture, development and age of the African baobab (*Adansonia digitata* L.). The research is based on our original methodology, which is not limited to dead specimens, but also allows to investigate and date live individuals. This approach uses AMS radiocarbon dating of tiny wood samples collected from inner cavities, deep incisions in the trunk, broken stems and from the outer part of trunk/stems of large baobabs [7-17]. We found that most large and old African baobabs are multi-stemmed and exhibit preferentially ring-shaped structures. The oldest African baobabs were found to have ages up to 2,500 years [10, 11,13-15].

In 2013, our research on the *Adansonia* genus was extended to big individuals of the most widespread three Malagasy species, namely the Fony baobab (*Adansonia rubrostipa* Jum. & H. Perrier), the Za baobab (*Adansonia za* Baill.) and the Grandidier baobab (*Adansonia grandidieri* Baill.), which grow in the west and south of the Big Island [6,19-22].

The Grandidier baobab, which is called Reniala (or Renala) by natives (in Masikoro, i.e., "Mother of the Forest"), is the largest and most famous of the six *Adansonia* species of Madagascar. *A. grandidieri* is represented by big trees with columnar trunks and flat-topped crowns with almost horizontal large branches [2,3,6].

Until 1998, *A. grandidieri* was observed in a limited number of locations in southwestern Madagascar. Consequently, according to the IUCN Red List, *A. grandidieri* was classified as endangered [23]. New investigations, based on photo-interpretation of very high resolution satellite images and validated by field investigations, demonstrated that *A. grandidieri* is distributed in a larger area than previously believed and its population is much larger than older estimates. According to recent research, the total population of *A. grandidieri*, which covers an area of 26,232 km^2 along the Mangoky river and in the west part of the Menabe region, is around 1.2-1.3 million mature specimens. However, the species is still classified as endangered for a new reason, namely the predicted population decline of at least 50% over the next three generations [18,21,23].

The biggest *A. grandidieri* can be found in the Morombe area, especially in the so-called Andombiry Forest. The Andombiry Forest hosts or hosted three very large *A. grandidieri* specimens, with wood volumes of over 500 m^3, namely the Big Reniala of Isosa, the famous Tsitakakoike, which died in 2019, and Tsitakakantsa [20,21].

Here we present the investigation and AMS radiocarbon dating results of another giant specimen, the Giant of Bevoay, which is situated on the lower course of the Mangoky river.

RESULTS AND DISCUSSION

The Giant of Bevoay and its area. The baobab is located on a small hill, in the proximity of a stone quarry, at 1 km from the southern (left) bank of the Mangoky river. It is close to the Bevoay village, in the Beroroha district, Atsimo-Andrefana region of southwestern Madagascar. The baobab can be found on the southern edge of the Ampanonga Forest. Its GPS coordinates are 21º57.974' S, 043º52.202' E and the altitude is 60 m. Mean annual rainfall in the area is around 400 mm.

Figure 1. General view of the Giant of Bevoay taken from the south-east.

The baobab has a maximum height of 20.3 m and the restored circumference at breast height (cbh; at 1.30 m above ground level) is 21.03 m (**Figure 1**). Its base is situated in a 5 m deep depression.

The big columnar trunk has a tall horizontal fissure. It forks at the height of 14.8 m into several branches, out of which 3 are very large, with diametres up to 2 m. According to the visual inspection and to the analysis of photographs, the quasi-cylindrical trunk is composed of 3 perfectly fused stems. The horizontal dimensions of the spectacular canopy are: 34.8 (WE) x 29.2 (NS) m (**Figure 2**).

ADRIAN PATRUT, ROXANA T. PATRUT, JEAN-MICHEL LEONG POCK-TSY, STEPHAN WOODBORNE, LASZLO RAKOSY, ILEANA-ANDREEA RATIU, JENŐ BODIS, PASCAL DANTHU

The calculated wood volume of the baobab is 520 m^3, out of which 480 m^3 represents the trunk and 40 m^3 the canopy. By this value, the Giant of Bevoay becomes the third largest *Adansonia grandidieri* in volume after the Big Reniala of Isosa and the famous fallen Tsitakakoike, both from the Andombiry Forest [21]. It is also bigger than any known African baobab.

Figure 2. The picture taken from south-west shows
the very large canopy of the Giant of Bevoay.

Wood samples. Two wood samples, labelled B-1 and B-2, were extracted from the big trunk with an increment borer. The first sample B-1 was too short (0.24 m) for investigation. Therefore, we investigated only the second sample B-2, collected at a height of 1.71 m above ground, which was sufficiently long (0.78 m). A number of five pieces/segments, each of the length of 10^{-3} m (marked from a to e), were extracted from determined positions of the sample.

AMS results and calibrated ages. Radiocarbon dates of the 5 sample segments are listed in Table 1. The radiocarbon dates are expressed in ^{14}C yr BP (radiocarbon years before present, i.e., before the reference year 1950). Radiocarbon dates and errors were rounded to the nearest year.

Calibrated (cal) ages, expressed in calendar years CE (CE, i.e., common era), are also shown in Table 1. The 1-σ probability distribution (68.3%) was selected to derive calibrated age ranges. For one sample segment (B-2e),

the 1-σ distribution is consistent with one range of calendar years. For two segments (B-2c, B-2d), the 1-σ distribution is consistent with two ranges of calendar years, while for one sample segment (B-2b), with a low radiocarbon date, it corresponds to four ranges of calendar years. In these cases, the confidence interval of one range is considerably greater than that of the other(s); therefore, it was selected as the cal CE range of the segment for the purpose of this discussion.

Table 1. AMS Radiocarbon dating results and calibrated
ages of samples collected from the Giant of Bevoay

Sample code	Depth[1] [height[2]] (m)	Radiocarbon date [error] (^{14}C yr BP)	Cal CE range 1σ [confidence interval]	Assigned year [error] (cal CE)	Sample age [error] (cal CE)
B-2a	0.02 [1.71]	-	-	>1950	>Modern
B-2b	0.15 [1.71]	98 [± 34]	1710-1719 (5.3%) 1813-1836 (17.3%) 1855-1866 (5.4%) **1880-1925 (40.4%)**	1902 [± 22]	120 [± 20]
B-2c	0.40 [1.71]	269 [± 17]	1628-1680 (31.2%) **1732-1803 (37.0%)**	1767 [± 35]	255 [± 35]
B-2d	0.65 [1.71]	346 [± 45]	**1506-1591 (54.5%)** 1618-1640 (13.8%)	1548 [± 42]	470 [± 40]
B-2e	0.81 [1.71]	525 [± 23]	**1424-1435 (68.3%)**	1434 [± 10]	585 [±10]

[1] Depth in the wood from the sampling point.
[2] Height above ground level.

For obtaining single calendar age values of sample segments, we derived a mean calendar age of each sample segment from the selected range (marked in bold). Sample/segment ages represent the difference between the year 2020 CE and the mean value of the selected range, with the corresponding error. Sample ages and errors were rounded to the nearest 5 yr. We used this approach for selecting calibrated age ranges and single values for sample ages in all our previous articles on AMS radiocarbon dating of large and old angiosperm trees, especially of baobabs [7-17,19-22].

For one sample segment (B-2a), which was collected close to the bark, the sample age falls after 1950 CE (0 BP), namely the ^{14}C activity, expressed by the ratio ^{14}C/^{12}C, is greater than the standard activity in the reference year 1950. Such values, which correspond to negative radiocarbon dates, are termed greater than Modern (>Modern). In such cases, the dated wood is young, being formed after the year 1950.

ADRIAN PATRUT, ROXANA T. PATRUT, JEAN-MICHEL LEONG POCK-TSY, STEPHAN WOODBORNE, LASZLO RAKOSY, ILEANA-ANDREEA RATIU, JENŐ BODIS, PASCAL DANTHU

Dating results of samples (segments). The oldest dated segment, i.e., B-2e, represents practically the sample end. It had a radiocarbon date of 525 ± 23 BP, which corresponds to a calibrated age of 585 ± 10 calendar yr. The lower ages of the other three segments, i.e., B-2b, B-2c and B-2d, are in good accordance with their positions in the stems. Eventually, the negative radiocarbon date and the age of segment B-1a, shows that the stem from which was extracted the sample B-2 was not affected by the growth-stop phenomenon [13].

Architecture of the Giant of Bevoay. Our extended research on the African baobab revealed that very large specimens are always multi-stemmed [10,13]. This feature also applies to the large Malagasy baobabs, including the Grandidier baobabs [20,21]. As mentioned, the Giant of Bevoay consists of 3 perfectly fused stems. For this very large Grandidier baobab, the age sequence of segments extracted from the investigated sample, which was collected from the exterior, shows a continuous increase with the depth in the wood, see Table 1. This demonstrates that the baobab of Bevoay exhibits a cluster structure.

Age of the Giant of Bevoay. The age of the baobab can be estimated by extrapolating the age of the oldest dated sample segment, namely B-2e, to the presumptive pith of the corresponding stem. Sample segment B-2e, which has an age of 585 ± 10 yr, originates from a depth of 0.81 m in the wood. In the sampling direction, the trunk has a diametre of 6.60 m. Due to the cylindrical shape of the trunk, we can consider that the 3 fused stems, which build the trunk, have close dimensions and ages. In this case, the presumptive pith of the sampled stem is located at a distance of 1.65 m from the sampling point. In a conservative estimate, the age of the Giant of Bevoay is 825 ± 50 years.

CONCLUSIONS

Our research discloses the AMS radiocarbon dating results of the Giant of Bevoay, a very big Grandidier baobab, located on the lower course of the Mangoky river, Madagascar. The baobab is composed of 3 fused stems and presents a cluster structure. The wood volume of the Giant of Bevoay is 520 m^3, which makes it the third largest known Grandidier baobab and also the third largest individual of all baobab species. Two wood samples were collected from the outer part of the trunk, out of which the longest was investigated. The oldest dated sample segment was found to have a radiocarbon date of 525 ± 23 BP, which corresponds to a calibrated age of 585 ± 10 years. This value indicates that the Giant of Bevoay is 825 ± 50 years old. Therefore, one can state that the baobab of Bevoay started growing around the year 1200 CE.

EXPERIMENTAL SECTION

Sample collection. The investigated wood sample was collected with a Haglöf CH 800 increment borer (0.80 m long, 0.0108 m inner diametre). A number of four tiny pieces/segments, of the length of 10^{-3} m, were extracted from predetermined positions along the sample. The segments were processed and investigated by AMS radiocarbon dating.

Sample preparation. The α-cellulose pretreatment method was used for removing soluble and mobile organic components [24]. The resulting samples were combusted to CO_2, which was next reduced to graphite on iron catalyst [25,26]. The resulting graphite samples were analysed by AMS.

AMS measurements. The radiocarbon measurements were done at the AMS Facility of the iThemba LABS, Johannesburg, Gauteng, South Africa, using the 6 MV Tandem AMS system [27]. In all cases, the obtained fraction modern values were finally converted to a radiocarbon date. The radiocarbon dates and errors were rounded to the nearest year.

Calibration. Radiocarbon dates were calibrated and converted into calendar ages with the OxCal v4.4 for Windows [28], by using the SHCal20 atmospheric data set [29].

ACKNOWLEDGMENTS

REFERENCES

1. G.E. Wickens, *Kew Bull.*, **1982**, *37(2)*, 172-209.
2. D.A. Baum, *Ann. Mo. Bot. Gard.*, **1995**, *82*, 440-471.
3. G.E. Wickens, P. Lowe, "The Baobabs: Pachycauls of Africa, Madagascar and Australia", Springer, Dordrecht, **2008**, pp. 232-234, 256-257, 295-296.
4. J.D. Pettigrew, L.K. Bell, A. Bhagwandin, E. Grinan, N. Jillani, J. Meyer, E. Wabuyele, C.E. Vickers, *Taxon*, **2013**, *61*, 1240-1250.
5. G.V. Cron, N. Karimi, K.L. Glennon, C.A. Udeh, E.T.F. Witkowski, S.M. Venter, A.E. Assobadjo, D.H. Mayne, D.A. Baum, *Taxon*, **2016**, *65*, 1037-1049.
6. A. Petignat, L. Jasper, "Baobabs of the world: The upside down trees of Madagascar, Africa and Australia", Struik Nature, Cape Town, **2015**, pp. 16-86.
7. A. Patrut, K.F. von Reden, D.A. Lowy, A.H. Alberts, J.W. Pohlman, R. Wittmann, D. Gerlach, L. Xu, C.S. Mitchell, *Tree Physiol.*, **2007**, *27*, 1569-1574.

8. A. Patrut, D.H. Mayne, K.F. von Reden, D.A. Lowy, R. Van Pelt, A.P. McNichol, M.L. Roberts, D. Margineanu, *Radiocarbon*, **2010**, *52(2-3)*, 717-726.

9. A. Patrut, K.F. von Reden, R. Van Pelt, D.H. Mayne, D.A. Lowy, D. Margineanu, *Ann. Forest Sci.*, **2011**, *68*, 93-103.

10. A. Patrut, S. Woodborne, R.T. Patrut, L. Rakosy, D.A. Lowy, G. Hall, K.F. von Reden, *Nat. Plants*, **2018**, *4(7)*, 423-426.

11. A. Patrut, K.F. von Reden, D.H. Mayne, D.A. Lowy, R.T. Patrut, *Nucl. Instrum. Methods Phys. Res. Sect. B*, **2013**, *294*, 622-626.

12. A. Patrut, S. Woodborne, K.F. von Reden, G. Hall, M. Hofmeyr, D.A. Lowy, R.T. Patrut, *PLOS One*, **2015**, *10(1): e0117193.*

13. A. Patrut, S. Woodborne, K.F. von Reden, G. Hall, R.T. Patrut, L. Rakosy, J-M. Leong Pock Tsy, D.A. Lowy, D. Margineanu, *Radiocarbon*, **2017**, *59(2)*, 435-448.

14. A. Patrut, L. Rakosy, R.T. Patrut, I.A. Ratiu, E. Forizs, D.A. Lowy, D. Margineanu, K.F. von Reden, *Studia UBB Chemia*, **2016**, *LXI, 4*, 7-20.

15. A. Patrut, R.T. Patrut, L. Rakosy, D.A. Lowy, D. Margineanu, K.F. von Reden, *Studia UBB Chemia*, **2019**, *LXIV, 2 (II)*, 411-419.

16. A. Patrut, S. Woodborne, R.T. Patrut, G. Hall, L. Rakosy, C. Winterbach, K.F. von Reden, *Forests*, **2019**, *10*, 983-993.

17. A. Patrut, A. Garg, S. Woodborne, R.T. Patrut, L. Rakosy, I.A. Ratiu, *PLOS One*, **2020**, *15(1): e0227352.*

18. G. Vieilledent, C. Cornu, A. Cuni Sanchez, J-M. Leong Pock-Tsy, P. Danthu, *Biological Conservation*, **2013**, *166*, 11-22.

19. A. Patrut, K.F. von Reden, P. Danthu, J-M. Leong Pock Tsy, R.T. Patrut, D.A. Lowy, *PLOS One*, **2015**, *10(3): e0121170.*

20. A. Patrut, K.F. von Reden, P. Danthu, J-M. Leong Pock-Tsy, L. Rakosy, R.T. Patrut, D.A. Lowy, D. Margineanu, *Nucl. Instrum. Methods Phys. Res. Sect. B,* **2015**, *361*, 591-598.

21. R.T. Patrut, A. Patrut, J-M Leong Pock-Tsy, S. Woodborne, L. Rakosy, P. Danthu, I-A. Ratiu, J. Bodis, K.F. von Reden, *Studia UBB Chemia*, **2019**, *LXIV, 4*, 131-139. doi:10.24193/subbchem.2019.4.10.

22. A. Patrut, R.T. Patrut, P. Danthu, J.-M. Leong Pock-Tsy, L. Rakosy, D.A. Lowy, K.F. von Reden, *PLOS One*, **2016**, *11(1)*, e0146977.

23. H. Ravaomanalina, J. Razafimanahaka, "2016. *Adansonia grandidieri.*" *The IUCN Red List of Threatened Species 2016: e.T30388A64007143*.

24. N.J. Loader, I. Robertson, A.C. Barker, V.R. Switsur, J.S. Waterhouse, *Chem. Geol.*,**1997**, 136(3), 313–317.

25. Z. Sofer, *Anal. Chem.*, **1980**, *52(8)*, 1389-1391.

26. J.S. Vogel, J.R. Southon, D.E. Nelson, T.A. Brown, *Nucl. Instrum. Methods Phys. Res. Sect. B*, **1984**, *5*, 289-293.

27. V.L. Mbele, S.M. Mullins, S.R. Winkler, S. Woodborne, *Phys. Procedia*, **2017**, *90*, 10-16.

28. C. Bronk Ramsey, *Radiocarbon*, **2009**, *51*, 337-360.

29. A.G. Hogg, T.J. Heaton, Q. Hua, J.G. Palmer, C.S.M. Turney, J. Southon, A. Bayliss, P.G. Blackwell, G. Boswijk, C.B. Ramsey, C. Pearson, F. Petchey, P.J. Reimer, R.W. Reimer, L. Wacher, *Radiocarbon*, **2020**, *62(4)*, 759-778.

THE IMPACT OF ANTHROPOGENIC ACTIVITIES TO THE LEVEL OF SOME POPS RESIDUES IN BOVINE MILK FROM SEVERAL FARMS IN ROMANIA

DIANA IONELA STEGARUS[a*], ROXANA ELENA IONETE[a], SIMONA OANCEA[b], ECATERINA LENGYEL[b], ADINA FRUM[b]

ABSTRACT. Bovine milk is a product with high consumption rate across the world and therefore its evaluation in terms of consumers' safety and public health is of extreme relevance. In this study, the occurrence of residues of polychlorinated biphenyls (PCBs), organochlorine pesticides and heavy metals was monitored in environmental samples (soil, grassland grass, water) and bovine milk collected from seven locations in Romania, for the assessment of their potential health risk. PCBs were detected in almost all the environmental and milk samples; it highlighted in soil values higher than the normal limit set by the national legislation, but below the alert thresholds and intervention levels. Dichlorodiphenyltrichloroethane (DDT) and its metabolites were found in consistently higher amounts in environmental samples and bovine milk at all sites. Increased values of hexachlorocyclohexane (HCH) were also found in milk samples but without exceeding the maximum admissible levels set by the Romanian legislation. High concentration of cadmium, copper and zinc were found in soil, grass and water samples from the industrial area. Lead exceeded the maximum admissible level in samples from the urban area. The results obtained confirmed the importance of surveilling persistent pollutants in raw milk as part of the healthcare system.

Keywords: PCBs, organochlorine pesticides, heavy metals

INTRODUCTION

The high bioaccumulation potential of persistent organic pollutants (POPs) in environmental matrixes poses serious problems to human health and environment, and therefore an increased concern related to inappropriate

[a] *National Research and Development Institute for Cryogenic and Isotopic Technologies – ICSI Ramnicu Valcea, 4 Uzinei Street, 240050 Ramnicu Valcea, Romania*
[b] *Lucian Blaga University of Sibiu, 10 Victoriei Bvd., 550024 Sibiu, Romania*
* *Corresponding author: diana.stegarus@icsi.ro*

use of pesticides in the agricultural processes is evident [1]. The use of pesticides for crop protection has increased with the rising demand of food quantities on the market due to growing world population and therefore health risk monitoring and assessment measures must be considered. So far, international and regional organizations have set maximum residue limits (MRLs) of different classes and representatives of main food contaminants. Monitoring programs of pesticides, in particular organochlorinated insecticides, have been adopted to ensure food safety, leading also to the enhancement of agricultural resources management and avoidance of economic loss [2,3].

Short-term exposure to pesticides can cause skin and eye irritation, headaches, dizziness, and nausea, and long-term exposure can cause diseases, like: cancer, asthma, diabetes, hormone disruption, cardiovascular diseases, obesity, reproductive and neurological diseases, and learning disabilities. The developing of diseases can start in women embryo. The health risks are difficult to elucidate, because of several factors, like: level of exposure and period of exposure and the type of pesticide, thus the prediction of health hazards is difficult [4, 5].

Another group of POPs used in many industrial applications and generally found at low concentrations as contaminant of animal and human food chains, are the polychlorinated biphenyls (PCBs). They decompose very slowly into the environment because of their low solubility in water and high thermal stability [6]. There are 209 congeners of PCBs, numbered from PCB-1 to PCB-209, based on different number and position of chlorine [7], from which six congeners (PCB-28, PCB-52, PCB-101, PCB-138, PCB-153, and PCB-180) occur in high levels in environmental, food and human fluids/tissues samples, being recommended by the *Stockholm Convention on Persistent Organic Pollutants* (*POPs)* in 2001 to be monitored. Based on different national recommendations, other congeners may be monitored. The POPs which are banned by *Stockholm Convention* (2001, 2009) exhibit a wide range of toxic effects [8].

A product with high consumption rate is the bovine milk and therefore investigation of its quality in terms of chemical hazard and impact to human health it is of great interest globally. Thus, in order to validate a solid phase extraction method for polychlorinated biphenyl compounds, comparative studies between ocean water and bovine milk were conducted resulting a greater sensibility for the sorbent coating based on polymeric ionic liquids (PIL), at the expense of the PDMS compounds (7 mm polydimethylsiloxane) due to the incorporation of the sorbent particles of the PIL structures. Also, Chen et al. [9] identified 12 polybrominated diphenyl ethers (PBDEs) and 19 polychlorinated biphenyl (PCBs) congeners in milk samples from California, by using rapid methods (QuEChERS, purified by gel permeation chromatography and quantified

by gas chromatography-mass spectrometry (GC-MS)), concluding that these congeners confirm the previous results of the high levels of PBDEs from California in comparison with other regions of the United States due to the high industrial emissions in the area [9]. In Italy, a series of studies regarding the presence of contamination compounds that can affect human health [10–13] have been performed on cow and buffalo milk samples. The contamination of milk from factories from Brescia (North Italy), was attributed to the contamination of the food of animals. The dioxin-like PCBs were the main contributors to the total levels of OMS-TEQ. They were found in proportions of 87%, in the most contaminated sample. By replacing the contaminated food with one from a non-contaminated region, the levels of OMS-TEQ were dropped up to the ones the European Commission approves of 2 pg OMS-TEQ/g fat [14].

Heavy metals transferred on the chain air-water-soil may pose risk of accumulation in plants through roots, stems or leaves [15–18]. They are also persistent chemicals with toxic effects due to the induced oxidative stress and disturbed metabolic processes, some of them being also carcinogenic agents [19–22].

POPs contamination of soil, water and grassland of agricultural areas can be of great concern for accumulation in the food chain (*e.g.* dairy and meat products). Therefore, assessing the impact of farms location in terms of the nearness with developed areas (e.g. industrial), but also of the specific agricultural practices used, it is of interest. In this work, the occurrence of residues of some persistent chemicals such as organochlorine pesticides, PCBs and heavy metals was investigated in environmental samples (soil, grass, and water) and bovine milk from farms located in different areas (rural and urban/industrial) in South Romania.

The sampling sites were selected in terms of the anthropogenic activities (e.g. chemical/ industrial companies in the area, and/or intensive agricultural practices), while the POPs were chosen due to their potential risk for health. The PCBs analytes included seven congeners, the PCB-28, PCB-52, PCB-101, PCB-138, PCB-153, PCB-180 and PCB-194; analyzed organochlorine pesticides were lindan α-, β- and δ- isomers of hexachlorocyclohexane (HCH), aldrin, dieldrin, endrin, endosulfan, dichlorodiphenyltrichloroethane (DDT) and its derivatives dichlorodiphenyldichloroethane (DDD), dichlorodiphenyldichloro-ethylene (DDE); and investigated heavy metals were the lead (Pb), cadmium (Cd), copper (Cu) and zinc (Zn).

The aim of this study is to assess the correlations between the contamination of the environment and bovine milk, regarding the location of farms in terms of nearness with developed areas or specific agricultural practices used.

DIANA IONELA STEGARUS, ROXANA ELENA IONETE,
SIMONA OANCEA, ECATERINA LENGYEL, ADINA FRUM

RESULTS AND DISCUSSIONS

Non-dioxin polychlorinated biphenyls in environmental and milk samples

The concentration of PCBs, pesticides and heavy metals were investigated in environmental samples collected from four counties located in the South of Romania, sites Valcea (VL), Arges (AG), Ialomita (IL) and Buzau (BZ). The sampling sites situated around individual farms were as follows: rural (VL-V, VL-E, AG, IL, and BZ), urban-industrial (VL-S near chemical/petrochemical plant) and urban (VL-N resort/thermal springs area/near mountain area). The results on seven investigated polychlorinated biphenyl congeners (PCB28, PCB52, PCB101, PCB138, PCB153, PCB180 and PCB194) are summarized in Figure 1.
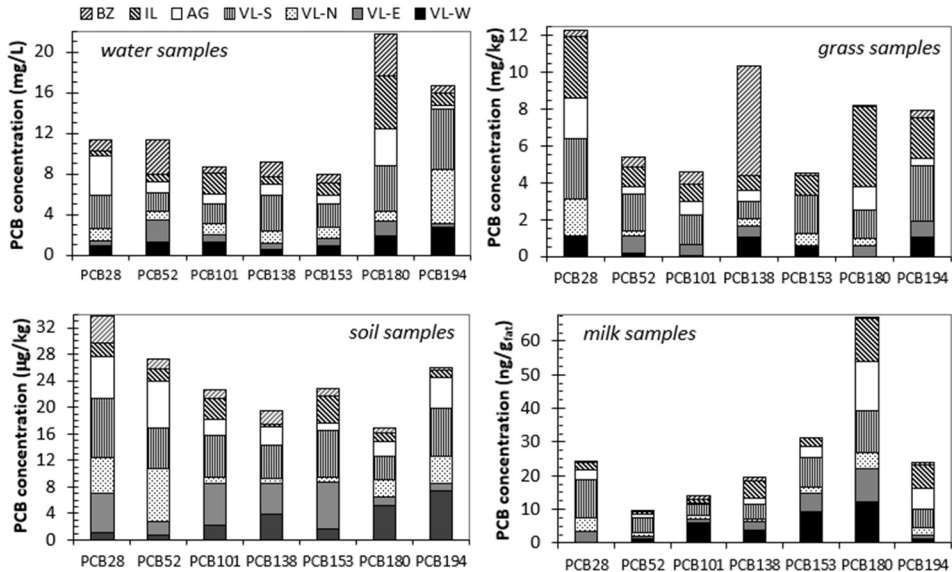
Figure 1. Concentrations of individual PCBs in soil, grass and water samples from the seven sites around the investigated farms and in collected bovine milk samples

The levels of individual PCBs in soil were found higher than normal values (< 0.1 µg/kg for PCB28 and PCB52; and < 0.4 µg/kg for PCB101, PCB 138, PCB 153 and PCB180, respectively) set by Romanian legislation [23]. However, values were situated below the alert thresholds (2 µg/kg for PCB28 and PCB52; and < 10 µg/kg for PCB101, PCB 138, PCB 153 and PCB180, respectively) for sensitive soils (residential and agriculture areas)

162

with the exception of PCB28 in samples from sites VL-Z (6.070 µg/kg), VL-N (5.240 µg/kg), AG (6.325 µg/kg), and BZ (4.095 µg/kg), and of PCB52 in samples from sites VL-N (8.030 µg/kg) and AG (7.045 µg/kg). All the obtained values were below the intervention levels (10 µg/kg for PCB28 and PCB52; and < 40 µg/kg for PCB101, PCB 138, PCB 153 and PCB180, respectively). The level of PCBs at VL-S site, an area located near a chemical plant with history in producing pesticides, was the highest found, but below the alert thresholds for less sensitive soils (industrial land use). The sum of PCB congeners (ΣPCB7) in soil samples from VL-S (Figure 2), which include PCB28, PCB52, PCB101, PCB138, PCB153, and PCB180, was 43.895 µg/kg, higher than normal value (< 10 µg/kg), but well below the alert thresholds (250 µg/kg) for sensitive soils. The lowest ΣPCB7 in soil samples was found in BZ site (11.385 µg/kg). The mean values of soil PCBs including the seven congeners ranged from 1.626 µg/kg (BZ) to 6.271 µg/kg (VL-S).

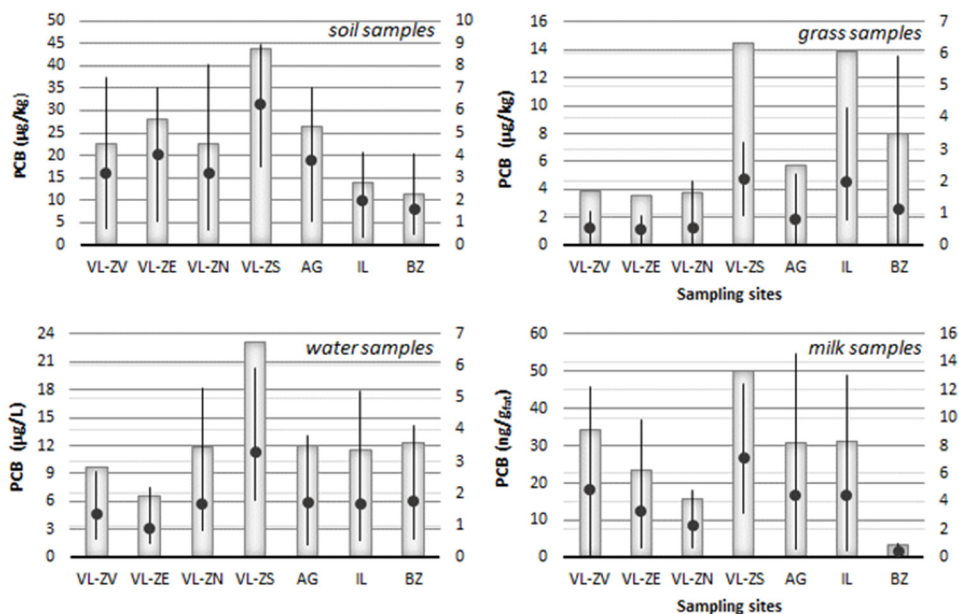**Figure 2.** Concentrations of PCBs (sum, min, max and average) in soil, grass and water samples from the seven sites around the investigated farms and in collected bovine milk samples

PCBs were detected in all investigated grass samples, with exception of PCB101 at VL-N site, PCB153 at VL-E and AG sites, PCB180 at VL-W site and PCB194 at VL-N site. Increased levels of PCBs, in particular of high

chlorinated ones (PCB138, PCB153, PCB180, and PCB194) were found in samples from VL-S (industrial area) and IL sites. The values were below the maximum admissible level imposed for animal feed [24].

Regarding the water samples, the highest mean values of seven PCB congeners and the ΣPCB7 were found in VL-S site (11.820 μg/L), while the lowest ones were detected in VL-E site (6.535 μg/L).

PCBs were detected in almost all bovine milk samples. The congener PCB153 was not found in sample BZ. With the exception of sample VL-S, none of the other samples exceeded the maximum level of 40 ng/g fat as the sum of the indicator of six congeners (PCB28, PCB52, PCB101, PCB138, PCB153 and PCB180) in raw milk as set by EU Regulation [25]. PCB180 showed increased contribution to total PCBs in bovine milk collected from farms at all sites, with exception of BZ site.

Organochlorine pesticides in environmental and bovine milk samples

Concentration of ten individual organochlorine pesticides (α-, β-, δ-HCH, aldrin, dieldrin, endrin, DDE, DDD, DDT and endosulfan) were detected in the investigated environmental samples and bovine milk (Table1).

From the individual pesticides, the DDT and/or its metabolites were found in consistently high amounts in environmental samples and bovine milk at all sites. The highest total concentration of selected pesticides was found in all samples at site VL-S, which is near a chemical industrial area.

However, the sum of DDTs (ΣDDT) in soil samples was below the Romanian reference values [23], the highest value being of 5.016 μg/kg in VL-S site. Other individual pesticides in higher concentration were the endosulfan (at VL-W and IL sites), aldrin (at BZ), HCH and endrin (at VL-E). The sum of HCHs (ΣHCH) in soil samples did not exceed the Romanian reference values, except to site VL-S (7.008 μg/kg).

Regarding grass samples, among organochlorine pesticides, the ΣDDTs (Figure 3) were predominant in samples from VL-S site (58.947 μg/kg) exceeding the maximum admissible level set by the EU Regulation [26]. Aldrin exceeded normal values in samples from VL-S site (12.079 μg/kg). The other samples showed pesticides values below the maximum admissible levels.

Among individual pesticides in water, the β-HCH, DDE and DDD exceeded normal values (0.60 μg/L) [27] in samples from VL-S, while α-, β- and δ -HCHs were found in high amounts in samples from IL site.

Table 1. Organochlorine pesticides concentration in the environmental samples from the seven sites around the investigated farms and in bovine milk sampled from the selected farms (max values in bold, min values highlighted).

Pesticides	Sampling sites						
	VL-W	VL-E	VL-N	VL-S	AG	IL	BZ
	SOIL (µg/kg)						
α-HCH	0.051 ±0.0040	1.026 ±0.0003	2.003 ±0.0004	**3.002** **±0.0004**	0.037 ±0.0001	1.122 ±0.0009	0.654 ±0.0002
β-HCH	0.014 ±0.0000	0.654 ±0.0002	0.003 ±0.0003	**4.000** **±0.0002**	0.003 ±0.0004	0.214 ±0.0003	0.983 ±0.0004
δ-HCH	0.003 ±0.0010	0.226 ±0.0001	0.144 ±0.0003	0.006 ±0.0005	1.001 ±0.0005	0.541 ±0.0003	**2.022** **±0.0003**
Aldrin	0.995 ±0.0070	0.364 ±0.0002	**1.555** **±0.0004**	0.325 ±0.0004	0.003 ±0.0006	0.654 ±0.0004	1.022 ±0.0001
Dieldrin	0.013 ±0.0009	1.025 ±0.0003	**3.003** **±0.0002**	0.257 ±0.0003	n.d.	n.d.	0.003 ±0.0002
Endrin	0.201 ±0.0006	**2.000** **±0.0006**	1.011 ±0.0003	0.015 ±0.0004	0.003 ±0.0004	0.011 ±0.0002	0.741 ±0.0004
DDE	0.039 ±0.0025	1.003 ±0.0003	0.642 ±0.0003	**2.004** **±0.0002**	0.007 ±0.0004	1.363 ±0.0005	0.856 ±0.0002
DDD	1.006 ±0.0008	0.003 ±0.0005	0.024 ±0.0003	1.005 ±0.0001	0.146 ±0.0001	2.024 ±0.0005	0.363 ±0.0005
DDT	0.003 ±0.0008	0.025 ±0.0007	0.255 ±0.0001	**2.006** **±0.0002**	1.003 ±0.0003	0.005 ±0.0005	0.025 ±0.0004
Endosulfan	1.037 ±0.0004	0.666 ±0.0004	1.000 ±0.0004	1.003 ±0.0004	0.364 ±0.0002	2.051 ±0.0004	0.644 ±0.0002
	GRASS (µg/kg)						
α-HCH	0.162 ±0.0046	0.406 ±0.0449	2.555 ±0.0045	**8.028** **±0.0035**	2.032 ±0.0007	0.150 ±0.0041	6.006 ±0.0044
β-HCH	0.844 ±0.0075	0.511 ±0.0425	1.027 ±0.0050	**10.521** **±0.0010**	3.023 ±0.0032	2.318 ±0.0458	2.024 ±0.0026
δ-HCH	1.002 ±0.0180	2.647 ±0.0038	1.868 ±0.0057	**16.058** **±0.0043**	6.873 ±0.0527	14.023 ±0.0093	2.102 ±0.0004
Aldrin	4.026 ±0.0025	2.131 ±0.0055	6.739 ±0.0040	**12.079** **±0.0024**	8.075 ±0.0648	1.307 ±0.0539	0.377 ±0.0145
Dieldrin	5.334 ±0.0006	7.056 ±0.0050	5.090 ±0.0015	7.089 ±0.0003	**11.081** **±0.0012**	4.461 ±0.0999	0.157 ±0.0054
Endrin	8.072 ±0.0497	5.639 ±0.0002	7.023 ±0.0030	**25.114** **±0.0006**	6.143 ±0.0028	4.091 ±0.0299	8.216 ±0.0346
DDE	9.235 ±0.0040	2.780 ±0.0024	6.358 ±0.0060	**17.250** **±0.0007**	11.225 ±0.0050	3.194 ±0.1688	7.256 ±0.0045

Pesticides	Sampling sites						
	VL-W	VL-E	VL-N	VL-S	AG	IL	BZ
DDD	8.046 ±0.0100	9.163 ±0.0015	4.546 ±0.0055	10.446 ±0.0027	4.355 ±0.0048	**11.016 ±0.0092**	1.009 ±0.0008
DDT	11.151 ±0.1210	16.091 ±0.0045	8.869 ±0.0045	**31.251 ±0.0027**	19.571 ±0.0306	15.062 ±0.0394	4.488 ±0.0741
Endosulfan	2.030 ±0.0055	6.078 ±0.0040	12.067 ±0.0040	**17.680 ±0.0002**	10.725 ±0.6350	5.144 ±0.1080	16.289 ±0.0320
WATER (µg/L)							
α-HCH	0.082 ±0.0012	0.046 ±0.0020	n.d.	0.149 ±0.0057	0.078 ±0.0034	**0.621 ±0.0114**	0.164 ±0.1390
β-HCH	0.003 ±0.0028	0.007 ±0.0070	0.016 ±0.0018	**0.917 ±0.0245**	0.059 ±0.0059	0.742 ±0.0008	0.191 ±0.0039
δ-HCH	0.006 ±0.0011	0.005 ±0.0045	0.044 ±0.0028	0.555 ±0.0049	0.104 ±0.0009	**0.849 ±0.0018**	0.031 ±0.0002
Aldrin	n.d.	0.082 ±0.0023	n.d.	0.004 ±0.0042	0.028 ±0.0275	**0.364 ±0.0020**	n.d.
Dieldrin	n.d.	**0.063 ±0.0118**	n.d.	0.002 ±0.0025	0.002 ±0.0020	0.007 ±0.0013	n.d.
Endrin	n.d.	0.026 ±0.0009	**0.054 ±0.0044**	n.d.	n.d.	n.d.	n.d.
DDE	0.015 ±0.0011	0.038 ±0.0018	n.d.	**0.831 ±0.0096**	0.004 ±0.0035	0.258 ±0.0031	0.508 ±0.1437
DDD	0.095 ±0.0012	0.022 ±0.0220	0.047 ±0.0004	**0.907 ±0.0038**	0.074 ±0.0004	n.d.	0.011 ±0.0003
DDT	0.079 ±0.0055	0.085 ±0.0058	n.d.	0.440 ±0.0041	**0.450 ±0.3708**	n.d.	0.449 ±0.0018
Endosulfan	0.028 ±0.0280	n.d.	n.d.	0.051 ±0.0074	**0.513 ±0.0035**	n.d.	0.035 ±0.0008
BOVINE MILK (ng/gfat)							
α-HCH	3.958 ±0.0632	n.d.	n.d.	**6.080 ±0.0018**	4.031 ±0.3331	0.004 ±0.0042	1.360 ±0.0973
β-HCH	2.065 ±0.0040	3.254 ±0.0039	4.266 ±0.0050	4.812 ±0.4419	**7.046 ±0.0048**	1.257 ±0.0049	3.031 ±0.0056
δ-HCH	2.225 ±0.0047	8.255 ±0.0050	3.077 ±0.0048	**9.261 ±0.0107**	3.333 ±0.0019	0.981 ±0.0064	0.768 ±0.0729
Aldrin	**3.123 ±0.0273**	n.d.	2.226 ±0.0057	n.d.	1.262 ±0.0027	2.353 ±0.0111	n.d.
Dieldrin	n.d.	n.d.	**4.256 ±0.0048**	4.149 ±0.0017	2.085 ±0.0051	2.118 ±0.0235	0.355 ±0.3030
Endrin	n.d.	**2.116**	n.d.	n.d.	1.556	n.d.	n.d.

Pesticides	Sampling sites						
	VL-W	VL-E	VL-N	VL-S	AG	IL	BZ
		±0.0046			±0.0047		
p,p'-DDE	**6.618** **±0.0233**	5.225 ±0.0050	3.331 ±0.0065	6.216 ±0.0048	4.256 ±0.0056	n.d.	1.358 ±0.0035
p,p'-TDE	5.259 ±0.0021	6.386 ±0.0043	**6.581** **±0.0073**	6.084 ±0.0016	6.576 ±0.0052	0.707 ±0.0674	0.958 ±0.0037
DDT	7.065 ±0.0038	6.181 ±0.0014	7.147 ±0.0034	**9.546** **±0.0046**	7.056 ±0.0042	6.377 ±0.0129	2.327 ±0.0047
Endosulfan	3.380 ±0.0008	2.359 ±0.0020	n.d.	**4.503** **±0.0071**	2.562 ±0.0025	2.019 ±0.0026	0.306 ±0.0151

Mean value (n=3) ± standard deviation

Concerning raw milk samples, the DDT was found in all samples. The highest amount of ΣDDTs was registered in sample from VL-S, of 21.846 ng/g$_{fat}$, followed by VL-W (18.942 ng/g$_{fat}$), while the lowest was found in BZ (4.642 ng/g$_{fat}$) and IL (7.084 ng/g$_{fat}$). The obtained values did not exceed the maximum admissible levels set by Romanian legislation [28].
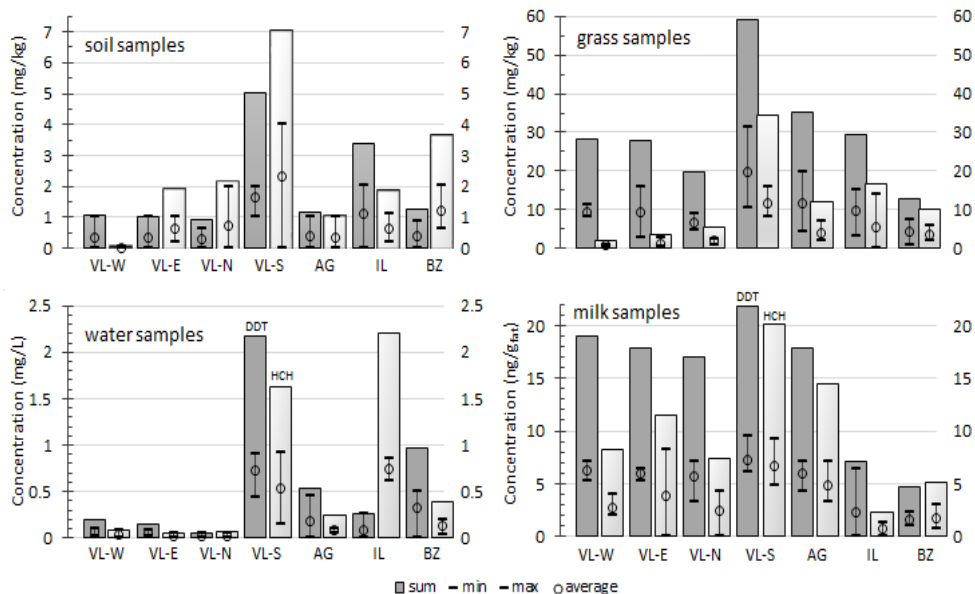

Figure 3. Concentrations of ΣDDTs (sum, min, max and average) in soil, grass and water samples from the seven sites around the investigated farms and in collected bovine milk samples

167

Our study revealed low levels of pesticides compared with other studies. A study provided by Deti et al. [29] on bovine milk from different regions of Ethiopia, empasized larger quantities of organochlorine pesticides than the ones found in this study, like: DDE, that reaches quantities of up to 91.9 ng/g fat and ΣDDT up to 1230 ng/g fat. The endosulfan was not detected in most of the samples, but in the samples that was detected it reached a quantum of up to 142.1 ng/g fat and aldrin was found in only one sample and it had a quantity of 11.6 ng/g fat.

However, increased values of α-, β-, and δ- HCH were found in milk sample from VL-S, β-, and δ- HCH in sample from VL-E and β-HCH to AG site. Endrin was absent in most of samples, except for VL-E and AG sites.

Heavy metals in environmental

Regarding the level of heavy metals (Pb, Cd, Cu and Zn), the obtained results are presented in Table 2. Heavy metals were detected in environmental samples in various concentrations, as follows:

  (i) Lead level varied in the range of 7.285 ÷ 321.110 µg/kg in soil samples (the highest concentration in sample from VL-N, exceeding the maximum admissible level [30], 0 ÷ 2.505 µg/kg in grass samples (highest value in VL-S) and 0.185 ÷ 8.020 µg/L in water sample (highest value in VL-S);
  (ii) Cadmium level varied in the range of 1.220 ÷ 9.965 µg/kg in soil samples (the highest concentration to IL), 0.025 ÷ 1.905 µg/kg in grass samples (highest value in VL-S) and 0.265 ÷ 2.235 µg/L in water sample (highest value in IL)
  (iii) Copper level varied in the range of 46.195 ÷ 226.725 µg/kg in soil samples (the highest concentration in sample VL-S), 1.430 ÷ 16.070 µg/kg in grass samples (highest value in VL-S) and 4.185 ÷ 69.030 µg/L in water sample (highest value to VL-S)
  (iv) Zinc level varied in the range of 88.600 ÷ 469.601 µg/kg in soil samples (the highest concentration in sample VL-S), 11.575 ÷ 67.110 µg/kg in grass samples (highest value in VL-S) and 539.185 ÷ 2306.090 µg/L in water sample (highest value in VL-ZE)

Soil, grass and water samples at VL-ZS showed high concentration of cadmium, copper and zinc.

Statistical analysis showed extremely significant positive Pearson's correlation coefficients ($p<0.01$) between cadmium-contaminated soil and cadmium-contaminated water ($R^2= 0.9765$), and between lead-contaminated water and copper-contaminated water ($R^2= 0.9093$), respectively. Copper residues in water high significantly correlated with those in soil ($R^2= 0.7976$) and in grass, respectively ($R^2= 0.8702$).

Table 2. Concentration of Fe, Cd, Cu and Zn in the environmental samples
(soil, grass and water) from the seven sites around the investigated farms

Samples	Sampling sites						
	VL-ZV	VL-ZE	VL-ZN	VL-ZS	VL-Z S-E	IL	BZ
	Lead (µg/kg)						
soil	9.170 ± 0.190	136.190 ± 0.060	321.110 ± 0.040	47.090 ± 0.030	156.225 ± 0.035	7.285 ± 0.035	215.135 ± 0.165
grass	1.085 ± 0.065	0.745 ± 0.115	0.910 ± 0.060	2.505 ± 0.145	0.125 ± 0.125	–	0.520 ± 0.030
water	0.185 ± 0.015	0.220 ± 0.040	4.900 ± 0.130	7.085 ± 0.065	1.225 ± 0.135	8.020 ± 0.130	0.370 ± 0.030
	Cadmium (µg/kg)						
soil	1.220 ± 0.030	5.320 ± 0.040	4.150 ± 0.060	9.215 ± 0.055	2.580 ± 0.030	9.965 ± 0.085	6.460 ± 0.21
grass	0.030 ± 0.030	0.025 ± 0.025	0.790 ± 0.050	1.905 ± 0.035	0.135 ± 0.035	0.050 ± 0.000	0.630 ± 0.060
water	0.265 ± 0.045	0.745 ± 0.095	0.685 ± 0.055	1.770 ± 0.250	0.385 ± 0.025	2.235 ± 0.105	1.305 ± 0.055
	Copper (µg/kg)						
soil	46.195 ± 0.055	63.28 ± 0.030	113.085 ± 0.055	226.725 ± 1.445	98.225 ± 0.055	97.620 ± 0.470	139.750 ± 0.310
grass	5.190 ± 0.170	7.320 ± 0.260	10.450 ± 0.070	16.070 ± 0.180	1.430 ± 0.110	14.065 ± 0.185	2.705 ± 0.345
water	12.165 ± 0.195	4.185 ± 0.335	36.300 ± 0.250	69.030 ± 0.120	12.880 ± 0.140	44.015 ± 0.075	15.605 ± 0.455
	Zinc (µg/kg)						
soil	88.600 ± 0.030	365.200 ± 0.320	118.380 ± 0.040	469.601 ± 0.030	105.280 ± 0.030	236.080 ± 0.07	364.180 ± 0.070
grass	17.225 ± 0.135	11.575 ± 0.065	44.785 ± 0.235	67.110 ± 0.140	25.160 ± 0.080	28.945 ± 0.205	18.140 ± 0.080
water	1216.065 ± 6.955	2306.090 ± 9.060	1718.100 ± 7.040	1107.050 ± 5.310	2230.930 ± 25.190	539.185 ± 438.935	2207.600 ± 6.430

Mean value (n=3) ± standard deviation

A significant correlation ($p < 0.05$) of PCBs in milk and PCBs in soil ($R^2 = 0.7548$) was observed. The correlation analysis of milk samples also indicated a good correlation of PCBs and pesticides ($R^2 = 0.7568$).

Regarding the residues in water samples, there was a highly significant correlation ($p < 0.05$) between PCBs and pesticide ($R^2 = 0.8068$), cadmium and pesticides ($R^2 = 0.8267$), and copper and pesticides ($R^2 = 0.8038$). Concerning grass samples, a very significant ($p < 0.05$) positive correlation was found between cadmium and pesticides ($R^2 = 0.8157$), and zinc and pesticides ($R^2 = 0.8344$).

DIANA IONELA STEGARUS, ROXANA ELENA IONETE,
SIMONA OANCEA, ECATERINA LENGYEL, ADINA FRUM

CONCLUSIONS

Residues of polychlorinated biphenyls, organochlorine pesticides and heavy metals from environment may enter the food webs and generate negative effects in the human body. Contaminated soil, water and grassland grass with organochlorine pesticides, PCBs and heavy metals in areas of farming may be of great concern of accumulation in raw bovine milk.

The results of the present investigation on levels of persistent chemicals (non-dioxin like PCBs, organochlorine pesticides and heavy metals) were determined for environmental and bovine milk samples of local origin. Sampling sites were selected based on historical contamination due to the presence of large chemical / industrial companies and /or intensive agricultural practices.

Samples from sites near industrial areas show relative high contamination. In particular, high chlorinated PCBs (PCB138, PCB153, PCB180, and PCB194), high ΣDDT, ΣHCH, cadmium, copper and zinc were detected in those areas. The analyzed samples did not exceed the maximum admissible levels set by the Romanian legislation for each contaminant, except for the site situated in the industrial are.

The results of this work confirmed the importance of surveilling POPs on the milk chain, from farm to fork, and are important for the public awareness regarding chemical hazards. Therefore, advanced strategy for monitoring milk safety should be applied to identify pathways for contamination.

EXPERIMENTAL SECTION

Sample collection and storage

Environmental samples (soil, grass and water) were collected in 2017 from four South Romanian counties, namely: Valcea (VL), Arges (AG), Ialomita (IL), and Buzau (BZ), at different sites around local farms, which regularly provide bovine milk for automatic milk dispensers (Figure 4). The sampling sites are listed in Table 3.

From each site (Table 3), approximately 1 kg of soil samples (7 cm deep) were collected from three sampling points situated near the pastures for animals, using a stainless-steel soil sampling probe with a conically-tapered tip for an easier drive-in sample extraction, and stored in zip lock bags to be investigated later in the laboratory. Also, approximately 1 kg of grass samples from pastures and 1 L of water were collected and kept at +4°C before analysis. Additionally, fresh bovine milk was sampled from the collecting centers in the investigated areas to assess the potentially residues of PCBs, pesticides and heavy metals. The selection of milk sample supplying sites was based on both economic and consumer safety criteria since the farms/collecting centers

provide important amounts of raw milk to farmers markets vending machines. Milk samples (2 L each) were collected in plastic bottles and transported to the laboratory in cooling boxes with ice packs where they were immediately stored in a freezer at -24°C until analyzed.
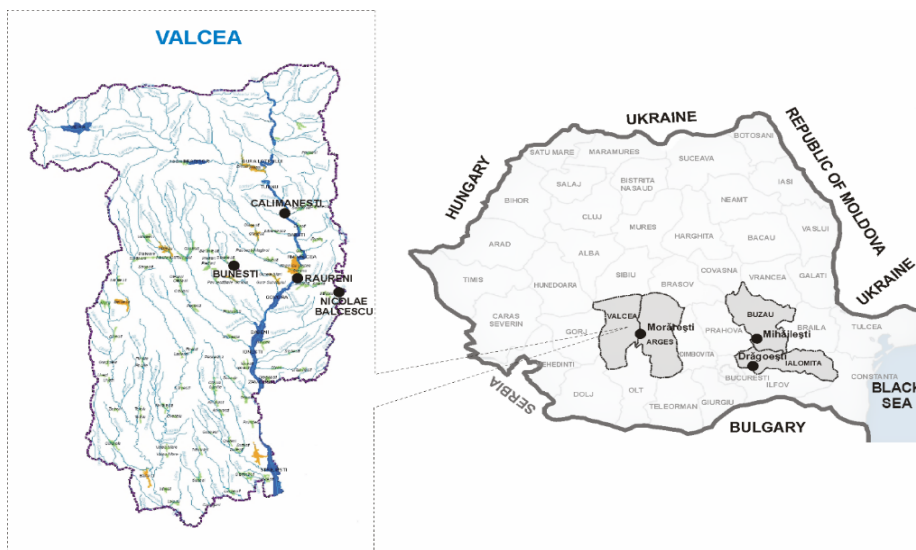

Figure 4. Location of sampling sites and surrounding areas

Table 3. Sampling sites

County	Location of farm/milk collecting centre	Site code	Altitude (average)	Latitude	Longitude	Description
Valcea	Calimanesti	VL-N	288 m	45.23910N	24.33986E	Resort/near mountain area
	Bunesti	VL-W	303 m	45.11434N	24.18899E	Rural/Agricultural area
	Raureni	VL-S	227 m	45.06129N	24.33649E	Urban/near industrial area
	Nicolae Balcescu	VL-E	490 m	45.10656N	24.43600E	Rural/Agricultural area
Arges	Moraresti	AG	548 m	45.01610N	24.56791E	Rural/Agricultural area
Ialomita	Dragoesti	IL	66 m	44.56535N	26.54118E	Rural/Agricultural area
Buzau	Mihailesti	BZ	75 m	44.91444N	26.67677E	Rural/Agricultural area

Reagents and reference solutions

Mix standard solutions for organochlorine pesticides (α-HCH, β-HCH, δ-HCH, aldrin, dieldrin, endrin, DDE, DDD, and DDT) and PCB congeners (PCB28, PCB52, PCB101, PCB138, PCB153, PCB180, and PCB194) were purchased from LGC (Germany). Proper amounts of stock solutions of all these standards were prepared in chromatography-grade *n*-hexane. Working standard solutions were prepared by appropriate dilution of the above mix standards in *n*-hexane at different concentrations for both, pesticides and PCBs. For each compound, linearity at six different concentrations, of 0.100, 0.070, 0.050, 0.010, 0.005, and 0.001µg/L, with triplicate measurements, were evaluated through a linear regression analysis. Both stock and working standards were stored at -24 ºC during the study.

Chromatography-grade acetonitrile, acetone, ethyl acetate, *n*-hexane, dichloromethane and sodium chloride were obtained from Merck (Darmstadt, Germany); anhydrous sodium sulphate of analytical grade was produced by Sigma Aldrich (Germany).

A multi-element standard solution XVI CertiPUR (a mixture of 21 elements in diluted nitric acid), with a certified value of 100±3 mg/L, purchased from Merck (Darmstadt, Germany) was used for the calibration curve in the quantitative analysis of metals (Pb, Cd, Cu, and Zn). Solutions of varying concentrations were prepared for the metals by diluting the standard solution. 65% HNO_3 from Merck (Darmstadt, Germany) and ultrapure water, with a maximum resistivity of 18.2 MΩ/cm, produced by a Milli-Q Millipore water purification system (Bedford, MA, USA), were used for sample treatment and dilution.

Extraction

Organochlorine pesticides from water and bovine milk - 10 mL of sample were introduced into a 100 mL centrifugation tube, 5 g natrium chloride (NaCl) and 30 mL of acetonitrile were added. The tubes were stirred at 250 rpm for 20 minutes, using an AREX Heating Magnetic Stirrer from VELP (Italy). The mixtures were centrifuged at 6000 rpm for 15 minutes for obtaining clear sample layers. After the centrifugation, approximately 90% of the acetonitrile superior layer was transferred into a centrifugation tube. Then, we added 5 g of anhydrous sodium sulphate and stirred the tube for 2 minutes. The sample was kept into the freezer for 15 minutes; next, 10 mL of the acetonitrile superior layer was mixed with 10 mL of a saturated solution of sodium chloride and 30 mL of ultrapure water, and then extracted twice with 20 mL dichloromethane using a separation funnel. The organic layer was filtered by using sodium sulphate and then evaporated to dryness.

The residue was taken with 2 mL of ethyl acetate and filtered by using filter paper purchased from Sigma Aldrich. The obtained solution was transferred into a 1.700 mL flask, analyzed and quantified by using the gas chromatography with an electron capture detector (GC/ECD), the results being confirmed after by using gas chromatography coupled with mass spectrometry (GC/MS).

Organochlorine pesticides and PCBs from soil and grass - 20 g of cryogenically triturated samples were stirred intensively for 15-20 minutes with 50 mL of acetone using an AREX Heating Magnetic Stirrer from VELP (Italy). 50 mL of ether were added, and the stirring continued for another 15 minutes. This procedure was executed twice. The combined extracts were washed twice into a separation funnel by using 500 mL distilled water. The resulted extract was dried on sodium sulphate (Sigma Aldrich, Germany) and concentrated at 1 mL, after which the sodium sulphate was washed three times with 10 mL of ether. In order to obtain satisfactory results, the acetone water ratio was 9:1, and the acetone ether ratio was kept constantly at 1:2.

Sample purification - Into a glass column of 25 cm length and 1 cm interior diameter, designed with a tap, a quartz wool plug and 3 g of aluminum oxide were inserted. The concentrate extract was introduced into the dry column by using a pipette. The concentration flask was washed twice with 1 mL of ether and the washing portions were transferred into the column immediately after the liquid reached the superior part of the columns filling. The elution was performed by using 20 mL ether and the resulted extract was concentrated to 1 mL. To the final extract, 1 μL of reference solution for the injection was added.

PCBs from water and bovine milk - The extraction was performed by using 500 mL of sample and 15 mL of n-hexane stirred for 1 hour. The organic layer was dried with sodium sulphate and concentrated to 2 mL by using a Turbo Vap 500 concentrator. The 2 mL were passed through a glass column designed with a tap and a glass wool plug, filled with silica gel 60 (70-230 mesh), with 7 cm length. The second layer was made of 0.5 cm, silica gel 60 (20 mesh). The column was washed with 10 mL n-hexane, after which the samples was run through and the column was washed again with 5 mL n-hexane. The extract was concentrated to 1 mL and then injected into the apparatus.

Heavy metals - Into a reaction vessel 1 g of dried sample (soil or grass) and 10 mL of HCl: HNO_3 (3:1) solution were inserted and left to react for 10 minutes, and then put through the digestion process [31]. 30 mL of milk were dried and solubilized in 35 mL of HNO_3 0.3% solution and then put through the digestion process [32]. For the determination of element contents, samples were digested with a microwave oven, at 400 W, 800 PSI pressure and a temperature of 180℃, maintained for 20 minutes.

DIANA IONELA STEGARUS, ROXANA ELENA IONETE,
SIMONA OANCEA, ECATERINA LENGYEL, ADINA FRUM

Chromatographic analysis of PCBs and pesticides

A number of 7 PCB congeners (PCB28, PCB52, PCB101, PCB138, PCB153, PCB180, PCB194) and 10 organochlorine pesticides (α-, β-, δ- HCH, aldrin, dieldrin, endrin, DDE, DDD, DDT and endosulfan) were measured by a GC-MS apparatus (Varian 450-GC coupled with a Varian 240-MS external ionization ion trap MS) in the collected samples (soil, water, grass and milk). Helium (purity 99.9999%) was employed as the carrier gas at a flow rate of 1 mL/min. Chromatographic separation was performed using a CP-Sil 8 CB column (50m x 0.25mm x 0.25µm, Agilent). During the analysis, the injector and detector temperatures were maintained at 240 °C and 270 °C. The temperature of the mass spectrometer ion source was maintained at 210 °C. The oven temperature was initially set at 60 °C (maintained for 5 minutes) and continued by increasing to 280°C (at a rate of 20 °C/min). An amount of 2 µL from each sample (extracts, standards and blanks) was used for injection in the apparatus.

The determination of the recovery yield - For every batch of analyzes performed, a sample of contaminants was prepared by using known concentrations from the compounds of interest. The analytical method was validated on the working matrix. The samples were divided in quantities of 20 g each and treated with a pesticide mix of concentrations between 0.05 and 10 µg/L. For the pesticide mix recovery tests, six replicas of every concentration were determined for the analyzed soil. The calibration curve and the samples' matrix were determined in double at the concentration levels stated before.

Heavy metals analysis

Concentrations of lead, cadmium, copper and zinc were measured by a method proposed by Miedico et al. in 2017 [33]. The quantification was performed by using calibration curves, determined with analytical standards purchased from LGC Dr. Ehrenstorfer.

Statistical analysis

Data are presented as a result of three replicas. Mean, standard deviation, maximum and minimum ranges were calculated using simple statistical analysis, and the correlation of variables was done by calculation of Pearson's correlation coefficients at significance level of risk α≤5%.

ACKNOWLEDGMENTS

REFERENCES

[1]. R. Jayaraj; P. Megha; P. Sreedev; *Int. Toxicol.,* **2016**, *9(3-4)*, 90–100

[2]. Y. Liu; S. Li; Z. Ni; M. Qu; D. Zhong; C. Ye; F. Tang; *Sci. Total Environ.*, **2016**, *542(15)*, 620-628

[3]. M.G. Barron; Z.J. Ashurova; M.A. Kukaniev; H.K. Avloev; K.K. Khaidarov; J.N. Jamshedov; O.S. Rahmatullova; S.S. Atolikshoeva; S.S. Mamadshova; O. Manzenyuk; *Environ. Pollut.*, **2017**, *224*, 494-502

[4]. K. Ki-Hyun; K. Ehsanul; A.J. Shamin;, *Sci. Total Environ.*, **2017**, *575*, 525-535

[5]. O.M.L. Alharbi; A.A. Basheer; R.A. Khattab; I. Ali; *J. Mol. Liq.,* **2018**, *263*, 442-453

[6]. FAO and WHO. *Codex Alimentarius, International food standards,* adopted in 2006, revised in 2018, CXC 62-2006

[7]. O.M. Faroon; L.S. Keith; C. Smith Simon; C.T. De Rosa; *WHO*, **2003**

[8]. S. Oancea, *The impact of persistent organic pollutants on human health*, in *The impact of persistent organic pollutants on freshwater ecosystems and human health*, A. Curtean-Banaduc Ed.; *"Lucian Blaga" University of Sibiu Publisher*, Sibiu, **2016**, pp. 57-84

[9]. X. Chen; Y. Yin; K. Dang; B. Puschner; *PLoS ONE,* **2017,** 12(1): e0170129

[10]. F. Donato; M. Magoni; R. Bergonzi; C. Scarcella; A. Indelicato; S. Carasi; P. Apostoli; *Chemosphere*, **2006**, *64(9)*, 1562-1572

[11]. M.M. Storelli; C. Scarano; C. Spanu; E.P.L. De Santis; V.P. Busco; A. Storelli; G.O. Marcotrigiano; *Food Chem. Toxicol.*, **2012**, *50*, 1413–1417

[12]. A. Abballe; P.G. Barbieri; A. Di Domenico; S. Garattini; N. Iacovella; A.M. Ingelido; V. Marra; R. Miniero; S. Valentini; E. Felip, *Chemosphere*, **2013**, *90*, 49–56

[13]. P. Tremolada; N. Guazzoni; M. Parolini; B. Rossaro; M.M. Bignazzi; A. Binelli; Sci. Total Environ., **2014**, *487*, 471–480

[14]. L. Bertocchi; S. Ghidini; G. Fedrizzi; V. Lorenzi; *Environ. Sci. Pollut. R.,* **2015**, *22(13)*, 9775-9785

[15]. V. Page; U. Feller; *Agron.*, **2015**, *5*, 447-463

[16]. L. Levei; E. Kovacs; M.A. Hoaghia; A. Ozunu; *Studia UBB Chemia*, **2018**, 1, 87-98

[17]. R.M. Hategan; G.M. Popita; I. Varga; A. Popovici, T. Frentiu; *Studia UBB Chemia*, **2012**, 1, 119-126

[18]. V.D.Dimitrijevic; M.N. Stankovic; D.M. Dordevic; I.M. Krstic; M.G. Nikolic; A.I.j. Bojic; N.S. Krstic; *Studia UBB Chemia*, **2019**, 1, 19-39

[19]. M. Jaishankar; T. Tseten; N. Anbalagan; B.B. Mathew; K.N. Beeregowda; *Int. Toxicol.*, **2014**, *7(2)*, 60–72

[20]. K. Rehman; F. Fatima; I. Waheed; M.S.H. Akash; *J. Cell. Biochem.*, **2018**, *119(1)*, 157-184

[21]. D.M. Popa; M. Moldovan; D. Prodan; C. Aldea; C. Lazar; C. Lazea; M. Crisan; L.M. Sur; S.C. Man; C. Borzan; *Environ. Geochem. Health*., **2020**, DOI:10.1007/s10653-020-00750-9

[22]. F. Miculescu; M. Miculescu; L.T. Ciocan; A. Ernuteanu; I. Antoniac; I. Pencea; E. Matei; *Dig. J. Nanomater. Bios*., **2011**, *6(3)*, 1117-1127

[23]. Ministry of Water, Forests and Environmental Protection, Order no. 756/1997, *Romanian Official Monitor*, 1997, revised in 2011

[24]. **Directive 2002/32/EC of the European Parliament and of the Council of 7 May 2002**, *Official Journal of the European Union*, **2002**, *L140*, 10-21

[25]. Commission Regulation (EC) No 1259/2011 of 2 December, *Official Journal of the European Union*, **2011**, *L320*, 18–23

[26]. Commission Regulation (UE) nr. 574/2011 of 16 June 2011, *Official Journal of the European Union*, **2011**, *L159*, 7-24

[27]. Romanian Parliament, Law no. 311/2004, *Romanian Official Monitor*, **2004**

[28]. National Sanitary, Veterinary and Food Safety Authority, Order no. 23/2007, *Romanian Official Monitor*, **2007**

[29]. H. Deti; A. Hymete; A.A. Bekhit; A.M.I. Mohamed; A.E.D.A. Bekhit; *Chemosphere*, **2014**, *106*, 70-74

[30]. Romanian Ministry of the Environment and Water Management, Order no. 344/2004, *Romanian Official Monitor*, **2004**

[31]. L. Yun; K.B. Jensen; Larson. *J. Agr. Sci.Bot.*, **2018**, *2(1)*, 19- 24

[32]. A. Ayar; D. Sert; N. Akin; *Environ. Monit. Assess.*, **2009**, *152*, 1-12

[33]. O. Miedico; M. Iammarino; M. Tarallo; A.E. Chiaravalle; *Int. J. Food Prop.*, **2017**, *20(12)*, 2888-2900

ADSORPTION AND CORROSION INHIBITIVE PROPERTIES OF *ORYZA GLABERRIMA* HUSK EXTRACT ON ALUMINIUM IN H_2SO_4 SOLUTION: ISOTHERM, KINETIC AND THERMODYNAMIC STUDIES

LEKAN TAOFEEK POPOOLA[a*]

ABSTRACT. In this study, isotherm, kinetic and thermodynamic studies of corrosion inhibitory properties of *Oryza Glaberrima* husk extract (OGHE) on aluminium in 1.5 M H_2SO_4 solution was investigated via mass loss measurement. Aluminium coupon and OGHE were characterized using SEM, EDS, FTIR and AAS. Increase in Al corrosion rate in H_2SO_4 solution was observed as exposure period (24 - 120 hrs) and temperature (293 - 333K) were increased but decreased with pH (2 - 6). Corrosion inhibition efficiency of OGHE is a function of its concentration and ability to be easily absorbed on Al surface to form thick protective films against H_2SO_4 attack. Adsorption of OGHE molecule on Al surface in 1.5 M H_2SO_4 solution agrees excellently well with Langmuir isotherm. Thermodynamic study revealed the adsorption process to be spontaneous, endothermic and physisorption in nature. Kinetic study affirmed adsorption of OGHE molecule on Al surface to obey second order reaction. Appropriate corrosion mechanisms of Al dissolution in H_2SO_4 and in the presence of OGHE were proposed. This study proved positive prospects of OGHE as effective corrosion inhibitor for Al in acidic medium.

Keywords: Aluminium, Sulphuric acid, Oryza Glaberrima, Corrosion, Inhibition

INTRODUCTION

It's no more new around the globe that corrosion is a deadly phenomenon [1] which could lead to loss of lives and properties. It also adversely affects the economy of developing and developed nations due to costs normally

---

[a] *Unit Operation and Material Science Laboratory, Chemical and Petroleum Engineering Department, Afe Babalola University, Ado-Ekiti, Ekiti State, Nigeria.*
* *Corresponding author: popoolalekantaofeek@yahoo.com*

assigned to replacement of damaged materials [2]. Thus, all hands must be on desk to safe our materials (metals and alloys) from corrosion. Among these materials that is abundantly available and cut across edges of processing industries is the aluminium (Al) due to its lightness; versatility; highness in corrosion resistance, conductivity and reflectivity; non-ferromagnetic and non-pyrophoric; non-toxic; attractiveness; recyclability and easily fabricated characteristics [3]. Also, the significance of sulphuric acid in process industries cannot be ignored due to its application in cleaning, oil wet cleaning, descaling and pickling [4]. Thus, availability of Al in abundance and its aforementioned properties qualify its application in aggressive medium (such as sulphuric acid solution) which causes its corrosion over time. This prompted researchers to investigate cheap and environmental friendly corrosion inhibition approaches of Al via the use of extracts from greeners as corrosion inhibitors for aluminium in sulphuric acid solution [3, 5-15]. They are blessed with organic compounds enriched with nitrogen, phosphorus, sulphur and/or oxygen which act as agents for aluminium steel surface protection from corrosion when absorbed (physically or chemically) on its surface via π bonds, heterogeneous atoms or aromatic rings [16].

Recently, studies have investigated isotherm, kinetic and thermodynamic nature of *Dryopteris cochleata* [14], *Solanummelongena L.* [8], *Euphorbia hirta* [10], *Anthocleista djalonesis* [17], *Spondias mombin* [11], *Ocimum gratissium* [18] and *Azadirachta indica* [12] plant extracts as corrosion inhibitors for aluminium in H_2SO_4 solution. However, there were none or limited studies on isotherm, kinetic and thermodynamic characteristics of rice husk extract as corrosion inhibitor for aluminium in sulphuric acid solution. Also, most previous studies only applied Langmuir isotherm to check for data fitness of existing interaction between adsorbed molecules of inhibitors and metal surface. They rarely examined other isotherm models for comparison purpose to reveal the best fit model. Recently, *Oryza Glaberrima* husk has been shown to be very rich in silicates which contain phenolic compounds that have strong affinity to form thick films on metal surface when absorbed and thus, prevent it from corrosion under acidic attack [15, 19-20]. This study uniquely investigated isotherm, kinetic and thermodynamic studies of corrosion inhibition of aluminium in 1.5 M sulphuric acid solution using *Oryza Glaberrima* husk extract (OGHE) as corrosion inhibitor. In this study, Langmuir, Freundlich, Frumkin, Temkin and Flory-Huggins isotherm models were used to validate experimental data. Characterization of aluminium and extract was done using SEM, EDS, FTIR and AAS.

RESULTS AND DISCUSSION

Aluminium coupon and OGHE characterization

SEM

Scanning electron microscope image revealed serious corrosion attack (leading to pitting corrosion) on Al surface in 1.5 M H_2SO_4 in the absence of OGHE (Figure 1a) resulting from the formation of aluminium sulphide complexes ($[AlSO_4]^+$ and $[AlOHSO_4]$) during dissolution of Al and H_2SO_4. It was obvious that Al surface porosity increased coupled with formation of small holes. Protective film formation as a result of OGHE molecules adsorption on Al surface serves as a barrier between Al surface and H_2SO_4 and thus, prevents it from corrosion attack (Figure 1b).
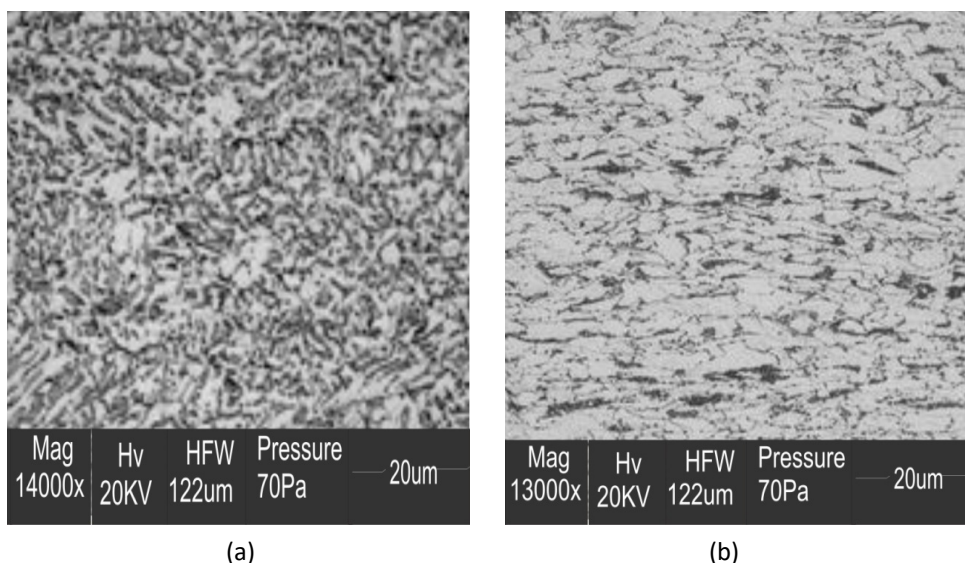

| Mag 14000x | Hv 20KV | HFW 122um | Pressure 70Pa | 20um |
| (a) |

| Mag 13000x | Hv 20KV | HFW 122um | Pressure 70Pa | 20um |
| (b) |

Figure 1. SEM micrographs of Al surfaces (a) after immersion in 1.5 M H_2SO_4 solution in the absence of OGHE and (b) after immersion in 1.5 M H_2SO_4 solution in the presence of 1.0 g L^{-1} OGHE for 24 h at 303 K

FT-IR

Table 1 presents wavelengths and respective assignments of sharp peaks from the FT-IR analysis executed for the OGHE and corrosion products of Al in 1.5 M H_2SO_4 and 1.0 g L^{-1} OGHE. The major assignments which have high significant contributions in corrosion inhibition of Al in H_2SO_4 solution with 1.0 g L^{-1} of OGHE are peaks at: (1) 4117.84 - 3428.15 cm^{-1} attributed to

-OH stretching of phenols and alcohols. (2) 2522.20 - 2861.88 cm^{-1} resulted from N-H stretching of amine. (3) 893.7 cm^{-1} attributed to Al=S stretching resulting from covalent bond between Al and S during dissolution of Al in the corrosive medium. (4) 615.35 – 644.93 cm^{-1} attributed to Si-O stretching resulting from covalent bond between free silicon from OGHE silicate and free valent oxygen in aqueous solution. and (5) 415 cm^{-1} resulting from Al=O stretching as a result of strong electrovalent bond between dissolved Al and oxygen during its dissolution in H_2SO_4 solution in the absence of OGHE. Above all, shift in the values of peaks at different wavelengths is a strong indication of OGHE adsorption onto Al surface in 1.5 M H_2SO_4.

Table 1. Wavenumbers and assignments of FTIR sharp peaks for OGHE; and Al corrosion products in 1.5 M H_2SO_4 and 1.0 g/L OGHE

FT-IR Wavenumber (cm^{-1})		Assignments	References
OGHE	Corrosion products of Al in 1.5 M H_2SO_4 + 1.0 g/L OGHE		
4103.72	4117.84	-OH stretching vibration of phenols and alcohols	[21]
3428.15	3432.78	-OH stretching of phenols and alcohols	[14]
2861.88	2522.2	N-H stretching of amine	[7]
1777.38	1781.59	-C=O stretching of aliphatic ketone	[21]
1536.02	1470.08	COO$^-$ stretching vibration	[4]
1386.20	-	NO$_2$ stretching vibration	[22]
-	1041.41	CO-O-CO stretching of anhydride	[7]
-	893.47	Al=S stretching	[23]
615.35	644.93	Si-O stretching	[24]
-	415	Al=O stretching	[24]

EDS

Table 2 presents the results of the energy dispersive spectroscopy analysis at certain points on the surface of Al coupon in (a) its purchased form (b) the presence of 1.5 M H_2SO_4 and (c) the presence of 1.0 g L^{-1} of OGHE with 1.5 M H_2SO_4. The following are strong evidences of Al loss to H_2SO_4 solution during dissolution in corrosive medium: (1) reduction in the weight percent of Al from 97.77 % (in its original form) to 90.04 % (in corrosive medium) (2) presence of sulphur, oxygen and hydrogen on Al surface which could be traced to corrosion attack from H_2SO_4 as these are major elements of

the acid in solution and (3) reduction in the weights of alloys of Al (except Si) during the dissolution of parent Al. The reason behind increase in the weight percent of silicon is opened for further studies. Though there was loss of Al to solution with presence of S, O and H on Al surface when 1.0 g L^{-1} of OGHE was added, the weight percentages in this regard were very minute. This proved the efficacy of OGHE to form protective films on Al surface acting as barrier between it and corrosive H_2SO_4 solution. This in return prevents the Al surface from pitting and restricts formation of small holes.

Table 2. Energy dispersive spectroscopy analysis of Al coupon in (a) purchased form (b) 1.5 M H_2SO_4 and (c) 1.5 M H_2SO_4 + 1.0 g L^{-1} OGHE

Element	Aluminium Sample (mass wt %)	Aluminium Sample in 1.5 M H_2SO_4 (mass wt %)	Aluminium Sample in 1.5 M H_2SO_4 + 1 g L^{-1} OGHE (mass wt %)
Al	97.77	90.04	97.68
S	-	3.91	0.11
O	-	2.81	0.090
H	-	1.37	0.089
Mg	1.12	0.91	1.03
Si	0.49	0.52	0.55
Mn	0.47	0.33	0.33
Fe	0.099	0.086	0.096
Zn	0.019	0.0092	0.0063
Ti	0.0096	0.0059	0.0082
Cu	0.0154	0.0044	0.0047
Cr	0.0043	0.0027	0.0036
Pb	0.0027	0.0018	0.0022

AAS

Figure 2 is the pictorial representation of the results of atomic adsorption spectroscopy analysis conducted to confirm concentration of Al^{3+} loss to H_2SO_4 solution during Al dissolution in the absence of OGHE. In contrary, Al^{3+} concentration was also checked in the presence of OGHE in H_2SO_4 to ascertain the effectiveness of OGHE as corrosion inhibitor for Al in this corrosive medium. The result revealed increase in Al^{3+} concentration in H_2SO_4 solution from 0.17 to 0.87 ppm as the exposure time increased from 24 to 120 hours. Thus, the higher the exposure period in the absence of OGHE, the higher the Al^{3+} concentration. However, reduction in Al^{3+} concentration in H_2SO_4 solution in the presence of OGHE was noticed as Al^{3+} concentration reduced

from 0.17 to 0.0096 ppm and 0.87 to 0.0696 ppm at 24 and 120 hours respectively. This affirms that OGHE is effective in minimising corrosion rate of Al in the acidic medium.
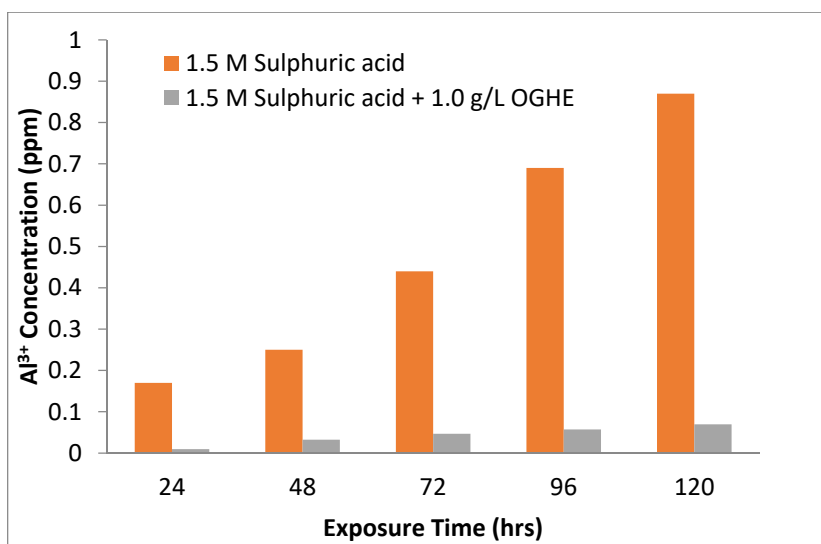

Figure 2. Al^{3+} variation after exposure period at 24 hrs interval in 1.5 M sulphuric acid solution in the absence and presence of OGHE

Effect of solution pH

The results showing pH effect (2, 4 and 6) of 1.5 M H_2SO_4 on corrosion rate of Al (Figure 3a) and inhibition efficiency of OGHE (Figure 3b) at constant temperature, exposure time and OGHE concentration of $40^{\circ}C$, 24 hours and 0.6 g L^{-1} respectively have been presented. Sodium hydroxide pellets was used to vary the pH of the acidic medium. The result revealed decrease in the rate of corrosion of Al from 2.718 to 0.982 mm y^{-1} as the solution pH increases from 2 to 6 while OGHE inhibition efficiency increases from 33.48 to 64.83% in this trend. These are strong indications of high activeness of the sulphuric acid to attack the Al substrate at low pH and OGHE to protect the Al surface from acidic attack at high pH via formation of protective films. Similar trends have been presented previously [6,9].
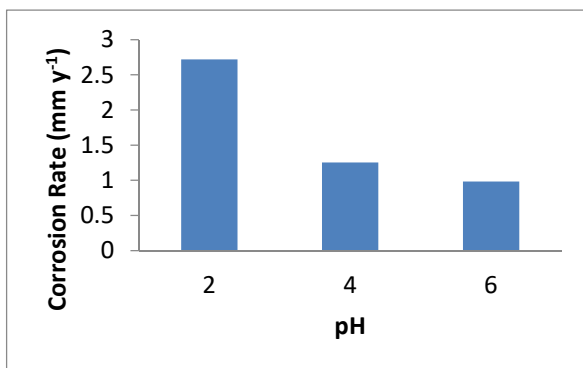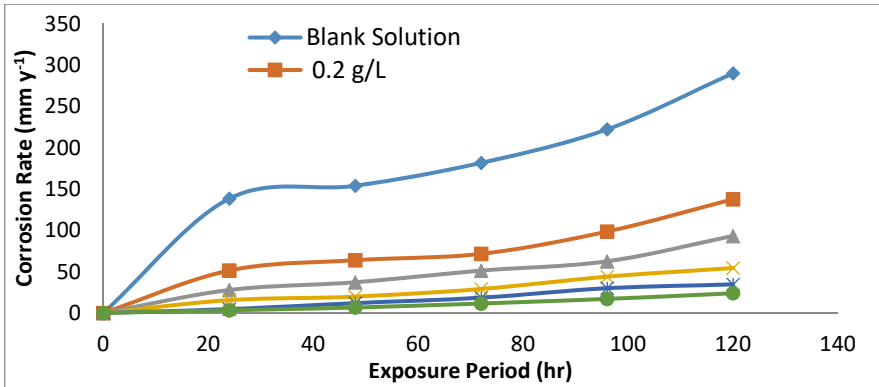
(a)
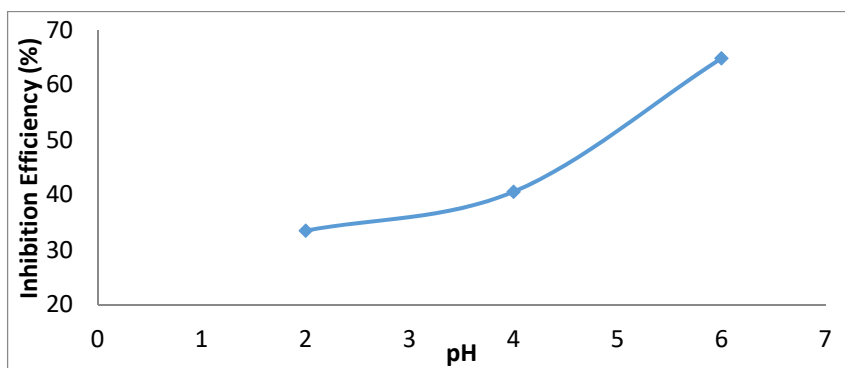
(b)

Figure 3. Effect of H_2SO_4 solution pH on (a) corrosion rate of Al and (b) inhibition efficiency of OGHE
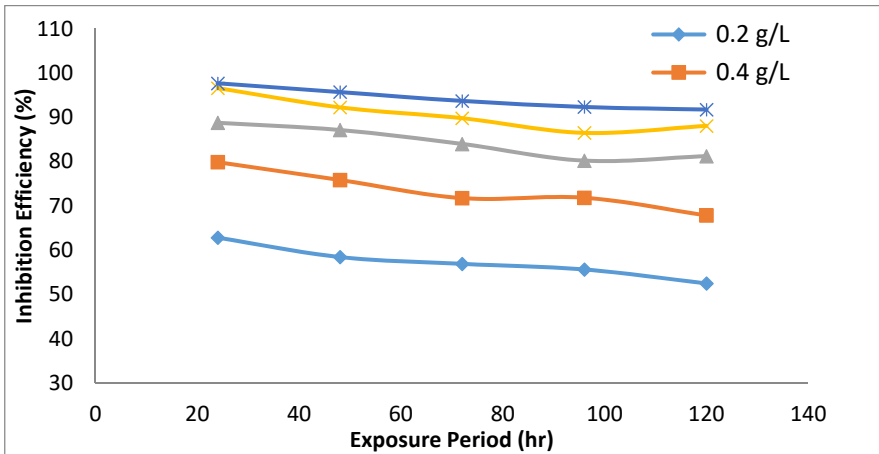
Effect of exposure period and OGHE concentration

Figure 4 presents the results showing the effect of exposure period of Al in 1.5 M H_2SO_4 solution on the corrosion rate (Figure 4a) and inhibition efficiency of OGHE (Figure 4b) at varying exposure period of 24, 48, 72, 96 and 120 hours and OGHE concentration of 0.2, 0.4, 0.6, 0.8 and 1.0 g L^{-1}. It was observed that the corrosion rate increases as the exposure period progresses but it decreases with increase in OGHE concentration (Figure 4a). This exhibition could be linked to blockage of Al surface from H_2SO_4 attack by increase protective films formation as the concentration of OGHE increases. The corrosion rate reduced from 289.99 mm y^{-1} (blank solution) to 23.93 mm y^{-1} (in the presence of 1.0 g L^{-1} of OGHE) after exposure period of 120 hours. Similar study had presented similar result [23].

Contrary result was observed for the inhibition efficiency of OGHE used as corrosion inhibitor as its capacity to block corrosion sites on the Al reduces as the exposure period increases. However, OGHE exhibited high inhibition efficiency of 91.75% when its concentration was increased to 1.0 g L^{-1} after Al was placed in 1.5 M H_2SO_4 solution for 120 hours. This affirms the effectiveness of OGHE at high concentration as good corrosion inhibitor for Al in 1.5 M H_2SO_4 solution. Previous study presented similar trend when *Dryopteris cochleata* leaf extracts was used as green corrosion inhibitor for aluminium in 1 M H_2SO_4 solution [14].

(a)

(b)

Figure 4: Effect of exposure period and OGHE concentration on (a) corrosion rate of Al and (b) inhibition efficiency of OGHE in 1.5 M H_2SO_4 solution

Temperature effects, isotherm and thermodynamic studies

The significance of studying the effects of temperature is to have thorough knowledge of adsorptive characteristics of green corrosion inhibitor molecules on metal surface when subjected to different temperature conditions [25]. Nevertheless, it's a major tool in thermodynamic and activation parameters calculation for the corrosion process. The effect of temperature on corrosion rate of Al in 1.5 M H_2SO_4 solution in the presence and absence of OGHE was examined. Also, adsorptive nature of OGHE molecules on Al surface at different temperature was investigated via inhibition efficiency measurement. Experiment was conducted at 293, 303, 313, 323 and 333K for varying OGHE concentrations of 0.2, 04, 0.6, 0.8 and 1.0 g L^{-1} while other parameters (pH = 2.0 and exposure period = 24 hours) were held constant. Increase in corrosion rate was observed in both the blank solution and presence of OGHE at different concentrations as the temperature increases (Figure 5a). Also, decrease in OGHE inhibition efficiencies was exhibited as the temperature was increased from 293 to 333 K (Figure 5b). However, the efficacy of used OGHE was displayed as its inhibition efficiency increases with increase in its concentration in H_2SO_4 solution. This affirms partial desorption of OGHE adsorbed molecules on Al surface at higher temperatures. This enhances exposure of Al surface to the corrosive medium and thus, manifested in the reduction of OGHE inhibition efficiency as solution temperature increases. However, inhibition efficiency of 88.60 % was recorded (even at high solution temperature of 333 K) when 1.0 g L^{-1} of OGHE was applied. This assures applicability of OGHE as excellent corrosion inhibitor even at relatively higher temperatures. Previous studies had presented similar results [18, 26].

Adsorption isotherm study gives insight into the nature of adsorption process showing the type of interaction existing between adsorbed molecules of green corrosion inhibitor (GCI) and metal surface which prevents its attack in aggressive media [23]. Research has shown influential factors to include: aggressive media type; chemical structures present in organic compounds of GCI; GCI molecules charge distribution; and surface charge available on metal type [5]. In this study, adsorption of OGHE molecules onto Al surface was achieved via replacement of adsorbed water molecules (H_2O_{ads}) on Al surface with OGHE molecules in aqueous phase ($OGHE_{soln}$) as written in Equation 4.

$$OGHE_{soln} + xH_2O_{ads} \longrightarrow OGHE_{ads} + xH_2O_{soln} \tag{4}$$

where $OGHE_{ads}$ stands for adsorbed OGHE molecules, H_2O_{soln} is the water molecules in solution and *x* is the number of replaced water molecules by unit molecule of adsorbed OGHE. A balanced adsorption process is then achieved when the chemical potential on both sides is the same.
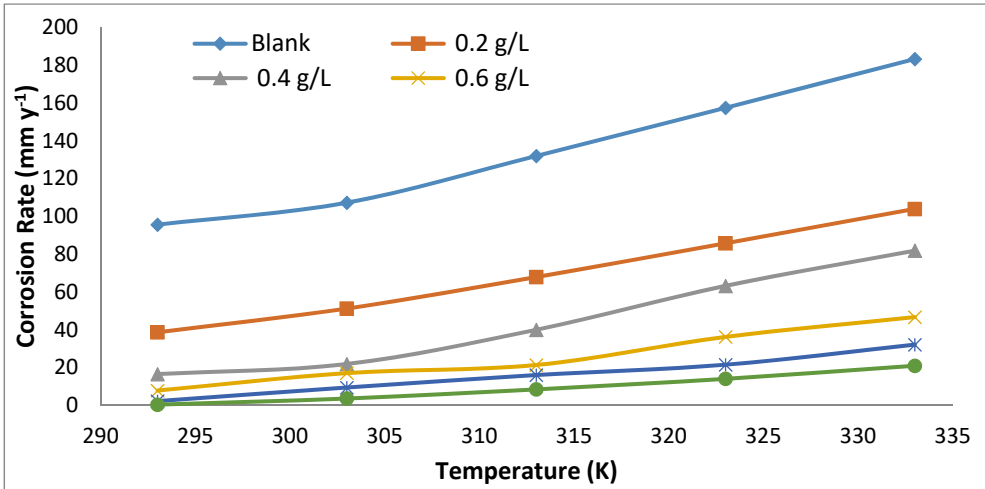
(a)
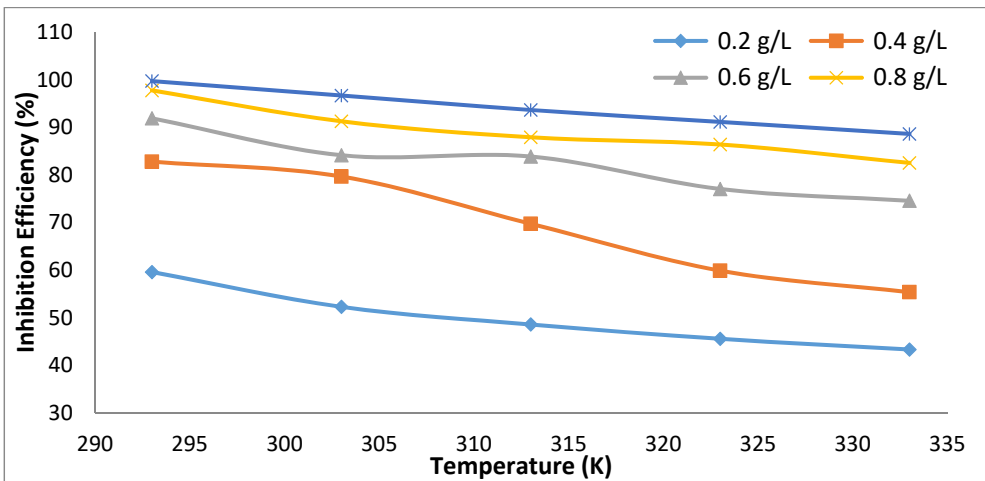
(b)

Figure 5. Effect of temperature on (a) corrosion rate of Al in H_2SO_4 solution and (b) inhibition efficiency of OGHE

In this study, linear forms of Langmuir, Freundlich, Frumkin, Temkin and Flory-Huggins stated as Equations 5-9 respectively were used to investigate nature of interaction existing between OGHE (green corrosion inhibitor) and Al surface.

$$\frac{C_{inh}}{\theta} = \frac{1}{K_{ads}} + C_{inh} \tag{5}$$

$$\log \theta = \log K_{ads} + n \log C_{inh} \qquad (0 < n < 1) \tag{6}$$

$$\log \left[C_{inh} \times \left(\frac{\theta}{1-\theta} \right) \right] = 2.303 \log K_{ads} + 2\alpha\theta \tag{7}$$

$$\theta = \frac{2.303 \log K_{ads}}{2a} - \frac{2.303 \log C_{inh}}{2a} \tag{8}$$

$$\log \left(\frac{\theta}{C_{inh}} \right) = \log K_{ads} + x \log (1-\theta) \tag{9}$$

where C_{inh} represents OGHE concentration (g L^{-1}), K_{ads} is the adsorption equilibrium constant (g^{-1} L), θ is the surface coverage, n is a constant that measures degree of heterogeneity, α is a constant that reveals adsorbed layer nature, a is the parameter of attractiveness and x is parameter size which measures adsorbed water molecules quantity displaced by molecules of inhibitor.

Based on the result obtained (Table 3) for all plotted isotherm models (Figures 6(a)-(e)), Langmuir revealed highest R^2 value (absolutely close to unity) at all temperatures examined which substantiates it as the model that best describes the experimental data. This suggests adsorption of OGHE on Al surface assumed a mono layer adsorption (each adsorption site on solid surface is attached to one adsorbed species) [27]. Similar study also revealed Langmuir as the best isotherm model for corrosion inhibition of aluminium alloys in acidic media [28]. Also, values of K_{ads} (Langmuir) decreases as the temperature increases which revealed reduction in the inhibition efficiency of OGHE in this trend (Table 3). Value of K_{ads} is a measure of adsorptive strength of inhibitors on metal surface. The higher the values of K_{ads}, the better the adsorption and inhibition efficiency [29].

Nonetheless, parameters from other isotherms (besides Langmuir) have their significance on isotherm study of OGHE on Al in H_2SO_4 solution irrespective of their low R^2 values. The values of lateral interaction constant (α) obtained from Frumkin isotherm were all positive at investigated temperatures (Table 3) which suggests OGHE efficacy as good corrosion inhibitor for Al in aggressive media [30]. Values of attractive parameter (a) gotten from Temkin isotherm were all negative (Table 3) suggesting existence of repulsive forces between adsorbed layer of OGHE molecules on Al surface and sulphuric acid

[10]. Also, values of size parameter (x) obtained from Flory-Huggins isotherm were all positive (Table 3) which proves the bulkiness of OGHE adsorbed species [31].
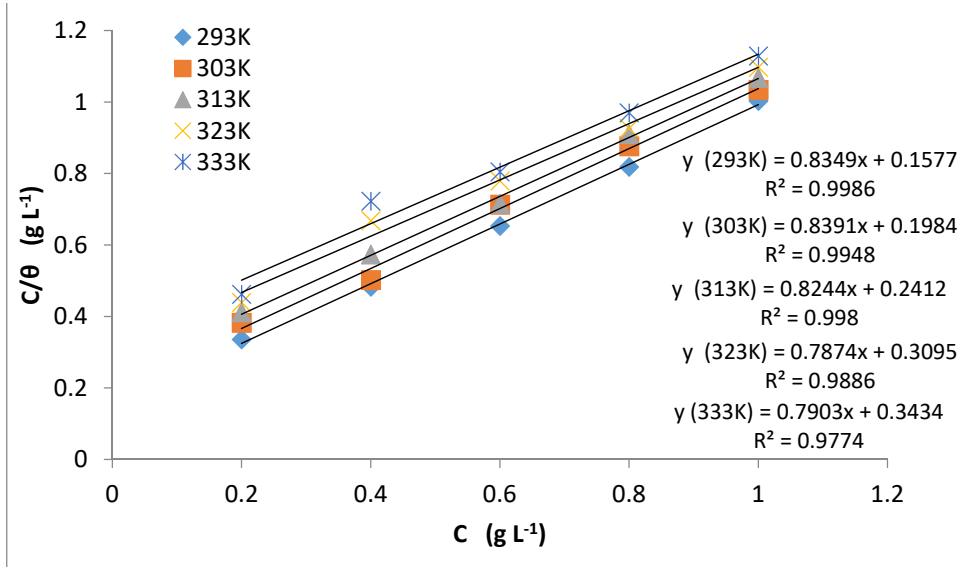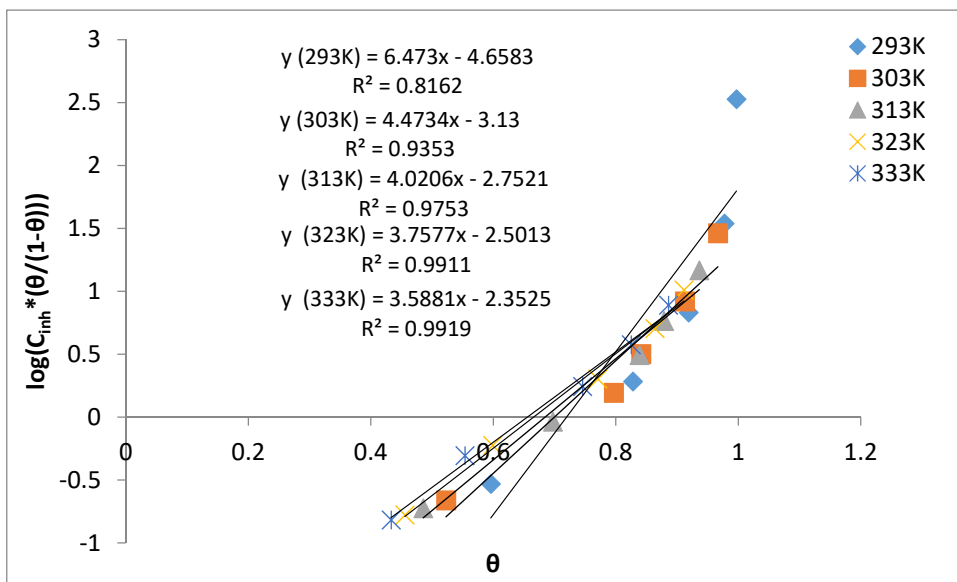

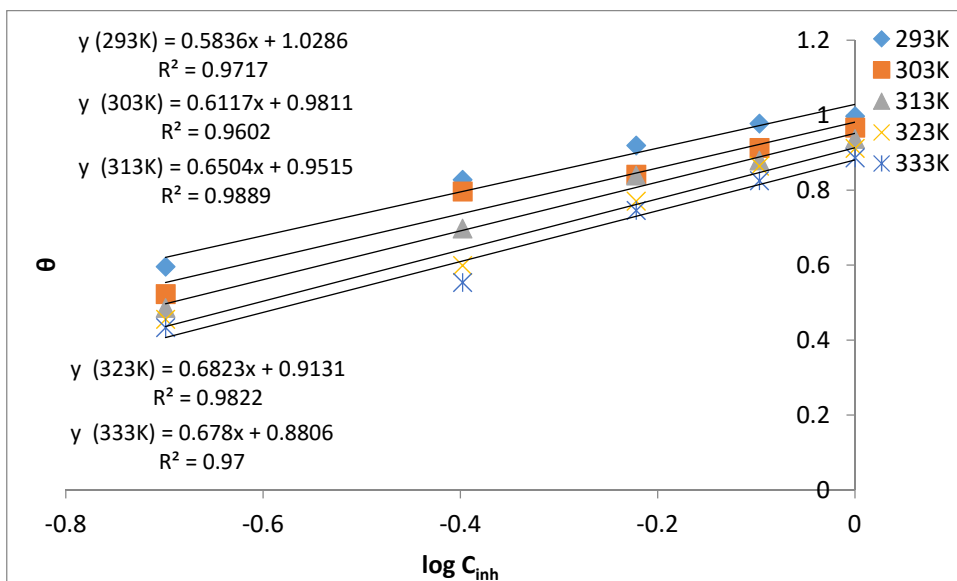
(a)
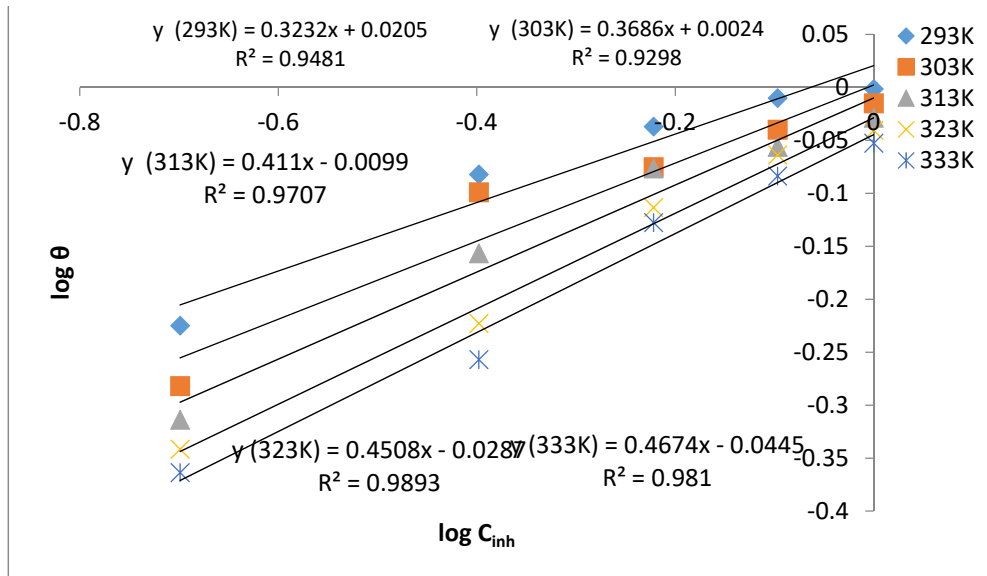
(b)

(c)

(d)
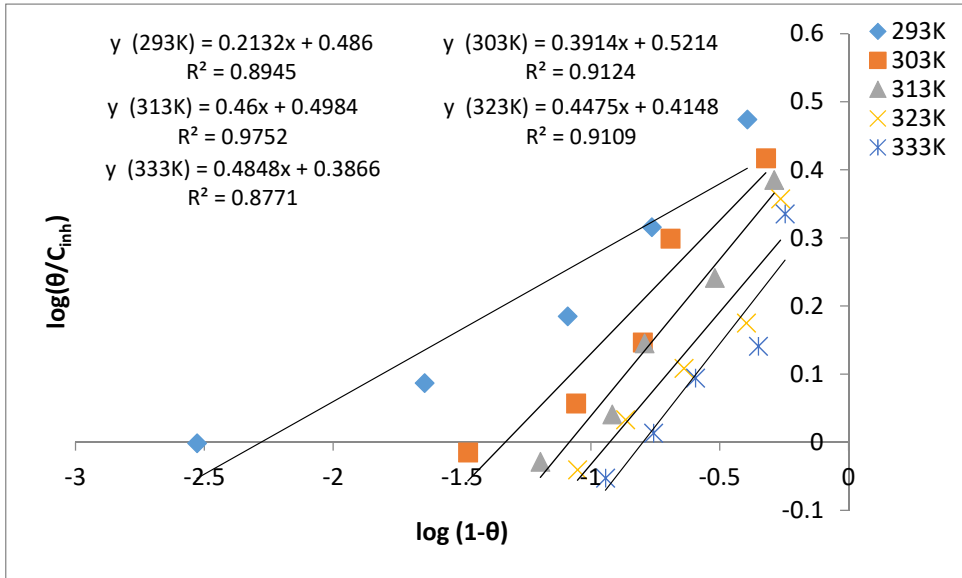
(e)

Figure 6: Isotherm study of OGHE adsorption onto Al in 1.5 M H_2SO_4 using (a) Langmuir (C_{inh}/θ vs. C_{inh}) (b) Freundlich (log θ vs. log C_{inh}) (c) Frumkin (log ($C_{inh}*(\theta/1-\theta)$) vs. θ) (d) Temkin (θ vs. log C_{inh}) and (e) Flory-Huggins (log (θ/C_{inh}) vs. log (1-θ)) isotherm models.

Table 3. Isotherm parameters of OGHE adsorption onto Al surface in 1.5 M H_2SO_4

T (K)	Langmuir		Freundlich			Frumkin			Temkin			Flory-Huggins		
	$K_{ads}{}^a$	R^2	K_{ads}	n	R^2	K_{ads}	α	R^2	K_{ads}	a	R^2	K_{ads}	x	R^2
293	6.34	0.999	1.05	0.323	0.948	0.009	3.237	0.816	0.017	-1.973	0.972	3.062	0.213	0.895
303	5.04	0.995	1.01	0.369	0.930	0.044	2.237	0.935	0.025	-1.882	0.960	3.322	0.391	0.912
313	4.15	0.998	0.98	0.411	0.971	0.064	2.010	0.975	0.034	-1.770	0.989	3.151	0.460	0.975
323	3.23	0.987	0.94	0.451	0.989	0.082	1.879	0.991	0.046	-1.688	0.982	2.599	0.448	0.911
333	2.91	0.977	0.90	0.467	0.981	0.095	1.794	0.992	0.050	-1.698	0.970	2.436	0.485	0.877

$^aK_{ads}$: g^{-1} L

The values of adsorption equilibrium constant (K_{ads}) obtained at different temperatures (Table 3) from the best fit isotherm (Langmuir) were used in determining thermodynamic adsorption parameters. The free energy of adsorption (ΔG^o_{ads}) was determined by solving Equation 10 at varying temperatures and K_{ads} values. The heat of adsorption (ΔH^o_{ads}) was determined from slope of a plot of $\Delta G^o_{ads}/T$ against $1/T$ using Equation 11. Gibbs-Helmholtz equation stated as Equation 12 was used to calculate the enthalpy of adsorption while Equation 13 was used to calculate the entropy of adsorption (ΔS^o_{ads}).

$$\Delta G^o_{ads} = -RTIn(55.5K_{ads}) \tag{10}$$

$$\frac{\Delta G^o_{ads}}{T} = -\frac{\Delta H^o_{ads}}{T} + \text{constant} \tag{11}$$

$$\frac{\partial \Delta G/T}{\partial T} = -\frac{\Delta H}{T^2} \tag{12}$$

$$\Delta G^o_{ads} = \Delta H^o_{ads} - T\Delta S^o_{ads} \tag{13}$$

where R = molar gas constant (8.314 $Jmol^{-1}K^{-1}$) , T = absolute temperature (K) and 55.5 = constant value denoting water concentration in solution (mol dm^{-3}).

It was observed that all the values of ΔG^o_{ads} obtained at the examined temperatures were all negative (Table 4) which suggests adsorption of OGHE on Al surface to be spontaneous with formation of stable protective film layers which protect metal surface from H_2SO_4 attack [32]. Also, values of ΔG^o_{ads} being less that -20 kJ mol^{-1} suggest existence of electrostatic attractive force of interaction (physisorption) between OGHE charged molecules and charged Al [33]. The value of ΔH^o_{ads} obtained via the linear plot of $\Delta G^o_{ads}/T$ against $1/T$ (Figure 7) was negative which signifies that the adsorption of OGHE molecules onto Al surface was exothermic in nature. Also, measured absolute value of ΔH^o_{ads} within the temperature range was less than 40 kJ mol^{-1} suggesting corrosion inhibition of Al in H_2SO_4 solution was as a result of physical adsorption of OGHE on Al surface. Nonetheless, mean positive value of ΔS^o_{ads} suggest substitution process between

adsorbed water molecules (H_2O_{ads}) on Al surface and OGHE molecules in aqueous phase ($OGHE_{soln}$) to cause rise in solvent entropy coupled with additional water desorption entropy [33].

Table 4. Thermodynamic parameters of OGHE adsorption
onto Al surface in 1.5 M H_2SO_4

T (K)	K_{ads}	ΔG^o_{ads} (kJ mol^{-1})	R^2	ΔH^o_{ads} (kJ mol^{-1})	ΔS^o_{ads} (J mol^{-1} K^{-1})
293	6.34	-14.28	0.992	-16.28	97.362
303	5.04	-14.19			
313	4.15	-14.15			
323	3.23	-13.93			
333	2.91	-14.08			
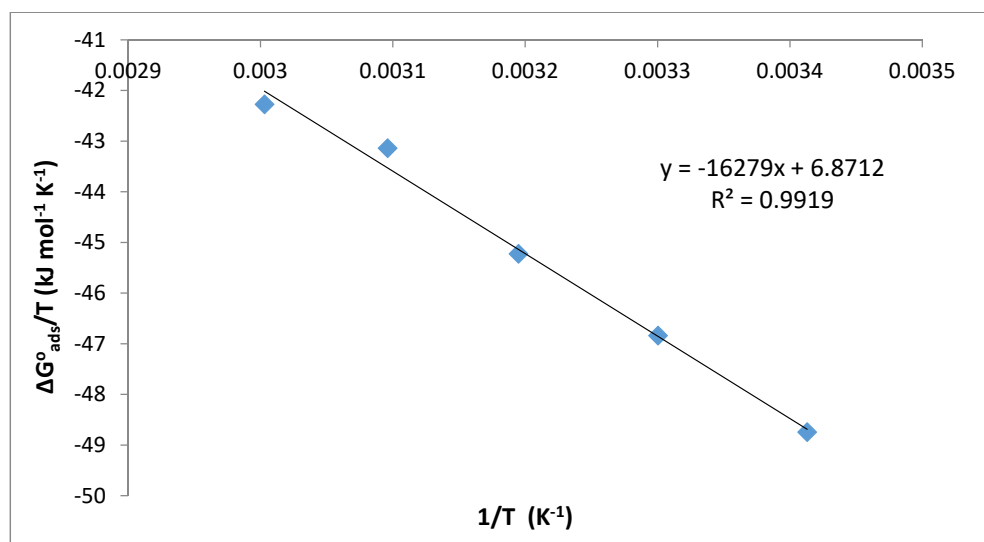
Figure 7. Plot of ΔG^o_{ads}/T vs. 1/T to determine ΔH^o_{ads} and ΔS^o_{ads} as thermodynamic parameters of OGHE adsorption onto Al surface in 1.5 M H_2SO_4

Kinetics and order of reaction

Analysis of kinetic data of corrosion reaction is imperative due to its heterogeneous nature (cathodic and anodic reaction pathways). To achieve this, determination of rate constants and half life parameters are required to identify the order of reaction. Table 5 presents the results of half life and rate constants obtained from first order plot (*ln (W_1 - W_2) vs. t*) presented as Figure 8a

and second order plot (t/W_2 vs. t) presented as Figure 8b via Equations 14 - 16 respectively [15] at varying OGHE concentrations (0.2 – 1.0 g/L), time (24 - 120 hours) and constant temperature of 313 K in 1.5 M H_2SO_4 solution.

$$t_{1/2} = \frac{0.693}{k} \tag{14}$$

$$\ln(W_1 - W_2) = -kt + \ln W_1 \tag{15}$$

$$\frac{t}{W_2} = \frac{1}{k_2 W_1^2} + \frac{t}{W_1} \tag{16}$$

where W_1 = initial weight of the metal (g), W_2 = final weight of the metal (g), k = rate constant, t = exposure time (h) and $t_{1/2}$ = half life.

The result (Table 5) revealed increase in rate constants for both order of reactions as the inhibitor concentration increases with decrease in corrosion rate. This substantiates the effectiveness of OGHE as corrosion inhibitor for Al in H_2SO_4. Also, the half-life decreases as the OGHE concentration increases which indicates decrease in the time required for Al to corrode to half of its initial weight resulting from its protection by OGHE extract via adsorption. Approximately unity values were obtained for R^2 of proposed second order linear model (Table 5) which supports it as the model that best describes the order of the corrosion reaction of Al in H_2SO_4 in the presence of OGHE. However, previous studies rarely considered this proposed second order linear model. They usually present first order linear model (Equation 15) as the best model for R^2 values between 0.930 and 0.980 [31, 34-35]. In this study, similar result was also revealed for the linear first order kinetic model as R^2 ranges between 0.930 and 0.992.

Results revealed by both first and second order kinetic linear models was substantiated via application of rate order reaction equation (Equation 17) to determine order of reaction (n). The linearized form of the equation is presented as Equation 18. The experiment was conducted for 120 hrs at 24 hrs time interval to obtain a linear plot of $\ln r_c$ vs. $\ln C_{inh}$ (Figure 9) such that the slope of each plot is the order of reaction. The result revealed all values of n to be greater than 1 with minimum and maximum values being 1.0898 and 1.7561 (Table 6) respectively. The order of reaction can be approximated to be 2 which affirms the result earlier presented.
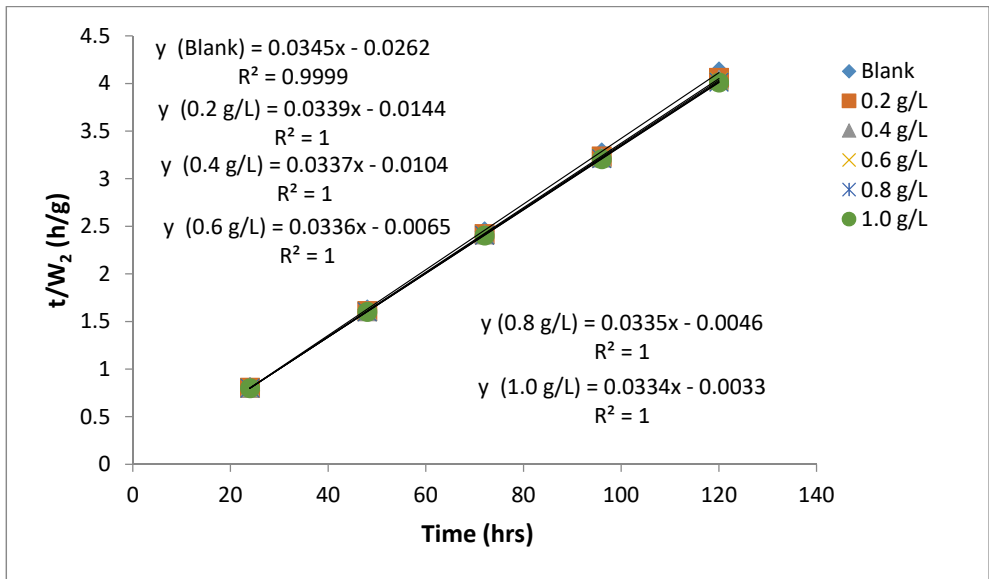
$$r_c = kC_{inh}^n \tag{17}$$

$$\ln r_c = \ln k + n \ln C_{inh} \tag{18}$$

where r_c is the rate of corrosion (mm y^{-1}), k is the reaction constant, n is the order of reaction and C_{inh} is concentration of OGHE (g L^{-1}).
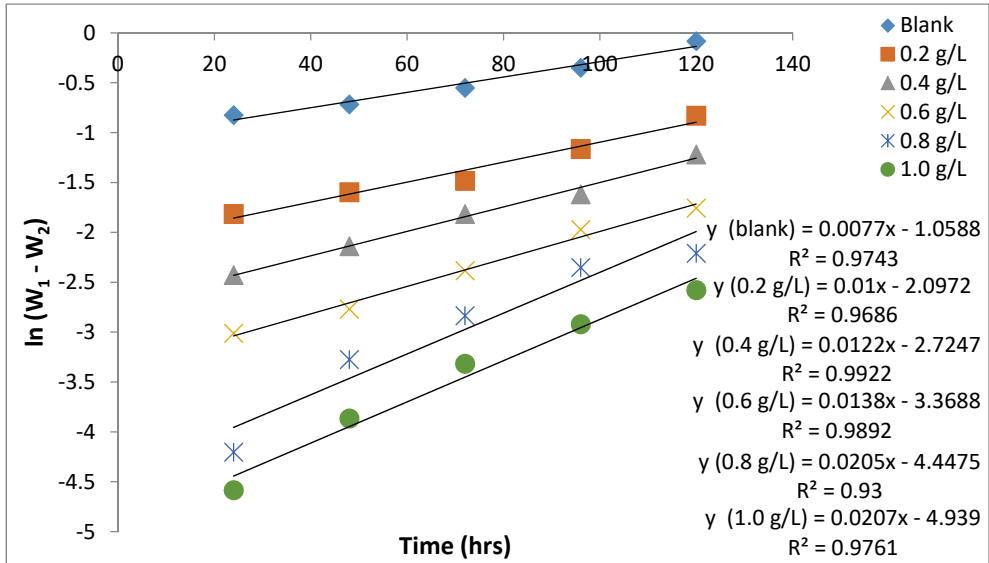
(a)

(b)

Figure 8. Kinetic study of OGHE adsorption onto Al surface in 1.5 M H_2SO_4 using (a) first order and (b) second order linear models

Table 5. Kinetic parameters of OGHE adsorption onto Al surface in 1.5 M H_2SO_4

System	First order			Second order		
	$k_1 \times 10^{-2}$ (hr^{-1})	$t_{1/2}$ (hr)	R^2	$k_2 \times 10^{-2}$ (g^{-1}hr^{-1})	$t_{1/2}$ (hr)	R^2
Blank	0.77	90.00	0.974	4.54	15.25	0.999
0.2 g/L	1.01	69.30	0.969	7.98	8.68	1.000
0.4 g/L	1.22	56.80	0.992	10.92	6.35	1.000
0.6 g/L	1.38	50.22	0.989	17.37	3.99	1.000
0.8 g/L	2.05	33.80	0.930	24.40	2.84	1.000
1.0 g/L	2.07	33.48	0.976	33.80	2.05	1.000
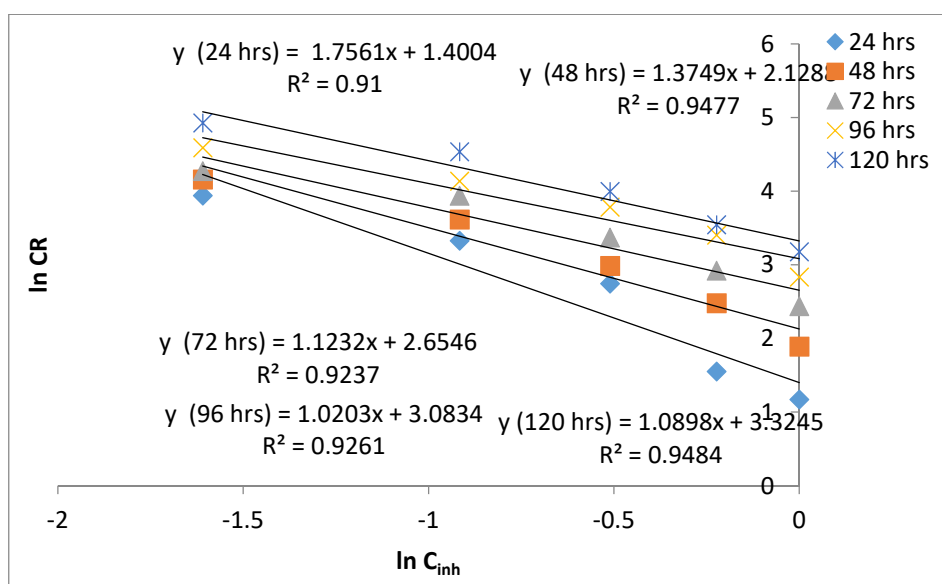
Figure 9. Plot of ln CR against ln C_{inh} to determine reaction order
for OGHE adsorption onto Al surface in 1.5 M H_2SO_4

Table 6. Kinetic parameters of OGHE adsorption
onto Al surface in 1.5 M H_2SO_4

Time (hrs)	n	R^2
24	1.7561	0.910
48	1.3749	0.948
72	1.1232	0.924
96	1.0203	0.926
120	1.0898	0.948

Corrosion inhibition mechanism

In the absence of OGHE, dissociation of H_2SO_4 and dissolution of Al (Equations 19-22) occur in solution to form 2 moles of H^+, 1 mole of SO_4^{2-}, 1 mole of Al^{3+} and 1 mole of $[AlOH]^{2+}$ ions. The sulphide ion is then adsorbed on Al surface to form aluminium sulphide complexes $[AlSO_4]^+$ and $[AlOHSO_4]$ with Al^{3+} and $[AlOH]^{2+}$ respectively in the anodic reaction. These complexes are the main soluble corroded Al form which makes its surface to corrode easily in H_2SO_4 solution in the absence of OGHE. In the cathodic reaction, 2 moles of H^+ picked up the released electron in the anodic reaction to produce chemisorbed hydrogen. The chemisorbed hydrogen then combines with each other to form H_2 gas molecule which escapes from the Al surface. The main controlling steps in the Al dissolution are the complexes formation reactions presented as Equations 23-24.
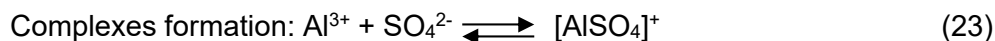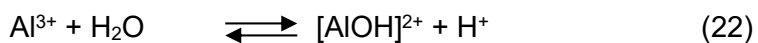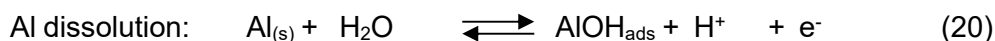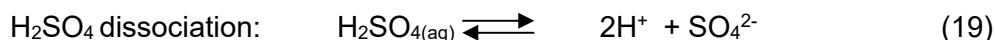
$$H_2SO_4 \text{ dissociation:} \qquad H_2SO_{4(aq)} \rightleftharpoons \qquad 2H^+ + SO_4^{2-} \qquad (19)$$

$$\text{Al dissolution:} \qquad Al_{(s)} + H_2O \rightleftharpoons AlOH_{ads} + H^+ + e^- \qquad (20)$$

$$AlOH_{ads} + 5H_2O + H^+ \rightleftharpoons Al^{3+} + 6H_2O + 2e^- \qquad (21)$$

$$Al^{3+} + H_2O \rightleftharpoons [AlOH]^{2+} + H^+ \qquad (22)$$

$$\text{Complexes formation:} \ Al^{3+} + SO_4^{2-} \rightleftharpoons [AlSO_4]^+ \qquad (23)$$

$$[AlOH]^{2+} + SO_4^{2-} \rightleftharpoons [AlOHSO_4] \qquad (24)$$

In the presence of OGHE, corrosion inhibition of Al surface in H_2SO_4 is enhanced by:

(1) formation of thin film protective coatings resulting from adsorption of anionic OGHE on positive sites formed on Al surface due to electron liberation during the anodic reactions (Equations 20-21). The thin film acts as a barrier between Al surface and H_2SO_4 and thus prevents loss of Al atoms into the acidic solution which in return limits the corrosion rate.

(2) replacement of water molecules present in solution by adsorbed soluble OGHE molecules on Al surface which alters kinetics of Al dissolution (Equation 4).

(3) presence of functional hydroxyl groups (revealed by FTIR) in the phenolic compounds of γ-oryzanols, α-tocopherol and γ-tocopherol (Figure 10) which are major constituents of OGHE molecules [36-38]. These –OH groups bridge the gap between OGHE molecules and Al surface and thus minimises corrosion rate.

(4) presence of valent heteroatom (oxygen) attached directly to aromatic rings of α- and γ-tocopherol (Figures 10(b-c)) enhances donor–acceptor surface complexes formation between OGHE p-electrons and Al vacant d-orbital. This alters the electrochemical characteristics of the system and thus, leads to reduction in corrosion.

(5) extended size and nature of γ-oryzanols, α-tocopherol and γ-tocopherol compounds present as OGHE molecules which cover large areas on the Al surface and thus inhibit its corrosion.
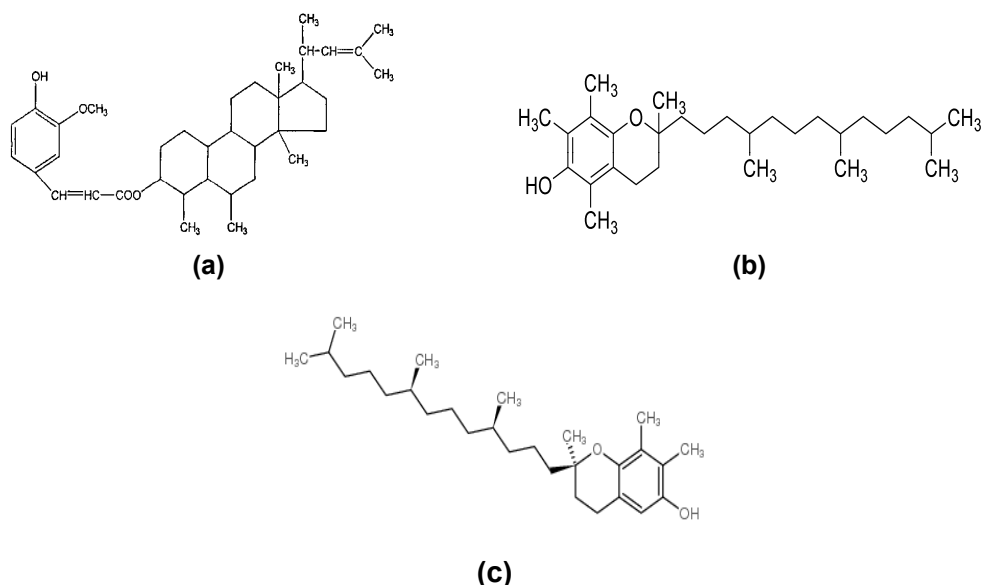
Figure 10: Phenolic compounds of (a) γ-oryzanols (b) α-tocopherol and (c) γ-tocopherol present in OGHE

CONCLUSIONS

Experimental works executed in this study revealed that Al has corrosion resistance attributes in H_2SO_4 solution in the presence of OGHE. Formation of pitting and small holes on Al surface in H_2SO_4 solution was revealed by SEM. Presence of –OH (attached to the phenolic rings of γ-oryzanols, α-tocopherol and γ-tocopherol) and –NH was revealed by FTIR. Attachment of sulphur, oxygen and hydrogen on Al surface in aqueous H_2SO_4 was shown by EDS. Reduction in concentration of Al^{3+} loss in acidic medium in the presence of OGHE was revealed by AAS. Corrosion rate of Al increased in H_2SO_4 solution as exposure period (24 - 120 hrs) and temperature

(293 - 333K) were increased but decreased with pH (2 - 6). Corrosion inhibition efficiency of OGHE primarily depends on its concentration and adsorptive capability on Al surface via formation of thick protective films. Adsorption of OGHE molecule on Al surface in 1.5 M H_2SO_4 solution agrees perfectly with Langmuir isotherm. Thermodynamic study revealed adsorption of OGHE molecule on Al surface to be spontaneous, endothermic and physisorption in nature. Kinetic study affirmed adsorption of OGHE molecule on Al surface to follow second order reaction. Corrosion mechanism was enhanced by Al dissolution in H_2SO_4 solution and presence of –OH group attached to phenolic compounds of γ-oryzanols, α-tocopherol and γ-tocopherol present in OGHE.

EXPERIMENTAL

Materials

Table 7 presents the chemical composition of commercial aluminium used for this study supplied by Alok Hefsibah Global Trust Limited. Ethanol, acetone, grades of silicon carbide paper and sulphuric acid (*all of analytical grades*) were supplied by Top-Jay Scientific. *Oryza Glaberrima* husk, left as remnant, was obtained from Bodija International Market, Oyo State, Nigeria.

Table 7. Chemical Composition of Aluminium Used

Element	Al	Mg	Si	Mn	Fe	Zn	Ti	Cu	Cr	Pb
(%)	97.82	1.06	0.57	0.41	0.11	0.0093	0.0082	0.0061	0.0039	0.0025

Aluminium coupon preparation

Grades of silicon carbide paper were used to polish the aluminium to remove dirts. Polished aluminium was then cut into coupons of same dimension (6×4×0.4 cm) and exposed surface area (24 cm^2) with aid of a digital vernier calliper. Acetone was used to degrease the aluminium coupons while distilled water was used to thoroughly rinse them. Samples were dried and kept in desiccator for subsequent weight loss experiment.

Extract and corrosion inhibitor preparation

Clean water was used to thoroughly wash the *Oryza Glaberrima* husk to remove unwanted dirt after which it was dried in an oven for 24 hours at 120°C. Mechanical grinder was used for the dried *Oryza Glaberrima* husk

and was later sieved to obtain fine particles of < 63 µm. The particles were kept in clean polythene bags and sealed to prevent further moisture contamination. Soxhlet extraction process was adopted to get extract from particles at room temperature (28 ± 3 °C) using analytical grade ethanol. The filtrate obtained (which stands as the extract used as corrosion inhibitor) was later subjected to evaporation to remove excess ethanol and then stocked for experiment. Different concentrations of *Oryza Glaberrima* husk extract (OGHE) (0.2, 0.4, 0.6, 0.8 and 1.0 g L^{-1}) were prepared and used as corrosion inhibitor for Al in 1.5 M H_2SO_4 solution.

Weight loss measurement

Aluminium coupons were tested in sulphuric acid using weight loss measurement. Weights of aluminium coupons were checked before and after immersion in 1.5 M H_2SO_4 solution in the presence and absence of OGHE. After the immersion time is elapsed, coupons were removed from acidic solution and then washed with distilled water and acetone. Specimens were dried using hot air and allowed to cool for 10 minutes. Equations 1-3 were used to calculate the corrosion rate, inhibition efficiency and surface coverage respectively using weight loss values after each experiment via digital weighing balance.

$$CR\ (mm/y) = \frac{87,500W}{A\rho t} \tag{1}$$

$$I.E.\% = \left(1 - \frac{CR_{inh}}{CR_{blank}}\right) \times 100 \tag{2}$$

$$\theta = \left(1 - \frac{CR_{inh}}{CR_{blank}}\right) \tag{3}$$

where CR = corrosion rate (mm y^{-1}), W = weight loss (g), A = coupon area (cm^2), ρ = density (g cm^{-3}), t = immersion time (hr), *I.E.%* = inhibition efficiency, CR_{inh} = corrosion rate in the presence of inhibitor and CR_{blank} = corrosion rate in the absence of inhibitor, θ = surface coverage.

Extract and coupon characterization

FTIR analysis

OGHE and corrosion products of aluminium in 1.5 M H_2SO_4 in the presence of OGHE were characterized by FTIR within wavelength of 400 - 4000 cm^{-1} via Nicolet iS10 Fourier transform infra-red spectrophotometer.
Scanning electron microscopy/energy dispersive spectroscopy

SEM/EDX-JEOL-JSM 7600F scanning electron microscope was used to examine the surface morphology of aluminium coupon in the presence and absence of OGHE. The energy dispersive spectroscopy (EDS) analysis was executed via attached accessories of scanning electron microscope.

Atomic absorption spectroscopy

AAS Buck Scientific 210 VGP atomic absorption spectrometer was used to check Al^{3+} concentration in H_2SO_4 solution after weight loss measurement.

REFERENCES

[1] D. Miller, *Mater Perform*, **1990**, *29*, 10–11.

[2] K.R. Trethewey, P.R. Roberge, *British Corro J*, **1995**, *30*, 192–197.

[3] S.K. Sharma, P. Anjali, O.I. Bassey, *J. Anal. Sci. Technol*., **2015**, *6*, 26-35.

[4] A.M. Abdel-Gaber, B.A. Abd-El-Nabey, M. Saadawy, *Corrosion Sci.*, **2009**, *51(5)* 1038-1042.

[5] A. Yurt, S. Ulutaas, H. Dal, *Appl. Sur. Sci.*, **2006**, 253, 919-925.

[6] I.B. Obot, N.O. Egbedi, S.A. Umoren, *Int. J. Electrochem. Sci.*, **2009**, *4*, 863–877.

[7] A.S. Fouda, A.A. Al-Sarawy, F.S. Ahmed, H.M. El-Abbasy, *Corros. Sci.*, **2009**, *51*, 485-492.

[8] M.M. Ihebrodike, A.U. Anthony, B.O. Kelechukwu, G.A. Alozie, *Afr. J. Pure Appl. Chem.*, **2010**, *4*, 158-165.

[9] Q. Zhang, Z. Gao, F. Xu, X. Zou, *Colloids Surf. A Physicochem. Eng. Aspects*, **2011**, *380*, 191–200.

[10] L. Nnanna, I. Anozie, A. Avoaja, C. Akoma, E. Eti, *Afr. J. Pure Appl. Chem.*, **2011**, *5*, 265-271.

[11] N.O. Obi-Egbedi, I.B. Obot, S.A. Umoren, *Arab. J. Chem.*, **2012**, *5(3)*, 361–373.

[12] K.S. Sanjay, P. Anjali, I.B. Obot, *J. Anal. Sci. Technol.*, **2015**, *6*, 26-33.

[13] M. Abdallah, B.A. Al-Jahdaly, *Int. J. Electrochem. Sci.*, **2015**, *10*, 9808–9823.

[14] R.S. Nathiya, R. Vairamuthu, *Egypt. J. Petroleum*, **2017**, *26*, 313-323.

[15] L.T. Popoola, *Corros Rev,* **2019**, *37(2)*, 71-102.

[16] M. Finsgar, J. Jackson, *Corros. Sci.*, **2014**, *86*, 17-41.

[17] O.O. Adeyemi, O.O. Olubomehin, *Pacific J. Sci. Technol*., **2010**, *11*, 455-462.

[18] D.I. Udunwa, O.D. Onukwuli, M. Omotioma, *Der Pharma Chemica*, **2017***, 9,* 19, 48–59.

[19] N. Mohamad, N.K. Othman, A. Jalar, *AIP Conference Proceedings*, Faculty of Science and Technology Post-Graduate Colloquium, Selangor, Malaysia, **2013**, *1571*, 136-140.

[20] M.H. Mahross, A.H. Naggar, T.A.S. Elnasr, M. Abdel-Hakim M, *Chem Adv Mater*, **2016**, *1*, 6-16.

[21] M. Grube, J.G. Lin, P.H. Lee, S. Kokorevicha, *Afr. J. Geo-chem*., **2006**, *130,* 324–333.

[22] J. Majedova, *Spectroscopy*, **2003**, *32,* 1–10.

[23] A.Y. Musa, A.A. Khadom, A.H. Kadhum, A.B. Mohamad, M.S. Takriff, *Res. Chem. Intermed*., **2012**, *38*, 91-103.

[24] H.B. Stuart, "Infrared Spectroscopy, Fundamentals and Applications", **2004**, John Wiley Sons Ltd.

[25] A. Singh, I. Ahamad, D.K Yadav, V.K. Singh, M.A. Quraishi, *Chem. Eng. Commun*., **2012**, *199*, 1, 63–77.

[26] A.J. Aldykewicz, H.S. Isaacs, A.J. Davenport, *J. Electrochem. Soc*., **1995**, *142*, 3342-3350.

[27] Q.B. Zhang, Y.X. Hua, *Electrochem. Acta*., **2009***, 54*, 1881-1887.

[28] R.M. Hassan, I.A. Zaafarany, *Materials*, **2013**, *6*, 2436-2451.

[29] R. Solmaz, *Corros. Sci*., **2014**, *79*, 169–176.

[30] V.C. Anadebe, O.D. Onukwuli, M. Omotioma, N.A. Okafor, *S. Afr. J. Chem*., **2018**, *71*, 51–61.

[31] G.A. Ijuo, H.F. Chahul, I.S. Eneji, *J. Adv. Electrochem*., **2016**, *2(3),* 107–112.

[32] H. Keleş, M. Keleş, I. Dehri, O. Serindağ, *Colloids Surf. A Physicochem. Eng. Asp*., **2008**, *320*, 138–145.

[33] M. Abdallah, M.A. Hegazy, M. Alfakeerd, H. Ahmeda, *Green Chem. Lett. Rev.*, **2018**, *11(4),* 457–468.

[34] A.O. James, N.C. Oforka, O.K Abiola, *Bull. Electrochem.*, **2006**, *22*, 111-116.

[35] O.O Fadare, A.E. Okoronkwo, E.F. Olasehinde, *African J. Pure Appl. Chem.*, **2016**, *10(1),* 8–22.

[36] A. Moongngarm, N. Daomukda, S. Khumpika, *APCBEE Procedia*, **2012,** *2*, 73–79.

[37] S.H. Huang, L.T. Ng, *J. Agric. Food Chem.,* **2011**, 59(20), 11150–11159.

[38] S. Yu, Z.T. Nehus, T.M. Badger, N. Fang, *J. Agric. Food Chem,* **2007**, *55(18),* 7308–7313.

LIPIDOMICS: ADVANCED ANALYTICAL TECHNOLOGY TO IDENTIFY BIOMARKERS OF COLORECTAL CANCER

**CLAUDIU RĂCHIERIU[a,b], DAN T. ENIU[b,c],
EMIL MOIŞ[b,d], FLORIN GRAUR[b,d], CARMEN SOCACIU[e*],
MIHAI ADRIAN SOCACIU[f], NADIM ALHAJJAR[b,d]**

ABSTRACT. Lipidomics is an advanced analytical technology applying techniques like Gas- or Liquid Chromatography coupled with Mass Spectrometry or Magnetic Resonance Spectrometry to find the lipid biomarkers in tissues, blood or urine. This review selected significant results which show the impact of lipidomic investigations for discriminating the metabolic profiles and dysregulation of metabolic pathways in CRC patient's comparative to healthy controls. It focuses on the description of best methods and procedures to separate and identify hydrophobic molecules with molecular weights under 1000 Daltons, especially using high pressure liquid chromatography coupled with mass spectrometry. The main lipid classes involved in the onset and progression of CRC are presented, as well the alterations of lipid-related cellular pathways during tumorigenesis. Especially lipid profile changes (of cerotic acid, hydroxylated, polyunsaturated fatty acids, free fatty acids, oxylipins, glycero-phospholipids, di- and triglycerides, sphingomyelins and ceramides) showed significant differences and can be considered reliable biomarkers to discriminate between early and advanced stages of CTC malignancy, prognosis or survival prediction.

Keywords: metabolomics, lipidomics, colorectal cancer, biomarkers.

[a] *Surgery Department. County Hospital Alba, Bld. Revolutiei 1989 No.23, Alba Iulia, Romania*
[b] *Department of Oncological Surgery and Gynecological Oncology, "Iuliu Haţieganu" University of Medicine and Pharmacy, 34-36 Republicii Str, 400015 Cluj-Napoca, Romania*
[c] *Department of Surgery, The Oncology Institute "Prof. Dr. Ion Chiricuţă", Cluj-Napoca*
[d] *Faculty of Medicine, Iuliu Hatieganu University of Medicine and Pharmacy, Cluj-Napoca, Romania; Surgery Department, Regional Institute of Gastroenterology and Hepatology "Octavian Fodor", 19-21 Croitorilor Street, Cluj-Napoca, Romania*
[e] *R&D Center for Applied Biotechnology in Diagnosis and Molecular Therapy, BIODIATECH-Proplanta Cluj-Napoca, Romania*
[f] *Faculty of Medicine, Iuliu Hatieganu University of Medicine and Pharmacy, Cluj-Napoca, Romania; Radiology Department, Regional Institute of Gastroenterology and Hepatology "Octavian Fodor", 19-21 Croitorilor Street, Cluj-Napoca, Romania*
* *Corresponding author: csocaciu@proplanta.ro*

CLAUDIU RĂCHIERIU, DAN T. ENIU, EMIL MOIŞ, FLORIN GRAUR,
CARMEN SOCACIU, MIHAI ADRIAN SOCACIU, NADIM ALHAJJAR

Abbreviations

Cer: Ceramide; CEA: carcinoembryonic antigen; CRC: Colorectal cancer; CTC: computed tomography colonography; FFA: Free fatty acid; GTA: Gastrointestinal tract acids; HETE: Hydroxyeicosatetraenoic acid; HODE: 13-hydroxyoctadecadienoic acid; LA: Linoleic acid; Lysophosphatidic acid; LOX- lipoxygenase; LPC: Lysophosphatidylcholine; MUFA: Monounsaturated fatty acid; PA: Phosphatidic acid PC: Phosphatidylcholine; PE: Phosphorylethanolamine; PG: Prostaglandin; PL: Phospholipid; PUFA: Polyunsaturated fatty acid; RBC: Red blood cell; SFA: Saturated fatty acid; SM: Sphingomyelin; SPL: Sphingolipid; TAG: Triacylglycerol;

INTRODUCTION

Colorectal Cancer (CRC) is an important public health issue, belongs to the three leading causes of cancer-related mortality in both men and women [1,2], particularly in Western Countries but also in developing countries, and is strongly related to stress and food habits. The American Cancer Society estimated 104610 cases in 2020, and other 43,340 new cases in US, around 12% diagnosed in patients less than 50 years old [3]. The incidence is 30% higher in men compared to women with an increased incidence (60%) for rectal cancer, compared to colon cancer. The early detection and endoscopic resection of adenomatous polyps (premalignant conditions) and screening colonoscopy improved significantly the survival rate (American Cancer Society, 2020). The decline of mortality during the last two decades are due to improvements in treatment (12%), changes in CRC risk factors (35%), and screening (53%) as well as due to early diagnosis, with a CRC decline of 64% after 5 years and 58% after 10 years [4].

Recent data compared different ways to diagnose CRC, many including a preliminary colonoscopy and biopsy [5-7] and more and more, imaging technologies [8-10].

Blood is particularly useful for biomarker research, as it can be obtained more easily and less invasively than other biological materials. That is the reason why scientists are searching for other screening methods with a good predictive value and high sensitivity. Metabolomics is an advanced non-invasive technology which includes a systematic screening, fingerprinting of small metabolites (with molecular weight less than 5000 Da) which are related to the metabolic signature of a certain tissue or biofluid (blood, urine, saliva).

Metabolomics and metabonomics offer a qualitative description (fingerprint) and the quantitative measurement, respectively. If the screening refers specifically to lipid molecules involved in metabolism, this screening is named Lipidomics, which include two types of techniques: untargeted lipidomics,

a comprehensive analysis of all the measurable lipid molecules in a sample including unknown chemicals, and targeted lipidomics, which measure defined groups of known lipids, that are characterized and chemically annotated [11, 12]. This technique uses advanced analytical platforms and techniques, such as gas-chromatography or high performance liquid chromatography coupled with mass spectrometry (GC-MS, HPLC-MS), Magnetic resonance (NMR), capillary electrophoresis (CE), which are improved continuously to identify constellations, patterns of metabolites related to specific pathways and pathologies [13].

Based on recent literature findings, this review focuses on the description of best methods and procedures to separate and identify hydrophobic molecules with molecular weights under 1000 Daltons, especially using liquid chromatography coupled with mass spectrometry. The changes of the turnover of these molecules in tissues or blood may reflect an accurate diagnosis of CRC. The main lipid classes involved in the progression of CRC are also presented, as well the alterations of lipid-related cellular pathways during tumorigenesis.

LIPID CLASSES AS PUTATIVE CRC BIOMARKERS

Lipids are a very complex category of metabolites, including molecules with multiple structures and roles in cellular signaling and energy fuels [14]. Lipids are considered potential biomarkers in malignancy, therefore lipidomic studies are strongly developed the last two decades, helping the understanding, diagnosis and treatment of cancer and meanwhile to be good prognostic or screening biomarkers for early diagnosis and targeted therapies [15].

Figure 1 represents the main classes of lipids which may be considered as diagnosis biomarkers of many pathologic disturbances.
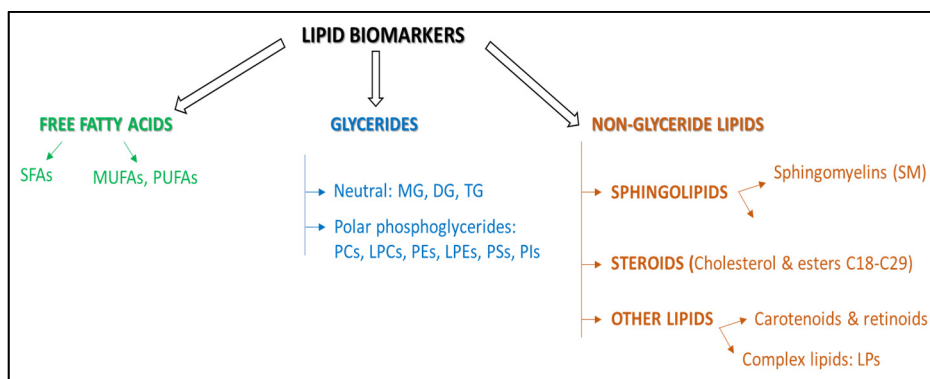

Figure 1. Main lipid classes, considered as potential biomarkers for many pathologies, including CRC. For details see abbreviations.

The lipid alterations are associated with colorectal cancer (CRC), since cancer cells can generate energy in a nutrient-deficient environment, prefer glycolysis against oxidative phosphorylation. However, recently this paradigm shifted towards a "reversed Warburg effect", some cancer cells, including CRC cells may synthesize ATP by of mitochondrial phosphorylation [16,17], opening new research directions for the identification of molecular therapeutic targets, such as fatty acids (FAs) synthesis and oxidation. The metabolization of exogenous glutamine represents another dependence of cancer cell, many oncogenic mutations affecting glutamine metabolism [18]. Meanwhile the alterations of lipid metabolism in CRC lead to structural changes in cell membranes, disruption of energy homeostasis, cell signaling, gene expression and protein distribution, affecting a number of cell functions, such as proliferation, differentiation, apoptosis, autophagy, necrosis, drug and chemotherapy resistance [19, 20]. The role of lipids and their metabolism in cancer development and spread raises a growing interest of researchers, as shown in previous reviews [1, 21]. The lipid metabolic pathways affected in CRC cells include FAs synthesis, desaturation, elongation and mitochondrial oxidation of the FAs. A summary of the main changes in the lipid composition of different biological samples from CRC patients, as shown in recent references, is presented in Table 1.

Table 1. Changes in lipid composition of different biological samples from CRC patients

Biological sample	Lipid species/potential biomarkers	Change tendency	References
Tissue	PCs, especially PC(16:0/16:1)	Increase	[22]
	Total lipids, Cerotic acid	Increase	[23-25]
	TAGs	Decrease	[26,27]
	Lipoxygenase	Increase	[28]
	FFAs 22:4	Increase	[21, 29, 30]
	Ceramides and endo cannabinoid	Decrease	[29]
	LPC 20:4,LPA	Increase	[31]
	LPC 22:6	Decrease	[31]
	PA 34:0, 36:2	Increase	[30, 31]
Plasma	LPC	Increase	[25, 31, 32]
	Fatty acids synthesis	increase	[33-35]
	MUFAs/PUFAs	Increase	[30]
	Ethanolamine plasmalogens fatty acids and polar lipids		[36, 37]
	Decanoic acid	Increase	[38]
	LPC18:0	Decrease	[39]
Serum	Total lipids C15:0, C18:0, C18:0,C18:2, C18:3	Decrease	[23, 40, 41]

Biological sample	Lipid species/potential biomarkers	Change tendency	References
	Total lipids C22:0, C24:0, C26:0, C26:0, C30:0, C18:1	Increase	[23, 41]
	Ultralong chain fatty acids	Decrease	[42]
	Oxilipins, HODE, HETE	Decrease	[43]
	Endocannabinoids and ceramides	Increase	[44]
	Sphingomyelins, Ceramides, eicosanoids	Increase	[45-47]
	GTA-446	Increase	[48]
	Succinate, N2, N2-dimetihylguanosine, adenine, citraconic acid,methylguanosine	Increase	[49]

The complex lipid metabolic changes may be explained by the high proliferation rate of the CRC cells, with high energetic needs, changes in the serum levels of phospholipid components derived from cell membrane degradation, accompanied by inflammation and changes in the arachidonic acid metabolites in serum or tissue.

A recent study focused on a single metabolite as a potential biomarker for early detection of CRC, namely long-chain (C28) hydroxylated polyunsaturated fatty acids or gastrointestinal tract acids (GTAs). Analyzing serum samples from 225 CRC patients and 916 healthy volunteers, it was concluded that GTA-446 does not reflect the presence of a tumor, but the susceptibility to CRC and helps to identify high-risk CRC patients with high sensitivity, encouraging the colonoscopy [46].

Another study identified decreases of LPCs, associated with body weight loss and activated inflammatory status in CRC patients [50]. Another 2019 published paper, based on the study of plasma form 268 CCR patients and 353 controls, finds all the LPC positively correlated as it follows: seven LPCs were detected at lower levels among colorectal cancer patients compared to controls, mainly LPC (16:0 and 18:0), in accordance with previous studies. This pattern might reflect an increased degradation rate of LPCs as a result of the accelerated cell proliferation (LPEs20:4 and 22:6) were increased in CRC patients compared to controls [51, 52].

An important aspect of CRC tumorigenesis is related to the eicosanoids (arachidonic acid metabolites) and their oxidized forms via cyclooxygenase-2 and 15- lipoxygenase-1 activities, these enzymes having opposite effects: the first one generates prostaglandin E2 which stimulates tumorigenesis while the second one inhibits interleukin-1 and tumor necrosis factor TNFα and suppresses colonic tumorigenesis [48]. Meanwhile 13-HODE levels were significantly decreased in cancer and colorectal polyp mucosa, as a specific alteration in the LOX product profile associated with human colorectal tumorigenesis. No significant differences between normal, polyp and cancer mucosa were noticed for 12-HETE, 15-HETE or leukotriene B4 levels [28].

CLAUDIU RĂCHIERIU, DAN T. ENIU, EMIL MOIŞ, FLORIN GRAUR,
CARMEN SOCACIU, MIHAI ADRIAN SOCACIU, NADIM ALHAJJAR

LIPID BIOMARKERS IN RELATION TO CRC DIAGNOSIS AND STAGE

In 2012, in a study including 52 CRC patients and 52 healthy controls there were 15 metabolites identified categorized in four lipid classes. The authors found a lipid metabolic model containing palmitic amide, oleamide, octadecanoic, hexadecanedioic, myristic and eicosatrienoic acids, lysophosphatidylcholines such as LPC(16:0), LPC(18:2), LPC(20:4), LPC(22:6) with a good statistics as potential biomarkers (AUROC value of 0.991) to discriminate early stage patients from healthy controls, above the prediction made by carcinoembryonic antigen (CEA) [31].

The up-regulated and down-regulated metabolites through the various stages of CRC were identified in a study which included 56 CRC patients, 60 healthy controls and 59 patients with adenomas. Benzoic acid showed high AUROC value, octanoic and decanoic acids were up-regulated and proportional to CRC stage, but their diagnostic predictability was not high [47].

A study on plasma samples of 30 CRC patients revealed changes of medium-chain fatty acids (6 up to 12 C) while a targeted metabolomic approach of further 117 patients revealed that decanoic acid (C10:0) had the best AUROC values in discriminating CRC patients from healthy individuals and may prove an excellent biomarker for screening [38].

A panel of 13 metabolites for the discrimination between CRC patients and healthy controls as well as 14 biomarkers for the discrimination between CRC and benign polyp patients, many of them derived from lipid metabolism: glyceraldehyde, hippuric acid, linolenic acid, glycochenodeoxycholate, glycocholate were recently reported [53]. Adding to the metabolic model four clinical factors (age, gender, smoking and alcohol consumption), the AUROC scores reached values of 0.93–0.95, in differentiating CRC patients from healthy controls or polyp patients respectively. Another study showed that β-hydroxybutyrate increased continuously from stage I to stage IV CRC while tryptophan and indole acrylic acid were decreasing continuously [54-56].

PREDICTIVE VALUE OF LIPID METABOLITES

The main predictive factor for CRC is considered to be the stage of diagnosis [57] underlying the importance of CRC screening and early diagnosis. A Japanese study reported a prediction model for 60 CRC patients comparative to 60 controls which included 4 metabolites (2-hydroxybutyrate, aspartic acid, kynurenine, and cysteamine) that showed better statistical power (AUROC, sensitivity, specificity and accuracy above 0.9 and 85% respectively) higher than CEA or CA 19.9 [58].

Using an MRI technique another model of 8 lipid and non-lipid metabolites (pyruvic, fumaric and glycolic acid, palmitoleic acid, ornithine, lysine tryptophan and 3-hydroxyisovaleric acid showed significant results [59]. Yang et al. [60] reported a 9 metabolites model that can predict the response to neoadjuvant chemotherapy for CRC. Metabolic profiles of 30 non-response patients were compared to those of 27 response cases and 6 metabolites related to lipid metabolism were found: Dioleoyl lecithin, 11-Keto-beta-boswellic acid, CE(18:2), SM(d16:1/18:1) and PCs 18:1/2:0 and16:1/22:6). All these lipids were upregulated in the response group compared with non-response group.

Another study [44] analyzed serum fingerprints from 20 CRC patients prior to surgery and one month after the radical intervention, compared to 20 healthy volunteers. The potential biomarkers were lipid classes PCs, LPCs and DGs, with low statistical difference between the pre-operative and post-operative status. One study developed in China and the United States found a common 15 metabolite pattern that could allow assessment of the CRC recurrence rate and survival of the patients after surgical intervention or chemotherapy. Using GC-MS of 376 surgical tissue specimens from four centers a panel of 15 metabolites was selected, able to distinguish between CRC patients having better prognostic outcomes, i.e., longer time-to-recurrence (52.9 vs 25.9 months), and better 5-year survival rate (67.0 vs 44.7 months), earlier recurrence and lower survival rates. Out of these 15 metabolites, 4 were lipid molecules: glycerol, myristate, palmitoleate, 2-aminobutyrate [24].

PROSPECTIVE STUDIES

Recently, a relevant serum MS study for lipophilic metabolites made on 66 patient-control pairs, under the European Prospective Investigation into Cancer and Nutrition (EPIC), reported 9 metabolites to be related to CRC etiology and were recommended for further CRC prospective studies. Four other features seem to be involved in disease progression (reverse causality), as a potential, valuable biomarkers for early CRC detection, e.g. ultralong chain fatty acids which are decreased in the serum sample of CRC patients [42].

In another prospective study published in 2018 that included 250 incident cases with CRC 35 metabolites were found associated with CRC risk, including 12 glycerophospholipids, 9 decreasing, 3 increasing the CRC risk. The dysregulation of glycerophospholipids might have an important role in the risk of developing colorectal cancer [51].

A German prospective study, with average follow-up of 8.3 years, investigated the association between the pre-diagnosis levels of 120 metabolites and the risk of breast, prostate and colorectal cancer. The study included a

subset of 163 CRC patients from over 25000 population of EPIC-Heidelberg study. It was concluded that changes in plasma lipid composition precede the appearance of neoplasia for several years and that tumor changes can cause a global change in LPC metabolism. It seems that the high level of LPC 18:0 (unsaturated fatty acids) would be a protective factor [39].

LIPID BIOMARKERS TO DISTINGUISHING BETWEEN ADENOMAS AND MALIGNANT TUMORS

Using ^{1}H-NMR spectrometry, the blood serum of 40 CRC patients, 32 polyp patients and 38 healthy controls was analyzed. Glutamine, succinate, glycerol, aspartate, and lactate were the potential non-lipid biomarkers in the colorectal polyp group data, while in the CRC patients' group, lactate, glycine, glutamate, glutamine, and aspartate were found as potential biomarkers. The authors observed similarities and differences between the metabolism of colorectal polyps and CRC patients, but the level of choline was significantly elevated in both CRC and colorectal polyp groups. On the other hand, 3-hydroxybutyrate, PUFAs and glycerol (from the glycerolipid metabolism), were abnormal in the colorectal polyp [45]. Regarding the specificity of lipid metabolites there are some similarities and differences between colorectal polyps and CRC, compared with healthy volunteers. Another group found in serum samples that glycerolipid metabolism was modified in the colorectal polyp (higher levels of lipids and PUFAs and lower level of glycerol) [61]. The authors draw the possible conclusion that glycerolipid metabolism is involved in the ATP generation. The explanation for increased levels of choline-related metabolites in tumors is probably the result of accelerated lipid membrane metabolism involved in the ATP generation, due to rapid cell proliferation. Glucose changes were consecutive to glycolysis, upregulated in CRC while increases of 3-hydroxybutyrate, an end metabolite of fatty acids suggests the upregulation of fatty acid β-oxidation needed as energy support cancer cell proliferation [45]. Increased oxidative stress is usually associated with increased oxidation of fatty acids, which may result in an accumulation of 3-hydroxybutyrate [24].

RELATIONSHIPS BETWEEN CRC AND OTHER METABOLIC DISEASES

There are some question marks about the specificity of above-mentioned biomarkers related specifically to CRC, or if these lipid metabolites are generally characteristic to tumoral processes or are influenced by other dysmetabolic

diseases (e.g. metabolic syndrome - obesity or diabetes). When the metabolic pathway differences between visceral and subcutaneous adipose tissue were studied in CRC patients by metabolomic and transcriptomic methods, increases of proinflammatory lipid metabolism was observed, increase of free arachidonic acid, activation of phospholipases and prostaglandin synthesis–related enzymes [62].

Many articles demonstrated positive relationships between obesity, diabetes, dyslipidemia and CRC. In the etiopathogenesis of CRC in obese/over-weight patients, fat tissue is very important in tumorigenesis, since it acts like glandular tissue, develop endocrine, paracrine and autocrine functions, controlling triglyceride metabolism, affecting the coagulation system and suppressing the anti-lipolytic action of insulin [63]. The literature data regarding the correlation between serum cholesterol, the triglycerides levels and the risk of CRC are not homogenous. In a large-scale cohort study, increased serum TGs levels were associated with higher risk of rectal cancer, as well as in lung, gynecological cancers and thyroid cancer, but not in colon cancer [64]. Another study showed good positive correlation between TG level and CRC, modest positive correlation between total cholesterol and CRC in male patients but not in women [65].

Meanwhile the levels of polar metabolites like nucleotides, nucleosides, and their metabolites, branched chain and aromatic amino acids have been correlated positively or negatively with obesity and diabetes, whereas glutamine and glycine levels are decreased, depending on the degree of insulin resistance in obese subjects. Serum concentrations of LPCs had inverse correlation with the body mass index, body weight and waist and hip circumference and treatment with metformin decreases the CRC risk in diabetic patients [66].

Men with type 2 diabetes mellitus have important risk in developing proximal CRC while in women no significant correlation was found [60, 67, 68]. Also, the particular association of fatty acids, high levels of linoleic acid, odd-chain and very long-chain fatty acids was correlated with a decreased incidence of type 2 diabetes and influenced by metabolic, genetic and nutritional factors [69, 70].

CONCLUSION

The recent evolution of metabolomics as a technology to investigate beyond fingerprints and biomarkers, the mechanisms of CRC evolution [71, 72] was diversified towards lipidomic profile, which already proved a great potential as a high value for a proper metabolic signature of tissues and biofluids from CRC patients and to discriminate significantly between healthy

controls, benign polyps versus malignant tumors [73]. Specific classes of lipids involved in cellular signaling and energy provision proved to be good biomarkers for CRC in different stages, during treatment monitoring or as prognosis factors.

Integrated approaches using advanced ultrahigh performance liquid chromatography-high resolution mass spectrometry revealed the deep involvement of lipid molecules in CRC pathology [74, 75]. Lipid profile alterations in particular, *e.g.* presence of cerotic acid or a decrease in hydroxylated, polyunsaturated long-chain fatty acids, an increase short free fatty acids, oxylipins, glycerophospholipids, di- and triglycerides, sphingomyelins and ceramides showed statistically significant differences and can be considered reliable biomarkers, differentiating between early and advanced stages of this malignancy or serving as survival predictors. The complex data base Lipid offers a great help for the identification of lipid biomarkers in CRC diagnosis and monitoring. Advanced methodology and studies on larger cohorts of patients are still needed for the development of clinically useful lipid biomarkers.

REFERENCES

1. R.L. Siegel; K.D. Miller; S.A. Fedewa; D.J. Ahnen; R.G.S. Meester; A Barzi; *Cancer J. Clin.,* **2017**, *67*, 177–179.
2. M.S. Cappell. *Gastroenterol Clin N Am*., **2008**, *37*, 1–12.
3. D.W. Sheneman; J.L. Finch; W.A. Messersmith; S. Leong; K.A. Goodman; S.L. Davis; *Colon Cancer*., **2017**, *6*, 49–56.
4. B.K. Edwards; E. Ward; B.A. Kohler; C. Eheman; A. G. Zauber; R. N.Anderson; L. A. G. Ries; *Cancer,* **2010**, *116*, 544-557.
5. Pakiet; J. Kobiela; P. Stepnowski;T.Sledzinski; A.Mika; *Lipids Health Dis.,* **2019**, *18*, 29-38.
6. A.E. Obaro; D.N. Burling; A.A. Plumb; *Br. J. Radiol.,* **2018**, *91*, art. 20180307
7. Y. Nasseri; S.J. Langenfeld;.*Surg. Clin. North Am.,* **2017**, *97*, 503-513.
8. J. Zhang; Z. Cheng; Y Ma; C. He; Y. Lu; Y. Zhao; X. Chang; Y. Zhang; Y. Bai; N. Cheng; *Clin Colorectal Cancer*, **2017,** *16*, 252-263.
9. U. Ladabaum; J.A. Dominitz; C. Kahi; R.E. Schoen; *Gastroenterology,* **2020**, *158*, 418-432.
10. P.J. Pickhardt; *Radiol. Clin. North Am*., **2017**, *55*, 1183-1196.
11. D.S. Wishart; R. Mandal; A. Stanislaus; M. Ramirez¬Gaona; *Metabolites*, **2016**, *6*, 10-21.
12. L. D. Roberts; A. L. Souza; R. E. Gerszten; C. B. Clish; Targeted metabolomics. *Curr. Protocols in Mol. Biol*., **2012**, 1(SUPPL.98), Chapter 30, Unit 30-30.2.24
13. A.D. Beggs; M. P. Dilworth; *Br. J. Surgery,* **2015**, *102*, e29-40.

14. E. Fahy; D. Cotter; M. Sud; S. Subramaniam; *Biochim. Biophys. Acta – Mol. Cell Biol. Lipids*, **2011**, *1811*, 637–647.
15. D.J. Stephenson; L.A. Hoeferlin; C.E. Chalfant; *Transl. Res.,***2017**,*189*,13–29
16. X.D. Xu; S.X. Shao; H.P. Jiang; Y.W. Cao; Y.H. Wang; X.C. Yang; *Oncol. Res. Treat*., **2015**, *38*,117–122.
17. V. Chekulayev; K. Mado; I. Shevchuk; A. Koit; A. Kaldma; A. Klepinin, *Biochem. Biophys. Reports,* **2015**, *4*, 11–25.
18. Y. Hao; Y. Samuels; Q. Li; D. Krokowski; B-J. Guan; C. Wang;*Nat.Commun.* **2016**, *7*, art.11971
19. C. Huang; C. Freter; *Int. J. Mol. Sci.,* **2015**, *16*, 924–949.
20. Y.Y.Zaytseva; J.W. Harris; M.I. Mitov; J.T. Kim; D.A. Butterfield; E.Y. Lee; *Oncotarget,* **2015**, *6*, 18891–904.
21. Currie E, Schulze A, Zechner R, Walther TC, Farese RV Jr.; *Cell Metab.,* **2013**,*18*, 15
22. N. Kurabe; T. Hayasaka; M. Ogawa; N. Masaki; Y. Ide; M. Waki;. *Cancer Sci.,* **2013**, *104*, 1295–1302
23. Mika; J. Kobiela; A. Czumaj; M. Chmielewski; P. Stepnowski; T. Sledzinski; *Cell Physiol. Biochem.,* **2017**, *41*, 722–730.
24. Y. Qiu; G. Cai; B. Zhou; D. Li; A. Zhao; G. Xie; H. Li; *Clin. Cancer Res.,* **2014**, *20*, 2136–2147.
25. Q. Zhang; H. Xu; R. Liu; R. Gao; X. Yang; W. Jin; Y. Zhang; K. Bi; Q. Li; *Anal. Chem.,* **2019**, *91*, 3389–3396.
26. Mika; A. Pakiet; A. Czumaj; Z. Kaczynski; I. Liakh; J. Kobiela; A. Perdyan; K. Adrych; W. Makarewicz; T. Sledzinski; *J. Clin. Med.,* **2020**, *9*, 1095-1105.
27. T. Liu; F. Peng; J. Yu; *Anal. Bioanal. Chem.,* **2019**, *411*, 5079–5088.
28. Shureiqi; D. Chen; R. S. Day; X. Zuo; F. L. Hochman; W. A. Ross; S. M. Lippman; *Cancer Prevention Res.,***2010**, *3*, 829–838.
29. L. Chen; H. Chen; Y. Li; L. Li; Y. Qiu; J. Ren; *Oncol Rep.,* **2015b**, *34*, 447– 454.
30. A. S. Guo; Y. Wang; D. Zhou; Z. Li; *Sci Rep.,* **2014**, *4*, 5959.
31. S. Li; B. Guo; J.W. Song; X.L. Deng; Y.S. Cong; P.F. Li; *Metabolomics*, **2013**, *9*, 202–212.
32. Z. Zhao; Y. Xiao; P. Elson; H. Tan; S.J. Plummer; M. Berk; *J Clin Oncol.* **2007**, *25*, 2696–2701.
33. M. Okuno; K. Hamazaki; T. Ogura; H. Kitade; T. Matsuura; R. Yoshida; *In Vivo,* **2013**, *27*, 203–210.
34. L.M. Butler; J-M. Yuan; J.Y. Huang; J.Su; R. Wang; W-P. Koh; *Precis Oncol.,* **2017**, *1*, 38.
35. J. Zhang; L. Zhang; X. Ye; L. Chen; L. Zhang; Y. Gao; *Prostaglandins Leukot Essent Fat Acids*., **2013**, *88*, 355–360.
36. S. Shen; L. Yang; L. Li; Y. Bai; C. Cai, H. Liu; *J. Chromatography B*, **2017**, *1068–1069*, 41-48.
37. T. Liu; Z. Tan; J. Yu; F. Peng; J. Guo; W. Meng; Y. Chen; T. Rao; Z. Liu; J. Peng; *Expert rev. Proteomics*, **2020**, *17*, 233-242.
38. S. Crotti; E. Agnoletto; G. Cancemi; V. Di Marco; P. Traldi; S. Pucciarelli; M. Agostini; *Anal. Bioanal.Chem.,* **2016**, *408*, 6321–6328.

39. T. Kühn; A. Floegel; D. Sookthai; T. Johnson; U. Rolle-Kampczyk; W. Otto; R. Kaaks; *BMC Medicine*, **2016**, *14*, 13-26.
40. J. Zhu; D. Djukovic; L. Deng; H. Gu; F. Himmati; E.G. Chiorean; *J. Proteome Res.,* **2014**, *13*, 4120–4130.
41. Y. Kondo; S. Nishiumi; M. Shinohara; N. Hatano; A. Ikeda; T. Yoshie; *Biomark Med.*, **2011**, *5*, 451–460.
42. K. Perttula; C. Schiffman; W. M. B. Edmands; L. Petrick; H. Grigoryan; X. Cai; S. M. Rappaport; *BMC Cancer*, **2018**, *18*, 996-1010.
43. L. Zhang; B. Chen; J. Zhang; J. Li; Q. Yang; Q. Zhong; *Prostaglandins Leukot Essent Fat Acids*, **2017**, *120*, 25–31.
44. L. Chen; C. Zhang, Q. Gui; Y. Chen; Y. Yang; *Molecular Medicine Reports*, **2015**, *12*, 6879–6886.
45. J.H. Jung; K. Taniguchi; H.M. Lee; R. Bandu; K. Komura; *Sci. Rep.,* **2020**, *10*, art nr.6124.
46. X. Zuo; I. Shureiqi; *Prostaglandins and Other Lipid Mediators*, **2013**, *104–105*; 139–143K. Uchiyama; N. Yagi; K. Mizushima; Y. Higashimura; Y. Hirai; T. Okayama; Y. Naito; *J. Gastroenterol.,* **2017**, *52*, 677–694.
47. J. Zhu; D. Djukovic; L. Deng; H. Gu; F. Himmati; M. Abu Zaid; D. Raftery; *Anal. Bioanal. Chem.,* **2015**, *407*, 7857–7863.
48. T. Hata; I. Takemasa; H. Takahashi;N.Haraguchi; J. Nishimura; *Br. J. Cancer,* **2017**, *117*, 227–232.
49. I. Tan; Y. Qiu; X. Zou; T. Chen; G. Xie; Y. Cheng; W. Jia; *J. Proteome Res.,* **2013**, *12*, 3000–3009.
50. X. Shu; Y. B. Xiang; N. Rothman; D. Yu; H. L. Li; G. Yang; W. Zheng; *Int. J. Cancer,* **2018**, *143*, 527–534.
51. J. M. R. Geijsen; S. Brezina; P. Keski-Rahkonen; A. Baierl; T. Bachleitner-Hofmann; M. M. Bergmann; C. M. Ulrich; *Int. J. Cancer*, **2019**, 145, 1221–1231.
52. D. Djukovic; J. Zhang; D. Raftery; Colorectal cancer detection using targeted LC-MS metabolic profiling. In: *Methods in Molecular Biology,* **2018**, *1765*, 229–240 Humana Press Inc.
53. F. Farshidfar; A. M. Weljie; K. Kopciuk; W. D. Buie; A. Maclean; E. Dixon; O.F. Bathe; *Genome Med.,* **2012**, *4,* article nr. 42
54. F. Farshidfar; A. M. Weljie; K. Kopciuk; S. E. Hilsden; F. Mcgregor; W. D. Buie; O. F. Bathe; *Br. J. Cancer,m***2016**, *115*, 848–857.
55. F. Farshidfar; K.A. Kopciuk; R. Hilsden; S.E. Mcgregor; V.C. Mazurak; W.D. Buie; *BMC Cancer,* **2018**, *18*, 26-36.
56. American Cancer Society. *Colorectal Cancer Facts & Figures 2020-2022 Atlanta: American Cancer Society Inc.*, **2020**, 32 pg.
57. S. Nishiumi; T. Kobayashi; S. Kawana; Y. Unno; T. Sakai; K. Okamoto; M. Yoshida; *Oncotarget,* **2017**, *8*, 17115–17126.
58. S. Nishiumi; T. Kobayashi; A. Ikeda; T. Yoshie; M. Kibi; Y. Izumi; M. Yoshida; *PLoS ONE*; **2012**, *7*, e40459.
59. K. Yang; F. Zhang; P. Han; Z. Wang; K. Deng; Y. Zhang; Z. J. Zhu; *Metabolomics*, **2018**, *14*, article nr. 110.

60. J. Gu; Y. Xiao; D. Shu; X. Liang; X. Hu; Y. Xie; D.Lin; H. Li; *Dis. Markers*, **2019**, ID 3491852.
61. D. B. Liesenfeld; D. Grapov; J. F Fahrmann; M. Salou; D. Scherer; R.Toth; N. Habermann; J. Böhm; P. Schrotz-King; B. Gigic; M. Schneider; A. Ulrich; E. Herpel; P. Schirmacher; O. Fiehn; J.W. Lampe; C.M. Ulrich; *Amer. J. Clin. Nutr.,* **2015**, *102*, 433–443.
62. M. Muc-Wierzgoń; E. Nowakowska-Zajdel; S. Dzięgielewska-Gęsiak; T. Kokot; *World J. Gastroenterol.,***2014**, *20*, 9759-9774
63. H. Ulmer; W. Borena; K. Rapp; J. Klenk; A. Strasak; G. Diem; G. Nagel; *Br. J. Cancer*, **2009**, *101*, 1202-1206.
64. S. Strohmaier; M. Edlinger; J. Manjer; T. Stocks; T. Bjørge; W. Borena; H. Ulmer; *PloS One*, **2013**, *8*, e54242.
65. O. D. Rangel-Huerta; B. Pastor-Villaescusa; A.Gil; *Metabolomics*, **2019**, *15*, art nr. 93.
66. P. J. Limburg; R. A. Vierkant; Z. S. Fredericksen; C. L. Leibson; R. A. Rizza; A. K. Gupta; J. R. Cerhan; *Am. J. Gastroenterol.*, **2006**, *101*, 1872–1879.
67. S-W. Oh; Y.-H. Kim; Y. S. Choi; D. K. Chang; H. J. Son; P-L. Rhee; S. G. Shim; *Diseases of the Colon and Rectum*, **2008,** *51*, 56–61.
68. F. Imamura; S. J. Sharp; A. Koulman; M. B. Schulze; J. Kröger; J. L. Griffin; N. J. Wareham; *PLoS Medicine*, **2017**, article nr. 1410.
69. Y. X. Yang; S. Hennessy; J. D. Lewis; *Clin. Gastroenterol. Hepatol.,* **2005**, *3*, 587–594.
70. C. Johnson; J. Ivanisevic; G. Siuzdak; *Nat. Rev Mol. Cell Biol.,* **2016**, *17*, 451–459.
71. F. Zhang; Y. Zhang; W. Zhao; K. Deng; Z. Wang, *Oncotarget*, **2017**, *8,* 35460-35472.
72. F. Yan; H. Zhao; Y. Zeng; *Clin. Trans. Med.,* **2018**, *7*, 21-29.
73. G. Charkoftaki; D.C. Thompson; J.P. Golla; R. Garcia-Milian; T.K.T. Lam; J. Engel; *Chem. Biol. Interact.*, **2019**, *304*, 88-96.
74. Triebl; M. Trötzmüller; J. Hartler; T. Stojakovic; H.C. Köfeler; *J. Chromatogr. B.,* **2017**, *1053*, 72–80.
75. Y. Wang; S. Hinz; O. Uckermann; P. Hönscheid; W. von Schönfels; G. Burmeister; A. Hendricks; *Biochim. Biophys. Acta, Mol. Cell Biol. Lipid*, **2020**, *1865*, 158579.